



MONASH University

**Preparation of graphene, bismuth chalcogenide
and their heterostructures with application in
photonics and optoelectronics**

Jingchao Song

Master of Science (M.Sc.)

National University of Singapore

Thesis in the fulfilment of the requirements for the degree of
Doctor of Philosophy

Department of Materials Science and Engineering

Monash University

Australia

September 2016

To my family

Table of contents

Table of contents.....	I
Copyright notice.....	II
Abstract.....	III
Declaration.....	V
Acknowledgement.....	VI
List of publications.....	VII
List of figures.....	XII
List of abbreviation.....	XIV
List of nomenclature.....	XV
Chapter 1 Introduction.....	1
Chapter 2 Literature review.....	6
2. 1 Background.....	6
2. 2 Structures and properties of graphene, and bismuth chalcogenides.....	7
2. 2. 1 Structure and properties of graphene.....	7
2. 2. 2 Structures and properties of bismuth chalcogenides.....	10
2. 2. 3 Graphene and bismuth chalcogenide heterostructures.....	13
2. 3 Preparation of graphene and bismuth chalcogenides.....	14
2. 3. 1 Mechanical exfoliation.....	15
2. 3. 2 Chemical vapour deposition.....	16
2. 3. 3 Solvothermal growth.....	17
2. 4 <i>in situ</i> Powder X-ray diffraction.....	19
2. 5 Photodetector applications.....	20
2. 6 Plasmon resonance studies in far-field and near-field.....	21
2. 7 Review summary and Aims.....	25
2. 7. 1 Review summary	25
2. 7. 2 Aims.....	26
2. 8 References.....	27
Chapter 3 Solvothermal Growth of Bismuth Chalcogenide Nanoplatelets by the Oriented Attachment Mechanism: An <i>in Situ</i> PXRD Study.....	42
Chapter 4 Large-Scale Production of Bismuth Chalcogenide and Graphene heterostructure and Its Application for Flexible Broadband Photodetector.....	64
Chapter 5 Efficient and Tunable Plasmon Excitation in Graphene-Bi ₂ Te ₃ Heterostructure.....	81
Chapter 6 Efficient Excitation of Multiple Plasmonic Modes on Three-dimensional Graphene: An Unexplored Dimension.....	88
Chapter 7 Conclusions and future work.....	122
7.1 Conclusions.....	122
7.2 Future work.....	123

Copyright notice

Under the Copyright Act 1968, this thesis must be used only under the normal conditions of scholarly fair dealing. In particular no results or conclusions should be extracted from it, nor should it be copied or closely paraphrased in whole or in part without the written consent of the author. Proper written acknowledgement should be made for any assistance obtained from this thesis.

I certify that I have made all reasonable efforts to secure copyright permissions for third party content included in this thesis and have not knowingly added copyright content to my work without the owner's permission.

Jingchao Song

September 2016

Abstract

Graphene, a novel 2-D allotrope form of carbon, has triggered intensive research interests in 2-D materials. 2-D materials' extraordinary properties promise various applications, such as electronics, optics and optoelectronics. Particularly, graphene and bismuth chalcogenides (Bi_2Se_3 , Bi_2Te_3 *et. al.*), which share similar Dirac bandgap structures and exotic surface states, are outstanding candidates in potential applications of broadband optoelectronic, plasmonic devices and future on-chip devices. Though researchers have dedicated their efforts in the 2-D materials, the attention being paid to the graphene and bismuth chalcogenides based materials remains low, especially in their large production and optoelectronic device applications.

This research dissertation starts with the preparation of high quality graphene, bismuth chalcogenide nanocrystals and their heterostructure. By taking advantages of the *in situ* Powder X-ray diffraction technique, better understanding in the growth mechanism of bismuth chalcogenides nanoplatelets and its graphene heterostructure has been obtained. Step by step growth mechanism is revealed and discussed. Thus large-scale prepared graphene and bismuth chalcogenides hybrid material has been integrated into a free standing thin film, which is further demonstrated as a broadband photodetector. On the other hand, it is found that the graphene and Bi_2Te_3 heterostructure films can effectively enhance plasmon resonance magnitude in its FTIR spectrum by increasing light-matter interactions. In order to better observe and understand the plasmonic resonance modes on these materials, the later sections of this dissertation investigated resonance modes on graphene surfaces from both far-field and near-field. The results show that the light-matter interaction can be further enhanced by modifying the geometry of the surface and the surface plasmon can be guided in a controlled manner. It is believed, this dissertation paves way for the photonic and optoelectronic researches of graphene, bismuth chalcogenides and their heterostructures.

This Page is intentionally blank

Monash University

Declaration for thesis based or partially based on conjointly published or unpublished work

General Declaration

In accordance with Doctorate Regulations 17/Doctor of Philosophy Regulation 61 at Monash University the following declarations are made:

I hereby declare that this thesis contains no material which has been accepted for the award of any other degree or diploma at any university or equivalent institution and that, to the best of my knowledge and belief, this thesis contains no material previously published or written by another person, except where due reference is made in the text of the thesis.

This thesis includes 4 original papers published in peer reviewed journals and 1 unpublished publication in the future work. The core theme of the thesis is Preparation of graphene, bismuth chalcogenide and their heterostructures with application in photonics and optoelectronics. The ideas, development and writing up of all the papers in the thesis were the principal responsibility of myself, the candidate, working within the Department of Materials Science and Engineering, Monash University, under the supervision of Prof. Qiaoliang Bao.

The inclusion of co-authors reflects the fact that the work came from active collaboration between researchers and acknowledges input into team-based research.

In the case of the 5 chapters below, my contribution to the work involved the following:

Thesis Chapter	Publication title	Publication status	Nature and extent of candidate's contribution
3	Solvothermal Growth of Bismuth Chalcogenide Nanoplatelets by the Oriented Attachment Mechanism: An in Situ PXRD Study	Published	Key ideas, experimental works, results analysis and writing up
4	Large-Scale Production of Bismuth Chalcogenide and Graphene heterostructure and Its Application for Flexible Broadband Photodetector	Published	Key ideas, experimental works, results analysis and writing up
5	Efficient and Tunable Plasmon Excitation in Graphene-Bi ₂ Te ₃ Heterostructure	Published	Key ideas, experimental works, results analysis and writing up
6	Efficient Excitation of Multiple Plasmonic Modes on Three-dimensional Graphene: An Unexplored Dimension	Just Accepted	Key ideas, experimental works, results analysis and writing up

I have renumbered sections if submitted or published papers in order to generate a consistent presentation within the thesis.

Signed:



Date:

22/09/2016

Acknowledgements

The last four years, no doubt, have been an important self-discovery journey in my life. During this precious time perusing my PhD degree, I have developed my understanding in science, critical reasoning and analytic skills, patience to details, and passion to life. Without the support from my mentors, friends and family, this journal could be a sailing in a dark night without stars.

Firstly, I would like to take this opportunity to give my sincere thanks to my supervisors, Prof. Qiaoliang Bao, Dr. Fang Xia and Prof. Rachel Caruso. Their combined support and guidance have enabled me to explore the scientific world continuously and consistently. What they have achieved in their own academic careers set excellent examples for me to follow, and largely enrich my mind and broaden my horizons. I believe I would be still appreciating for their guidance on the rest voyage of my life. Particularly, I would like to express my special thanks to my supervisor Dr. Fang Xia for his patient guidance and help on my writing.

Secondly, I would like to thank all my colleagues and collaborators for their supports, kind help and valuable advises throughout my PhD career. Many thanks to Dr. Yulin Zhong, Dr. Shenghuang Lin, Dr. Yunzhou Xue, Dr. Yupeng Zhang, Dr. Xiang Qi, Dr. Zaiquan Xu, Dr Jie Zhang, Dr. Xudong Jiang, Ms. Jingying Liu, Mr. Jialu Zheng, Mr. Ziyu Wang, Mr. Zhipeng Li, Mr. Qingdong Ou, Mr. Zhichen Wan, Dr. Ling Qiu, Dr. Chi Cheng, Dr. Yufei Wang, Dr. Xiaowei Yang, Mr. Zhiming Tian, Mr. Diyan Liu, Ms. Mengyang Zhang, Ms. Jing Xiao, Mr. Jian Yuan, Mr. Yao Lu, Dr. Kai Zhang, Dr. Yuefeng Yin, Dr. Yuan Wang, Dr. Zuoran Zeng, Dr. Ruifeng Zhang, Mr. Yuanming Yan for their kind discussions and experience sharing during these years.

Particular, I would like to thank my collaborators in National University of Singapore, Swinburne University and RMIT. They are always a phone call away when I seek for a quick discussion or professional advices. Sincere thanks to Dr. Lei Zhang, Prof. Cheng-Wei Qiu, Dr. Meng Zhao, Prof. Kian Ping Loh, Dr. Qiming Zhang, Dr. Jiao Lin, Dr. Guanyuan Si. I would also like to thank the staffs in Melbourne Centre for Nanofabrications for their kind training and technical support through these years. Thanks to Dr. Paul Spizzirri, Dr. Sean Langelier, Dr Fatima Eftekhari, Dr Gediminas Gervinskas, Dr Hemayet Uddin, Dr. John Zhu, Dr Lacklan Hede, Dr Ricky Tjeung, Dr. Yang Lim.

Finally, infinity thanks go to my family. Thanks to my parents for their long-term emotional and financial support. Their love is my endless power source to live, work and explore the world. My greatest thanks to my beloved wife, Ms. Jingying Liu, who was always accompanying me for last important four years and is going to give me the best gift in my whole life – my first son. I am grateful to take this opportunity to express my deepest thanks to my family. Wish you all the best, good health and happiness!

Thank you very much!!

List of publications

1. **Jingchao Song**, Fang Xia, Meng Zhao, Yu Lin Zhong, Wei Li, Kian Ping Loh, Rachel A. Caruso, and Qiaoliang Bao, Solvothermal Growth of Bismuth Chalcogenide Nanoplatelets by the Oriented Attachment Mechanism: An in Situ PXRD Study, *Chem. Mater.* 29 (9), 3471-3482, 2015.
2. **Jingchao Song**, Jian. Yuan, Fang Xia, Jingying Liu, Yupeng Zhang, Yu Lin Zhong, Jialu Zheng, Yan Liu, Jian Yuan, Shaojuan Li, Meng Zhao, Zhiming Tian, Rachel A. Caruso, Kian Ping Loh and Qiaoliang Bao, Large-scale production of bismuth chalcogenide and graphene heterostructure and its application for flexible broadband photodetector, *Adv. Electro. Mater.* 2 (5), 1600077, 2016.
3. Yao Lu, **Jingchao Song (co-first author)**, Jian Yuan, Lei Zhang, Steve Qing Yang Wu, Wenzhi Yu, Meng Zhao, Jinghua Teng, Kian Ping Loh, Chao Zhang, Qiaoliang Bao, Highly efficient plasmon excitation in graphene-Bi₂Te₃ heterostructure, *J. Opt. Soc. Am. B*, 33, 1842-1846, 2016.
4. **Jingchao Song**, Lei Zhang, Yunzhou Xue, Qing Yang Steve Wu, Fang Xia, Chew Ah Bian, Yu-Lin Zhong, Yupeng Zhang, Jinghua Teng, Cheng-Wei Qiu, Qiaoliang Bao, Three-dimensional graphene pillar enables highly efficient multi-mode excitations, *ACS Photonics*. (Accepted)
5. Hong Qiao, Jian Yuan, Zaiquan Xu, Caiyun Chen, Shenghuang Lin, Yusheng Wang, **Jingchao Song**, Yan Liu, Qasim Khan, Hui Ying Hoh, Chun-Xu Pan, Shaojuan Li, and Qiaoliang Bao, Broadband Photodetectors Based on Graphene Bi₂Te₃ Heterostructure. *ACS Nano*, 9 (2), 1886-1894, 2015.

6. Ganaka G. Chandrakumara, Jin Shang, Ling Qiu, Xi-Ya Fang, Frank Antolasic, Christopher D. Easton, **Jingchao Song**, Tuncay Alan, Dan Li and Jefferson Zhe Liu, Tuning the oxygen functional groups in reduced graphene oxide papers to enhance the electromechanical actuation. *RSC Adv.* 5, 68052-68060, 2015.
7. Jing Wei , Yaixin Hu , Yan Liang , Biao Kong , Jin Zhang , **Jingchao Song**, Qiaoliang Bao , George P. Simon , San Ping Jiang , and Huanting Wang, Nitrogen-Doped Nanoporous Carbon/Graphene Nano-Sandwiches: Synthesis and Application for Efficient Oxygen Reduction, *Adv. Funct. Mater.* 10, 1002, 2015.
8. Qiming Zhang, Xiangping Li, Md Muntasir Hossain, Yunzhou Xue, Jie Zhang, **Jingchao Song**, Jingying Liu, Mark D Turner, Shanhui Fan, Qiaoliang Bao, Min Gu, Graphene surface plasmons at the near-infrared optical regime, *Sci. Rep.* 4, 6559, 2014.
9. Caiyun Chen, Hong Qiao, Yunzhou Xue, Wenzhi Yu, **Jingchao Song**, Yao Lu, Shaojuan Li, Qiaoliang Bao, Growth of large area atomically thin MoS₂ film via ambient pressure chemical vapour deposition. *Photon. Res.* 3 (4), 110-114, 2015.
10. Caiyun Chen, Hong Qiao, Shenghuang Lin, Chi Man Luk, Zaiquan Xu, **Jingchao Song**, Yunzhou Xue, Delong Li, Jian Yuan, Wenzhi Yu, Chunxu Pan, and Shu Ping Lau, Qiaoliang Bao, Highly responsive MoS₂ photodetectors enhanced by graphene quantum dots, *Sci. Rep.* 5, 11830, 2014.
11. Haoran Mu, Zhiteng Wang, Jian Yuan, Si Xiao, Caiyun Chen, Yu Chen, Yao Chen, **Jingchao Song**, Yusheng Wang, Yunzhou Xue, Han Zhang, Qiaoliang Bao. Graphene–Bi₂Te₃ Heterostructure as Saturable Absorber for Short Pulse Generation, *ACS Photon.* 2 (7), 832-841, 2015.

12. Wei Li, Dehong Chen, Fang Xia, Jeannie Z. Y. Tan, **Jingchao Song**, Wei-Guo Song and Rachel A. Caruso, Flowerlike WSe₂ and WS₂ microspheres: one-pot synthesis, formation mechanism and application in heavy metal ion sequestration, *Chem. Comm.* 52, 4481-4484, 2016.
13. Ziyu Wang, Jingying Liu, Zai-Quan Xu, Yunzhou Xue, Liangcong Jiang, **Jingchao Song**, Fuzhi Huang, Yusheng Wang, Yu Lin Zhong, Yupeng Zhang, Yi-Bing Cheng, Qiaoliang Bao, Wavelength-tunable waveguides based on polycrystalline organic-inorganic perovskite microwires, *Nanoscale*. 8 (12), 6258-6264, 2016.
14. Liangmiao Zhang, Fang Xia, Zhengdong Song, Nathan A. S. Webster, **Jingchao Song**, Hongjie Luo and Yanfeng Gao, Phase and morphology evolution during the solvothermal synthesis of VO₂ polymorphs, *Inorg. Chem. Front.*, 3 (1), 117-124, 2016.
15. Yusheng Wang, Yupeng Zhang, Yao Lu, Weidong Xu, Haoran Mu, Caiyun Chen, Hong Qiao, **Jingchao Song**, Shaojuan Li, Baoquan Sun, Yi-Bing Cheng, and Qiaoliang Bao, Hybrid Graphene–Perovskite Phototransistors with Ultrahigh Responsivity and Gain, *Adv. Opt. Mater.* 3 (10), 1389-1396, 2015.
16. Yunzhou Xue, Yupeng Zhang, Yan Liu, Hongtao Liu, **Jingchao Song**, Joice Sophia, Jingying Liu, Zaiquan Xu, Qingyang Xu, Ziyu Wang, Jialu Zheng, Yunqi Liu, Shaojuan Li, and Qiaoliang Bao, Scalable Production of a Few-Layer MoS₂/WS₂ Vertical Heterojunction Array and Its Application for Photodetectors, *ACS Nano*, 10 (1), 573-580, 2016.
17. Jingying Liu, Yunzhou Xue, Ziyu Wang, Zai-Quan Xu, Changxi Zheng, Bent Weber, **Jingchao Song**, Yusheng Wang, Yuerui Lu, Yupeng Zhang, Qiaoliang Bao, Two-Dimensional CH₃NH₃PbI₃ perovskite: Synthesis and Optoelectronic Application, *ACS Nano*, 10 (3), 3536-3542, 2016.

18. Zhengdong Song, Liangmiao Zhang, Fang Xia, Nathan A. S. Webster, **Jingchao Song**, Bin Liu, Hongjie Luo and Yanfeng Gao, Controllable Synthesis of VO₂(D) and Their Conversion to VO₂(M) nanostructures with Thermochromic Phase Transition Properties, *Inorg. Chem. Front*, 00, 1-3, 2016.
19. Yupeng Zhang, Yusheng Wang, Zaiquan Xu, Jingying Liu, **Jingchao Song**, Yunzhou Xue, Ziyu Wang, Jialu Zheng, Liangcong Jiang, Chengxi Zheng, Fuzhi Huang, Baoquan Sun, Yi-Bing Cheng, Qiaoliang Bao, Reversible Structural Swell- Shrink and Recoverable Optical Properties in Hybrid Inorganic-Organic Perovskite, *ACS Nano*, 10 (7), 7031-7038, 2016.
20. Zhengyang Zhao, Yi Feng, Ezzat Shamsaei, **Jingchao Song**, Huangting Wang, Lizheng He, Highly stable enzymatic membrane for fast treatment of antibiotic-polluted water, *Journal of Membrane Science*. 518, 15, 1-9, 2016.
21. Fang. Xia, Wei. Li, **Jingchao, Song**, Qiaoliang. L. Bao, Rachel. A. Caruso, In situ PXRD studies of the solvothermal syntheses of WO₃ -ethylenediamine hybrid nanowires and Bi₂Sex Te_{3-x} nanoplatelets, *7th Conference on Advanced Materials and Nanotechnology (AMN 7)*, Nelson, New Zealand, 8-12, 2015.
22. Fang. Xia, Wei. Li, **Jingchao. Song**, Qiaoliang. Bao, Rachel A. Caruso, In Situ PXRD Studies of the Solvothermal Syntheses of WO₃-Ethylenediamine Hybrid Nanowires and Bi₂SexTe_{3-x} Nanoplatelets, *Australian Synchrotron User Meeting 2014, Melbourne, Australia*, 20-21, (2014).
23. Qiming. Zhang, Xiangping. Li, Muntasir. Hossain, **Jingchao. Song**, Qiaoliang. Bao, Min. Gu, Enhancement of the propagation length of graphene surface plasmons on silicon waveguides at the telecommunication frequencies, *Conference: Australian and New Zealand Conference on Optics and Photonics*, At Fremantle, Western Australia, 2013.

Manuscripts in preparation

1. **Jingchao Song**, Lei Zhang, Jingying Liu, Fang Xia, Weiliang Ma, Qingyang Xu, Yao Lu, Yu-Lin Zhong, Yupeng Zhang, Cheng-Wei Qiu, Qiaoliang Bao, Manipulating the propagating surface plasmon with nanoscale graphene photonic crystal structures. (In preparation)
2. Pei Yu, Zhiming Tian, Sean E. Lowe, **Jingchao Song**, Zhirui Ma, Xin Wang, Zhaojun Han, Qiaoliang Bao, George P. Simon, Dan Li, Yu Lin Zhong. Mechanically- Assisted Electrochemical Production of Graphene Oxide, Chemistry of Materials. (In Revision)
3. Zhiming Tian, Pei Yu, Sean E. Lowe, A. G Pandolfo, Thomas Gengenbach, **Jingchao Song**, Yu Lin Zhang, Dan Li. Facile Electrochemical Approach for the Production of conductive Graphite oxide with Tuneable Chemistry. (Submitted)
4. Zhiming Tian, Chi Cheng, Pei Yu, **Jingchao Song**, Yu Lin Zhong, Dan Li. Electrochemical evaluation of the stacking behaviour of graphite nanoflakes prepared by direct liquid phase exfoliation. (In Preparation)

List of figures

Figure 1. 2-D Materials with different band structures cover a broad range of the optical spectral range.

Figure 2. Graphene, a single layer of graphite, is the original building block of its other allotropes. It can be wrapped up to 0D fullerene, rolled up to 1-D carbon nanotube or stacked into 3-D graphite.

Figure 3. Three dimensional representation of the electronic band structure of graphene. The region near the Fermi level in on K point has been enlarged in the right panel, which shows two Dirac cones touching at a single point.

Figure 4. Graphene based display (green), electronic (blue) optical (pink), optical interconnect (brown) applications with possible application timeline.

Figure 5. (a) Crystal structure and electron microscopy characterizations of the Bi_2Se_3 nanoribbons and thin films. (b) Exotic electronic states in topological insulators, metallic edge of 2-D topological insulator and 3-D topological insulator, the quantum Hall effect in a 2-D electron system from top to bottom. (dissipationless metallic edge or surface are shown in yellow)

Figure 6. Strong spin-orbit interaction gives rise to a single SS Dirac cone. (a, b) High-resolution APRES mapping of the surface electronic band dispersion on Bi_2Se_3 with different momentum-space cuts. (c) Momentum distribution curves corresponding to the surface bands.

Table 1. Properties of graphene prepared by different methods.

Figure 7. (a) Schematic shows the mechanical exfoliation procedure performed on HOPG (Highly Oriented Pyrolytic Graphite) with Scotch-tape. (b) Optical image, Raman and AFM characterizations of the exfoliated graphene with different layer thicknesses.

Figure 8. (a) Schematic showing the CVD procedure of growing graphene on copper foil. Firstly, the copper foil with native oxide is treated to CH_4/H_2 atmosphere at 1000°C ; then, the nuclei of graphene islands started to grow and merged to larger flakes. (b) shows SEM images of graphene on copper foil at different growth time from 1 min, 2.5 min to 10 min.

Figure 9. (a) Growth process of nanoparticles according to time scale. (b) Integrated characterization of Bi_2Te_3 nanoplates obtained by solvothermal growth method.

Figure 10. (a) Schematic of the Powder Diffraction (PD) beamline at Australian Synchrotron. (b) A photograph of the experimental setup at the end station of the PD beam line.

Figure 11. Examples of graphene based heterostructure for photodetection applications:(a) G-Bi₂Te₃ heterostructure. (b) G-MoS₂ heterostructure. (c) G-MoS₂-G heterostructure. (d) G-WSe₂-G heterostructure. (e) MoS₂-G (quantum dots) heterostructure.

Figure 12. Patterned graphene and their FTIR spectrum. Graphene nanoribbons (a) and their corresponding spectrum with different width (b). Graphene and boron nitride multilayer stacking disks (c) and their spectrum with different layer thickness (d). Graphene photonic crystal (e), and their representative spectrum (f).

Figure 14. (a) Schematic of NSOM with aperture at its probe tip. (b) SEM image of the 50 nm wide aperture at the tip. (c) Schematic of the scattering type NSOM. Scheme shows the scattering type NSOM can be used to study the graphene plasmon on the SiO₂ substrate.

Figure 15. NSOM measurement of (a) graphene taper and defects, (b) Au scatter on graphene sheet, (c) graphene ribbons, (d) graphene disks.

Figure 16. Schematic shows the preliminary near -field optical signal measured in a graphene based photonic crystal waveguide by the scattering NSOM.

List of abbreviation

2-D	Two-Dimensional
3-D	Three-Dimensional
AFM	Atomic Force Microscopy
BN	Boron Nitride
BP	Black phosphorus
DP	Dirac Point
EBL	Electron Beam Lithography
EVE	Electron Beam Evaporation
EDX	Energy-dispersive X-ray spectroscopy
FIB	Focus Ion Beam
FTIR	Fourier Transform Infrared Spectroscopy
G	Graphene
GO	Graphene Oxide
NSOM	Near-field Scanning Optical Microscope
PC	Photonic Crystal
PCW	Photonic Crystal Waveguide
PXRD	Powder X-ray Diffraction
PD	Power Diffraction
QD	Quantum Dots
SEM	Scanning Electron Microscopy
SPP	Surface plasmon polariton
TEM	Transmission Electron Microscopy
TGA	Thermal Gravimetric analysis
TI	Topological Insulator
TMDC	Transition metal dichalcogenides
VWG	Van Der Waals Gap
XPS	X-ray Photoelectron spectroscopy

List of nomenclature

A	Ampere
nm	Nanometer
μm	micrometer
min	minute
$^{\circ}$	Degree (in terms of XRD angle)
V	Voltage
AW^{-1}	Amperes per Watt
$^{\circ}\text{C}$	Celsius
Ω	ohm

Chapter 1: Introduction

Graphene is a novel two dimensional (2-D) allotrope of carbon. Its success in the last a few years has unveiled the era of exploring unusual physical properties and practical applications of atomic thin layered materials, which are well known as 2-D materials. The prosperous 2-D materials' family includes members from elementally and covalently-bonded black phosphorous, boron nitride, silicene, to those more complexly structured chalcogenide materials (*e. g.* topological insulators (TI) such as Bi_2Se_3 , Bi_2Te_3 *et. al.* and transition metal dichalcogenides (TMDC) like MoS_2 , WS_2 *et. al.*). 2-D materials' practical applications are deeply rooted into many chemical and physical regions, and promise fascinating efficiency in electric and photonic devices, such as super capacitors, photodetectors, storage devices, solar cells, biosensors and nonlinear optical devices. Here, this thesis focuses on the study of graphene and bismuth chalcogenides (Bi_2Se_3 , Bi_2Te_3 *et. al.*) based 2-D materials, and explores the preparation, photonic and optoelectronic applications of them and their heterostructures.

Recently, graphene and bismuth chalcogenides (TI) have shown excellent electronic and optoelectronic properties due to their unique Dirac cone like energy band structures. They have also revealed potential applications in optoelectronic and plasmonic devices. However, the large scale production of graphene and bismuth chalcogenides with low defects and controllable cost is only accessible with chemical vapour deposition and solution process methods. In the sense of practical applications, the production of large area (or large quantity) of defect free 2-D materials is critically important. Unfortunately, due to the chemical complexity in these synthesis methods, the large area (or large quantity) controllable production of 2-D materials remains a big challenge, especially in solution process. Understanding the growth mechanism behind the growth of bismuth chalcogenides is the key to solve this problem. Thus, the first part of this thesis investigated the growth mechanism of bismuth chalcogenides nanocrystals, and their graphene hybrid structures, with applications in the optoelectronic devices and plasmonics.

In the study of graphene and TI plasmons in first part, it was found that many aspects of this new research realm remain challenging and unexplored. For examples, the plasmon excitation efficiency of these 2-D material is still quite low, and the localized modes existing in the materials are difficult to be fully interpreted as there is a lack of direct observation tool to

visualize them. Therefore, the understanding and interpretation of these mode existing on the 2-D materials' surfaces are of great academia importance before they can be transferred into practical applications. Here, the second part of this thesis focuses on the research of the excitation and observation of various plasmonic modes on the 2-D materials, especially graphene. It is believed that this part will contribute to the fundamental understanding of the plasmonic behaviour supported by 2-D materials as well as their practical plasmonic applications.

In summary, this PhD thesis discusses three fundamental aspects of the graphene and bismuth chalcogenide materials, which are material preparation, optical characterization and device applications. In order to address the aforementioned challenges and introduce the major findings in this research project, a brief description of the chapters presented in this dissertation is introduced in a progressive, chapter-by-chapter manner as below.

Chapter 1 firstly introduces the research road map of 2-D materials, specifically graphene and bismuth chalcogenides (TI). Their physical properties and potential applications in electronics and optoelectronics are discussed. For example, graphene and bismuth chalcogenides both have Dirac surface properties, which promises the Dirac electron spin-orbital coupling and unidirectional-polarized propagation on their surface, respectively. According to their unique physical properties, graphene and bismuth chalcogenides (TI) differs from other traditional materials in terms of practical applications, and results in new types of electronic and optoelectronic devices, such as spintronic devices and plasmonic devices. Finally, this chapter concludes the main challenges in synthesising, precise nanofabrication and characterization of such materials before they can be fully used into the high performance devices.

Chapter 2 in-depth surveys several interesting aspects directly related to the main scope of this thesis. For example, various synthesis methods of graphene and bismuth chalcogenides; nanofabrication and post production process for graphene and bismuth chalcogenides; far-field and near-field photonic research of the graphene and bismuth chalcogenides and their practical device applications. Detailed literature reviews of these areas are provided in this chapter.

Chapter 3 studies the growth mechanism of bismuth chalcogenide nanocrystals ($\text{Bi}_2\text{Se}_x\text{Te}_{3-x}$) in its solvothermal growth process with *in-situ* powder X-ray diffraction (PXRD) techniques. As previously discussed that the large scale growth of these 2-D materials is

challenging as the mechanism behind them are complex. However, the growth mechanism of solvothermal growth of bismuth chalcogenide nanocrystals remains unclear due to the lack of efficient *in-situ* characterization tool. In this chapter, the PXRD technique enables investigation of crystallization curves, lattice parameters, and crystal size evolution under a variety of synthesis conditions in the real time. On the basis of the crystallization curves and crystal size evolution, a general 3-step crystallization process has been deduced: (1) An induction period for the dissolution of the precursor and nucleation of $\text{Bi}_2\text{Se}_x\text{Te}_{3-x}$, followed by (2) rapid growth of planar crystals through the oriented attachment, and finally (3) a diffusion-controlled slow growth step consuming the remaining precursor from the solution. Oriented attachment has been proved to be very effective for the growth of binary composites, resulting in a high yield of large planar crystals; however, it is much less effective for the growth of ternary composites due to lattice mismatch of the nuclei formed at the induction period, producing much smaller crystals accompanied by a limited yield of large planar crystals. Additionally, three intermediate phases (Bi_2TeO_5 , Bi_2SeO_5 , and Na_2SeO_3) were observed that played an important role in controlling the phase separation as well as the composition of the final ternary compounds. This chapter serves as the basis of preparation of such material and support the later studies.

Chapter 4 studies the precisely controlled large-scale production of graphene and bismuth chalcogenide heterostructure, and explored its practical electric and optoelectronic applications. As been proved in the previous chapter that ternary bismuth chalcogenide nanocrystals are hard to form as they have versatile chemical compositions at the beginning of the induction period. However, the ternary composited bismuth chalcogenides are particularly interesting as their bandgap can be tuned by different chemical compositions. Furthermore, the heterostructure of graphene and ternary bismuth chalcogenides, which may have new applications, have never been reported in the solution phase. In this chapter, a solvothermal method is demonstrated to produce van der Waals heterostructures consisting of metal chalcogenides and graphene in a large scale. In situ powder X-ray diffraction reveals that graphene plays an important role as atomic template to grow bismuth chalcogenide nanoplatelets with preferential stoichiometry of $\text{Bi}_2\text{Se}_{1.5}\text{Te}_{1.5}$, which is naturally unstable. It is found that $\text{Bi}_2\text{Se}_{1.5}\text{Te}_{1.5}$ has the minimum lattice mismatch with graphene (<0.1%). The release of lattice mismatch strain between $\text{Bi}_2\text{Se}_{1.5}\text{Te}_{1.5}$ and graphene sheet is evidenced by a new peak in the ultraviolet photoelectron spectroscopy. A macroscale free-standing heterostructured thin film with excellent mechanical flexibility is fabricated by simply filtering the large-scale solution processed heterostructure. The

heterostructure film is used to fabricate a flexible photodetector, which shows a broadband photo response and excellent durability in a bending test. The heterostructure material and device demonstrated in this work may shed light to flexible optoelectronic devices and applications.

Chapter 5 reports a strong and tuneable plasmonic coupling in graphene-Bi₂Te₃ heterostructure with the help of silicon (Si) gratings. Graphene and bismuth chalcogenides both support Dirac plasmons. However, due to many reasons, such as sample imperfection and materials handling difficulties, the coupling between these two plasmon systems were not reported. In this work, we fabricated the graphene and Bi₂Te₃ thin films on Si gratings. The plasmonic resonance of graphene-Bi₂Te₃ can be largely tuned by changing the grating period. Unlike individual layered materials either graphene or Bi₂Te₃, the plasmonic wave in heterostructure graphene-Bi₂Te₃ has enhanced resonance magnitude and large shift to lower frequency. The idea to hybridize Dirac plasmons in different layered materials will stimulate the interest to study variant plasmonic heterostructures and trigger new terahertz device applications.

Chapter 6 focuses on the plasmonic mode excitation and observation in 2-D materials. In this chapter, continuous graphene wrapped pillar structure fabricated by one-step direct growth of graphene on pre-shaped silicon substrates is presented. Graphene is known as a flat 2-D material. However, the plasmon resonance on the flat surface normally supports only low order modes, which limited the application of graphene plasmons. In this chapter, various plasmonic modes supported on the 3-D graphene pillars are observed and studied with their comparative graphene pillar components. It is found that the existence of sidewalls in the vertical dimension have an enormous influence on the transmission spectrum dip. Furthermore, the graphene sidewall thickness, together with the pillar width is proved having the most significant impact to change the first mode dip position among other parameters, such as pillar height, spacing and periodicity. In sum, this work draws our attention to the ‘vertical’ dimension of the 2-D materials, and provides a practical solution to easily achieve the 3-D graphene structure with novel controllable vertical feature. The graphene pillar structure reported in this work can be easily adopted by many other applications including the active or passive tuneable THz modulation. It is believed that the graphene pillar promises future applications in the THz communication and surveillance components such as modulators, phase-shifters, attenuators, and polarizers.

Chapter 7 summarizes the previous chapters in this PhD project, discusses the major findings and proposals of the future perspective of this research area, particularly in disciplines of fundamental plasmonic research and miniaturized device design and fabrication. In this chapter, we also propose the further investigation of graphene surface plasmon wave in the photonic crystal waveguide (PCW) structures by near field techniques. In sum, this work contributes to the knowledge of preparation of graphene and bismuth chalcogenides, and their photonic and optoelectronic applications.

Chapter 2: Literature review

2.1 Background

Two-dimensional (2-D) materials aren't new at all. The history of 2-D materials dates back to 1930s, when Landau and Peierls argued that atomic thin 2-D crystals were thermodynamically unstable and therefore could not exist.^{1,2} However, the passion in studying the “none-existing” single sheet of graphite didn't fade for the next a few decades.³⁻⁵ Actually, the enthusiasm in the new type of material gave rise to a tide in researching the unusual physical phenomena in 2-D materials, such as charge density waves⁶ and high-temperature superconductivity.^{7,8} In 1987, Mouras proposed the single sheet of the graphite can be produced via fluorides intercalation.⁹ Nevertheless, facing production and characterization challenges, the experimental demonstration of single layer graphite has not been achieved until 2004 by Novoselov and Geim with another simple Scotch-tape method.¹⁰ This discovery soon makes graphene famous and a broad research topic due to graphene's many fascinating physical properties.^{11,12}

Graphene's success triggered the researchers' curiosity into many other 2-D crystals.¹³ Some other representative 2-D family members are black phosphorus,^{14- 21} boron nitride,^{22, 23} transition metal dichalcogenides (TMDC)^{24- 26} and bismuth chalcogenides.²⁷⁻³⁵ (Figure 1.) All these 2-D materials play important roles where graphene is out of reach. For example, graphene's zero bandgap dims itself when coming to the semiconductor applications. Specifically, the electronic devices requires semiconducting materials, which can be switch on and off under certain condition. However, graphene is more metal-like conductor. Therefore, small band gap materials are needed. On the other hand, when constructing complex multi-stacking geometry of the 2-D materials based electronic devices, the boron nitride becomes necessary for its large bandgap and insulating nature in order to prevent a short circuit in the device. In this sense, the various 2-D materials and their combinations provide even greater technology payoffs than graphene along.^{36- 39} In all, considering all the other fascinating physical properties of the 2-D materials' family, we are confident in envision a future with graphene and other 2-D materials filling our daily applications from the next generation flexible optoelectronic chips to high density energy storage devices.

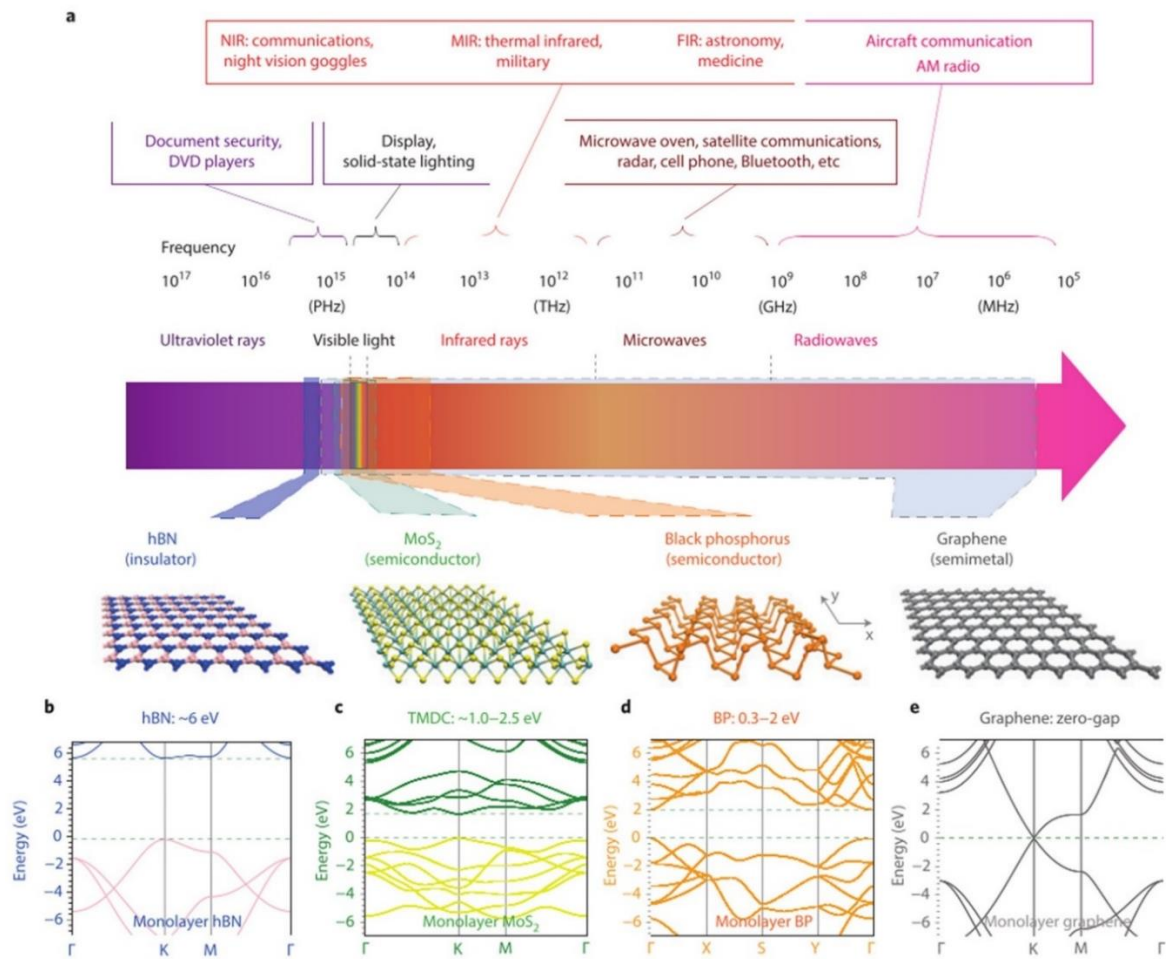


Figure 1. 2-D Materials with different band structures cover a broad range of the optical spectral range.³⁷

2.2 Structures and properties of graphene, and bismuth chalcogenides

2. 2. 1 Structure and properties of graphene

Graphene is a single atom-thick layer of hexagonal lattice arranged carbon atoms. It can also be considered as an ultimate large flat polycyclic aromatic molecule. Similar to the carbon atoms in its aromatic molecule family, each carbon atom in graphene has four bonds, including three head-to-head σ bonds and one shoulder-to-shoulder π -bond. The σ bond, with a length of 1.42 \AA , connects two neighbour carbon atoms, and the π -bond in each carbon atom contribute to a delocalized electron hybridization for the large aromatic ring. Thanks to the sp^2 hybridization of the carbon atoms, graphene and its “rolled up” occurrences (fullerene and carbon nanotubes) (Figure 2.) become stabilized and obtain fascinating mechanical and electronic properties.

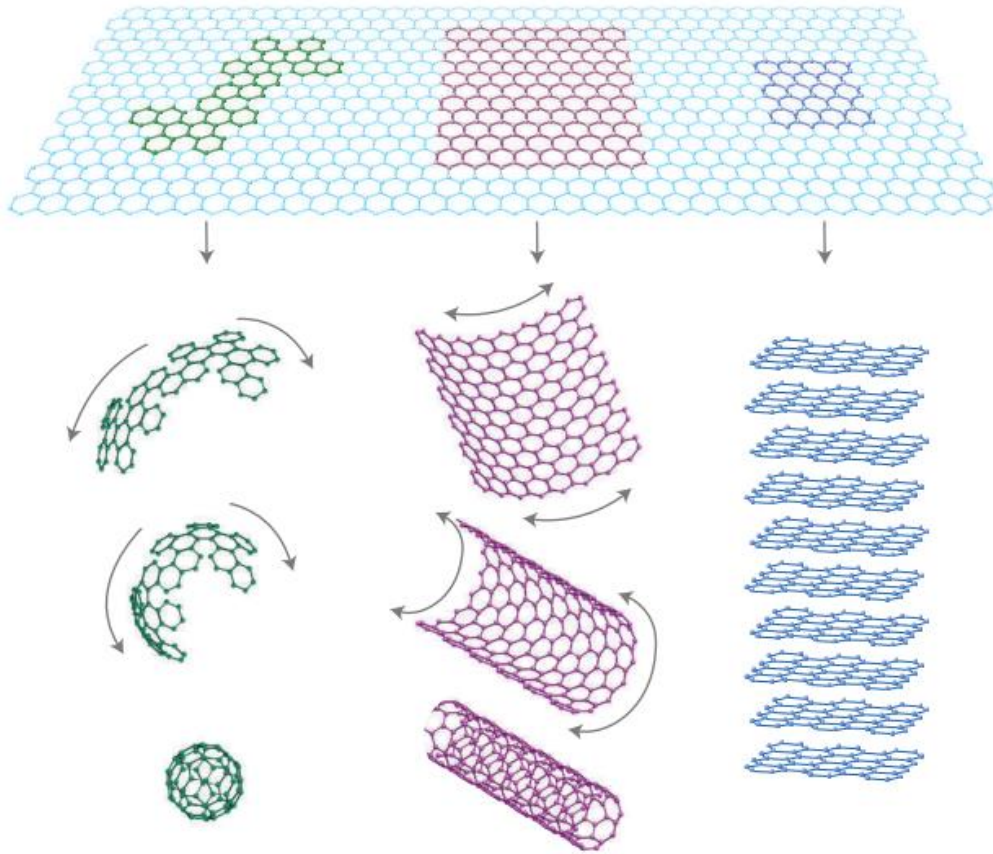


Figure 2. Graphene, a single layer of graphite, is the original building block of its other allotropes. It can be wrapped up to 0D fullerene, rolled up to 1-D carbon nanotube or stacked into 3-D graphite. ¹¹

New materials yield new physical properties. Single layer graphene has demonstrated extremely large surface area of $2,630 \text{ m}^2\text{g}^{-1}$, ^{40, 41} high optical transparency up to 97.7% per layer, ^{42,43} 1,100 GPa of Young's modulus and 125 GPa of fracture strength, which is even stronger than steel.⁴⁰ Furthermore, with the symmetry caused by one carbon atom at each lattice point, graphene's conduction and valence bands meet at the corner of the Brillouin zone (Figure 3.). These crystallographic points (K and K'), known as Dirac points, coincide with the Fermi energy E_F . As a consequence, graphene has the linear energy-momentum dispersion of electrons, which is described by Dirac equation instead of the dominating Schrödinger equation.

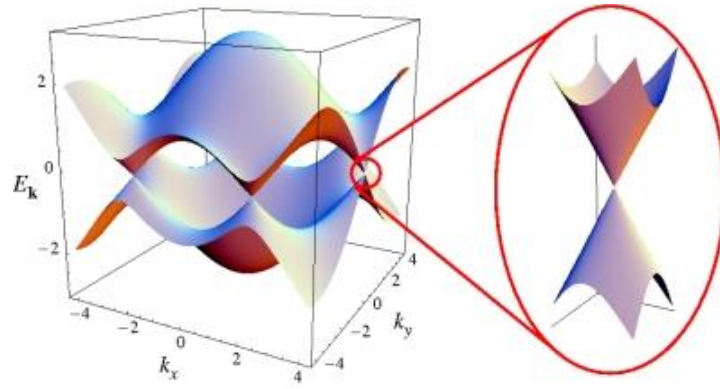


Figure 3. Three dimensional representation of the electronic band structure of graphene. The region near the Fermi level in on K point has been enlarged in the right panel, which shows two Dirac cones touching at a single point.⁴⁵

This feature makes graphene's charge carriers transport relativistically, ballistically, and continuously tuneable. Graphene's electrons and holes in concentrations n can be tuned to as high as 10^{13} cm^{-2} and their mobility μ can exceed $15,000 \text{ cm}^2\text{V}^{-1}\text{s}^{-1}$ even under ambient conditions. $200,000 \text{ cm}^2\text{V}^{-1}\text{s}^{-1}$ of charge carriers' mobility can even be achieved on suspended graphene.⁴⁶ Graphene's band structures can also be tuned with different layer numbers,⁴⁷ stacking geometries^{48,49} and substrate selection.⁵⁰ On the other hand, graphene has high thermal conductivity around $2,000 \text{ Wm}^{-1}\text{K}^{-1}$. These unique features of graphene make it an excellent candidate in the electronic applications.

Last a few years saw graphene's prosperous growth in various applications, such as electronic devices,^{51, 52} optoelectronic devices^{53- 55}supercapacitors⁵⁶, chemical sensors⁵⁷ and mode locked lasers.^{58, 59} Besides the interesting electronic properties mentioned before,^{60, 61} the metallic surface of graphene greatly meets the requirement of the surface plasmon polaritons (SPPs) and enriches the field of plasmonics. The surface plasmon polaritons are collective electron oscillations that exist on the metal-dielectric interfaces. Graphene's large real part, while much smaller imaginary part in its refractive index makes it an excellent material to support the SPPs.⁶² Graphene surface plasmons, characterized by relatively low loss, high confinement, flexible feature and excellent tuneability not only provide valuable insights into many-body effects, including electron-phonon, electron-electron, and plasmon-phonon interaction, but also trigger potential applications, such as optics transformation, plasmonic metamaterials, light harvesting and other applications in electronics, optics energy storage, THz technology and potentially in the biotechnology.^{63, 64} In particular, the recent advancement in graphene metamaterials and plasmonics promises novel optical devices

working at broader ranges with extremely high speed, low driving voltage, low power consumption and compact sizes.⁶² (Figure 4.)

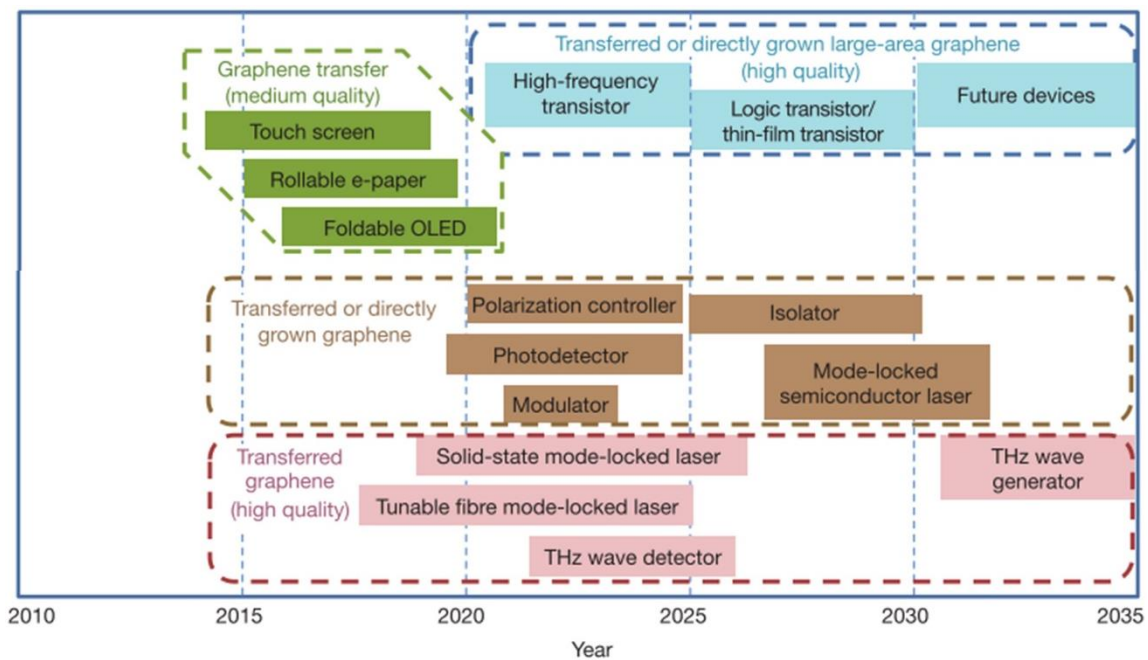


Figure 4. Graphene based display (green), electronic (blue) optical (pink), optical interconnect (brown) applications with possible application timeline.¹²

2. 2. 2 Structures and properties of bismuth chalcogenides

Bismuth chalcogenides refer to a group of materials consist of the bismuth and chalcogenides elements, specifically Se and Te in this work. Their combinations result in Bi_2Se_3 , Bi_2Te_3 and $\text{Bi}_2\text{Se}_x\text{Te}_{3-x}$ depending on different Se : Te stoichiometric ratios. The bismuth chalcogenides crystals discussed in this work shares the rhombohedral crystal structure ($a = b \neq c$, $\alpha = \beta = 90^\circ$, and $\gamma = 120^\circ$; space group = R-3m), which composed of hexagonal close-packed atomic layers periodically arranged along the c axis.^{65,66} Each five atomic alternative layers is known as a quintuple layer, between which lies the van der Waals gap (VWG).⁶⁷ (Figure 5a) As the bismuth chalcogenide is a layered semiconductor material, it cleaves easily along the trigonal axis due to the Van der Waals bonding between neighbouring tellurium/selenium atoms. In the early times, the bulk phase bismuth chalcogenides were often used as a group of high temperature solid lubricant for mechanical machining. Due to the fact that heavier element compound with larger atomic mass can reduce the thermal conductivity, it is not a surprise that it has also been widely used as a type of thermoelectric materials in recycling waste heat since 1950s.⁶⁸

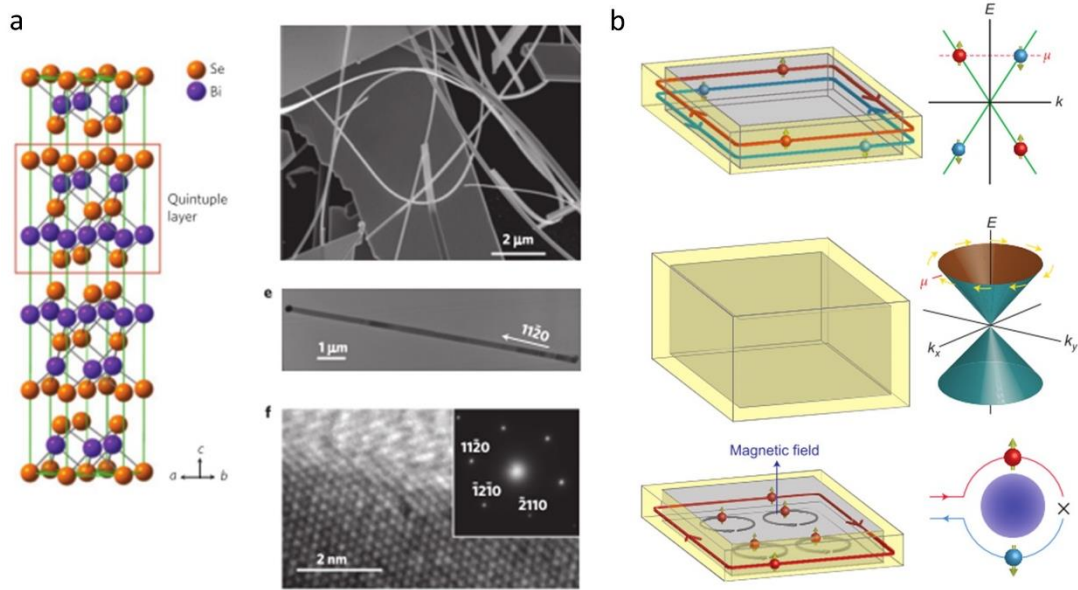


Figure 5. (a) Crystal structure and electron microscopy characterizations of the Bi₂Se₃ nanoribbons and thin films.⁶⁷ (b) Exotic electronic states in topological insulators, metallic edge of 2-D topological insulator and 3-D topological insulator, the quantum Hall effect in a 2-Delectron system from top to bottom. (dissipationless metallic edge or surface are shown in yellow)⁶⁹

In the last few years, lower dimensional materials have been intensively studied, and their properties have been proven to be significant different from the properties of their 3-D parent materials. The bismuth chalcogenides family is no exception. Thus many nanostructured bismuth chalcogenides such as nanowires^{70, 71} and thin films⁷² have been prepared. A significant improvement of the Seebeck coefficient (voltage per unit temperature difference) has been observed in their nanostructures.^{31, 73, 74} The nanobulk structures of bismuth chalcogenides possess characteristic low thermal conductivity and excellent electrical conductivity.⁷⁵ These properties can even be tuned by different levels of chemical doping.³⁵ For example, by optimizing the chemical composition ($x=0.3$) in Bi₂Se_xTe_{3-x}, the thermoelectric figure of merit ZT can reach 0.54 (RT), five times as that of Bi₂Te₃.³⁵ Furthermore, hybrid structures and nanometer confinement have been proven to improve the thermoelectric performance of resulting products.^{69, 76, 77}

More interestingly, it is found that a special spin orbital coupling state exists in the Bi₂Se₃ and Bi₂Te₃. Therefore, the 2-D bismuth chalcogenides have been recently recognized as topological insulators.⁶⁹ In brief, topological insulators are a type of materials with insulating interior but conducting surface. The key mechanism underlying behind the materials is the

time-reversal symmetry, which means the materials' physical behaviour is independent of whether time is flowing forward or backward. This makes the surface states robust, be maintained even when the surface defects are inevitable. Such surface state further promises the fascinating potential applications in the electronics devices due to the facts that electrons are not very likely to be back scattered in charge transport processes.⁶⁹ Moreover, the complete suppression of backscattering has prevented the Anderson localization and render the crystal conductive even when the crystal defects exist, famously known as dissipationless process.⁷⁸

This topological surface attracts great of attention because it has surpass several limitations of the quantum Hall effect, mostly the requirement of strong magnetic field. The quantum Hall effect was a major discovery in physics in 1980s.⁷⁹ In a two dimensional quantum Hall system, the electrons can only circulate in quantized orbitals in one direction along the edge in the presence of magnetic field, resulting an inert internal. This special quantum Hall system provide vast opportunities in electrical applications. In contrast, topological insulator system employs a quantum spin Hall system^{80, 81, 82}, in which its electron spin is "locked up" with its motion momentum. Instead of under an external magnetic field, the propagation electrons have to flip the spin, either spin up or spin down, in helical metal to be reflected or scattered by a defect, which is potentially more interesting in terms of multiple areas of applications.

The topological insulators are known for their separate bulk state and the non-trivial surface state. For the common semiconductors, the surface states are usually fragile due to the dangling bonds on the surface, which store residing energy in the bandgap. However, on the surface of the topological insulator, the properties are governed by the topological invariant, which cannot be changed as long as the material remains interior insulating.^{80- 82} In other words, the gapless surface state is an effect that occurs at the interfaces of topological insulators and insulating media. Therefore, the existence of these surface states is relatively irrespective of local chemical bonding structures.

The theoretical prediction of the topological insulators dates back to 1987⁸³ and subsequently supported by a series of experimental evidences in 2007.^{69, 81} The first generation of topological insulators in the (Hg, Cd)Te materials.^{80, 82} Accordingly to the quantum spin Hall effect, electrons flows along the time-reversal symmetry protected edges freely.^{80, 82} Thus they have been named as 2-D topological insulators. The next generation of topological insulators refer to Bi, Sb, Te alloys,^{84, 85} including Bi₂Se₃ and Bi₂Te₃, which have their whole surfaces time-reversal symmetry protected. In contrast to the 2-D TIs, they are known as 3-D topological

insulators. (Figure 5b) The 3-D TIs, such as Bi_2Se_3 and Bi_2Te_3 , scatter electrons in multi-directions, however will also force the electrons to propagate in low dissipation state. Since the first simple three-dimensional (3-D) topological insulator Bi_2Se_3 the theoretically predicted in 2007,⁸⁵ the topological insulator band structure (Figure 6) has been revealed with angle resolved photoemission spectroscopy (ARPES) by Chen *et al.*²⁷. Many researchers from physics, materials science and chemistry have been attracted to join the study of this new research field^{27, 29, 85} in spintronics⁸⁶, thermoelectronics^{35, 74}, memory devices^{31-33, 74, 87- 91}, microelectronics^{70, 92, 93}, plasmonics⁹⁴⁻⁹⁹, mode locked laser¹⁰⁰ and other THz applications^{30, 101-104}.

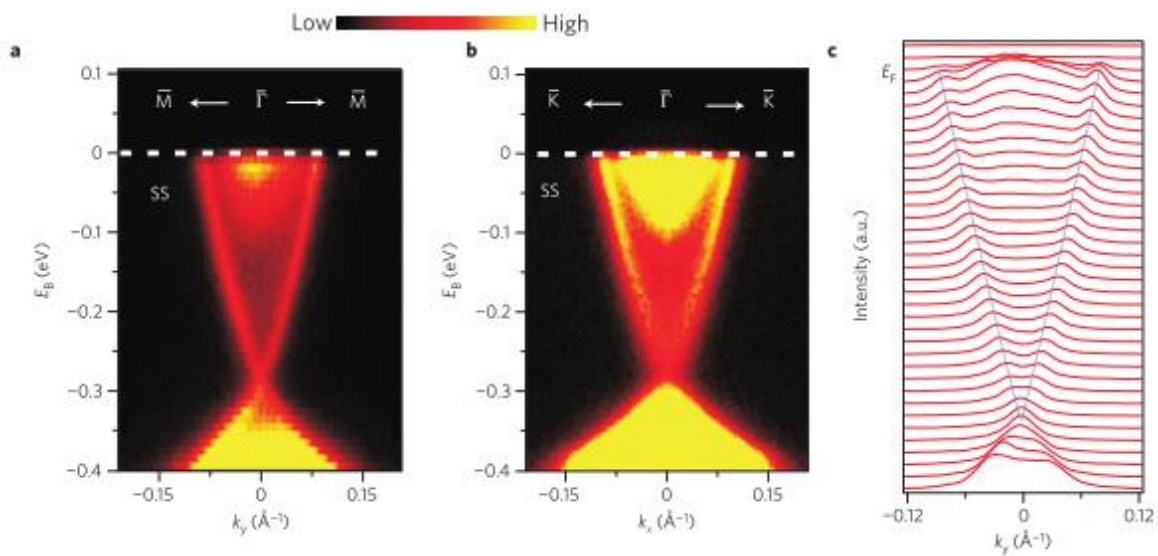


Figure 6. Strong spin-orbit interaction gives rise to a single SS Dirac cone. (a, b) High-resolution APRES mapping of the surface electronic band dispersion on Bi_2Se_3 with different momentum-space cuts. (c) Momentum distribution curves corresponding to the surface bands.

105

2. 2. 3 Graphene and bismuth chalcogenides heterostructures

The surface states of the topological insulators are not only fundamentally interesting for novel physics, but also expected to be practically important for innovative applications.⁶⁹ Recently, by using different TI- based heterostructures, emergent properties of topological surface states have been observed or predicted¹⁰⁶⁻¹²¹ For instance, induced energy gap can lead to different exotic surface states at the surface of a 3-D topological insulator according to various proximity effect.¹²² Specifically, when heterostructure is formed between topological insulators and superconductors, superconducting proximity effect is observed. This provides a platform to observe Majorana fermions^{123, 124} and a new venue for realization proposals of

non-Abelian topological quantum computing.^{106, 125, 126} By replacing the superconductor with ferromagnet in a TI based heterostructure, the magnetic gap can lead to a novel quantum Hall state and topological magnetoelectric effect,^{127, 128} which will further reveal inverse spin-galvanic effect and gain spin battery effect.^{129, 130} Additionally, enhancement of the catalysis effect by the robust topological surface states in Au-covered TI has been observed due to the proximity effect.¹¹²

As the surfaces of three-dimensional (3-D) topological insulators (TIs) and graphene both share low energy electronic structure, in which the conduction and valence bands touch at isolated points, the Dirac points, the Dirac fermions at both surfaces are expected to generate new physics.^{69, 131} For example, the heterostructure of Dirac materials, graphene and topological insulators, provides interesting platform to explore novel physics, such as exotic quantum states of electrons in solids and spin-orbital coupling.¹³² In Jin's work, the epitaxial grown graphene on the topological insulators is turned to quantum spin hall phase, and developed a spin-orbital gap of 20 meV.¹³² In 2014, Zhang and *et. al.* have provided evidence that the lattice matched system plays a crucial role of the proximity effect. Strong spin-orbital coupling enhancement induced by TI (Bi_2Se_3 , Bi_2Te_3 and Sb_2Te_3) and graphene heterostructures can be tuned effectively by the stacking angle.¹³³ Kou and *et. al.* have demonstrated that graphene's Dirac states can be significantly influenced by the strong spin-orbital coupling in BiTeX ($X = \text{Cl}, \text{Br}$ and I), and turned to a nontrivial topological band structure.¹³⁴ Their calculation with nontrivial Z_2 index also confirms the unique Dirac transport system in the heterostructure, which combines the Dirac states from both graphene and topological insulator. The theoretical prediction of the intrinsic spin Hall effect in metals and insulator has generated great interest in the field of spintronics, because the facts that this effect allows direct electric manipulation of the spin degrees of freedom without a magnetic field, and the resulting spin current can flow without dissipation. The Spin-momentum locking properties observed in the topological insulators found its potential applications in the surface plasmon resonance, photoelectron spin-flipping and texture manipulation.^{135,136} Practical applications of graphene and topological insulators include flexible electric devices,^{137, 138} photodetectors,^{39, 139} and other THz applications.^{51, 101, 140 - 145}

2.3 Preparation of graphene and bismuth chalcogenides

The widely used methods to prepare graphene and 2-D materials are generally divided into two major approaches: top down methods and bottom up methods.^{77, 146} Top down methods refer to the processes which breaks materials down from a bulk form to a lower dimension

form. These methods include mechanical exfoliation,¹⁰ solution exfoliation,¹⁴⁷⁻¹⁴⁹ intercalation methods.¹⁵⁰⁻¹⁵² Bottom up approaches refer to the processes which synthesis the 2-D materials from atomic scale. They include solution synthesis,¹⁵³⁻¹⁵⁶ chemical vapour deposition,¹⁵⁷⁻¹⁶⁴ and molecular beam epitaxial.¹⁶⁵⁻¹⁶⁸ These methods have their advantages and disadvantages which could be adapted for various applications. (Table 1) Three representative methods will be further discussed in the following section.

Method	Crystallite size (μm)	Sample size (mm)	Charge carrier mobility (at ambient temperature) ($\text{cm}^2\text{V}^{-1}\text{s}^{-1}$)	Applications
Mechanical exfoliation	>1,000	>1	$>2 \times 10^9$ and $>10^6$ (at low temperature)	Research
Chemical exfoliation	≤ 0.1	Infinite as a layer of overlapping flakes	100 (for a layer of overlapping flakes)	Coatings, paint/ink, composites, transparent conductive layers, energy storage, bioapplications
Chemical exfoliation via graphene oxide	~ 100	Infinite as a layer of overlapping flakes	1 (for a layer of overlapping flakes)	Coatings, paint/ink, composites, transparent conductive layers, energy storage, bioapplications
CVD	1,000	$\sim 1,000$	10,000	Photonics, nanoelectronics, transparent conductive layers, sensors, bioapplications
SIC	50	100	10,000	High-frequency transistors and other electronic devices

Table 1. Properties of graphene prepared by different methods.¹²

2. 3. 1 Mechanical exfoliation

Graphene was firstly prepared by mechanical exfoliation method by Professor Andre Geim and Konstantin Novoselov in 2004.¹⁰ Because the mechanical exfoliation method employs a scotch tape to peel off the 2-D material layers, it is also known as a Scotch-tape method. (Figure 7.) The advantage of this method is it creates the high crystalline single layer 2-D material without complex techniques. Thus made materials are perfect for physical properties study and device fabrications in a lab scale.¹⁶⁹ However, the mechanical exfoliation method performed with simple scotch tape usually requires experienced hands. The produced samples are usually in micro-meter size and in random shapes. Lack of receptivity and process standards hinder this method from larger scale production.

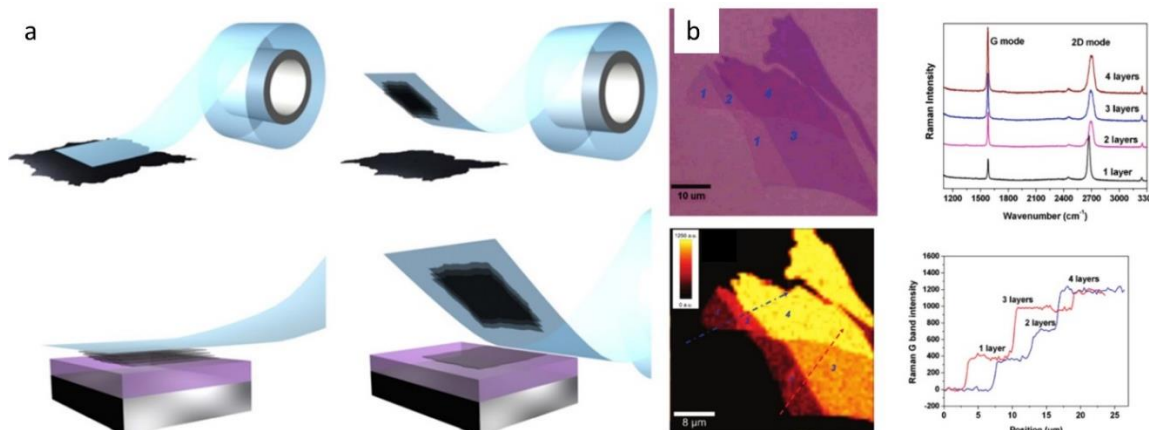


Figure 7. (a) Schematic shows the mechanical exfoliation procedure performed on HOPG (Highly Oriented Pyrolytic Graphite) with Scotch-tape.¹⁷⁰ (b) Optical image, Raman and AFM characterizations of the exfoliated graphene with different layer thicknesses.⁴²

2. 3. 2 Chemical vapour deposition

Chemical Vapour Deposition (CVD) is a solid state process used to synthesis high quality, large area 2-D materials.¹⁶¹ This process is also widely used in the semiconductor industry to produce thin films. The conventional CVD process takes place in a quartz tube under high vacuum, in which a metal foil substrate is usually placed in the furnace to serve as a catalysis for the graphene growth. Then the H₂ gas is introduced into the furnace to protect the environment and active the metal catalysis during the annealing of the substrate. The annealing step allows the growth of the copper crystal grains to a few micrometer size under high temperature (>1000 °C). Then the carbon species such as CH₄ and C₂H₂ are introduced to the furnace, and decomposed into carbon atoms with the help of H₂. H₂ is also used to activate the metal catalysis and assist the nucleation of the graphene.¹⁷¹ In this way the single crystals of graphene are formed on the surface of the metal surface. (Figure 8a) As the time passes, the single crystals grow larger and merge into a whole complete polycrystalline graphene film. (Figure 8b) Graphene produced by this method is suitable for electronics and optoelectronic device applications.^{162, 172} Depending on the reaction condition, the CVD method has been developed into other subclasses, such as ambient pressure CVD,¹⁷³ plasmon enhanced CVD^{174, 175} and physical vapour deposition.⁷⁵ The physical vapour deposition method, which evaporates the chemical compounds from bulk form to deposit into lower dimension form without chemistry reactions, are also widely used in the preparation of the 2-D crystals. The

major challenges faced by this methods are controlling of the material coverage, uniformity, and the number of layers as well as transferring techniques onto the desired substrates.⁶⁰ Overall, the CVD method is a great process can be used in large scale production of each 2-D materials and their heterostructures.^{138, 176, 177}

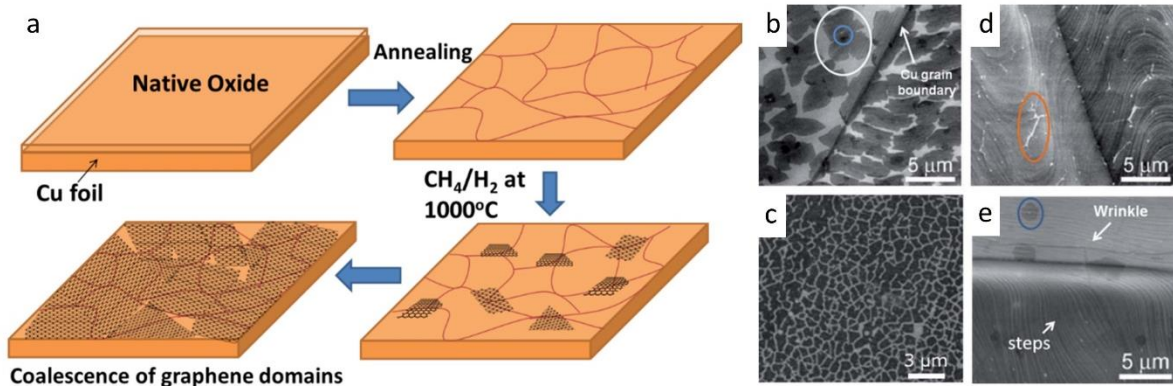


Figure 8. (a) Schematic showing the CVD procedure of growing graphene on copper foil. Firstly, the copper foil with native oxide is treated to CH_4/H_2 atmosphere at 1000°C ; then, the nuclei of graphene islands started to grow and merged to larger flakes.¹⁶¹ (b) shows SEM iamges of graphene on copper foil at different growth time from 1 min, 2.5 min to 10 min.¹⁶¹

2. 3. 3 Solvothermal growth

Solvothermal growth method is one of the most important chemical synthesis methods for growing nanocrystals in a liquid phase.¹⁷⁸ The precursors are introduced in the solution phase with a predesigned chemical stoichiometry, then react at an elevated temperature and high pressure. As this chemical process is performed in a sealed autoclave, it is easily scalable and a cost efficient method. Nevertheless, the main challenges behind this process are: 1. the crystal growth in the solution phase is a relatively complex process and involves competitive growth mechanism; 2. it lacks direct monitoring tools, which remains the process opaque to the researchers; 3. precise experimental environment control is critical in order to grow a target crystal type. Therefore, the understanding of the growth mechanism of each 2-D crystals become extremely important for step by step process.¹⁷⁹

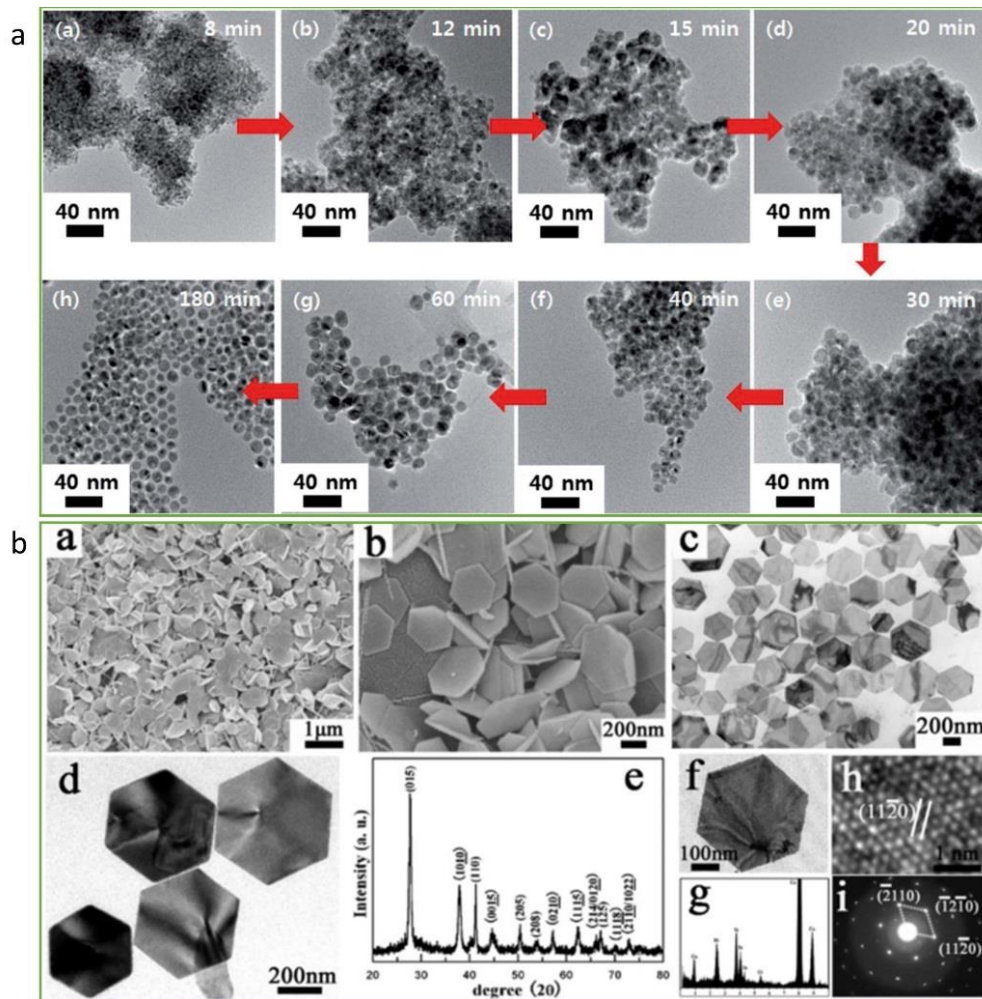


Figure 9. (a) Growth process of nanoparticles according to time scale¹⁷⁸. (b) Integrated characterization of Bi_2Te_3 nanoplates obtained by solvothermal growth method.¹⁸⁰

Figure 9a shows traditional methods to observe the nanoparticle growth with *ex situ* method, which means the samples are retrieved observed under microscopy. However, the observation is usually inconsistent during a large time scale. In term of the synthesis of 2-D materials mechanism and kinetics involved in the solvothermal synthesis of the 2-D materials are more important as their crystal growth are anisotropic. As to our knowledge, several attempts have been made to demonstrate the controlled synthesis of Bi_2Te_3 ¹⁸⁰⁻¹⁸², Bi_2Se_3 ¹⁸³, and ternary $\text{Bi}_2\text{Se}_x\text{Te}_{3-x}$ ³⁵ nanocrystals. The oriented attachment (OA) growth mechanism was proposed in an *ex situ* transmission electron microscopy (TEM) characterization study of Bi_2Se_3 and Bi_2Te_3 ¹⁸⁴. However, lacking a view of the whole process, more evidences are required to support the proposed mechanism.

2.4 *in situ* Powder X-ray diffraction monitoring

In situ powder X-ray diffraction (PXRD) is a powerful technique in advanced materials science¹⁸⁵⁻¹⁸⁷ to solve the problem of direct monitoring the whole crystal growth process. It usually employs a synchrotron, a magnetic field guided cyclic particle accelerator, as a light source to bend electrons in a ring geometry route and generate photons at the ring's tangential direction. The generated synchrotron beam is filtered through various filters and aligned afterwards to a specific beam line (Powder X-ray Diffraction beamline), as shown in Figure 10a. The first idea of synchrotron was conceived in 2000 by Sir Marcus Oliphant.¹⁸⁸ Compared with TEM, the PXRD has the advantage of characterizing bulk sample, hence is statistically more reliable for elucidating kinetics and mechanisms. Compared with laboratory based *in situ* PXRD, synchrotron based *in situ* PXRD has the advantages of higher angular resolution, higher signal to noise ratio, faster data acquisition to follow rapid reactions, and wavelength selectability to minimize fluorescence and absorption. However, its application to solvothermal synthesis has only been available in recent years due to the development of customized micro-autoclaves^{146, 193, 195, 201-203}. In the real experiment, the starting slurry is injected into a quartz glass microreactor (1 mm in outer diameter, 0.1 mm in wall thickness, and 35 mm in length). The microreactor was then sealed into a custom-made stainless steel holder that was initially designed by Norby.¹⁹³ External N₂ pressure (2.5 MPa) is applied to the microreactor through a pressure line during the solvothermal synthesis to prevent boiling of the solvent. The loaded microreactor is fixed at the X-ray beam center for signal measurement and collection.²⁰⁴ (Figure 10b) By now, lots of chemistry processes have been successfully studied by the *in situ* Powder X-ray diffraction techniques. For example, it is capable of providing real time information of phase transition^{185-186, 189, 190} nanoparticle crystallization¹⁹⁹⁻¹⁹⁸, energy storage^{199, 200} and metal organic framework synthesis.^{193, 198}

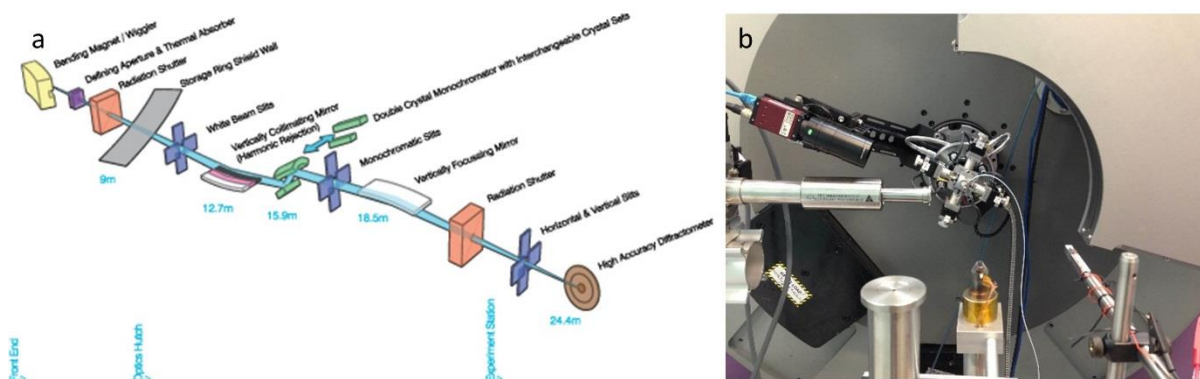


Figure 10. (a) Schematic of the Powder Diffraction (PD) beamline at Australian Synchrotron. (Retrieved from: <http://www.synchrotron.org.au/aussyncbeamlines/powder-diffraction/technical-information>) (b) A photograph of the experimental setup at the end station of the PD beam line.

2. 5 Photodetector applications

Graphene is famous for its significant wavelength independent absorption and high carrier mobility, which make it an excellent candidate for the optical and optoelectronic devices. One of the most important application in this field is photodetection.^{205, 206} Past few years have witnesses the outstanding fast development of graphene photodetectors, which are characterized by high response speed, broadband detection and flexibility.²⁰⁶ However, the relatively inefficient excitation separation mechanism in the pure graphene photodetector results in low photoresponsivity¹¹ and low photocountductive gain^{207, 208}. In order to improve the performance of the device by modify the properties of materials, there are several common approaches. The straight forward one is opening a band gap on graphene,²⁰⁹⁻²¹¹ However, this method is strongly limited on the fabrication process and tuneability. Second approach is to involve the other two-dimensional materials with controllable bandgaps into the photodetector system. Commonly reported materials include the transition metal dichalcogenides (TMDCs).^{212, 213} Though there are other approaches, such as introducing semiconducting quantum dots (QD) on graphene,²¹⁴ the much smaller optical gaps in these semiconducting materials strongly limit their application in the near-infrared spectra range, which was a great advantage of graphene. To solve this critical problem, researchers attempt to introduce small band gap materials into the photodetection system. Bi_2Te_3 , Bi_2Se_3 , Sb_2Te_3 , which have a very small band gap (0.15~0.3 eV) become a favourable choice.^{122, 215, 216} Employing the van der Waals heterostructures of graphene and bismuth chalcogenides not only retain the merits of graphene,

but also take advantages of exotic properties of bismuth chalcogenides to enhance light-matter interaction and reduce carrier recombination. Pioneer work has demonstrated that the graphene–Bi₂Te₃ heterostructure photodetector shows about 1000 times improvement in the responsivity of the monolayer graphene based device.¹³⁹ (Figure 11a) With proper band structure alignment, G-MoS₂,²²³ G-MoS₂-G,²²⁴ G-WSe₂-G,²²⁵ MoS₂-G quantum dots²²⁶ and other^{217-222, 227} heterostructures are used for photodetections. (Figure 11b-e)

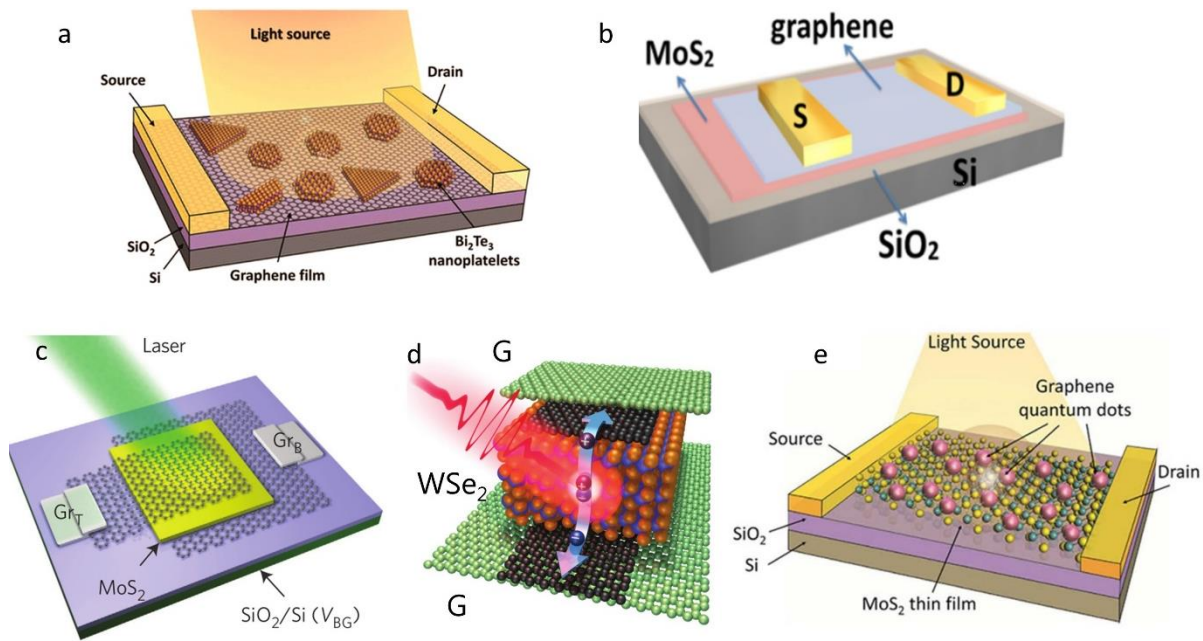


Figure 11. Examples of graphene based heterostructure for photodetection applications. (a) G-Bi₂Te₃ heterostructure.¹³⁹ (b) G-MoS₂ heterostructure.²²³ (c) G-MoS₂-G heterostructure²²⁴. (d) G-WSe₂-G heterostructure.²²⁵ (e) MoS₂-G (quantum dots) heterostructure.²²⁶

2.6 Plasmon resonance studies in far-field and near-field

Due to graphene's zero-band gap nature, it has obtained relatively high Dirac charge conductivity,²²⁸ large mode confinement²²⁹⁻²³¹ and chemical/electrical tunability.^{229, 232} More importantly, the lifetime of SP modes in graphene can reach hundreds of optical cycles, which potentially circumvent one of the major bottlenecks faced by noble-metal plasmonics.^{233, 234} As a consequence, graphene is able to support highly localised plasmon resonance (LPR) modes, which makes it possible to observe stronger light-matter interactions in graphene based structures. In 2011, Ju *et al.* pioneers plasmon excitations by engineering graphene film into

micro-ribbon arrays, and found that graphene plasmon resonance peak can be tuned over a broad terahertz frequency range by changing micro-ribbon width and *in situ* electrostatic doping.²²⁹ After the demonstration of graphene plasmon, graphene plasmon research has been boosted in the terahertz (THz) range,²⁰⁶ and led to a variety of practical applications in plasmonic devices.²³⁵⁻²⁵¹ Various flat graphene structures, such as graphene films,²⁵⁰ ribbons,^{229, 235-237} rings,²³⁸⁻²³⁹ disks,²²³⁸⁻²⁴⁰ holes arrays,²⁵¹ patches²⁵² and graphene photonic crystal structures²⁵³ have been proposed and studied. (Figure 12) In these graphene patterns, the light-matter interaction has been enhanced by summing up each individual localized coupling effect from neighbouring patterns.²³⁸ However, single layer of graphene supports relatively low resonance frequency/ magnitude dependence on carrier concentration. Thus, Yan *et. al.* fabricated graphene/ insulator multilayer stacks to enhance the plasmonic resonance magnitude according to the Dirac fermions' carrier density scaling law.²⁴⁰ Similarly, Zhang *et. al.* used atomically thin hexagonal boron nitride (h-BN) films as insulating spacers to enable strong plasmon coupling between adjacent graphene layers in vertical direction, which produces plasmonic resonance frequency upshift by two times and enhances its magnitude by three times.²²⁰ Further efforts of making stronger light-matter interaction calls for novel materials and innovative structures in the future.

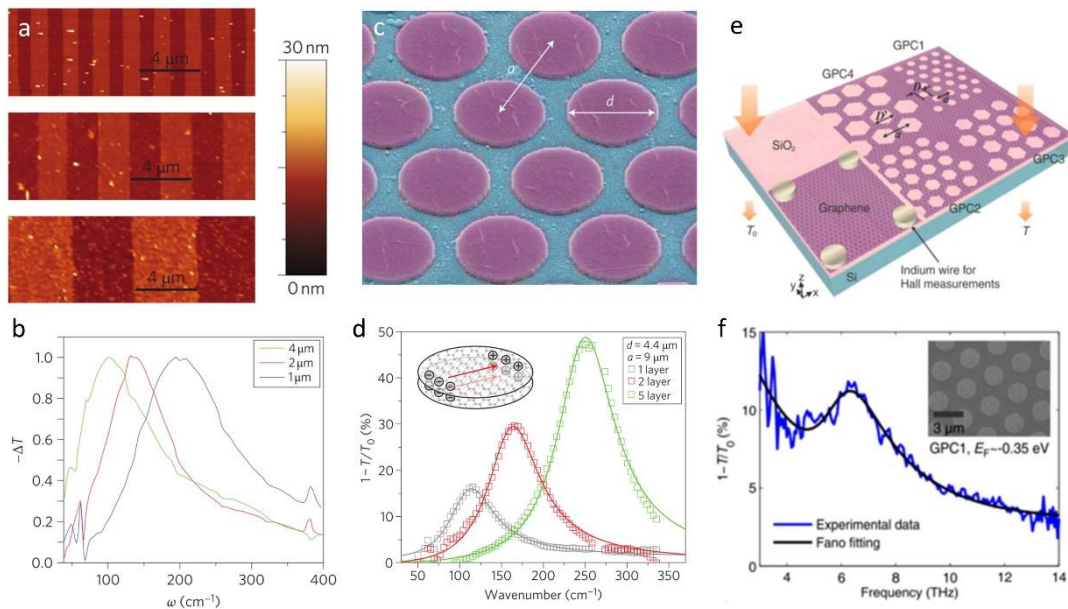


Figure 12. Patterned graphene and their FTIR spectrum. Graphene nanoribbons (a) and their corresponding spectrum with different width (b).²²⁹ Graphene and boron nitride multilayer stacking disks (c) and their spectrum with different layer thickness (d).²⁴⁰ Graphene photonic crystal (e), and their representative spectrum (f).²⁵³

The far-field technique of studying the graphene based plasmon resonance is a relatively indirect technique as it only observe the spectrum instead of the true electric-magnetic field distribution. Deep understanding of the graphene plasmonic modes in subwavelength scale is becoming critical to full master the potential applications of it.²⁵⁴ As a result, the strong requirement to image the real surface of the graphene plasmon has boosted the development of specialized measurement techniques, the near field optical microscopy.^{231, 235, 255}

Near-field Scanning Optical Microscopy (NSOM) is a microscopy used for investigating and exploiting the properties of evanescent waves that are beyond the far field resolution limit governed by conventional Abbe limit. In 1982, Synge conceived the first idea of near-field imaging by a pinhole tip.²⁵⁶ In his idea, the detecting tip operates at very close distance, same as aperture size, to the specimen surface. The tip serves as an opaque screen which illuminate light, and the transmitted light through the sample is collected by a remote detector on the other side. However, this setup is technically challenging at that time due to the lack of precise positioning system. Therefore, the first generation of scanning near-field optical microscopy design is not achieved until the 1980s by Zurich Research Laboratory^{257, 258} and Cornell University individually²⁵⁹⁻²⁶² with imaging resolution around $\lambda/20$. (Figure 14a, b) In order to further enhance the scanning resolution, apertureless probe is later invented to replace the apertured probe, and applied to the near field optical microscopy.²⁶³⁻²⁶⁵ This type of probe is also known as scattering type probe.(Figure 14c, d) One of the major advantage of this probe is its ability on confining the IR light onto a nanoscale tip, which enables an increase of the in-plane component of the momentum. This increasement further overcomes the mismatch of the wavevectors between the plasmons in extended monolayer graphene and freely propagating photons, leading to the efficient coupling of light to plasmons. Since this tip-enhanced technique greatly increased the resolution of the near field mapping results, developing of such techniques has continued during the last decade and became a powerful commercialized tool that delivers high spatial resolution near field optical image with strong signal enhancement.²⁶⁶⁻²⁷² The near field optical microscopy has also been employed in investigating graphene,^{231, 273-275} boron nitride,²⁷⁶ metal structures²⁷⁷ and semiconductors.²⁷⁸

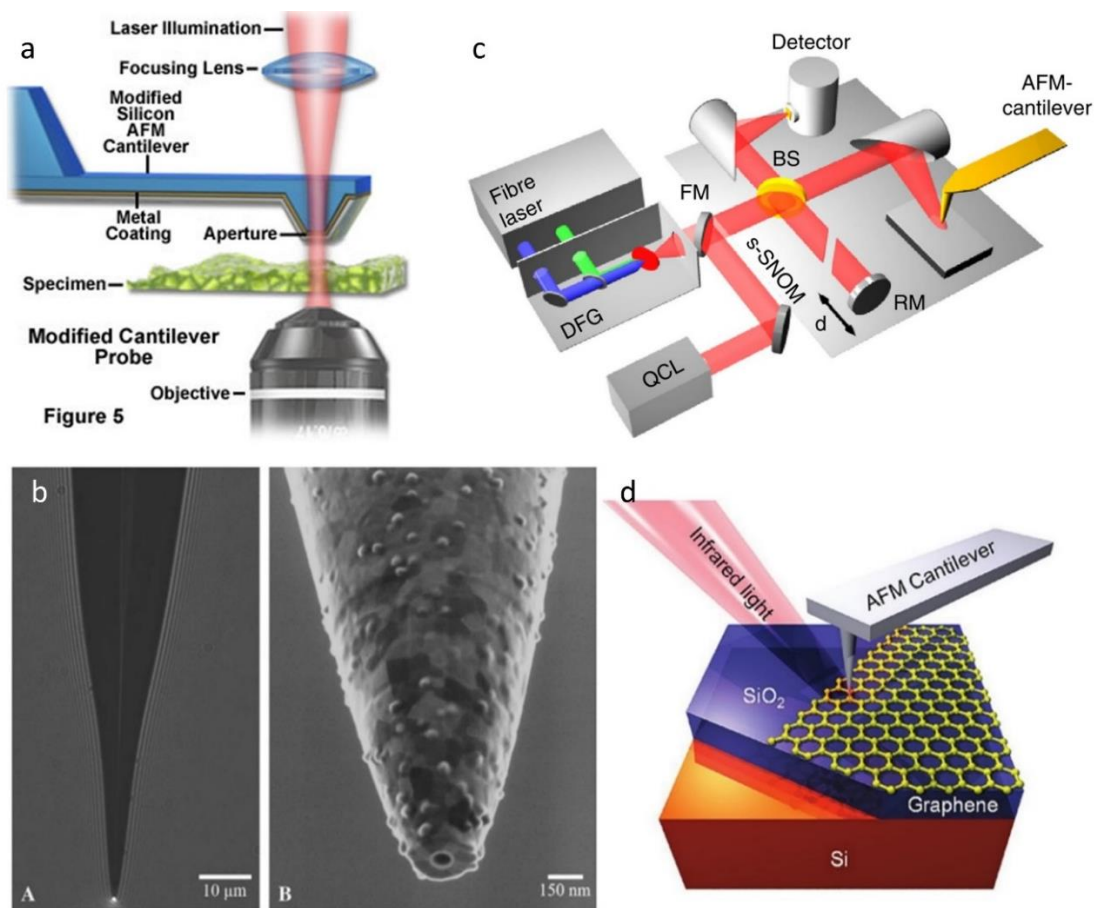


Figure 14. (a) Schematic of NSOM with aperture at its probe tip. (Retrieved from <http://www.olympusmicro.com/primer/techniques/nearfield/nearfieldprobes.html>) (b) SEM image of the 50 nm wide aperture at the tip.²⁷⁹ (c) Schematic of the scattering type NSOM.²⁸⁰ Scheme shows the scattering type NSOM can be used to study the graphene plasmon on the SiO₂ substrate.²⁷⁴

NSOM was firstly used to capture the real surface plasmon electric field distribution properties on the graphene surface by F. Zhe. et al.^{231, 275}. (Figure 15a) This research inspires researchers' interests in the exploring of real space graphene surface plasmon and its application of the next generation on-chip communication devices. In 2014, Alonso-Gonzalez *et. al.* demonstrate that graphene plasmons can be excited with resonant metal antennas.²⁸¹ (Figure 15b) Subsequently, other graphene ribbons and disks are intensively studied.²⁸⁴ Though, researchers argue that the graphene propagation length is limited on common substrates²⁵⁴, Woessner *et. al.* demonstrated that the damping of SPP on graphene surface can be compensated with a layer of BN underneath.²⁸² Further evidences have also shown that the surface plasmon losses have been further reduced in the quasi-suspended graphene due to the

weaker coupling with the substrate phonons.²⁸³ Therefore, the loss of graphene-based SPP waveguide, characterized by the intraband scattering rate, is only limited by the quality of graphene, which is continuously being improved with the development of fabrication technology. In sum, as the graphene surface plasmon properties and modes are better understood in the near field real space,²⁸⁴ the applications of graphene SPP waves are at the horizon.

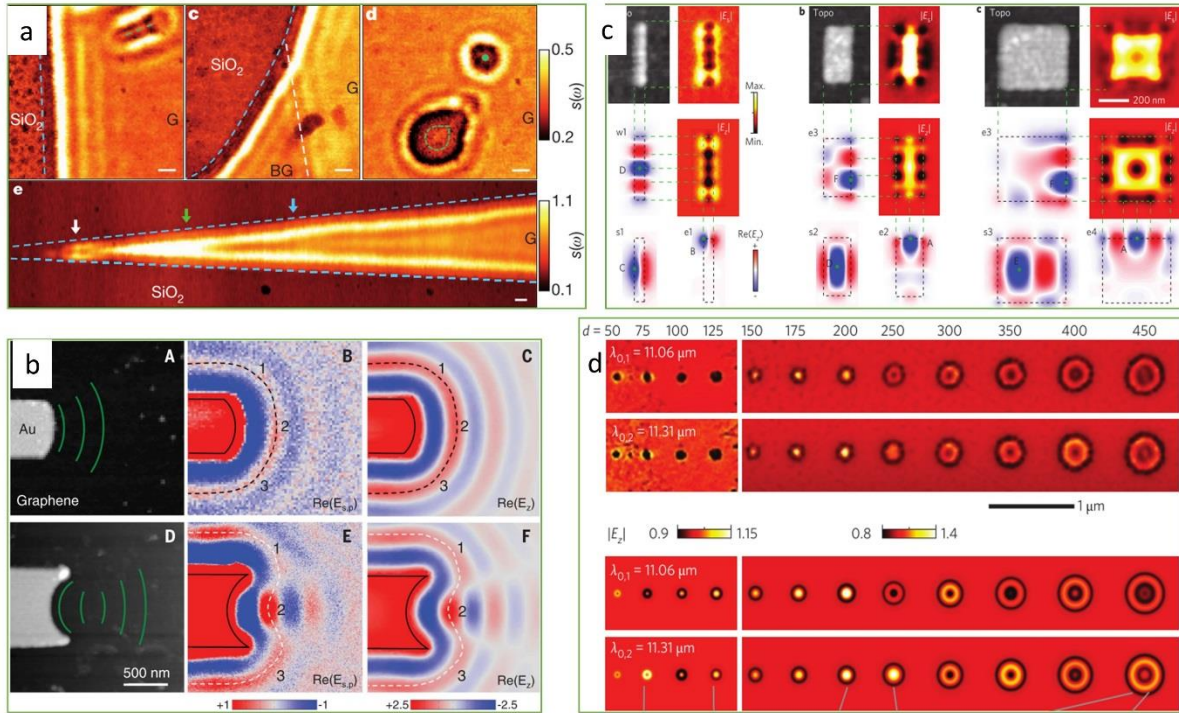


Figure 15. NSOM measurement of (a) graphene taper and defects²³¹, (b) Au scatter on graphene sheet,²⁸¹ (c) graphene ribbons,²⁸⁴ (d) graphene disks.²⁸⁴

2. 7 Review summary and Aims

2.7.1 Review summary

In summary, this chapter reviews the structures and properties of graphene, bismuth chalcogenides and their heterostructures with practical applications in photonics and optoelectronics. We have discussed the general synthesis methods of these 2-D materials, particularly mechanical exfoliation, chemical vapour deposition and solvothermal methods. The advanced characterization technique, *in situ* X-ray powder diffraction, involved in the main chapter of this dissertation has also been introduced and reviewed. With these advanced

material preparation, fabrication and characterization technologies. We can further study the growth and properties of graphene, bismuth chalcogenides and their heterostructures. Although the graphene and bismuth chalcogenides based topological insulators attracted lots of interests in the recent years, there are still many obstacles in preparation and fabrication before they can be fully realized in the practical application areas such as electronics and optoelectronics. Furthermore, the understanding of their application in the photonic devices, particular plasmonic devices, remains low.

2.7.2 Aims

The aims of this dissertation are to explore preparation and optoelectronic applications of the 2-D materials, specifically graphene and bismuth chalcogenides. The details of these aims are listed as below: 1. This dissertation aims to study and understand the crystals growth mechanism of the bismuth chalcogenides crystals and their graphene heterostructures in solution. 2. This dissertation aims to produce graphene and bismuth chalcogenides nanocrystals in large quantities. 3. This dissertation aims to demonstrate working devices of thus produced graphene and bismuth chalcogenides heterostructures. 4. This dissertation also aims to deliver the understanding and exploration of the plasmon resonance in graphene, bismuth chalcogenides and their heterostructures.

2.8 References:

1. Peierls, R. E. Quelques propriétés typiques des corps solides. *Ann. I. H. Poincaré* **5**, 177–222 (1935).
2. Landau, L. D. Zur Theorie der Phasenumwandlungen II. *Phys. Z. Sowjetunion* **11**, 26–35 (1937).
3. Wallace, P. R. The band theory of graphite. *Phys. Rev.* **71**, 622–634 (1947).
4. McClure, J. W. Diamagnetism of graphite. *Phys. Rev.* **104**, 666–671 (1956).
5. Slonczewski, J. C. & Weiss, P. R. Band structure of graphite. *Phys. Rev.* **109**, 272–279 (1958).
6. Wilson JA, Yoffe AD. The transition metal dichalcogenides discussion and interpretation of the observed optical, electrical and structural properties. *Adv Phys* **18**, 193-335 (1969).
7. Bednorz JG, Müller KA. Possible high T_c superconductivity in the Ba–La–Cu–O system. *Zeitschrift für Physik B Condensed Matter* **64**, 189-193 (1986).
8. Kamihara Y, *et al.* Iron-Based Layered Superconductor: LaOFeP. *J Am Chem Soc* **128**, 10012-10013 (2006).
9. Mouras, S.; *et al.* Synthesis of first stage graphite intercalation compounds with fluoride. *Revue de Chimie Minérale.* **24**, 572 (1987).
10. Novoselov KS, *et al.* Electric Field Effect in Atomically Thin Carbon Films. *Science* **306**, 666-669 (2004).
11. Geim AK, Novoselov KS. The rise of graphene. *Nature materials* **6**, 183-191 (2007).
12. Novoselov KS, Falco VI, Colombo L, Gellert PR, Schwab MG, Kim K. A roadmap for graphene. *Nature* **490**, 192-200 (2012).
13. Novoselov KS, *et al.* Two-dimensional atomic crystals. *Proc Natl Acad Sci USA* **102**, 10451-10453 (2005).
14. Wang X, *et al.* Highly anisotropic and robust excitons in monolayer black phosphorus. *Nat Nano* **10**, 517-521 (2015).
15. Li L, *et al.* Black phosphorus field-effect transistors. *Nat Nano* **9**, 372-377 (2014).
16. Appalakondaiah S, Vaitheeswaran G, Lebègue S, Christensen NE, Svane A. Effect of van der Waals interactions on the structural and elastic properties of black phosphorus. *Physical Review B* **86**, 035105 (2012).
17. Koenig SP, Doganov RA, Schmidt H, Castro Neto AH, Özyilmaz B. Electric field effect in ultrathin black phosphorus. *Appl Phys Lett* **104**, 103106 (2014).
18. Liu H, *et al.* Phosphorene: An Unexplored 2-D Semiconductor with a High Hole Mobility. *ACS nano* **8**, 4033-4041 (2014).
19. Xia F, Wang H, Jia Y. Rediscovering black phosphorus as an anisotropic layered material for optoelectronics and electronics. *Nature communications* **5**, 4458 (2014).
20. Rodin A, Carvalho A, Neto AC. Strain-induced gap modification in black phosphorus. *Phys Rev Lett* **112**, 176801 (2014).
21. Youngblood N, Chen C, Koester SJ, Li M. Waveguide-integrated black phosphorus photodetector with high responsivity and low dark current. *Nat Photo* **9**, 247-252 (2015).

22. Kim KK, *et al.* Synthesis of monolayer hexagonal boron nitride on Cu foil using chemical vapor deposition. *Nano Lett* **12**, 161-166 (2012).
23. Ismach A, *et al.* Toward the controlled synthesis of hexagonal boron nitride films. *ACS nano* **6**, 6378-6385 (2012).
24. Gutiérrez HR, *et al.* Extraordinary Room-Temperature Photoluminescence in Triangular WS₂ Monolayers. *Nano Lett* **13**, 3447-3454 (2012).
25. Tongay S, *et al.* Tuning Interlayer Coupling in Large-area Heterostructures with CVD-grown MoS₂ and WS₂ monolayers. *Nano Lett*, (2014).
26. Zhang X, *et al.* Vertical Heterostructures of Layered Metal Chalcogenides by van der Waals Epitaxy. *Nano Lett*, (2014).
27. Chen YL, *et al.* Experimental realization of a three-dimensional topological insulator, Bi₂Te₃. *Science* **325**, 178-181 (2009).
28. Hajlaoui M, *et al.* Ultrafast surface carrier dynamics in the topological insulator Bi(2)Te(3). *Nano Lett* **12**, 3532-3536 (2012).
29. Zhang H, Liu C-X, Qi X-L, Dai X, Fang Z, Zhang S-C. Topological insulators in Bi₂Se₃, Bi₂Te₃ and Sb₂Te₃ with a single Dirac cone on the surface. *Nature Physics* **5**, 438-442 (2009).
30. Zhu L-G, Kubera B, Fai Mak K, Shan J. Effect of Surface States on Terahertz Emission from the Bi₂Se₃ Surface. *Scientific reports* **5**, 10308 (2015).
31. Saleemi M, Toprak MS, Li S, Johnsson M, Muhammed M. Synthesis, processing, and thermoelectric properties of bulk nanostructured bismuth telluride (Bi₂Te₃). *J Mater Chem* **22**, 725-730 (2012).
32. Scheele M, Oeschler N, Meier K, Kornowski A, Klinke C, Weller H. Synthesis and Thermoelectric Characterization of Bi₂Te₃ Nanoparticles. *Adv Funct Mater* **19**, 3476-3483 (2009).
33. Kadel K, Kumari L, Li WZ, Huang JY, Provencio PP. Synthesis and Thermoelectric Properties of Bi₂Se₃ Nanostructures. *Nanoscale Research Letters*, (2010).
34. Zimmer A, Stein N, Johann L, Terryn H, Boulanger C. Characterizations of bismuth telluride films from Mott-Schottky plot and spectroscopic ellipsometry. *Surf Interface Anal* **40**, 593-596 (2008).
35. Soni A, Yanyuan Z, Ligen Y, Aik MK, Dresselhaus MS, Xiong Q. Enhanced thermoelectric properties of solution grown Bi₂Te(3-x)Se(x) nanoplatelet composites. *Nano Lett* **12**, 1203-1209 (2012).
36. Butler SZ, *et al.* Progress, Challenges, and Opportunities in Two-Dimensional Materials Beyond Graphene. *ACS nano* **7**, 2898-2926 (2013).
37. Xia F, Wang H, Xiao D, Dubey M, Ramasubramaniam A. Two-dimensional material nanophotonics. *Nat Photon* **8**, 899-907 (2014).
38. Service RF. Beyond graphene. *Science* **348**, 490-492 (2015).
39. Buscema M, *et al.* Photocurrent generation with two-dimensional van der Waals semiconductors. *Chem Soc Rev* **44**, 3691-3718 (2015).
40. Lee C, Wei X, Kysar JW, Hone J. Measurement of the Elastic Properties and Intrinsic Strength of Monolayer Graphene. *Science* **321**, 385-388 (2008).
41. Balandin AA, *et al.* Superior Thermal Conductivity of Single-Layer Graphene. *Nano Lett* **8**, 902-907 (2008).

42. Ni ZH, *et al.* Graphene Thickness Determination Using Reflection and Contrast Spectroscopy. *Nano Lett* **7**, 2758-2763 (2007).
43. Nair RR, *et al.* Fine Structure Constant Defines Visual Transparency of Graphene. *Science* **320**, 1308-1308 (2008).
44. Novoselov KS, *et al.* Two-dimensional gas of massless Dirac fermions in graphene. *Nature* **438**, 197-200 (2005).
45. Mas-Balleste R, Gomez-Navarro C, Gomez-Herrero J, Zamora F. 2-D materials: to graphene and beyond. *Nanoscale* **3**, 20-30 (2011).
46. Bolotin KI, *et al.* Ultrahigh electron mobility in suspended graphene. *Solid State Commun* **146**, 351-355 (2008).
47. Geim AK. Graphene: Status and Prospects. *Science* **324**, 1530-1534 (2009).
48. Latil S, Henrard L. Charge Carriers in Few-Layer Graphene Films. *Phys Rev Lett* **97**, 036803 (2006).
49. Shallcross S, Sharma S, Kandelaki E, Pankratov OA. Electronic structure of turbostratic graphene. *Physical Review B* **81**, 165105 (2010).
50. Zhou SY, *et al.* Substrate-induced bandgap opening in epitaxial graphene. *Nature materials* **6**, 770-775 (2007).
51. Vicarelli L, *et al.* Graphene field-effect transistors as room-temperature terahertz detectors. *Nature materials* **11**, 865-871 (2012).
52. Bae S, *et al.* Roll-to-roll production of 30-inch graphene films for transparent electrodes. *Nature nanotechnology* **5**, 574-578 (2010).
53. Liu C-H, Chang Y-C, Norris TB, Zhong Z. Graphene photodetectors with ultra-broadband and high responsivity at room temperature. *Nat Nano* **9**, 273-278 (2014).
54. Bao Q, Loh KP. Graphene Photonics, Plasmonics, and Broadband Optoelectronic Devices. *ACS nano* **6**, 3677-3694 (2012).
55. Yao X, Tokman M, Belyanin A, Efficient Nonlinear Generation of THz Plasmons in Graphene and Topological Insulators. *Physical Review Letters* **112**, 055501 (2014).
56. Chee WK, Lim HN, Zainal Z, Huang NM, Harrison I, Andou Y. Flexible Graphene-Based Supercapacitors: A Review. *The Journal of Physical Chemistry C* **120**, 4153-4172 (2016).
57. Duy LT, *et al.* High Performance Three-Dimensional Chemical Sensor Platform Using Reduced Graphene Oxide Formed on High Aspect-Ratio Micro-Pillars. *Adv Funct Mater* **25**, 883-890 (2015).
58. Bao Q, *et al.* Atomic-Layer Graphene as a Saturable Absorber for Ultrafast Pulsed Lasers. *Adv Funct Mater* **19**, 3077-3083 (2009).
59. Bao Q, *et al.* Monolayer graphene as a saturable absorber in a mode-locked laser. *Nano Res* **4**, 297-307 (2011).
60. Zhang Y, Zhang L, Zhou C, Review of Chemical Vapor Deposition of Graphene and Related Applications. *Acc. Chem. Res.* **46**, 2329-2339 (2013).

61. Castro Neto AH, Guinea F, Peres NMR, Novoselov KS, Geim AK. The electronic properties of graphene. *Rev Mod Phys* **81**, 109-162 (2009).
62. Grigorenko AN, Polini M, Novoselov KS. Graphene plasmonics. *Nat Photon* **6**, 749-758 (2012).
63. Jablan M, Solja M, x010D, x, Buljan H. Plasmons in Graphene: Fundamental Properties and Potential Applications. *Proc IEEE* **101**, 1689-1704 (2013).
64. Xiao S, Zhu X, Li B-H, Mortensen NA. Graphene-plasmon polaritons: From fundamental properties to potential applications. *Frontiers of Physics* **11**, 1-13 (2016).
65. Kullmann W, Eichhorn G, Rauh H, Geick R, Eckold G, Steigenberger U. Lattice Dynamics and Phonon Dispersion in the Narrow Gap Semiconductor Bi₂Te₃ with Sandwich Structure. *physica status solidi (b)* **162**, 125-140 (1990).
66. Cava R, Ji H, Fuccillo M, Gibson Q, Hor Y. Crystal structure and chemistry of topological insulators. *Journal of Materials Chemistry C* **1**, 3176-3189 (2013).
67. Peng H, *et al.* Aharonov-Bohm interference in topological insulator nanoribbons. *Nature materials* **9**, 225-229 (2010).
68. Satterthwaite CB, Ure RW. Electrical and Thermal Properties of Bi₂Te₃. *Phys Rev* **108**, 1164-1170 (1957).
69. Kong D, Cui Y. Opportunities in chemistry and materials science for topological insulators and their nanostructures. *Nature chemistry* **3**, 845-849 (2011).
70. Zhu H, *et al.* Topological Insulator Bi₂Se₃ Nanowire High Performance Field-Effect Transistors. *Sci Rep* **3**, (2013).
71. Kong D, *et al.* Topological insulator nanowires and nanoribbons. *Nano Lett* **10**, 329-333 (2010).
72. Song C-L, *et al.* Topological insulator Bi₂Se₃ thin films grown on double-layer graphene by molecular beam epitaxy. *Appl Phys Lett* **97**, - (2010).
73. Tan J, *et al.* Thermoelectric properties of bismuth telluride thin films deposited by radio frequency magnetron sputtering. (ed^(eds) (2005).
74. Venkatasubramanian R, Siivola E, Colpitts T, O'Quinn B. Thin-film thermoelectric devices with high room-temperature figures of merit. *Nature* **413**, 597-602 (2001).
75. Peng H, *et al.* Topological insulator nanostructures for near-infrared transparent flexible electrodes. *Nature chemistry* **4**, 281-286 (2012).
76. Mahan GD, Sofo JO, Bartkowiak M. Multilayer thermionic refrigerator and generator. *J Appl Phys* **83**, 4683-4689 (1998).
77. Ashalley E, Chen H, Tong X, Li H, Wang ZM. Bismuth telluride nanostructures: preparation, thermoelectric properties and topological insulating effect. *Frontiers of Materials Science* **9**, 103-125 (2015).
78. Roushan P, *et al.* Topological surface states protected from backscattering by chiral spin texture. *Nature* **460**, 1106-1109 (2009).
79. Klitzing Kv, Dorda G, Pepper M. New Method for High-Accuracy Determination of the Fine-Structure Constant Based on Quantized Hall Resistance. *Phys Rev Lett* **45**, 494-497 (1980).
80. Bernevig BA, Hughes TL, Zhang S-C. Quantum Spin Hall Effect and Topological Phase Transition in HgTe Quantum Wells. *Science* **314**, 1757-1761 (2006).

81. König M, *et al.* Quantum Spin Hall Insulator State in HgTe Quantum Wells. *Science* **318**, 766-770 (2007).
82. Kane CL, Mele EJ. Z₂ topological order and the quantum spin Hall effect. *Phys Rev Lett* **95**, 146802 (2005).
83. Pankratov OA, Pakhomov SV, Volkov BA. Supersymmetry in heterojunctions: Band-inverting contact on the basis of Pb_{1-x}Sn_xTe and Hg_{1-x}Cd_xTe. *Solid State Commun* **61**, 93-96 (1987).
84. Hsieh D, *et al.* A topological Dirac insulator in a quantum spin Hall phase. *Nature* **452**, 970-974 (2008).
85. Fu L, Kane C. Topological insulators with inversion symmetry. *Physical Review B* **76**, (2007).
86. Pesin D, MacDonald AH. Spintronics and pseudospintronics in graphene and topological insulators. *Nature materials* **11**, 409-416 (2012).
87. Lu Y, Guo J. Topological-insulator-based non-volatile memory cells: A quantum device simulation. In: *Electron Devices Meeting (IEDM), 2012 IEEE International* (2012).
88. Kim D, Syers P, Butch NP, Paglione J, Fuhrer MS. Ambipolar surface state thermoelectric power of topological insulator Bi₂Se₃. *Nano Lett* **14**, 1701-1706 (2014).
89. Chang PH, Bahramy MS, Nagaosa N, Nikolic BK. Giant Thermoelectric Effect in Graphene-Based Topological Insulators with Heavy Adatoms and Nanopores. *Nano Lett* **14**, 3779-3784 (2014).
90. Sung JH, *et al.* Atomic Layer-by-Layer Thermoelectric Conversion in Topological Insulator Bismuth/Antimony Tellurides. *Nano Lett*, (2014).
91. Sun Y, *et al.* Atomically Thick Bismuth Selenide Freestanding Single Layers Achieving Enhanced Thermoelectric Energy Harvesting. *J Am Chem Soc* **134**, 20294-20297 (2012).
92. Zhang J-M, *et al.* Stability, electronic, and magnetic properties of the magnetically doped topological insulators Bi₂Se₃, Bi₂Te₃, and Sb₂Te₃. *Physical Review B* **88**, 235131 (2013).
93. Chadov S, Qi X, Kübler J, Fecher GH, Felser C, Zhang SC. Tunable multifunctional topological insulators in ternary Heusler compounds. *Nature materials* **9**, 541-545 (2010).
94. Siroki G, Lee DKK, Haynes PD, Giannini V. Single-electron induced surface plasmons on a topological nanoparticle. *Nature communications* **7**, (2016).
95. Di Pietro P, *et al.* Observation of Dirac plasmons in a topological insulator. *Nat Nano* **8**, 556-560 (2013).
96. Autore M, *et al.* Observation of Magnetoplasmons in Bi₂Se₃ Topological Insulator. *ACS Photonics*, (2015).
97. Qi J, Liu H, Xie XC. Surface plasmon polaritons in topological insulators. *Physical Review B* **89**, 155420 (2014).
98. Karch A. Surface plasmons and topological insulators. *Physical Review B* **83**, (2011).
99. Politano A, *et al.* Interplay of Surface and Dirac Plasmons in Topological Insulators: The Case of Bi₂Se₃. *Phys Rev Lett* **115**, 216802 (2015).
100. Luo ZC, *et al.* 2 GHz passively harmonic mode-locked fiber laser by a microfiber-based topological insulator saturable absorber. *Opt Lett* **38**, 5212-5215 (2013).

101. Zhang X, Wang J, Zhang S-C. Topological insulators for high-performance terahertz to infrared applications. *Physical Review B* **82**, 245107 (2010).
102. Luo CW, *et al.* THz Generation and Detection on Dirac Fermions in Topological Insulators. *Advanced Optical Materials* **1**, 804-808 (2013).
103. Valdés Aguilar R, *et al.* Terahertz Response and Colossal Kerr Rotation from the Surface States of the Topological Insulator Bi₂Se₃. *Phys Rev Lett* **108**, 087403 (2012).
104. Tang CS, *et al.* Terahertz conductivity of topological surface states in Bi_{1.5}Sb_{0.5}Te_{1.8}Se_{1.2}. *Scientific reports* **3**, 3513 (2013).
105. Xia Y, *et al.* Observation of a large-gap topological-insulator class with a single Dirac cone on the surface. *Nature Physics* **5**, 398-402 (2009).
106. Fu L, Kane CL. Superconducting Proximity Effect and Majorana Fermions at the Surface of a Topological Insulator. *Phys Rev Lett* **100**, 096407 (2008).
107. Stanescu TD, Sau JD, Lutchyn RM, Das Sarma S. Proximity effect at the superconductor-topological insulator interface. *Physical Review B* **81**, 241310 (2010).
108. Mahfouzi F, Nikolić BK, Chen S-H, Chang C-R. Microwave-driven ferromagnet-topological-insulator heterostructures: The prospect for giant spin battery effect and quantized charge pump devices. *Physical Review B* **82**, 195440 (2010).
109. Garate I, Franz M. Inverse Spin-Galvanic Effect in the Interface between a Topological Insulator and a Ferromagnet. *Phys Rev Lett* **104**, 146802 (2010).
110. Hutasoit JA, Stanescu TD. Induced spin texture in semiconductor/topological insulator heterostructures. *Physical Review B* **84**, 085103 (2011).
111. Hirahara T, *et al.* Interfacing 2-D and 3-D Topological Insulators: Bi(111) Bilayer on Bi₂Te₃. *Phys Rev Lett* **107**, 166801 (2011).
112. Chen H, Zhu W, Xiao D, Zhang Z. CO Oxidation Facilitated by Robust Surface States on Au-Covered Topological Insulators. *Phys Rev Lett* **107**, 056804 (2011).
113. Cook A, Franz M. Majorana fermions in a topological-insulator nanowire proximity-coupled to an *s*-wave superconductor. *Physical Review B* **84**, 201105 (2011).
114. Zhang Q, Zhang Z, Zhu Z, Schwingenschlögl U, Cui Y. Exotic Topological Insulator States and Topological Phase Transitions in Sb₂Se₃-Bi₂Se₃ Heterostructures. *ACS nano* **6**, 2345-2352 (2012).
115. Nakayama K, *et al.* Manipulation of Topological States and the Bulk Band Gap Using Natural Heterostructures of a Topological Insulator. *Phys Rev Lett* **109**, 236804 (2012).
116. Shevtsov O, Carmier P, Petitjean C, Groth C, Carpentier D, Waintal X. Graphene-Based Heterojunction between Two Topological Insulators. *Physical Review X* **2**, 031004 (2012).
117. Qu F, *et al.* Strong Superconducting Proximity Effect in Pb-Bi₂Te₃ Hybrid Structures. *Scientific reports* **2**, 339 (2012).
118. Ueda S, Kawakami N, Sigrist M. Proximity effects in a topological-insulator/Mott-insulator heterostructure. *Physical Review B* **87**, 161108 (2013).
119. Luo W, Qi X-L. Massive Dirac surface states in topological insulator/magnetic insulator heterostructures. *Physical Review B* **87**, 085431 (2013).

120. Wu G, *et al.* Tuning the vertical location of helical surface states in topological insulator heterostructures via dual-proximity effects. *Scientific reports* **3**, 1233 (2013).
121. Björnson K, Black-Schaffer AM. Vortex states and Majorana fermions in spin-orbit coupled semiconductor-superconductor hybrid structures. *Physical Review B* **88**, 024501 (2013).
122. Hasan MZ, Kane CL. Colloquium : Topological insulators. *Rev Mod Phys* **82**, 3045-3067 (2010).
123. Qi X-L, Zhang S-C. Topological insulators and superconductors. *Rev Mod Phys* **83**, 1057-1110 (2011).
124. Xu J-P, *et al.* Experimental Detection of a Majorana Mode in the core of a Magnetic Vortex inside a Topological Insulator-Superconductor Bi₂Te₃/NbSe₂ Heterostructure. *Phys Rev Lett* **114**, 017001 (2015).
125. Nayak C, Simon SH, Stern A, Freedman M, Das Sarma S. Non-Abelian anyons and topological quantum computation. *Rev Mod Phys* **80**, 1083-1159 (2008).
126. Zareapour P, *et al.* Proximity-induced high-temperature superconductivity in the topological insulators Bi₂Se₃ and Bi₂Te₃. *Nature communications* **3**, 1056 (2012).
127. Qi XL, Li R, Zang J, Zhang SC. Inducing a magnetic monopole with topological surface States. *Science* **323**, 1184-1187 (2009).
128. Chen YL, *et al.* Massive Dirac fermion on the surface of a magnetically doped topological insulator. *Science* **329**, 659-662 (2010).
129. Qi X-L, Hughes TL, Zhang S-C. Topological field theory of time-reversal invariant insulators. *Physical Review B* **78**, 195424 (2008).
130. Xu S-Y, *et al.* Hedgehog spin texture and Berry's phase tuning in a magnetic topological insulator. *Nat Phys* **8**, 616-622 (2012).
131. Virk N, Yazyev OV. Dirac fermions at high-index surfaces of bismuth chalcogenide topological insulator nanostructures. *Scientific reports* **6**, 20220 (2016).
132. Jin K-H, Jhi S-H. Proximity-induced giant spin-orbit interaction in epitaxial graphene on a topological insulator. *Physical Review B* **87**, 075442 (2013).
133. Zhang J, Triola C, Rossi E. Proximity Effect in Graphene-Topological-Insulator Heterostructures. *Phys Rev Lett* **112**, 096802 (2014).
134. Kou L, Wu S-C, Felser C, Frauenheim T, Chen C, Yan B. Robust 2-D Topological Insulators in van der Waals Heterostructures. *ACS nano* **8**, 10448-10454 (2014).
135. Jozwiak C, *et al.* Photoelectron spin-flipping and texture manipulation in a topological insulator. *Nat Phys* **9**, 293-298 (2013).
136. Zhu ZH, *et al.* Photoelectron Spin-Polarization Control in the Topological Insulator Bi₂Se₃. *Phys Rev Lett* **112**, 076802 (2014).
137. Guo Y, *et al.* 2-D Hybrid Nanostructured Dirac Materials for Broadband Transparent Electrodes. *Adv Mater* **27**, 4315-4321 (2015).
138. Kim N, *et al.* Persistent Topological Surface State at the Interface of Bi₂Se₃ Film Grown on Patterned Graphene. *ACS nano* **8**, 1154-1160 (2014).

139. Qiao H, *et al.* Broadband Photodetectors Based on Graphene–Bi₂Te₃ Heterostructure. *ACS nano* **9**, 1886-1894 (2015).
140. Sensale-Rodriguez B, *et al.* Broadband graphene terahertz modulators enabled by intraband transitions. *Nature communications* **3**, 780 (2012).
141. Shi SF, *et al.* Optimizing Broadband Terahertz Modulation with Hybrid Graphene/Metasurface Structures. *Nano Lett* **15**, 372-377 (2015).
142. Cai X, *et al.* Plasmon-Enhanced Terahertz Photodetection in Graphene. *Nano Lett* **15**, 4295-4302 (2015).
143. Shigekawa H, Yoshida S, Takeuchi O. Spectroscopy: Nanoscale terahertz spectroscopy. *Nat Photon* **8**, 815-817 (2014).
144. Tomaino JL, *et al.* Terahertz imaging and spectroscopy of large-area single-layer graphene. *Opt Express* **19**, 141-146 (2011).
145. Sensale-Rodriguez B, *et al.* Terahertz imaging employing graphene modulator arrays. *Opt Express* **21**, 2324-2330 (2013).
146. Dikin D. A. *et al.* Preparation and characterization of graphene oxide paper. *Nature*. **448**. 457-460 (2007).
147. Coleman JN, *et al.* Two-Dimensional Nanosheets Produced by Liquid Exfoliation of Layered Materials. *Science* **331**, 568-571 (2011).
148. Hernandez Y, *et al.* High-yield production of graphene by liquid-phase exfoliation of graphite. *Nat Nano* **3**, 563-568 (2008).
149. Bourlinos AB, Georgakilas V, Zboril R, Steriotis TA, Stubos AK. Liquid-Phase Exfoliation of Graphite Towards Solubilized Graphenes. *Small* **5**, 1841-1845 (2009).
150. Viculis LM, Mack JJ, Kaner RB. A Chemical Route to Carbon Nanoscrolls. *Science* **299**, 1361-1361 (2003).
151. Cano-Márquez AG, *et al.* Ex-MWNTs: Graphene Sheets and Ribbons Produced by Lithium Intercalation and Exfoliation of Carbon Nanotubes. *Nano Lett* **9**, 1527-1533 (2009).
152. Kosynkin DV, Lu W, Sinitskii A, Pera G, Sun Z, Tour JM. Highly Conductive Graphene Nanoribbons by Longitudinal Splitting of Carbon Nanotubes Using Potassium Vapor. *ACS nano* **5**, 968-974 (2011).
153. Qian H, Negri F, Wang C, Wang Z. Fully Conjugated Tri(perylene bisimides): An Approach to the Construction of n-Type Graphene Nanoribbons. *J Am Chem Soc* **130**, 17970-17976 (2008).
154. Yan X, Cui X, Li L-s. Synthesis of Large, Stable Colloidal Graphene Quantum Dots with Tunable Size. *J Am Chem Soc* **132**, 5944-5945 (2010).
155. Yan X, Cui X, Li B, Li L-s. Large, Solution-Processable Graphene Quantum Dots as Light Absorbers for Photovoltaics. *Nano Lett* **10**, 1869-1873 (2010).
156. Hamilton IP, Li B, Yan X, Li L-s. Alignment of Colloidal Graphene Quantum Dots on Polar Surfaces. *Nano Lett* **11**, 1524-1529 (2011).
157. Forbeaux I, Themlin JM, Debever JM. Heteroepitaxial graphite on 6H-SiC(0001): Interface formation through conduction-band electronic structure. *Physical Review B* **58**, 16396-16406 (1998).

158. Coraux J, N'Diaye AT, Busse C, Michely T. Structural Coherency of Graphene on Ir(111). *Nano Lett* **8**, 565-570 (2008).
159. Obraztsov AN. Chemical vapour deposition: Making graphene on a large scale. *Nat Nano* **4**, 212-213 (2009).
160. Vázquez de Parga AL, *et al.* Periodically Rippled Graphene: Growth and Spatially Resolved Electronic Structure. *Phys Rev Lett* **100**, 056807 (2008).
161. Mattevi C, Kim H, Chhowalla M. A review of chemical vapour deposition of graphene on copper. *J Mater Chem* **21**, 3324 (2011).
162. Kim KS, *et al.* Large-scale pattern growth of graphene films for stretchable transparent electrodes. *Nature* **457**, 706-710 (2009).
163. Li X, *et al.* Large-area synthesis of high-quality and uniform graphene films on copper foils. *Science* **324**, 1312-1314 (2009).
164. Lee Y, *et al.* Wafer-Scale Synthesis and Transfer of Graphene Films. *Nano Lett* **10**, 490-493 (2010).
165. Berger C, *et al.* Ultrathin Epitaxial Graphite: 2-D Electron Gas Properties and a Route toward Graphene-based Nanoelectronics. *The Journal of Physical Chemistry B* **108**, 19912-19916 (2004).
166. Berger C, *et al.* Electronic Confinement and Coherence in Patterned Epitaxial Graphene. *Science* **312**, 1191-1196 (2006).
167. Borovikov V, Zangwill A. Step-edge instability during epitaxial growth of graphene from SiC(0001). *Physical Review B* **80**, 121406 (2009).
168. Charrier A, *et al.* Solid-state decomposition of silicon carbide for growing ultra-thin heteroepitaxial graphite films. *J Appl Phys* **92**, 2479-2484 (2002).
169. Yi M, Shen Z. A review on mechanical exfoliation for the scalable production of graphene. *Journal of Materials Chemistry A* **3**, 11700-11715 (2015).
170. Novoselov KS, Neto AHC. Two-dimensional crystals-based heterostructures: materials with tailored properties. *Phys Scr* 2012, 014006 (2012).
171. Zhang X, Wang L, Xin J, Yakobson BI, Ding F. Role of Hydrogen in Graphene Chemical Vapor Deposition Growth on a Copper Surface. *J Am Chem Soc* **136**, 3040-3047 (2014).
172. Lee J-H, *et al.* Wafer-scale growth of single-crystal monolayer graphene on reusable hydrogen-terminated germanium. *Science* **344**, 286-289 (2014).
173. Vlassiuk I, *et al.* Large scale atmospheric pressure chemical vapor deposition of graphene. *Carbon* **54**, 58-67 (2013).
174. Nandamuri G, Roumimov S, Solanki R. Remote plasma assisted growth of graphene films. *Appl Phys Lett* **96**, 154101 (2010).
175. Kim J, Ishihara M, Koga Y, Tsugawa K, Hasegawa M, Iijima S. Low-temperature synthesis of large-area graphene-based transparent conductive films using surface wave plasma chemical vapor deposition. *Appl Phys Lett* **98**, - (2011).
176. Dang W, Peng H, Li H, Wang P, Liu Z. Epitaxial heterostructures of ultrathin topological insulator nanoplate and graphene. *Nano Lett* **10**, 2870-2876 (2010).

177. Zhang C, *et al.* Facile fabrication of graphene-topological insulator Bi₂Se₃ hybrid Dirac materials via chemical vapor deposition in Se-rich conditions. *CrystEngComm* **16**, 8941-8945 (2014).
178. Chee S-S, Lee J-H. Preparation and oxidation behavior of Ag-coated Cu nanoparticles less than 20 nm in size. *Journal of Materials Chemistry C* **2**, 5372-5381 (2014).
179. Kong, D. S.; Koski, K. J.; Cha, J. J.; Hong, S. S.; Cui, Y. Ambipolar field effect in Sb-doped Bi₂Se₃nanoplates by solvothermal synthesis. *Nano Lett.* 2013, **13**, 632–636.
180. Zhang Y, Hu LP, Zhu TJ, Xie J, Zhao XB. High Yield Bi₂Te₃ Single Crystal Nanosheets with Uniform Morphology via a Solvothermal Synthesis. *Crystal Growth & Design* **13**, 645-651 (2013).
181. He H, Huang D, Zhang X, Li G. Characterization of hexagonal Bi₂Te₃ nanosheets prepared by solvothermal method. *Solid State Commun* **152**, 810-815 (2012).
182. Mi J-L, *et al.* Biomolecule-Assisted Hydrothermal Synthesis and Self-Assembly of Bi₂Te₃ Nanostring-Cluster Hierarchical Structure. *ACS nano* **4**, 2523-2530 (2010).
183. Liu K, Wang J, Liu H, Xiang D. Preparation and characterization of nanostructured Bi₂Se₃ and Sn_{0.5}-Bi₂Se₃. *Rare Metals* **28**, 112-116 (2009).
184. Zhang G, Wang W, Lu X, Li X. Solvothermal Synthesis of V–VI Binary and Ternary Hexagonal Platelets: The Oriented Attachment Mechanism. *Crystal Growth & Design* **9**, 145-150 (2009).
185. McKinnon WR, Dahn JR, Jui CCH. Determining ternary phase diagrams with electrochemical cells and in situ X-ray diffraction. *Acta Metall* **34**, 1879-1883 (1986).
186. Jensen KM, Tyrsted C, Bremholm M, Iversen BB. In Situ studies of solvothermal synthesis of energy materials. *ChemSusChem* **7**, 1594-1611 (2014).
187. Kellarakis A, Yoon K, Sics I, Somani RH, Hsiao BS, Chu B. Uniaxial deformation of an elastomer nanocomposite containing modified carbon nanofibers by in situ synchrotron X-ray diffraction. *Polymer* **46**, 5103-5117 (2005).
188. Rotblat J. Obituary: Mark Oliphant (1901-2000). *Nature* **407**, 468-468 (2000).
189. Kim WK, Payzant EA, Anderson TJ, Crisalle OD. In situ investigation of the selenization kinetics of Cu–Ga precursors using time-resolved high-temperature X-ray diffraction. *Thin Solid Films* **515**, 5837-5842 (2007).
190. Filinchuk Y, *et al.* In Situ Diffraction Study of Catalytic Hydrogenation of VO₂: Stable Phases and Origins of Metallicity. *J Am Chem Soc* **136**, 8100-8109 (2014).
191. Wang Z, *et al.* Deviatoric Stress Driven Formation of Large Single-Crystal PbS Nanosheet from Nanoparticles and in Situ Monitoring of Oriented Attachment. *J Am Chem Soc* **133**, 14484-14487 (2011).
192. Li W, *et al.* Versatile inorganic-organic hybrid WO_x-ethylenediamine nanowires: Synthesis, mechanism and application in heavy metal ion adsorption and catalysis. *Nano Res* **7**, 903-916 (2014).
193. Norby P. Hydrothermal Conversion of Zeolites: An in Situ Synchrotron X-ray Powder Diffraction Study. *J Am Chem Soc* **119**, 5215-5221 (1997).
194. Xia F, *et al.* Understanding Solvothermal Crystallization of Mesoporous Anatase Beads by In Situ Synchrotron PXRD and SAXS. *Chem Mater* **26**, 4563-4571 (2014).

195. Laumann A, *et al.* In-situ Synchrotron X-ray Diffraction Study of the Formation of Cubic Li₂TiO₃ Under Hydrothermal Conditions. *Eur J Inorg Chem* **2011**, 2221-2226 (2011).
196. Jensen KM, Tyrsted C, Bremholm M, Iversen BB. In Situ studies of solvothermal synthesis of energy materials. *ChemSusChem* **7**, 1594-1611 (2014).
197. Brand HEA, Scarlett NVY, Grey IE. In situ studies into the formation kinetics of potassium jarosite. *J Appl Crystallogr* **45**, 535-545 (2012).
198. Li W-J, Gao S-Y, Liu T-F, Han L-W, Lin Z-J, Cao R. In Situ Growth of Metal–Organic Framework Thin Films with Gas Sensing and Molecule Storage Properties. *Langmuir : the ACS journal of surfaces and colloids* **29**, 8657-8664 (2013).
199. Ryan KR, Trahey L, Okasinski JS, Burrell AK, Ingram BJ. In situ synchrotron X-ray diffraction studies of lithium oxygen batteries. *Journal of Materials Chemistry A* **1**, 6915-6919 (2013).
200. Wang X-J, *et al.* A new in situsynchrotron X-ray diffraction technique to study the chemical delithiation of LiFePO₄. *Chem Commun* **47**, 7170-7172 (2011).
201. Millange F, Medina MI, Guillou N, Ferey G, Golden KM, Walton RI. Time-resolved in situ diffraction study of the solvothermal crystallization of some prototypical metal-organic frameworks. *Angew Chem Int Ed Engl* **49**, 763-766 (2010).
202. Saha D, *et al.* In situ total X-ray scattering study of WO₃ nanoparticle formation under hydrothermal conditions. *Angew Chem Int Ed Engl* **53**, 3667-3670 (2014).
203. Zhou Y, Antonova E, Bensch W, Patzke GR. In situ X-ray diffraction study of the hydrothermal crystallization of hierarchical Bi₂WO₆ nanostructures. *Nanoscale* **2**, 2412-2417 (2010).
204. Song J, *et al.* Solvothermal Growth of Bismuth Chalcogenide Nanoplatelets by the Oriented Attachment Mechanism: An in Situ PXRD Study. *Chem Mater*, **27**, 3471-3482 (2015).
205. Cho S, Fuhrer MS. Charge transport and inhomogeneity near the minimum conductivity point in graphene. *Physical Review B* **77**, 081402 (2008).
206. Li ZQ, *et al.* Dirac charge dynamics in graphene by infrared spectroscopy. *Nat Phys* **4**, 532-535 (2008).
207. Xia F, Mueller T, Lin Y-m, Valdes-Garcia A, Avouris P. Ultrafast graphene photodetector. *Nat Nano* **4**, 839-843 (2009).
208. Zhang BY, *et al.* Broadband high photoresponse from pure monolayer graphene photodetector. *Nature communications* **4**, 1811 (2013).
209. Fekete L, Hlinka JY, Kadlec F, Kužel P, Mounaix P. Active optical control of the terahertz reflectivity of high-resistivity semiconductors. *Opt Lett* **30**, 1992-1994 (2005).
210. Fekete L, Kadlec F, Němec H, Kužel P. Fast one-dimensional photonic crystal modulators for the terahertz range. *Opt Express* **15**, 8898-8912 (2007).
211. Chen H-T, Padilla WJ, Zide JMO, Gossard AC, Taylor AJ, Averitt RD. Active terahertz metamaterial devices. *Nature* **444**, 597-600 (2006).
212. Roy K, *et al.* Graphene-MoS₂ hybrid structures for multifunctional photoresponsive memory devices. *Nat Nano* **8**, 826-830 (2013).
213. Zhang W, *et al.* Ultrahigh-Gain Photodetectors Based on Atomically Thin Graphene-MoS₂ Heterostructures. *Sci Rep* **4**, (2014).

214. Konstantatos G, et al. Hybrid graphene-quantum dot phototransistors with ultrahigh gain. *Nat Nano* 7, 363-368 (2012).
215. Wang Y, et al. Gate-Controlled Surface Conduction in Na-Doped Bi₂Te₃ Topological Insulator Nanoplates. *Nano Lett* 12, 1170-1175 (2012).
216. Xiu F-X, Zhao T-T. Topological insulator nanostructures and devices. *Chinese Physics B* 22, 096104 (2013).
217. Dean CR, et al. Boron nitride substrates for high-quality graphene electronics. *Nat Nano* 5, 722-726 (2010).
218. Bertolazzi S, Krasnozhan D, Kis A. Nonvolatile Memory Cells Based on MoS₂/Graphene Heterostructures. *ACS nano* 7, 3246-3252 (2013).
219. Huang C, et al. Lateral heterojunctions within monolayer MoSe₂-WSe₂ semiconductors. *Nature materials* 13, 1096-1101 (2014).
220. Zhang K, Yap FL, Li K, Ng CT, Li LJ, Loh KP. Large Scale Graphene/Hexagonal Boron Nitride Heterostructure for Tunable Plasmonics. *Adv Funct Mater* 24, 731-738 (2014).
221. Deng Y, et al. Black Phosphorus-Monolayer MoS₂ van der Waals Heterojunction p-n Diode. *ACS nano* 8, 8292-8299 (2014).
222. Mu H, et al. Graphene-Bi₂Te₃ Heterostructure as Saturable Absorber for Short Pulse Generation. *ACS Photonics* 2, 832-841 (2015).
223. Zhang W, et al. Ultrahigh-Gain Photodetectors Based on Atomically Thin Graphene-MoS(2) Heterostructures. *Scientific reports* 4, 3826 (2014).
224. Yu WJ, et al. Highly efficient gate-tunable photocurrent generation in vertical heterostructures of layered materials. *Nat Nano* 8, 952-958 (2013).
225. Massicotte M, et al. Picosecond photoresponse in van der Waals heterostructures. *Nat Nano* 11, 42-46 (2016).
226. Chen C. Highly responsive MoS₂ photodetectors enhanced by graphene quantum dots. *Scientific reports* 5, 11830 (2015).
227. Koppens FHL, Mueller T, Avouris P, Ferrari AC, Vitiello MS, Polini M. Photodetectors based on graphene, other two-dimensional materials and hybrid systems. *Nat Nano* 9, 780-793 (2014).
228. Takatsuka Y, Takahagi K, Sano E, Ryzhii V, Otsuji T. Gain enhancement in graphene terahertz amplifiers with resonant structures. *J Appl Phys* 112, 033103 (2012).
229. Ju L, et al. Graphene plasmonics for tunable terahertz metamaterials. *Nature nanotechnology* 6, 630-634 (2011).
230. Chen J, et al. Optical nano-imaging of gate-tunable graphene plasmons. *Nature* 487, 77-81 (2012).
231. Fei Z, *et al.* Gate-tuning of graphene plasmons revealed by infrared nano-imaging. *Nature* **487**, 82-85 (2012).
232. Schwierz F. Graphene transistors. *Nat Nano* 5, 487-496 (2010).
233. Gao W, Shu J, Qiu C, Xu Q. Excitation of Plasmonic Waves in Graphene by Guided-Mode Resonances. *ACS nano* 6, 7806-7813 (2012).

234. Grigorenko AN, Polini M, Novoselov KS. Graphene plasmonics. *Nat Photon* 6, 749-758 (2012).
235. Yan H, et al. Damping pathways of mid-infrared plasmons in graphene nanostructures. *Nat Photon* 7, 394-399 (2013).
236. Brar VW, et al. Hybrid Surface-Phonon-Plasmon Polariton Modes in Graphene/Monolayer h-BN Heterostructures. *Nano Lett* 14, 3876-3880 (2014).
237. Freitag M, Low T, Zhu W, Yan H, Xia F, Avouris P. Photocurrent in graphene harnessed by tunable intrinsic plasmons. *Nature communications* 4, (2013).
238. Hugen Y, Fengnian X, Zhiqiang L, Phaedon A. Plasmonics of coupled graphene microstructures. *New Journal of Physics* 14, 125001 (2012).
239. Fang Z, et al. Gated Tunability and Hybridization of Localized Plasmons in Nanostructured Graphene. *ACS nano* 7, 2388-2395 (2013).
240. Yan H, et al. Tunable infrared plasmonic devices using graphene/insulator stacks. *Nature nanotechnology* 7, 330-334 (2012).
241. Pechtel L, Song L, Schuh D, Ajayan P, Wegscheider W, Holleitner AW. Time-resolved ultrafast photocurrents and terahertz generation in freely suspended graphene. *Nature communications* 3, 646 (2012).
242. Ramakrishnan G, Chakkittakandy R, Planken PCM. Terahertz generation from graphite. *Opt Express* 17, 16092-16099 (2009).
243. Schmadel D, Jenkins GS, Drew HD. Proposal for a Graphene Plasmonic THz Emitter. arXiv preprint arXiv:13111605, (2013).
244. Wu Y, et al. Graphene Terahertz Modulators by Ionic Liquid Gating. *Adv Mater* 27, 1874-1879 (2015).
245. Rahm M, Li J-S, Padilla W. THz Wave Modulators: A Brief Review on Different Modulation Techniques. *Journal of Infrared, Millimeter, and Terahertz Waves* 34, 1-27 (2013).
246. Sensale-Rodriguez B, et al. Broadband graphene terahertz modulators enabled by intraband transitions. *Nature communications* 3, 780 (2012).
247. Tong J, Muthee M, Chen S-Y, Yngvesson SK, Yan J. Antenna Enhanced Graphene THz Emitter and Detector. *Nano Lett* 15, 5295-5301 (2015).
248. Tomaino JL, et al. Terahertz imaging and spectroscopy of large-area single-layer graphene. *Opt Express* 19, 141-146 (2011).
249. Sensale-Rodriguez B, et al. Terahertz imaging employing graphene modulator arrays. *Opt Express* 21, 2324-2330 (2013).
250. Vicarelli L, et al. Graphene field-effect transistors as room-temperature terahertz detectors. *Nature materials* 11, 865-871 (2012).
251. Kleine-Ostmann T, Nagatsuma T. A Review on Terahertz Communications Research. *Journal of Infrared, Millimeter, and Terahertz Waves* 32, 143-171 (2011).
252. Llatser I, Kremers C, Cabellos-Aparicio A, Jornet JM, Alarcón E, Chigrin DN. Graphene-based nano-patch antenna for terahertz radiation. *Photonics and Nanostructures-Fundamentals and Applications* 10, 353-358 (2012).

253. Yeung KYM, Chee J, Yoon H, Song Y, Kong J, Ham D. Far-Infrared Graphene Plasmonic Crystals for Plasmonic Band Engineering. *Nano Lett* **14**, 2479-2484 (2014).
254. Politano A, Chiarello G. Plasmon modes in graphene: status and prospect. *Nanoscale* **6**, 10927-10940 (2014).
255. Lereu AL, Passian A, Dumas P. Near field optical microscopy: a brief review. *International Journal of Nanotechnology* **9**, 488-501 (2012).
256. Synge EH. XXXVIII. A suggested method for extending microscopic resolution into the ultra-microscopic region. *The London, Edinburgh, and Dublin Philosophical Magazine and Journal of Science* **6**, 356-362 (1928).
257. Pohl DW, Denk W, Lanz M. Optical stethoscopy: Image recording with resolution $\lambda/20$. *Appl Phys Lett* **44**, 651-653 (1984).
258. Dürig U, Pohl DW, Rohner F. Near-field optical-scanning microscopy. *J Appl Phys* **59**, 3318-3327 (1986).
259. Lewis A, Isaacson M, Harootunian A, Muray A. Development of a 500 Å spatial resolution light microscope. *Ultramicroscopy* **13**, 227-231 (1984).
260. Betzig E, Lewis A, Harootunian A, Isaacson M, Kratschmer E. Near Field Scanning Optical Microscopy (NSOM): Development and Biophysical Applications. *Biophys J* **49**, 269-279 (1986).
261. Betzig E, Harootunian A, Lewis A, Isaacson M. Near-field diffraction by a slit: implications for superresolution microscopy. *Appl Opt* **25**, 1890-1900 (1986).
262. Harootunian A, Betzig E, Isaacson M, Lewis A. Super-resolution fluorescence near-field scanning optical microscopy. *Appl Phys Lett* **49**, 674-676 (1986).
263. Fischer UC. Submicrometer aperture in a thin metal film as a probe of its microenvironment through enhanced light scattering and fluorescence. *J Opt Soc Am B* **3**, 1239-1244 (1986).
264. Fischer UC, Dürig UT, Pohl DW. Near-field optical scanning microscopy in reflection. *Appl Phys Lett* **52**, 249-251 (1988).
265. Umeda N, Hayashi Y, Nagai K, Takayanagi A. Scanning Wiener-fringe microscope with an optical fiber tip. *Appl Opt* **31**, 4515-4518 (1992).
266. Novotny L, Stranick SJ. NEAR-FIELD OPTICAL MICROSCOPY AND SPECTROSCOPY WITH POINTED PROBES. *Annu Rev Phys Chem* **57**, 303-331 (2006).
267. Mauser N, Hartschuh A. Tip-enhanced near-field optical microscopy. *Chem Soc Rev* **43**, 1248-1262 (2014).
268. Hartschuh A. Tip-Enhanced Near-Field Optical Microscopy. *Angew Chem Int Ed* **47**, 8178-8191 (2008).
269. Yeo B-S, Stadler J, Schmid T, Zenobi R, Zhang W. Tip-enhanced Raman Spectroscopy – Its status, challenges and future directions. *Chem Phys Lett* **472**, 1-13 (2009).
270. Ming T, Chen H, Jiang R, Li Q, Wang J. Plasmon-Controlled Fluorescence: Beyond the Intensity Enhancement. *The Journal of Physical Chemistry Letters* **3**, 191-202 (2012).
271. Pettinger B, Schambach P, Villagómez CJ, Scott N. Tip-enhanced Raman spectroscopy: near-fields acting on a few molecules. *Annu Rev Phys Chem* **63**, 379-399 (2012).

272. Atkin JM, Berweger S, Jones AC, Raschke MB. Nano-optical imaging and spectroscopy of order, phases, and domains in complex solids. *Adv Phys* **61**, 745-842 (2012).
273. Fei Z, *et al.* Edge and Surface Plasmons in Graphene Nanoribbons. *Nano Lett* **15**, 8271-8276 (2015).
274. Fei Z, *et al.* Infrared Nanoscopy of Dirac Plasmons at the Graphene–SiO₂ Interface. *Nano Lett* **11**, 4701-4705 (2011).
275. Fei Z, *et al.* Electronic and plasmonic phenomena at graphene grain boundaries. *Nat Nano* **8**, 821-825 (2013).
276. Dai S, *et al.* Tunable Phonon Polaritons in Atomically Thin van der Waals Crystals of Boron Nitride. *Science* **343**, 1125-1129 (2014).
277. Alonso-Gonzalez P, *et al.* Resolving the electromagnetic mechanism of surface-enhanced light scattering at single hot spots. *Nature communications* **3**, 684 (2012).
278. Huber AJ, Ziegler A, Kock T, Hillenbrand R. Infrared nanoscopy of strained semiconductors. *Nature nanotechnology* **4**, 153-157 (2009).
279. Mooren OL, Erickson ES, Dickenson NE, Dunn RC. Extending Near-Field Scanning Optical Microscopy for Biological Studies. *Journal of the Association for Laboratory Automation* **11**, 268-272 (2006).
280. Amenabar I, *et al.* Structural analysis and mapping of individual protein complexes by infrared nanospectroscopy. *Nature communications* **4**, (2013).
281. Alonso-Gonzalez P, *et al.* Controlling graphene plasmons with resonant metal antennas and spatial conductivity patterns. *Science* **344**, 1369-1373 (2014).
282. Woessner A, *et al.* Highly confined low-loss plasmons in graphene–boron nitride heterostructures. *Nature materials* **14**, 421-425 (2015).
283. Dubrovkin AM, Tao J, Chao Yu X, Zheludev NI, Jie Wang Q. The reduction of surface plasmon losses in quasi-suspended graphene. *Scientific reports* **5**, 9837 (2015).
284. Nikitin AY, *et al.* Real-space mapping of tailored sheet and edge plasmons in graphene nanoresonators. *Nat Photon* **10**, 239-243 (2016).

**Chapter 3: Solvothermal growth of Bismuth Chalcogenide
Nanoplatelets by the Oriented Attachment Mechanism:
An in Situ PXRD Study**

Declaration for Thesis Chapter 3

Declaration by candidate

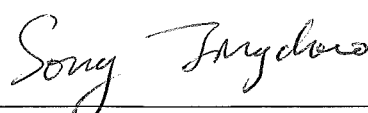
In the case of Chapter 3, the nature and extent of my contribution to the work was the following:

Nature of contribution	Extent of Contribution (%)
Key ideas, experimental works, analysis of results, writing up	60

The following co-authors contributed to the work. If co-authors are students at Monash University, the extent of their contribution in percentage terms must be stated:

Name	Nature of contribution	Extent of contribution (%) for student co-authors only
Fang Xia	Analysis of results, writing up	
Meng Zhao	Experimental works	
Yu Lin Zhong	Experimental works	
Wei Li	Experimental works	
Kian Ping Loh	Analysis of results	
Rachel A. Caruso	Analysis of results	
Qiaoliang Bao*	Key ideas, analysis of results, writing up	Supervisor

The undersigned hereby certify that the above declaration correctly reflects the nature and extent of the candidate's and co-authors' contributions to this work*.

Candidate's Signature		Date: 16/09/2016
Main Supervisor's Signature		Date: 16/09/2016

Solvothermal Growth of Bismuth Chalcogenide Nanoplatelets by the Oriented Attachment Mechanism: An in Situ PXRD Study

Jingchao Song,^{†,‡,§} Fang Xia,^{‡,||,§} Meng Zhao,[⊥] Yu Lin Zhong,[†] Wei Li,[‡] Kian Ping Loh,[⊥] Rachel A. Caruso,^{*,‡,‡} and Qiaoliang Bao^{*,†,§}

[†]Department of Materials Science and Engineering, Monash University, Wellington Road, Clayton, Victoria 3800, Australia

[‡]Manufacturing Flagship, The Commonwealth Scientific and Industrial Research Organization (CSIRO), Clayton, Victoria 3168, Australia

^{||}School of Engineering and Information Technology, Murdoch University, Murdoch, Western Australia 6150, Australia

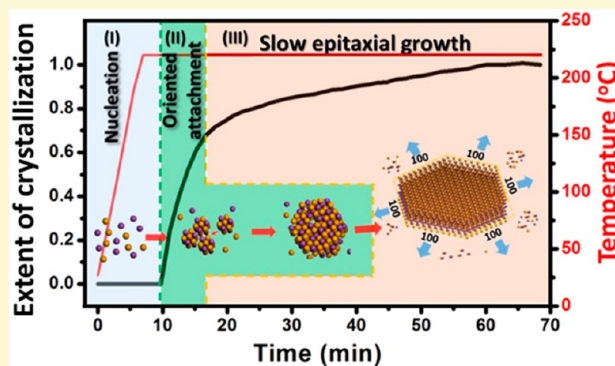
[⊥]Department of Chemistry, and Graphene Research Centre, National University of Singapore, 3 Science Drive 3, Singapore 117543, Singapore

[#]Particulate Fluids Processing Centre, School of Chemistry, The University of Melbourne, Melbourne, Victoria 3010, Australia

[§]Institute of Functional Nano and Soft Materials (FUNSOM), Jiangsu Key Laboratory for Carbon-Based Functional Materials and Devices, and Collaborative Innovation Center of Suzhou Nano Science and Technology, Soochow University, Suzhou 215123, People's Republic of China

Supporting Information

ABSTRACT: Ultrathin two-dimensional bismuth chalcogenide materials have received substantial research attention due to their potential applications in electronics and optoelectronics. While solvothermal synthesis is considered to be one of the most promising methods for large-scale production of such materials, the mechanisms that govern the crystallization during solvothermal treatment are still poorly understood. In this work, the solvothermal syntheses of $\text{Bi}_2\text{Se}_x\text{Te}_{3-x}$ ($x = 0-3$) hexagonal nanoplatelets were monitored by synchrotron-based in situ powder X-ray diffraction, which enabled investigation of crystallization curves, lattice parameters, and crystal size evolution under a variety of synthesis conditions. On the basis of the crystallization curves and crystal size evolution, a general 3-step crystallization process has been deduced: (1) An induction period for the dissolution of the precursor and nucleation of $\text{Bi}_2\text{Se}_x\text{Te}_{3-x}$, followed by (2) rapid growth of planar crystals through the oriented attachment, and finally (3) a diffusion-controlled slow growth step consuming the remaining precursor from the solution. Oriented attachment is very effective for the growth of binary composites, resulting in a high yield of large planar crystals; however, it is much less effective for the growth of ternary composites due to lattice mismatch of the nuclei formed at the induction period, producing much smaller crystals accompanied by a limited yield of large planar crystals. Additionally, three intermediate phases (Bi_2TeO_5 , Bi_2SeO_5 , and Na_2SeO_3) were observed that played an important role in controlling the phase separation as well as the composition of the final ternary compounds.



1. INTRODUCTION

Bismuth chalcogenides such as Bi_2Te_3 and Bi_2Se_3 are well-known thermoelectric materials^{1,2} and recently have been demonstrated to be the first generation of simple 3-dimensional topological insulators.³⁻⁵ Topological insulators are a group of insulators or semiconductors having an insulating interior (large energy gap) in their bulk states and a time-reversal symmetry-protected metallic surface.⁵ Owing to their special physical properties, the topological insulators have a wide range of potential applications in spintronics,⁶ nanoelectronics,⁷⁻⁹ thermoelectric devices,^{1,10} and optoelectronics.^{11,12}

Two-dimensional bismuth chalcogenides, $\text{Bi}_2\text{Se}_x\text{Te}_{3-x}$ ($x = 0-3$), are hexagonal plates with a thickness on the nanometer

scale and width on the micrometer scale. They can be synthesized by mechanical, physical, or chemical approaches.¹³ Examples include mechanical exfoliation,^{14,15} chemical vapor deposition (CVD),¹⁶⁻¹⁸ and molecular beam epitaxy (MBE).^{19,20} However, these techniques often have limited control over product composition and normally produce a small quantity of materials, sufficiently only for the demonstration of device fabrication. On the other hand, solvothermal synthesis has proved to be a very efficient and cost-effective

Received: March 10, 2015

Revised: April 14, 2015

Published: April 17, 2015

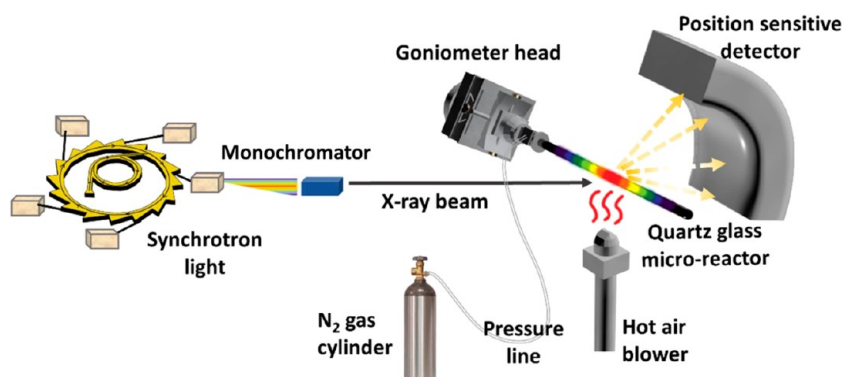


Figure 1. Schematic of the experimental setup for in situ PXRD at the Australian Synchrotron. The color of the microreactor represents the temperature distribution; temperatures from high to low are red, orange, yellow, green, purple, blue, and black; only the red zone is monitored by PXRD.

approach for producing these materials of designed composition and has a greater potential to realize mass production for many practical applications.¹⁰

However, the mechanism and kinetics involved in the solvothermal synthesis of bismuth chalcogenides have received little attention, even though they are vital for optimizing the synthesis parameters for desired products. Several attempts have been made to demonstrate the controlled synthesis of Bi_2Te_3 ,^{21–23} Bi_2Se_3 ,²⁴ and ternary $\text{Bi}_2\text{Se}_x\text{Te}_{3-x}$ nanocrystals. In an attempt to synthesize Bi_2Se_3 and Bi_2Te_3 , the growth was suggested to follow an oriented attachment (OA) mechanism rather than the seed-mediated growth.²⁵ Crystal growth by OA occurs by smaller crystals formed at the early stage of synthesis attaching together. However, this conclusion was based on ex situ transmission electron microscopy (TEM) characterization, which has its limitation in viewing the whole synthesis process. To reveal a clearer picture of the solvothermal synthesis, in situ characterization to obtain direct reaction information is required. Nonetheless, it is not an easy task to observe the crystal growth under solvothermal conditions owing to the fact that the reactions occur in a sealed autoclave.

In situ powder X-ray diffraction (PXRD) is a powerful technique in advanced materials science.^{26–28} For example, it is capable of providing real-time information on phase transition,^{26,27,29,30} nanoparticle crystallization,^{31–34} electrochemical electrolysis,³⁵ energy storage,^{36,37} and metal organic framework synthesis.^{38,39} Compared with TEM, PXRD has the advantage of characterizing bulk sample and hence is statistically more reliable for elucidating kinetics and mechanisms, and compared with laboratory-based in situ PXRD, synchrotron-based in situ PXRD has the advantages of higher angular resolution, higher signal-to-noise ratio, faster data acquisition to follow rapid reactions, and wavelength selectability to minimize fluorescence and absorption. However, its application to solvothermal synthesis has only been available in recent years thanks to the development of customized microautoclaves.^{32,39–42}

In this work, we report the first synchrotron-based in situ PXRD investigation on the solvothermal synthesis of a series of binary and ternary bismuth chalcogenide $\text{Bi}_2\text{Se}_x\text{Te}_{3-x}$ ($x = 0–3$) nanoplatelets. In situ PXRD was able to provide a complete and unambiguous picture of the crystal growth process. The synthesis is surprisingly complex, being very sensitive to temperature, precursor type, and precursor concentration. Five of the six syntheses involved one or two intermediate phases (Bi_2TeO_5 , Bi_2SeO_5 , or Na_2SeO_5) that play a vital role in

determining the final product composition. On the basis of in situ PXRD and electron microscopy results, we propose a 3-step growth mechanism: (1) an induction period for precursor dissolution and product nucleation, followed by (2) a rapid growth step through the oriented attachment mechanism, and finally (3) a diffusion-controlled slow epitaxial growth period consuming the remaining precursor in the solution. Additionally, we found that oriented attachment is very effective in binary composition due to perfect lattice match of nuclei but ineffective in ternary composition due to poor lattice match of nuclei, producing very small sized nanoplatelets.

2. EXPERIMENTAL SECTION

2.1. Preparation of $\text{Bi}_2\text{Se}_x\text{Te}_{3-x}$ Precursor Slurries. The precursor slurries for synthesizing $\text{Bi}_2\text{Se}_x\text{Te}_{3-x}$ were prepared with Bi:Se:Te molar ratios of (1) 2:3:0, (2) 2:0:3, (3) 2:1:2, and (4) 2:1.5:1.5. The following chemicals were used: bismuth oxide (Bi_2O_3 , Townson & Mercer), bismuth nitrate ($\text{BiNO}_3 \cdot \text{H}_2\text{O}$, Fluka), sodium selenite (Na_2SeO_3 , 99%, BDH Chemicals Ltd.), sodium telluride (Na_2TeO_3 , 99.5%, Alfa Aesar), ethylene glycol (EG) (BDH Chemicals Ltd.), and polyvinylpyrrolidone (PVP) ($M_n = 40\text{K}$, Sigma-Aldrich). Here EG serves both as a solvent and as a reducing agent, and PVP acts as the capping agent, which attaches to the (001) facets, hence facilitating the formation of the planar nanoplatelets.²⁵

For the preparation of precursor slurries, 0.15 g of PVP was dissolved in 2 mL of EG. To this solution, various amounts of the Bi, Se, and Te sources (stoichiometric ratios) were added under vigorous stirring. For the Bi_2Se_3 precursor slurry, either 0.100 g of Bi_2O_3 + 0.111 g of Na_2SeO_3 or 0.200 g of $\text{BiNO}_3 \cdot \text{H}_2\text{O}$ + 0.170 g of Na_2SeO_3 were added. For the Bi_2Te_3 precursor slurry, either 0.100 g of Bi_2O_3 + 0.143 g of Na_2TeO_3 or 0.200 g of $\text{BiNO}_3 \cdot \text{H}_2\text{O}$ + 0.218 g of Na_2TeO_3 were added. For the Bi_2SeTe_2 precursor slurry, 0.100 g of Bi_2O_3 + 0.037 g of Na_2SeO_3 + 0.095 g of Na_2TeO_3 were added. For the $\text{Bi}_2\text{Se}_{1.5}\text{Te}_{1.5}$ precursor slurry, 0.100 g of Bi_2O_3 + 0.056 g of Na_2SeO_3 + 0.071 g of Na_2TeO_3 were added. In order to study the effect of precursor concentration on the crystal growth, another $\text{Bi}_2\text{Se}_{1.5}\text{Te}_{1.5}$ precursor slurry was prepared with the concentration doubled. All these mixtures were stirred vigorously for 20 min and then used for the solvothermal synthesis of $\text{Bi}_2\text{Se}_x\text{Te}_{3-x}$ materials during the in situ PXRD experiments.

2.2. Monitoring of the Solvothermal Synthesis Using In Situ PXRD. In situ PXRD experiments were conducted at the Australian Synchrotron powder diffraction beamline. Figure 1 shows the configuration of the experiments. The X-ray energy was 12.4 keV, and the wavelength (1.0000 Å) was calibrated using a LaB_6 standard (NIST SRM 660b). The starting slurry was injected into a quartz glass microreactor (1 mm in outer diameter, 0.1 mm in wall thickness, and 35 mm in length). The microreactor was then sealed into a custom-made stainless steel holder that was initially designed by Norby.³²

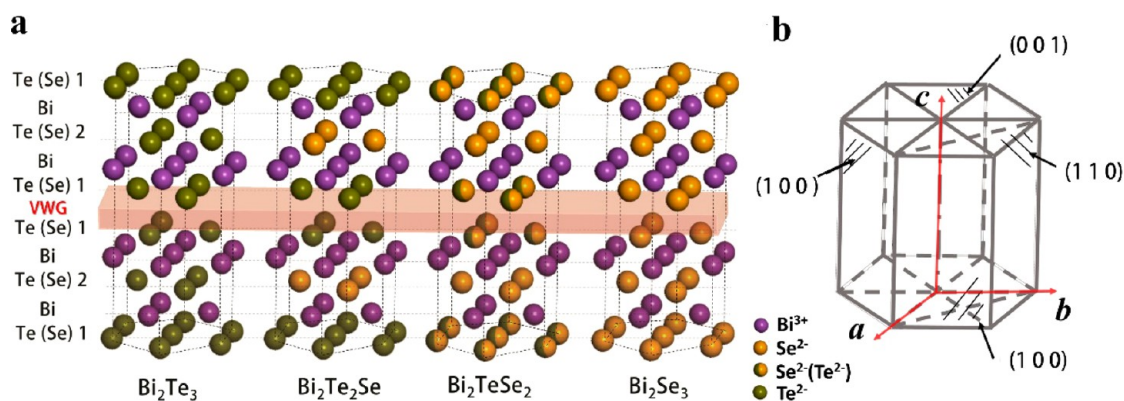


Figure 2. (a) Schematic of the lattice structures of Bi_2Te_3 , $\text{Bi}_2\text{Te}_2\text{Se}$, Bi_2TeSe_2 , and Bi_2Se_3 . Bi atoms are colored purple, and Te atoms (dark green) are replaced by Se atoms (yellow) from left to right according to the stoichiometric ratio. Double colored atoms indicate that either Se or Te could fill these positions. Light red area represents the van der Waals gap (VWG) in between two quintuple layers. (b) Schematic of a rhombohedral unit cell showing the (0 0 1), (1 1 0) and (1 0 0) facets.

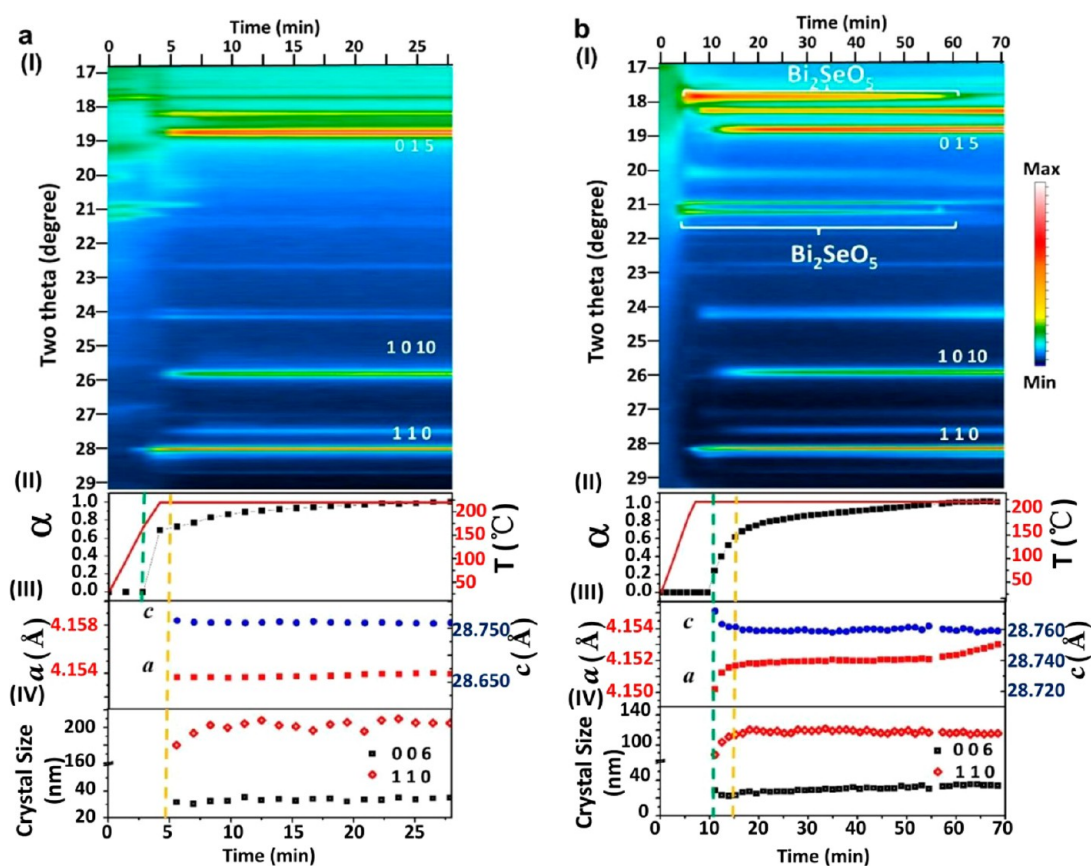


Figure 3. In situ PXRD results for the syntheses of Bi_2Se_3 using (a) Bi_2O_3 and (b) $\text{Bi}(\text{NO}_3)_3 \cdot 5\text{H}_2\text{O}$ as Bi precursors. (I) PXRD patterns (viewed down the intensity axis); (II) extent of crystallization of the product (squares) and temperature profile (red line); (III) lattice parameters (a and c); and (IV) Bi_2Se_3 crystal sizes perpendicular to the (0 0 6) and (1 1 0) crystal facets. Green and yellow dashed lines indicate the boundaries between the nucleation and the rapid growth stages and the rapid and the slow growth stages, respectively.

External N_2 pressure (2.5 MPa) was applied to the microreactor through a pressure line during the solvothermal synthesis to prevent boiling of the solvent. The loaded microreactor was fixed at the X-ray beam center and heated ($50\text{ }^\circ\text{C min}^{-1}$) to the synthesis temperature (205 or $220\text{ }^\circ\text{C}$) by a hot air blower. The temperature was calibrated using a KNO_3 temperature standard and monitored by a K-type thermocouple 3.5 mm beneath the microreactor. In situ diffraction patterns were collected every 0.6–2.4 min by a position-sensitive MYTHEN detector over the 2-theta range $1\text{--}81^\circ$. The synthesis was terminated when no noticeable change in diffraction patterns was observed.

2.3. PXRD Data Analysis. **2.3.1. Rietveld Analysis.** PXRD data were analyzed sequentially by the Rietveld method using the software TOPAS v4.2 (Bruker-AXS) for determining the phase scale factor, lattice parameters, and crystallite size. The extent of crystallization, α , was then calculated by dividing the refined scale factor of the individual PXRD patterns by the refined scale factor from a pattern where crystallization was considered to be complete (typically the last PXRD pattern). The composition of the product was determined from the relationship between the Se/Te ratio and the d_{015} spacing in the ternary $\text{Bi}_2\text{Se}_x\text{Te}_{3-x}$ system (Figure S1, Supporting Information), using d_{015} spacing of Bi_2Se_3 and Bi_2Te_3 calculated from Rietveld analysis.

The initial structure models were from the ICSD database: No. 42545 for Bi₂Se₃, No. 74348 for Bi₂Te₃, No. 43512 for Bi₂SeTe₂, and No. 54838 for Bi₂Se₂Te.

2.3.2. Avrami Analysis. Kinetic analysis can provide insight into reaction mechanisms. The kinetic analysis was performed using the Avrami–Erofe'ev equation, which has previously been used successfully in modeling crystallization involving a solution phase.^{39,43} The Avrami–Erofe'ev equation^{44,45} is written as follows

$$\alpha = 1 - \exp\{-[k(t - t_0)]^n\}$$

where α is the extent of crystallization, k is the rate constant, t is the reaction time, t_0 is the induction time, and n is the Avrami exponent, which is related to the reaction mechanism.^{27,43} The values of n and k can be conveniently obtained by applying the Sharp–Hancock plot,⁴⁶ which plots $\ln[-\ln(1 - \alpha)]$ against $\ln(t - t_0)$ and gives a straight line with a slope of n and an intercept of $n \ln(k)$. A change in the reaction mechanism can be identified by a change in the slope.

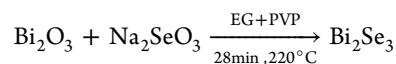
2.4. Electron Microscopy Characterization. The samples in the heating zone were extracted from the microreactor and characterized by SEM and TEM. The morphology was studied with a FEI Nova NanoSEM 450 and FEI Nova NanoSEM 430. Chemical compositions of the samples were qualitatively analyzed by energy-dispersive X-ray spectroscopy (EDX) equipped on the FEI Nova NanoSEM 450. The microstructure was investigated with a FEI Tecnai G2 T20 TWIN TEM operated at 200 kV.

3. RESULTS AND DISCUSSION

In this in situ PXRD study, the growth dynamics of binary compositions Bi₂Se₃ and Bi₂Te₃ and ternary compositions Bi₂Se_xTe_{3-x} were explored. For the binary compositions, the effect of Bi precursor type (Bi₂O₃ vs BiNO₄·H₂O) was investigated, and for the ternary compositions the effect of precursor slurry composition (Se/Te molar ratio), temperature, and precursor concentration to the growth dynamics were studied. The produced Bi₂Se_xTe_{3-x} nanoplatelets in these syntheses share the same rhombohedral crystal structure ($a = b \neq c$, $\alpha = \beta = 90^\circ$, and $\gamma = 120^\circ$; space group $R\bar{3}m$) (Figure 2) composed of hexagonal close-packed atomic layers periodically arranged along the c axis.^{47,48} Every five alternative atomic layers are known as a quintuple layer, between which lies the van der Waals gap (VWG).⁴⁹ Interestingly, synthesis of each composition showed distinguished features in terms of kinetics, nanoplatelet size, or the appearance of intermediate phases. In the following sections, the results for each composition will be presented and discussed in detail.

3.1. Synthesis of Bi₂Se₃. Syntheses of binary compound Bi₂Se₃ with two different Bi precursors (Bi₂O₃ and BiNO₄·H₂O) were carried out, and the corresponding in situ PXRD results are shown in Figure 3.

When Bi₂O₃ was used as the Bi precursor (Figure 3a), the in situ PXRD patterns show a straightforward growth of Bi₂Se₃ at the expense of the Bi₂O₃ and Na₂SeO₃ precursor phases (Figure 3a(I)). A series of diffraction peaks appeared after 4 min, and all these peaks can be assigned to paragonajuatite-type Bi₂Se₃ (JCPDS Card No. 33-0214). The refined lattice parameters are $a = b = 4.154 \text{ \AA}$ and $c = 28.760 \text{ \AA}$. The three strongest peaks appeared at 18.849° , 27.856° , and 25.711° , correspond to the (0 1 5), (1 1 0), and (1 0 10) facets of the Bi₂Se₃ crystal, respectively. The positions of these peaks remain almost unchanged during the entire synthesis, and no intermediate or impurity phases were detected. Therefore, the synthesis can be described by the following chemical reaction (chemical composition of the final product was confirmed by PXRD as shown in Figure S2, Supporting Information)



The extent of crystallization of Bi₂Se₃ is plotted as a function of time (Figure 3a(II)). The synthesis follows a 3-step process. A 3 min induction period was followed by a sudden rapid growth period in the temperature range from 166 to 220 °C. In just 1.4 min 69% of Bi₂Se₃ growth was completed, indicating the sudden rapid growth. This is in agreement with the observation that at about 166 °C the light yellow slurry turned to black (the color of bismuth chalcogenides). After the rapid growth was a 24 min slow growth period, which accounted for the growth of the remaining 31% Bi₂Se₃. From this observation, we propose that the nucleation and growth are two separate processes. In the induction period, at temperatures below 166 °C, the dissolution of the precursor phases resulted in a solution supersaturated with respect to Bi₂Se₃, triggering the nucleation of Bi₂Se₃. This resulted in the formation of a great number of nuclei, giving rise to the rapid and sudden growth of Bi₂Se₃. The nucleation and sudden growth of Bi₂Se₃ consumed the majority of the precursor species in the solution, leaving a solution with a relatively low concentration of the precursor species; hence, further nucleation was limited and growth slowed down.

The refined lattice parameters a and c slightly varied during the synthesis (the change was -0.014% for c and 0.007% for a) (Figure 3a(III)). The mean crystallite size as a function of synthesis time (Figure 3a(IV)) shows that the sudden growth of Bi₂Se₃ within 1.4 min resulted in plates of 32 nm in thickness (calculated from the (0 0 6) peak broadening) and 180 nm in width (calculated from the (1 1 0) peak broadening). In the following slow growth period the thickness kept relatively constant while the width increased by 14% to 205 nm. This corresponds to a volume increase of about 30% assuming constant plate numbers (no further nucleation events). This 30% volume increase of the plates accounts for the remaining Bi₂Se₃, which is $100\% - 69\% = 31\%$. Therefore, the nucleation and growth are indeed separate processes. The fast nucleation was followed by a rapid sudden growth of Bi₂Se₃ plates and finally slow further epitaxial growth along the edges of the hexagonal plates on the (1 0 0) facets.

The precursor type influenced the growth dynamics of Bi₂Se₃. Using BiNO₄·H₂O as the Bi precursor also produced Bi₂Se₃ nanoplatelets by the three-step crystallization process (Figure 3b). However, the in situ PXRD experiment revealed several differences compared with the synthesis using the Bi₂O₃ precursor. First, the synthesis is much slower, as both the induction time (~ 10 min) and the complete crystallization time (~ 65 min) were around 3 times of that observed for the synthesis using the Bi₂O₃ precursor (compare Figure 3a(II) and 3b(II)); as a result, the onset of crystallization occurred at a higher temperature of 220 °C. Second, the lattice parameter c decreased rapidly (by -0.040%) during the rapid crystal growth stage and then very slowly (by -0.002%) during the slow crystal growth stage, while the lattice parameter a experienced the opposite trend, a rapid increase (by 0.040%) followed by a slow increase (by 0.030%) (Figure 3b(III)). Third, there is no sudden growth of crystals—during the rapid growth stage, the plate width grew from 87 to 119 nm but the thickness was almost constant, while during the slow growth stage, the width remained almost unchanged but the thickness increased to 33 nm (Figure 3b(IV)). This means (1) the late slow growth occurred on the (0 0 1) facets (the hexagonal surface of the

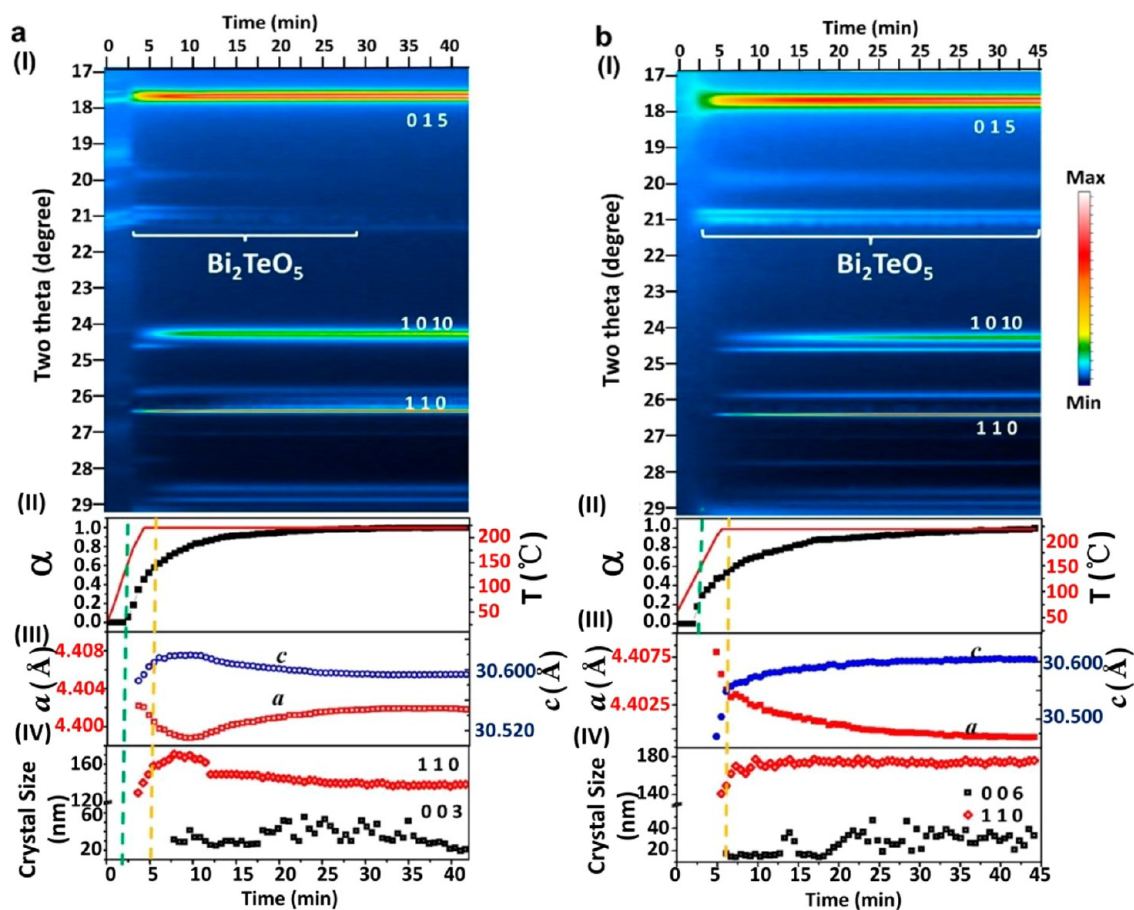
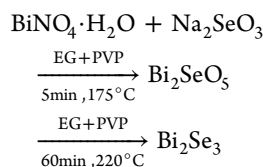


Figure 4. In situ PXRD results of the syntheses of Bi_2Te_3 using (a) Bi_2O_3 and (b) $\text{BiNO}_4 \cdot \text{H}_2\text{O}$ as Bi precursors. (I) PXRD patterns (viewed down the intensity axis); (II) extent of crystallization of the product (squares) and temperature profile (red line); (III) lattice parameters (a and c); and (IV) Bi_2Te_3 crystal sizes perpendicular to the (0 0 6) and (1 1 0) crystal facets. Green and yellow dashed lines indicate the boundaries between the nucleation and the rapid growth stages and the rapid and the slow growth stages, respectively.

nanoplatelets) rather than on the (1 0 0) facets as for the synthesis using the Bi_2O_3 precursor and (2) the produced nanoplatelets have a similar thickness (33 nm) but the width (116 nm) is only about one-half of the width of the nanoplatelets when the Bi_2O_3 precursor was used (compare Figure 3a(IV) and 3b(IV)). Finally, the most distinguished difference is the appearance of an intermediate phase, Bi_2SeO_5 (JCPDS Card No. 70-5102). This phase appeared after the dissolution of the precursors at 175 °C, and then it dissolved slowly during the growth of Bi_2Se_3 . It is most likely that this intermediate phase provided slow release of Bi and Se species into the solution and consequently influenced the growth dynamics of Bi_2Se_3 . Hence, the synthesis using the $\text{BiNO}_4 \cdot \text{H}_2\text{O}$ precursor can be described by the following chemical reaction (chemical composition of the final product was confirmed by PXRD as shown in Figure S3, Supporting Information)



3.2. Synthesis of Bi_2Te_3 . In situ PXRD results for the syntheses of Bi_2Te_3 using Bi_2O_3 and $\text{BiNO}_4 \cdot \text{H}_2\text{O}$ as Bi precursors are summarized in Figure 4a and 4b, respectively. Both syntheses produced tellurobismuthite-type Bi_2Te_3 nano-

platelets (JCPDS Card No. 89-2009) as the final product and followed the 3-step crystallization process.

When the Bi_2O_3 precursor was used, in situ PXRD patterns and the derived crystallization curve reveal a fast crystallization process (Figure 4a(I) and 4a(II)). The induction period took only 2 min, and crystallization was complete within 30 min. Similar to the synthesis of Bi_2Se_3 , the crystallization can be divided into a rapid growth stage at the beginning and a slow growth stage toward the end of the synthesis (Figure 4a(II)). The rapid growth occurred as the temperature rose from 135 to 220 °C. In just 4 min, 65% of the total Bi_2Te_3 was produced. In the later slow growth stage, crystallization of the remaining 35% Bi_2Te_3 took 24 min.

The unit cell parameters varied during the crystallization (Figure 4a(III)). Parameter c first increased during the rapid growth stage and then decreased during the slow growth stage, while parameter a showed the opposite trend. The nanoplatelets have a thickness of 21 nm and a width of 140 nm (Figure 4a(IV)), being thinner and smaller than Bi_2Se_3 . The width of the nanoplatelets increased rapidly from 130 to 170 nm during the rapid growth stage and then gradually decreased from 170 to 140 nm during the slow growth stage. The thickness appeared to fluctuate in the 20–55 nm range, which is likely due to the weak diffraction of the (0 0 3) peak, and hence, the accuracy of Rietveld analysis was compromised.

A distinct difference when compared with the synthesis of Bi_2Se_3 using the Bi_2O_3 precursor is that an intermediate phase

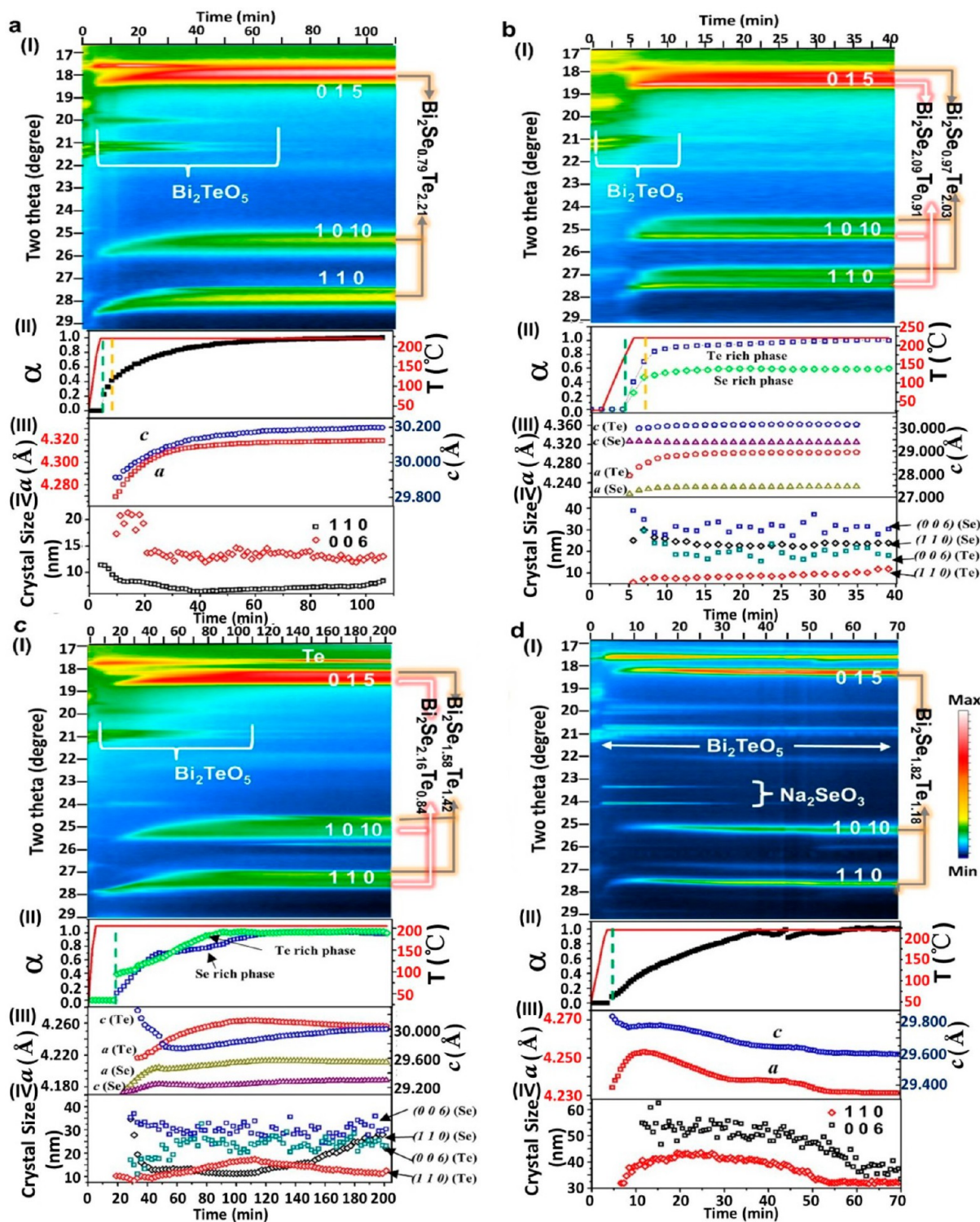
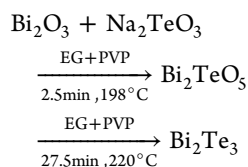


Figure 5. In situ PXRD results of the synthesis of $\text{Bi}_2\text{Se}_x\text{Te}_{3-x}$ obtained under different reaction conditions: (a) molar ratio of Se:Te = 1:2, precursor concentration 5 wt %, and temperature 220 °C; (b) molar ratio of Se:Te = 1:1, precursor concentration 5 wt %, and temperature 220 °C; (c) molar ratio of Se:Te = 1:1, precursor concentration 5 wt %, and temperature 205 °C; (d) molar ratio of Se:Te = 1:1, precursor concentration 10 wt %, and temperature 220 °C. (I) PXRD patterns; (II) extent of crystallization of product (squares) and temperature curve (red line); (III) lattice parameters (a and c); and (IV) crystal sizes of $\text{Bi}_2\text{Se}_x\text{Te}_{3-x}$ composites in the directions perpendicular to the (0 0 6) and (1 1 0) crystal facets. Green and yellow dashed lines indicate the boundaries between the nucleation and the rapid growth stages and the rapid and the slow growth stages, respectively.

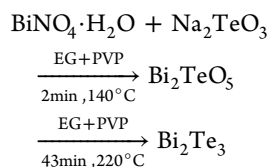
Bi_2TeO_5 (JCPDS Card No. 70-5000) formed at 198 °C after the initial dissolution of the precursor phases ($\text{Bi}_2\text{O}_3 + \text{Na}_2\text{TeO}_3$). After the formation of Bi_2TeO_5 , Bi_2Te_3 grew at the expense of Bi_2TeO_5 and complete Bi_2Te_3 crystallization occurred at the point where Bi_2TeO_5 completely dissolved.

The Bi_2TeO_5 acted as a reservoir that constantly and slowly released Bi and Te species into the solution for the growth of Bi_2Te_3 . Hence, the synthesis can be expressed as the following chemical reaction (chemical compositions of the final and

intermediate products were confirmed by PXRD as shown in Figures S4 and S5, Supporting Information, respectively)



The influence of the different Bi precursor ($\text{BiNO}_4 \cdot \text{H}_2\text{O}$, Figure 4b) for the Bi_2Te_3 synthesis is not as significant as for the synthesis of Bi_2Se_3 . The synthesis using $\text{BiNO}_4 \cdot \text{H}_2\text{O}$ had the same induction time as the synthesis using Bi_2O_3 (2 min) but longer total crystallization time (45 min), consisting of rapid and slow growth stages (Figure 4b(II)); the same intermediate phase Bi_2TeO_5 was formed at a lower temperature (140°C) and had a longer lifetime. Again, the dissolution of the intermediate Bi_2TeO_5 determined the rate for crystallization. The reason for the slower dissolution of Bi_2TeO_5 may be due to the fact that the physical properties (size and morphology) of the Bi_2TeO_5 may be different when formed using different Bi precursors, hence affecting the dissolution kinetics later. In terms of lattice parameters, the unit cell experienced an expansion along the c direction (by 0.400%) and contraction along the a direction (by -0.200%). Additionally, the size of the nanoplatelets synthesized using $\text{BiNO}_4 \cdot \text{H}_2\text{O}$ was generally wider (176 nm) and thicker (30 nm) compared with the synthesis using Bi_2O_3 precursor (Figure 4a(IV) and 4b(IV)). The chemical reaction for the synthesis of Bi_2Te_3 using $\text{BiNO}_4 \cdot \text{H}_2\text{O}$ as the precursor can be described as (chemical compositions of the final and intermediate products were confirmed by PXRD as shown in Figures S6 and S7, Supporting Information, respectively)

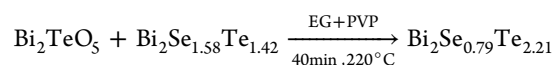
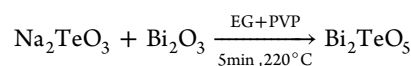
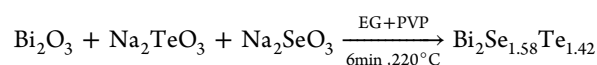


3.3. Synthesis of Ternary Compounds—The Importance of Intermediate Phases to the Product Composition. In the syntheses of ternary $\text{Bi}_2\text{Se}_x\text{Te}_{3-x}$ compounds, the effects of precursor slurry composition ($x = 1$ and 1.5), temperature (205 and 220°C), and precursor concentration (5 and 10 wt %) were investigated.

According to the Bi_2S_3 – Bi_2Se_3 – Bi_2Te_3 ternary phase diagram (Figure S8, Supporting Information) established by plotting mineral compositions found in nature,⁵⁰ the Bi_2SeTe_2 composition is a stable phase, found in nature as the mineral kawzulite, while the $\text{Bi}_2\text{Se}_{1.5}\text{Te}_{1.5}$ phase may be a nonstable phase, as it has not been found in the natural environment. The synthesis of the stable phase Bi_2SeTe_2 at 220°C was successful (Figure 5a), although the product composition $\text{Bi}_2\text{Se}_{0.79}\text{Te}_{2.21}$ deviated slightly from the ideal Bi_2SeTe_2 composition. The composition was determined from the relationship between composition and d_{015} spacing of the ternary $\text{Bi}_2\text{Se}_x\text{Te}_{3-x}$ composition (Figure S1, Supporting Information). Similar to the synthesis of Bi_2Te_3 , the synthesis of $\text{Bi}_2\text{Se}_{0.79}\text{Te}_{2.21}$ also involved the formation of the intermediate Bi_2TeO_5 phase after the dissolution of the precursors and just before the onset of $\text{Bi}_2\text{Se}_x\text{Te}_{3-x}$ crystallization (Figure 5a(I)). However, in this case the intermediate phase had a much more profound impact. The

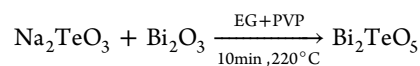
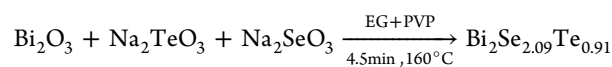
formation of Bi_2TeO_5 changed the solution composition significantly from its initial Te/Se molar ratio of 2. As a consequence, a Se-rich product $\text{Bi}_2\text{Se}_{1.58}\text{Te}_{1.42}$ was formed at the early stage of crystallization. Dissolution of Bi_2TeO_5 slowly supplied more Bi and Te species, and the product gradually became more Te rich, eventually forming $\text{Bi}_2\text{Se}_{0.79}\text{Te}_{2.21}$.

The $\text{Bi}_2\text{Se}_{0.79}\text{Te}_{2.21}$ crystallization also followed a 3-step crystallization process but was a slower process than for the crystallization of binary compounds. After a 4 min induction period for precursor dissolution and product nucleation, there was an 8 min rapid growth of the Se-rich composition, $\text{Bi}_2\text{Se}_{1.58}\text{Te}_{1.42}$, achieving 50% crystallization. This was followed by slow Te enrichment, which lasted for 77 min. Accordingly, the synthesis mechanism can be described by the following chemical reactions (PXRD patterns of the final and intermediate products are shown in Figures S9 and S10, Supporting Information, respectively)



Quantitatively, the Te-enrichment process resulted in an increase in lattice parameter a by 0.980% and c by 6.020% (Figure 5a(III)), which was more than 20 times greater than the lattice changes observed for the binary compounds. This significant change is due to the fact that the radius of Te atoms is 16% larger than that of Se atoms. However, the synthesis produced nanocrystals (~ 15 nm) rather than large hexagonal nanoplatelets, as determined from the calculated crystal sizes perpendicular to the (0 0 6) and (1 1 0) planes (Figure 5a(IV)). This is in agreement with SEM observation (to be discussed later), which showed a low yield of the large-sized hexagonal planar crystals.

Attempts were also made to synthesize the naturally unstable $\text{Bi}_2\text{Se}_{1.5}\text{Te}_{1.5}$ phase. The synthesis was first conducted at 220°C using a 5 wt % precursor concentration (Figure 5b). The in situ PXRD patterns (Figure 5b(I)) suggested that phase-pure $\text{Bi}_2\text{Se}_{1.5}\text{Te}_{1.5}$ was not formed. Instead, 2 naturally stable compositions were formed, $\text{Bi}_2\text{Se}_{2.09}\text{Te}_{0.91}$ (an analogue to skippenite) and $\text{Bi}_2\text{Se}_{0.97}\text{Te}_{2.03}$ (an analogue to kawzulite). The Se-rich phase ($\text{Bi}_2\text{Se}_{2.09}\text{Te}_{0.91}$) had lattice parameters of $a = b = 4.232 \text{ \AA}$ and $c = 29.393 \text{ \AA}$, and the Te-rich phase ($\text{Bi}_2\text{Se}_{0.97}\text{Te}_{2.03}$) had lattice parameters of $a = b = 4.304 \text{ \AA}$ and $c = 30.162 \text{ \AA}$. From the diffraction patterns (Figure 5b(I)), a peak-shifting phenomenon was also observed at the early growth stage during the dissolution of the intermediate phase Bi_2TeO_5 . After complete dissolution of Bi_2TeO_5 , a second set of sharp diffraction peaks corresponding to the Te-rich composition started to appear and kept increasing in intensity during the rest of the synthesis. Therefore, the chemical reactions can be described as follows (PXRD pattern of the final product is shown in Figure S11, Supporting Information)



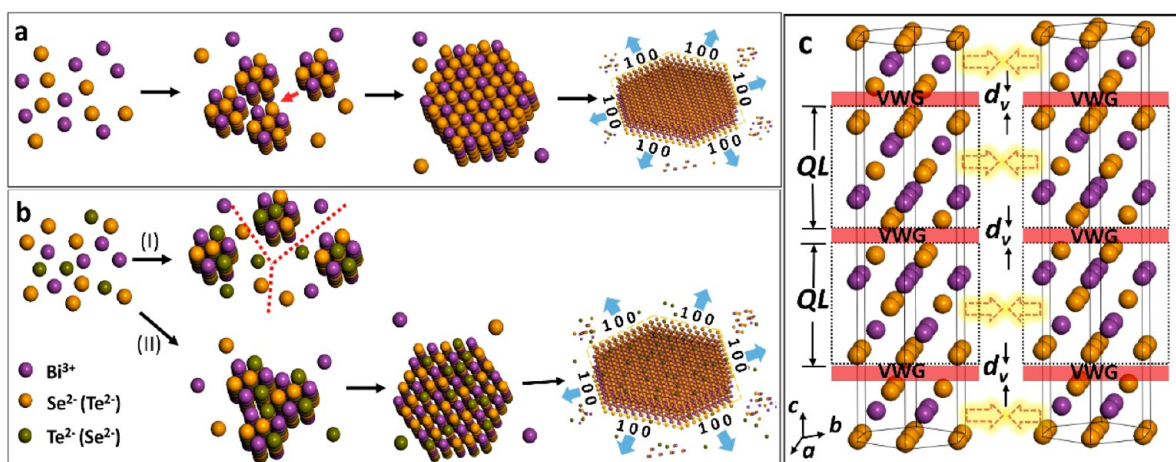
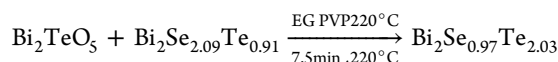


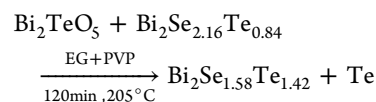
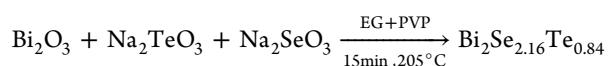
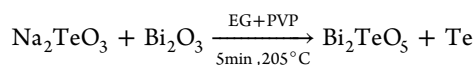
Figure 6. Schematic illustration of the growth steps of bismuth chalcogenide crystals. (a) Three-step crystal growth for the binary compounds, showing oriented attachment for the rapid growth step and then epitaxial growth for the slow growth step. (b) For ternary compounds the possibility of oriented attachment is decreased due to different composition of the nuclei (I), but a small amount of nuclei still meet the requirements for oriented attachment (II). (c) Lattice space adjustment occurs in d_v (distance of the van der Waals gap between two quintuple layers (QL)) when two adjacent crystals approach, which contributes to the lattice match in process II.



Interestingly, the Te-rich phase grew slightly faster than the Se-rich phase, and there is no obvious competition between them. As a result, no obvious fluctuation was observed in the lattice parameters during the growth stage. Nanocrystals were formed with a size less than 40 nm (Figure 5b(IV)), which is similar to the synthesis of $\text{Bi}_2\text{Se}_{0.79}\text{Te}_{2.21}$.

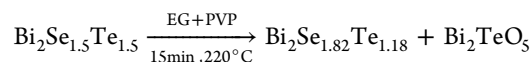
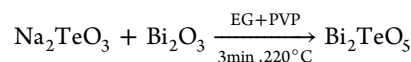
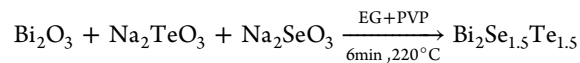
Since phase separation between Se-rich phase and Te-rich phase did not occur during the lifetime of the intermediate phase Bi_2TeO_5 , it is likely that a phase-pure composition close to $\text{Bi}_2\text{Se}_{1.5}\text{Te}_{1.5}$ may be produced from a Se-rich precursor solution with continued slow supply of Te species by the dissolution of Bi_2TeO_5 . To confirm this hypothesis, the effects of temperature and precursor concentration were studied with the aim of prolonging the lifetime of the intermediate phase.

To study the impact of temperature, synthesis at a lower temperature, 205°C , was carried out (Figure 5c). The reduction in temperature resulted in slower induction and crystallization, and the lifetime of the Bi_2TeO_5 intermediate was much longer. Again, before the complete dissolution of Bi_2TeO_5 , the product gradually became more Te-rich and no phase separation was observed. After that, however, phase separation occurred again, producing a Se-rich composition $\text{Bi}_2\text{Se}_{2.16}\text{Te}_{0.84}$ and a less Se-rich composition $\text{Bi}_2\text{Se}_{1.58}\text{Te}_{1.42}$. It is interesting to note that the less Se-rich composition is very close to $\text{Bi}_2\text{Se}_{1.5}\text{Te}_{1.5}$. However, the remaining Te species in the solution produced elemental Te after 120 min treatment. The diffraction peaks are very broad, indicating very small crystallite sizes, possibly due to the low reaction temperature. The crystal sizes calculated are in the range of 1–25 nm (Figure 5c(IV)). The chemical reactions responsible for this synthesis can be described as follows (PXRD pattern of the final product is shown in Figure S12, Supporting Information)



The precursor concentration had the most profound effect in preventing the phase separation. In a synthesis with the precursor concentration doubled to 10 wt % there was no obvious peak splitting observed in the in situ PXRD patterns (Figure 5d(I)), which means that only one phase ($\text{Bi}_2\text{Se}_{1.82}\text{Te}_{1.18}$ with lattice parameters of $a = b = 4.231 \text{ \AA}$ and $c = 29.595 \text{ \AA}$, Figure S12, Supporting Information) was obtained. The crystallization curve for this synthesis was quite different from the others (Figure 5d(II)). There was no rapid growth stage. Instead, after a 4 min induction period the growth took place gradually and lasted about 40 min before reaching 100% crystallization.

The dominant feature of this reaction is that the intermediate phase Bi_2TeO_5 has a much longer lifetime, and the initially dissolved precursor Na_2SeO_3 recrystallized and then redissolved slowly. As a consequence, the competition for Te between the intermediate phase and the desired product leads to the small change in the stoichiometric ratio of Se and Te in the product, and the phase separation was prevented. Thus, the chemical reactions can be summarized as follows (PXRD pattern of the final product is shown in Figure S13, Supporting Information)



3.4. Oriented Attachment Mechanism for the Rapid Growth Stage. The 3-step crystallization (nucleation \rightarrow rapid growth \rightarrow slow growth) was observed in the syntheses of $\text{Bi}_2\text{Se}_x\text{Te}_{3-x}$ except for the synthesis with the precursor concentration doubled (10 wt %) in which the rapid growth stage was not observed. It is very interesting that crystallization can reach such a high extent so rapidly and then slow down

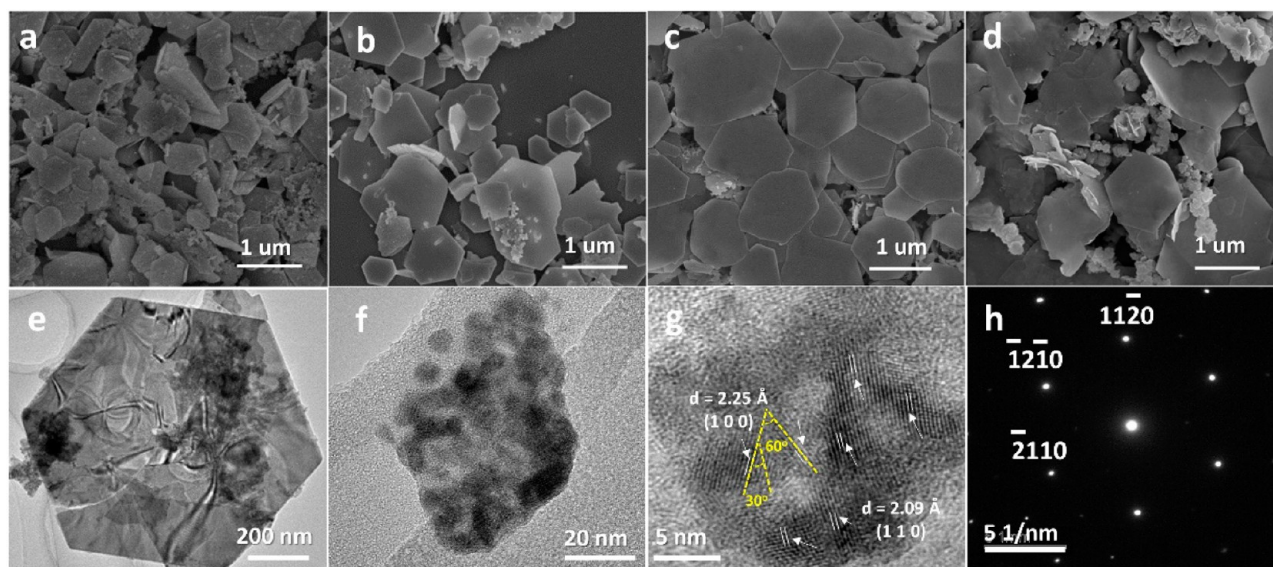


Figure 7. Representative SEM images of (a) Bi_2Se_3 , (b) Bi_2Te_3 , (c) Bi_2SeTe_2 , and (d) $\text{Bi}_2\text{Se}_{1.5}\text{Te}_{1.5}$. (e) TEM image of a representative hexagonal nanoplatelet with a composition of $\text{Bi}_2\text{Se}_{0.79}\text{Te}_{2.21}$ and small crystal segments. (f) TEM image of a small crystal cluster extracted from a reaction mixture after 15 min synthesis at 220°C using a precursor composition of $\text{Bi}:\text{Se}:\text{Te} = 2:1:2$. (g) HRTEM image of a small crystal cluster. Grains align reasonably well along the grain boundaries perpendicular to either the $(1\ 1\ 0)$ or the $(1\ 0\ 0)$ facets. (h) Selected-area electron diffraction pattern of the hexagonal single crystal shown in e.

drastically. It is most likely that different mechanisms were responsible for the rapid growth and slow growth stages. It was discussed in the synthesis of the binary Bi_2Se_3 that the slow growth stage was a result of epitaxial growth onto the existing crystal facets of the crystals consuming the remaining dissolved species from solution, but what is the mechanism for the rapid growth stage?

Two common mechanisms to describe crystal growth are (1) Ostwald ripening (OR)^{51–53} and (2) oriented attachment (OA). OR is a thermodynamically driven process in which smaller crystals dissolve at high surface energy facets and coalescence occurs on the surface of larger crystals. OR generally leads to the formation of crystals with high symmetry, such as isotropic microspheres and hollow microspheres.^{54–61} On the other hand, the OA mechanism was established more recently and is primarily responsible for the formation of nanoscale crystals.^{62,63} Under the context of the OA mechanism, crystallographically oriented nanoparticles attach together to form larger particles. This process follows epitaxial assembly and can lead to the anisotropic growth of low-dimensional crystals.^{64–66} It also plays an important role in directing the size distribution and shape development of nanocrystals.⁶⁷

Our observations for the rapid growth stage are in excellent agreement with the OA mechanism. First, the induction period produced a great number of nanometer-sized nuclei by consuming the majority of the dissolved species. The size of nuclei nanocrystals was only a few nanometers as observed in TEM (we will discuss this later), and hence, they were too small to be detected by PXRD. Once the nuclei concentration reached a critical point the internuclei interactions become strong and they rapidly attached to each other epitaxially. Such oriented attachment allowed the crystals to quickly grow to larger sizes and contributed to the significant increase in peak intensity in the PXRD patterns. This is most obvious for the synthesis of Bi_2Se_3 using Bi_2O_3 as the precursor in which the

synthesis reached an extent of crystallization of 69% in just 1.4 min, producing planar crystals with a width of 180 nm.

Second, in the OA process, crystals prefer to attach along the same crystal facets for best lattice match. The lattice match is hence playing a vital role in determining whether OA can actively occur. Figure 6 illustrates the OA mechanism for the binary and ternary compounds. In the binary compounds (Figure 6a), there was negligible lattice mismatch due to the fixed stoichiometry of either Bi_2Se_3 or Bi_2Te_3 . Therefore, the nuclei quickly attached to each other and the crystals grew to large sizes of hundreds of nanometers in width. This is in excellent agreement with the calculated size evolution in the binary compounds and with the high yield of hexagonal plates from SEM observations (Figure 7a and 7b). For the ternary compounds (Figure 6b), however, the OA was not as efficient as the binary compounds, because the composition was variable as indicated by the significant change in lattice parameters. The composition for the nanometer-sized nuclei can be different from the adjacent nuclei, and in most cases the lattice mismatch was large enough to hinder OA (Figure 6b(I)). The direct consequence was that the crystals were much smaller compared with the binary compounds.

However, some lattice mismatch can be tolerated in the OA, due to the unique lattice along the c axis (Figure 6c). The $\text{Bi}_2\text{Se}_x\text{Te}_{3-x}$ crystals are covalently bonded within each quintuple layer while being weakly bonded between the interquintuple layers with van der Waals interactions.^{13,14} The VWG is so weak that the gap is slightly adjustable when required. During OA, the adjustable VWG can play a critical role in releasing the strain induced by lattice mismatch and hence allow limited OA to occur in ternary $\text{Bi}_2\text{Se}_x\text{Te}_{3-x}$ compounds (Figure 6b(II)). As a result, though a great number of nanoparticles were formed in the solution, when nuclei compositions were similar active OA under VWG adjustment can occur. As a result, there were still some large hexagonal plates in the ternary composition found under SEM (Figure 7c and 7d).

OA mechanism in the rapid growth step is supported by TEM. Figure 7e shows a typical TEM image of the hexagonal ternary compound nanoplatelet. The hexagonal nanoplatelet is surrounded by many smaller particles that gave the small average crystal size calculated by the Rietveld analysis (Figure 5c(IV)). Selected-area electron diffraction (SAED) indicates that the hexagonal nanoplatelet is a single crystal (Figure 7h). The characteristic (0 0 1) facet dominates the crystal growth, which is in agreement with PXRD results. To further confirm the OA mechanism, partially crystallized samples were extracted from the synthesis and examined under TEM. Large numbers of small nanoclusters were found (Figure 7f), indicating the beginning of the OA. From high-resolution transmission electron microscopy (HRTEM) images of the small nanocluster segments (see Figure 7g) the grains are well aligned with minimum lattice mismatches along the grain boundaries. The (1 1 0) facets are parallel to each other, the intersection angle between the (1 0 0) facets is close to 60° , and the intersection angle between the (1 1 0) and the (1 0 0) facets is close to 30° . This suggests that the OA mechanism is occurring during the rapid growth stage.

3.5. Kinetic Analysis for the Slow Growth Stage. To get further insights into the mechanism of the slow growth stage, the growth kinetics were analyzed by the Avrami–Erofe'ev model. It has been suggested that this model is appropriate when the extent of crystallization is greater than 0.15.^{46,68} This was the case when crystallization reached the slow growth stage in the syntheses of $\text{Bi}_2\text{Se}_x\text{Te}_{3-x}$. The results are presented in Figure 8. Except for the synthesis with double precursor concentration (10 wt %), the other syntheses have an Avrami exponent (n) value in the range between 0.5 and 1.0 (Figure

8a–e), indicating a combined diffusion and phase boundary controlled crystallization mechanism with zero nucleation rate. This is in agreement with the proposed mechanism that slow growth is dominated by the epitaxial growth on existing crystals rather than by forming more nuclei and subsequent growth. Also, as the nucleation and rapid growth stages have consumed the majority of the dissolved species, the slow growth from the remaining diluted solution is likely controlled by species diffusion.

For the synthesis with high precursor concentration (10 wt %), however, the Avrami–Erofe'ev analysis produced an n value of 1.31 (Figure 8f), which indicates a phase boundary controlled mechanism with decreasing nucleation rate. This also makes sense. The high precursor concentration significantly reduced the diffusion length between the dissolved species and the crystal surface, and hence, the crystallization rate was limited by the epitaxial growth on the crystal surface, and overall the crystallization was controlled at the phase boundary. Additionally, the high precursor concentration did not prohibit the nucleation at the later stage of crystallization, but with continued decreasing concentration, the nucleation rate was also reduced.

4. CONCLUSION

This in situ PXRD study reveals that the solvothermal crystallization of $\text{Bi}_2\text{Se}_x\text{Te}_{3-x}$ nanoplatelets can generally be divided into 3 steps: (i) an induction period for precursor dissolution and $\text{Bi}_2\text{Se}_x\text{Te}_{3-x}$ nucleation, which is followed by (ii) a rapid crystal growth stage through oriented attachment of the nuclei, and finally (iii) a slow epitaxial growth stage consuming the remaining species from the solution. It is generally easier to synthesize large-sized binary nanoplatelets (Bi_2Se_3 and Bi_2Te_3) compared with the synthesis of ternary compositions because oriented attachment is more efficient for binary compositions. The ternary compositions suffer from phase separation and inefficient oriented attachment growth due to compositional variation. Additionally, the intermediate phases (Bi_2TeO_5 , Bi_2SeO_5 , Na_2SeO_3) were identified and found to play a vital role in preventing the phase separation in the synthesis of ternary compositions. This study also shows that solvothermal synthesis can be a very complicated process. The synthesis of $\text{Bi}_2\text{Se}_x\text{Te}_{3-x}$ is sensitive to synthesis parameters including temperature, synthesis time, precursor type, precursor concentration, and the Se/Te ratio in the initial precursor slurry. Extreme care needs to be taken when designing solvothermal conditions for synthesizing products with optimized size and morphology for desired applications.

■ ASSOCIATED CONTENT

Supporting Information

d_{015} spacing as a function of Te concentration, phase diagram and additional PXRD patterns. The Supporting Information is available free of charge on the ACS Publications website at DOI: 10.1021/acs.chemmater.5b00903.

■ AUTHOR INFORMATION

Corresponding Authors

*E-mail: rcaruso@unimelb.edu.au.

*E-mail: qlbao@suda.edu.cn; qiaoliang.bao@monash.edu.

Author Contributions

§Jingchao Song and Fang Xia contributed equally to this work.

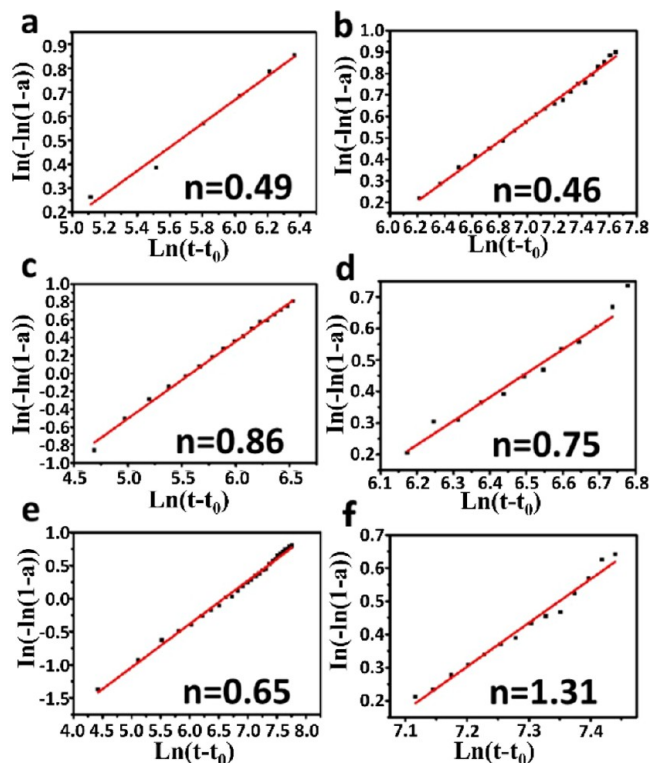


Figure 8. Sharp–Hancock plots for the syntheses of (a) Bi_2Se_3 using BiO_3 , (b) Bi_2Se_3 using $\text{BiNO}_4 \cdot \text{H}_2\text{O}$, (c) Bi_2Te_3 using BiO_3 , (d) Bi_2Te_3 using $\text{BiNO}_4 \cdot \text{H}_2\text{O}$, (e) $\text{Bi}_2\text{Se}_{0.79}\text{Te}_{2.21}$, and (f) $\text{Bi}_2\text{Se}_{1.82}\text{Te}_{1.18}$ (with double precursor concentration).

Notes

The authors declare no competing financial interest.

ACKNOWLEDGMENTS

This research was undertaken on the powder diffraction beamline at the Australian Synchrotron, Victoria, Australia (beam time awards AS131/PDFI/S998 and AS132/PD/6494), through the Science and Industry Endowment Fund Special Research Program-Synchrotron Science. This work was performed in part at the Melbourne Centre for Nanofabrication (MCN) in the Victorian Node of the Australian National Fabrication Facility (ANFF). We thank Ms. Nicola Scarlett, Mr. Zaiquan Xu, and Dr. Shenghuang Lin for assistance with synchrotron data collection, Dr. Helen Brand for beamline setup, and Dr. Xi Zhang for helpful discussions regarding the crystal structure. We also thank Dr. Nathan Webster and Ian Madsen for accessing and setting up a lab-based in situ PXRD instrument at CSIRO Mineral Resources Flagship for early screening experiments. Q.B. acknowledges the support of the 863 Program (Grant No. 2013AA031903) and the 973 Program (Grant No. 2015CB932700), NSFC grants (Grant No. 51222208, 51290273, and 91433107), the Australian Research Council (ARC) DECRA (DE120101569), and DP (DP140101501). R.A.C. acknowledges the ARC for a Future Fellowship (FT0990583). The CSIRO Office of the Chief Executive (OCE) Postdoctoral and Science Leader Schemes are also acknowledged for financial support. J.C.S. acknowledges a New Horizon Scholarship for his Ph.D. research.

REFERENCES

- (1) Venkatasubramanian, R.; Siivola, E.; Colpitts, T.; O'Quinn, B. *Nature* **2001**, *413*, 597.
- (2) Saleemi, M.; Toprak, M. S.; Li, S.; Johnsson, M.; Muhammed, M. *J. Mater. Chem.* **2012**, *22*, 725.
- (3) Zhang, H.; Liu, C.-X.; Qi, X.-L.; Dai, X.; Fang, Z.; Zhang, S.-C. *Nat. Phys.* **2009**, *5*, 438.
- (4) Fu, L.; Kane, C. *Phys. Rev. B* **2007**, *76*, 045302.
- (5) Chen, Y. L.; Analytis, J. G.; Chu, J. H.; Liu, Z. K.; Mo, S. K.; Qi, X. L.; Zhang, H. J.; Lu, D. H.; Dai, X.; Fang, Z.; Zhang, S. C.; Fisher, I. R.; Hussain, Z.; Shen, Z. X. *Science* **2009**, *325*, 178.
- (6) Pesin, D.; MacDonald, A. H. *Nat. Mater.* **2012**, *11*, 409.
- (7) Zhu, H.; Richter, C. A.; Zhao, E.; Bonevich, J. E.; Kimes, W. A.; Jang, H.-J.; Yuan, H.; Li, H.; Arab, A.; Kirillov, O.; Maslar, J. E.; Ioannou, D. E.; Li, Q. *Sci. Rep.* **2013**, *3*, 01757.
- (8) Zhang, J.-M.; Ming, W.; Huang, Z.; Liu, G.-B.; Kou, X.; Fan, Y.; Wang, K. L.; Yao, Y. *Phys. Rev. B* **2013**, *88*, 235131.
- (9) Chadov, S.; Qi, X.; Kubler, J.; Fecher, G. H.; Felser, C.; Zhang, S. C. *Nat. Mater.* **2010**, *9*, 541.
- (10) Soni, A.; Yanyuan, Z.; Ligen, Y.; Aik, M. K.; Dresselhaus, M. S.; Xiong, Q. *Nano Lett.* **2012**, *12*, 1203.
- (11) Roslyak, O.; Gumbs, G.; Huang, D. *Phys. Rev. B* **2013**, *87*, 045121.
- (12) Di Pietro, P.; Ortolani, M.; Limaj, O.; Di Gaspare, A.; Giliberti, V.; Giorgianni, F.; Brahlek, M.; Bansal, N.; Koirala, N.; Oh, S.; Calvani, P.; Lupi, S. *Nat. Nano* **2013**, *8*, 556.
- (13) Kong, D.; Cui, Y. *Nat. Chem.* **2011**, *3*, 845.
- (14) Hong, S. S.; Kundhikanjana, W.; Cha, J. J.; Lai, K.; Kong, D.; Meister, S.; Kelly, M. A.; Shen, Z. X.; Cui, Y. *Nano Lett.* **2010**, *10*, 3118.
- (15) Tweldejbrhan, D.; Goyal, V.; Balandin, A. A. *Nano Lett.* **2010**, *10*, 1209.
- (16) Cao, H.; Venkatasubramanian, R.; Liu, C.; Pierce, J.; Yang, H.; Zahid Hasan, M.; Wu, Y.; Chen, Y. P. *Appl. Phys. Lett.* **2012**, *101*, 162104.
- (17) Li, H.; Cao, J.; Zheng, W.; Chen, Y.; Wu, D.; Dang, W.; Wang, K.; Peng, H.; Liu, Z. *J. Am. Chem. Soc.* **2012**, *134*, 6132.
- (18) Kong, D.; Dang, W.; Cha, J. J.; Li, H.; Meister, S.; Peng, H.; Liu, Z.; Cui, Y. *Nano Lett.* **2010**, *10*, 2245.
- (19) Tabor, P.; Keenan, C.; Urazdzhin, S.; Lederman, D. *Appl. Phys. Lett.* **2011**, *99*, 013111.
- (20) Jerng, S.-K.; Joo, K.; Kim, Y.; Yoon, S.-M.; Lee, J. H.; Kim, M.; Kim, J. S.; Yoon, E.; Chun, S.-H.; Kim, Y. S. *Nanoscale* **2013**, *5*, 10618.
- (21) He, H.; Huang, D.; Zhang, X.; Li, G. *Solid State Commun.* **2012**, *152*, 810.
- (22) Zhang, Y.; Hu, L. P.; Zhu, T. J.; Xie, J.; Zhao, X. B. *Cryst. Growth Des.* **2013**, *13*, 645.
- (23) Mi, J.-L.; Lock, N.; Sun, T.; Christensen, M.; Sondergaard, M.; Hald, P.; Hng, H. H.; Ma, J.; Iversen, B. B. *ACS Nano* **2010**, *4*, 2523.
- (24) Liu, K.; Wang, J.; Liu, H.; Xiang, D. *Rare Met.* **2009**, *28*, 112.
- (25) Zhang, G.; Wang, W.; Lu, X.; Li, X. *Cryst. Growth Des.* **2009**, *9*, 145.
- (26) McKinnon, W. R.; Dahn, J. R.; Jui, C. C. H. *Acta Metall.* **1986**, *34*, 1879.
- (27) Jensen, K. M.; Tyrsted, C.; Bremholm, M.; Iversen, B. B. *ChemSusChem* **2014**, *7*, 1594.
- (28) Kelarakis, A.; Yoon, K.; Sics, I.; Somani, R. H.; Hsiao, B. S.; Chu, B. *Polymer* **2005**, *46*, 5103.
- (29) Filinchuk, Y.; Tumanov, N. A.; Ban, V.; Ji, H.; Wei, J.; Swift, M. W.; Nevidomskyy, A. H.; Natelson, D. *J. Am. Chem. Soc.* **2014**, *136*, 8100.
- (30) Kim, W. K.; Payzant, E. A.; Anderson, T. J.; Crisalle, O. D. *Thin Solid Films* **2007**, *515*, 5837.
- (31) Xia, F.; Chen, D.; Scarlett, N. V. Y.; Madsen, I. C.; Lau, D.; Leoni, M.; Ilavsky, J.; Brand, H. E. A.; Caruso, R. A. *Chem. Mater.* **2014**, *26*, 4563.
- (32) Norby, P. *J. Am. Chem. Soc.* **1997**, *119*, 5215.
- (33) Wang, Z.; Schliehe, C.; Wang, T.; Nagaoka, Y.; Cao, Y. C.; Bassett, W. A.; Wu, H.; Fan, H.; Weller, H. *J. Am. Chem. Soc.* **2011**, *133*, 14484.
- (34) Li, W.; Xia, F.; Qu, J.; Li, P.; Chen, D.; Chen, Z.; Yu, Y.; Lu, Y.; Caruso, R. A.; Song, W. *Nano Res.* **2014**, *7*, 903–916.
- (35) Styles, M. J.; Rowles, M. R.; Madsen, I. C.; McGregor, K.; Urban, A. J.; Snook, G. A.; Scarlett, N. V.; Riley, D. P. *J. Synchrotron Radiat.* **2011**, *19*, 39.
- (36) Ryan, K. R.; Trahey, L.; Okasinski, J. S.; Burrell, A. K.; Ingram, B. J. *J. Mater. Chem. A* **2013**, *1*, 6915.
- (37) Wang, X.-J.; Chen, H.-Y.; Yu, X.; Wu, L.; Nam, K.-W.; Bai, J.; Li, H.; Huang, X.; Yang, X.-Q. *Chem. Commun.* **2011**, *47*, 7170.
- (38) Li, W. J.; Gao, S. Y.; Liu, T. F.; Han, L. W.; Lin, Z. J.; Cao, R. *Langmuir* **2013**, *29*, 8657.
- (39) Millange, F.; Medina, M. I.; Guillo, N.; Ferey, G.; Golden, K. M.; Walton, R. I. *Angew. Chem., Int. Ed. Engl.* **2010**, *49*, 763.
- (40) Saha, D.; Jensen, K. M.; Tyrsted, C.; Bojesen, E. D.; Mamakhel, A. H.; Dippel, A. C.; Christensen, M.; Iversen, B. B. *Angew. Chem., Int. Ed. Engl.* **2014**, *53*, 3667.
- (41) Laumann, A.; Ørnsbjerg Jensen, K. M.; Tyrsted, C.; Bremholm, M.; Fehr, K. T.; Holzapfel, M.; Iversen, B. B. *Eur. J. Inorg. Chem.* **2011**, *2011*, 2221.
- (42) Zhou, Y.; Antonova, E.; Bensch, W.; Patzke, G. R. *Nanoscale* **2010**, *2*, 2412.
- (43) Brand, H. E. A.; Scarlett, N. V. Y.; Grey, I. E. *J. Appl. Crystallogr.* **2012**, *45*, 535.
- (44) Avrami, M. *J. Chem. Phys.* **1939**, *7*, 1103.
- (45) Khanna, Y. P.; Taylor, T. J. *Polym. Eng. Sci.* **1988**, *28*, 1042.
- (46) Hancock, J.; Sharp, J. *J. Am. Ceram. Soc.* **1972**, *55*, 74.
- (47) Kullmann, W.; Eichhorn, G.; Rauh, H.; Geick, R.; Eckold, G.; Steigenberger, U. *Phys. Status Solidi (B)* **1990**, *162*, 125.
- (48) Cava, R.; Ji, H.; Fuccillo, M.; Gibson, Q.; Hor, Y. J. *Mater. Chem. C* **2013**, *1*, 3176.
- (49) Peng, H.; Lai, K.; Kong, D.; Meister, S.; Chen, Y.; Qi, X.-L.; Zhang, S.-C.; Shen, Z.-X.; Cui, Y. *Nat. Mater.* **2010**, *9*, 225.
- (50) Cook, N. J.; Ciobanu, C. L.; Wagner, T.; Stanley, C. J. *Can. Mineral.* **2007**, *45*, 665.
- (51) Wagner, C. Z. *Elektrochem., Ber. Bunsen Ges. Phys. Chem.* **1961**, *65*, 581.

- (52) Lifshitz, I. M.; Slyozov, V. V. *J. Phys. Chem. Solids* **1961**, *19*, 35.
- (53) Kahlweit, M. *Adv. Colloid Interface Sci.* **1975**, *5*, 1.
- (54) Chen, Z.; Geng, Z.; Shi, M.; Liu, Z.; Wang, Z. *CrystEngComm* **2009**, *11*, 1591.
- (55) Li, J.; Zeng, H. C. *J. Am. Chem. Soc.* **2007**, *129*, 15839.
- (56) Wang, W.-S.; Zhen, L.; Xu, C.-Y.; Shao, W.-Z. *J. Phys. Chem. C* **2008**, *112*, 14360.
- (57) Wang, W.-S.; Zhen, L.; Xu, C.-Y.; Yang, L.; Shao, W.-Z. *J. Phys. Chem. C* **2008**, *112*, 19390.
- (58) Yang, H. G.; Zeng, H. C. *J. Phys. Chem. B* **2004**, *108*, 3492.
- (59) Zhang, L.; Yang, H.; Xie, X.; Zhang, F.; Li, L. *J. Alloys Compd.* **2009**, *473*, 65.
- (60) Ham, H.; Park, N.-H.; Kim, S. S.; Kim, H. W. *Sci. Rep.* **2014**, *4*, 3579.
- (61) Xue, X.; Penn, R. L.; Leite, E. R.; Huang, F.; Lin, Z. *CrystEngComm* **2014**, *16*, 1419.
- (62) Banfield, J. F.; Welch, S. A.; Zhang, H.; Ebert, T. T.; Penn, R. L. *Science* **2000**, *289*, 751.
- (63) Penn, R. L. *Science* **1998**, *281*, 969.
- (64) Lee, E. J.; Ribeiro, C.; Longo, E.; Leite, E. R. *J. Phys. Chem. B* **2005**, *109*, 20842.
- (65) Deng, Y.; Nan, C.-W.; Guo, L. *Chem. Phys. Lett.* **2004**, *383*, 572.
- (66) Tang, Z.; Kotov, N. A.; Giersig, M. *Science* **2002**, *297*, 237.
- (67) Zhang, J.; Huang, F.; Lin, Z. *Nanoscale* **2010**, *2*, 18.
- (68) Foqq, A. M.; Price, S. J.; Francis, R. J.; O'Brien, S.; O'Hare, D. J. *Mater. Chem.* **2000**, 2355.

Supporting information for

**Solvothermal growth of bismuth chalcogenide
nanoplatelets by the oriented attachment mechanism: An *in situ*
PXRD study**

Jingchao Song^{†,‡,#}, Fang Xia^{‡,†,#}, Meng Zhao[§], Yu Lin Zhong[†], Wei Li[‡], Kian Ping Loh[§],

Rachel A. Caruso^{*,‡,||} & Qiaoliang Bao^{*,†,±}

[†] Department of Materials Science and Engineering, Monash University, Wellington Road, Clayton, VIC 3800, Australia.

[‡] Manufacturing Flagship, The Commonwealth Scientific and Industrial Research Organization (CSIRO), Clayton, VIC 3168, Australia.

[†] School of Engineering and Information Technology, Murdoch University, Murdoch, WA 6150, Australia.

[§] Department of Chemistry, and Graphene Research Centre, National University of Singapore, 3 Science Drive 3, 117543, Singapore.

^{||} Particulate Fluids Processing Centre, School of Chemistry, The University of Melbourne, Melbourne, VIC 3010, Australia.

[±] Institute of Functional Nano and Soft Materials (FUNSOM), Jiangsu Key Laboratory for Carbon-Based Functional Materials and Devices, and Collaborative Innovation Center of Suzhou Nano Science and Technology, Soochow University, Suzhou 215123, P. R. China.

Corresponding Authors

* (Q. Bao) E-mail: qlbao@suda.edu.cn, qiaoliang.bao@monash.edu;

* (R. A. Caruso) E-mail: rcaruso@unimelb.edu.au

Notes

#These authors contributed equally to this work.

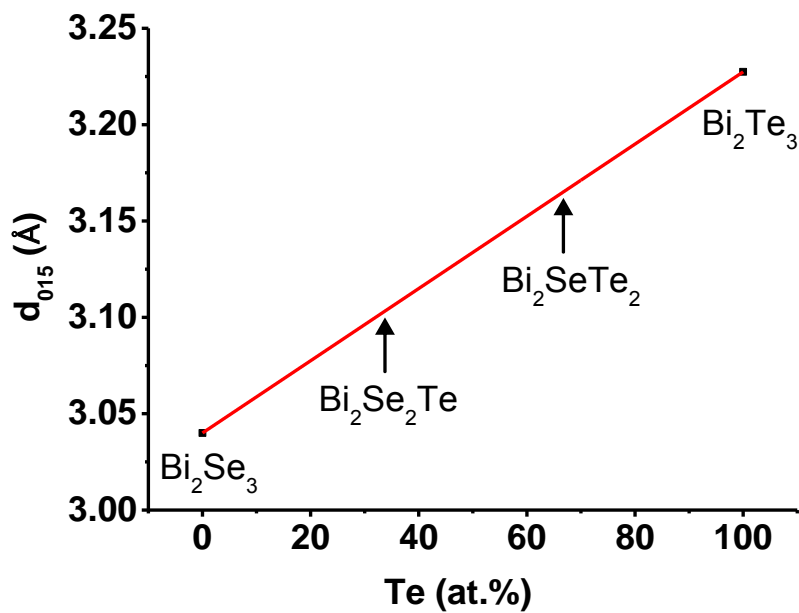


Figure S1. The d_{015} -spacing as a function of Te concentration (at. %) for the ternary $\text{Bi}_2\text{Te}_x\text{Se}_{3-x}$ composition.

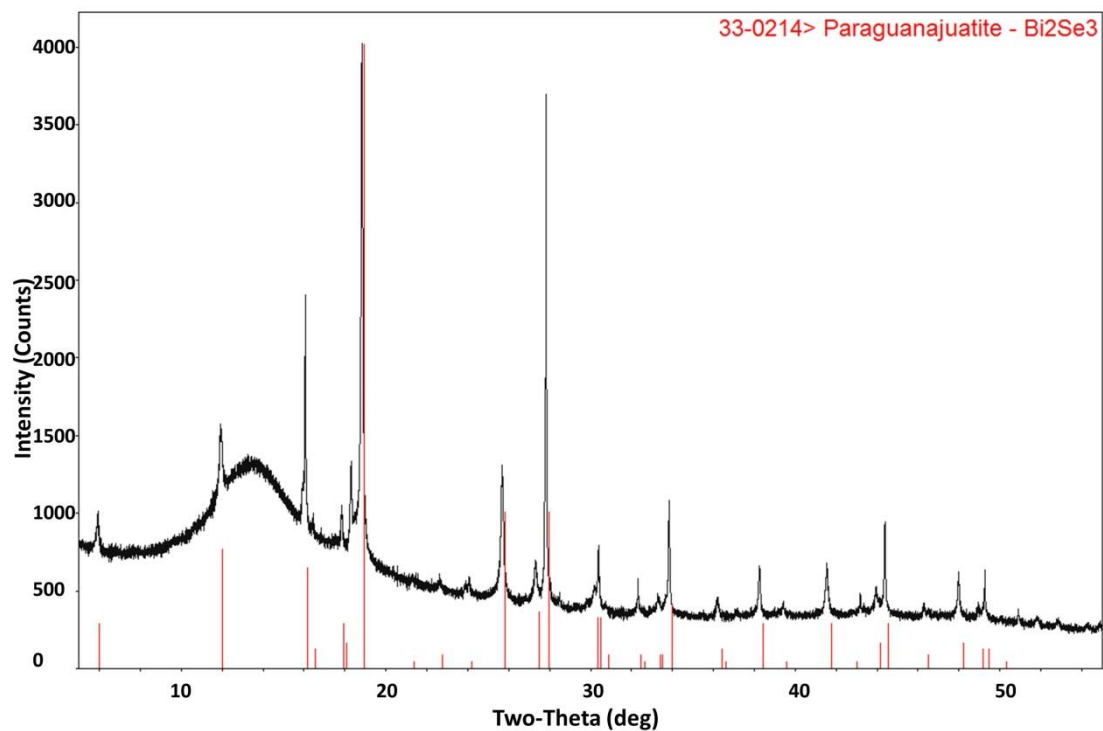


Figure S2. Final *in situ* PXRD pattern in the synthesis of Bi_2Se_3 using Bi_2O_3 as the bismuth source.

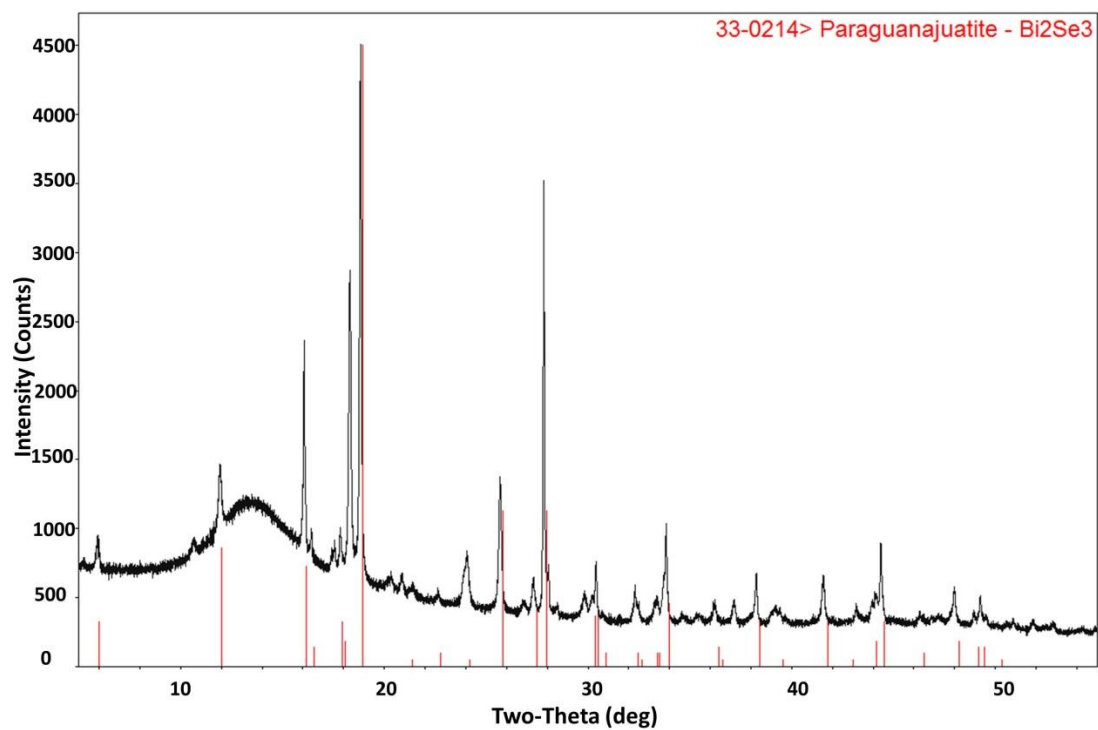


Figure S3. Final *in situ* PXRD pattern in the synthesis of Bi₂Se₃ using BiNO₄·H₂O as the bismuth source.

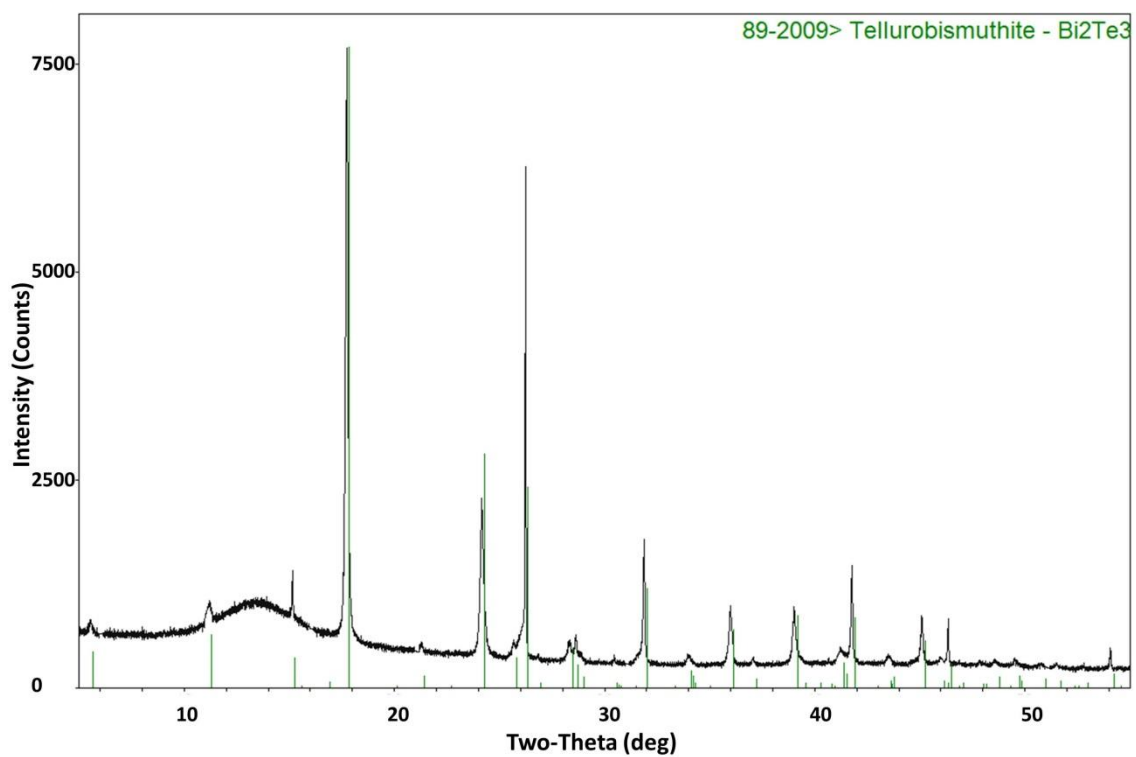


Figure S4. Final *in situ* PXRD pattern in the synthesis of Bi₂Te₃ using Bi₂O₃ as the bismuth source.

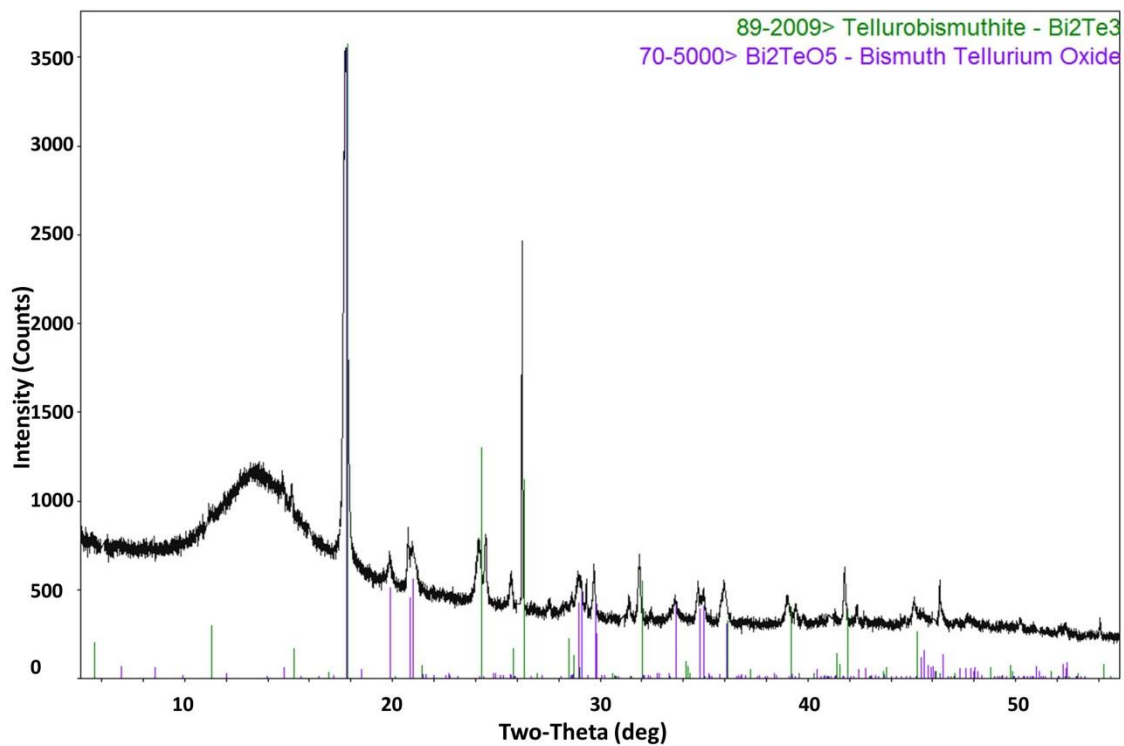


Figure S5. *In situ* PXRD pattern in the synthesis of Bi_2Te_3 at 5 min using Bi_2O_3 as the bismuth source.

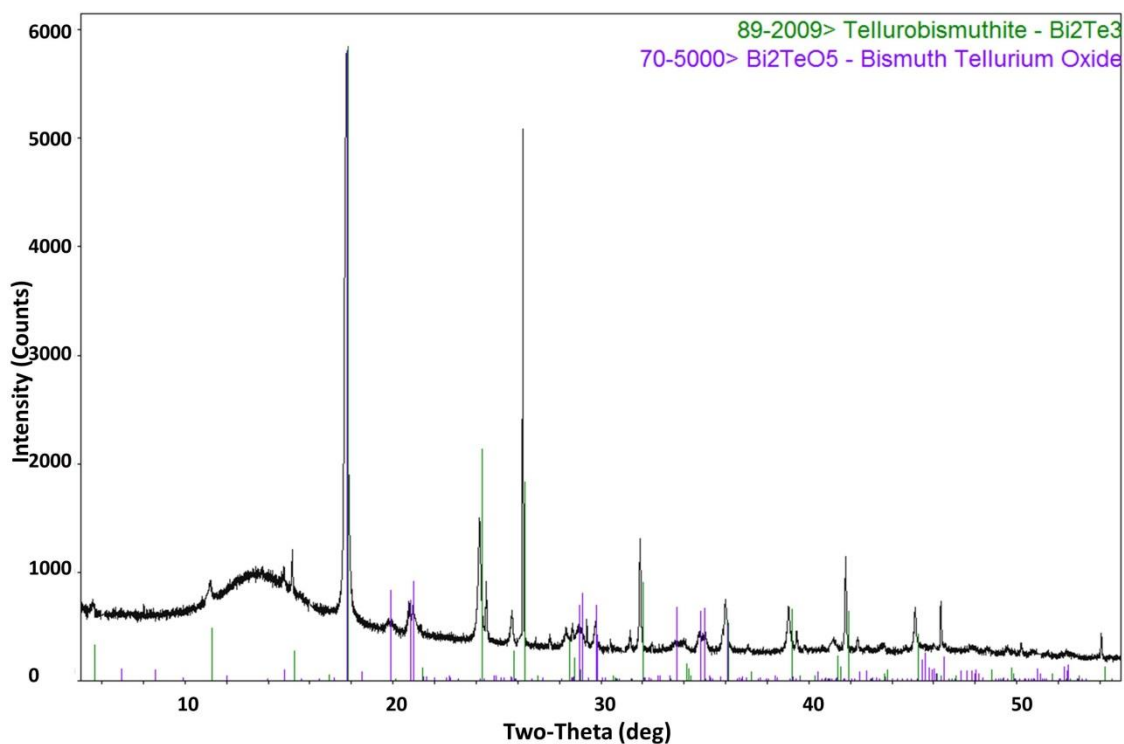


Figure S6. Final *in situ* PXRD pattern in the synthesis of Bi_2Te_3 using $\text{BiNO}_4 \cdot \text{H}_2\text{O}$ as the bismuth source.

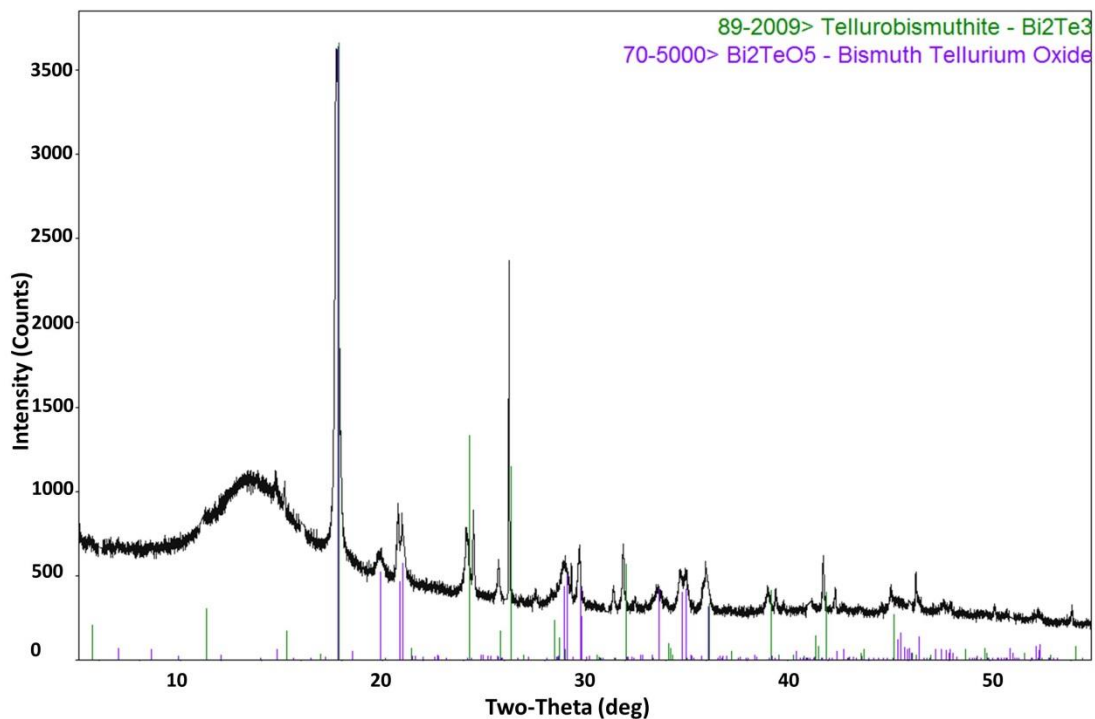


Figure S7. *In situ* PXRD pattern in the synthesis of Bi₂Te₃ at 12 min using BiNO₄·H₂O as the bismuth source

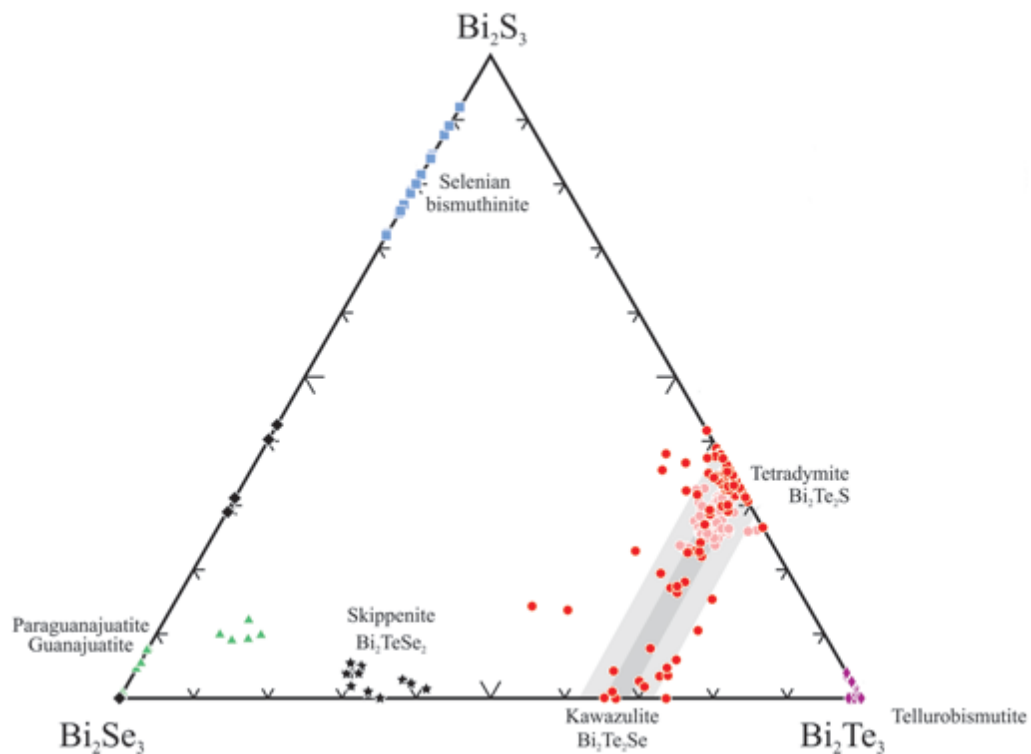


Figure S8. Phase diagram in the Bi₂S₃-Bi₂Se₃-Bi₂Te₃ system based on the mineral compositions found in nature.¹

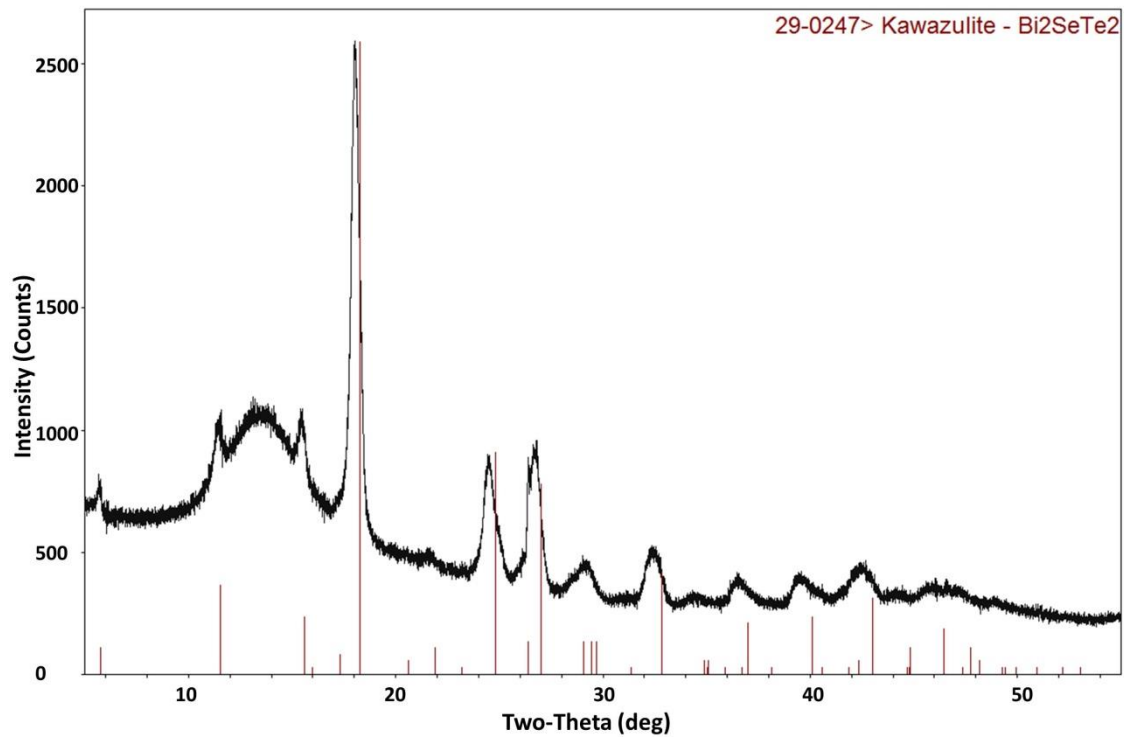


Figure S9. Final *in situ* PXRD pattern in the synthesis of ternary compound using a 5 wt% precursor solution with Se:Te=1:2 at 220 °C.

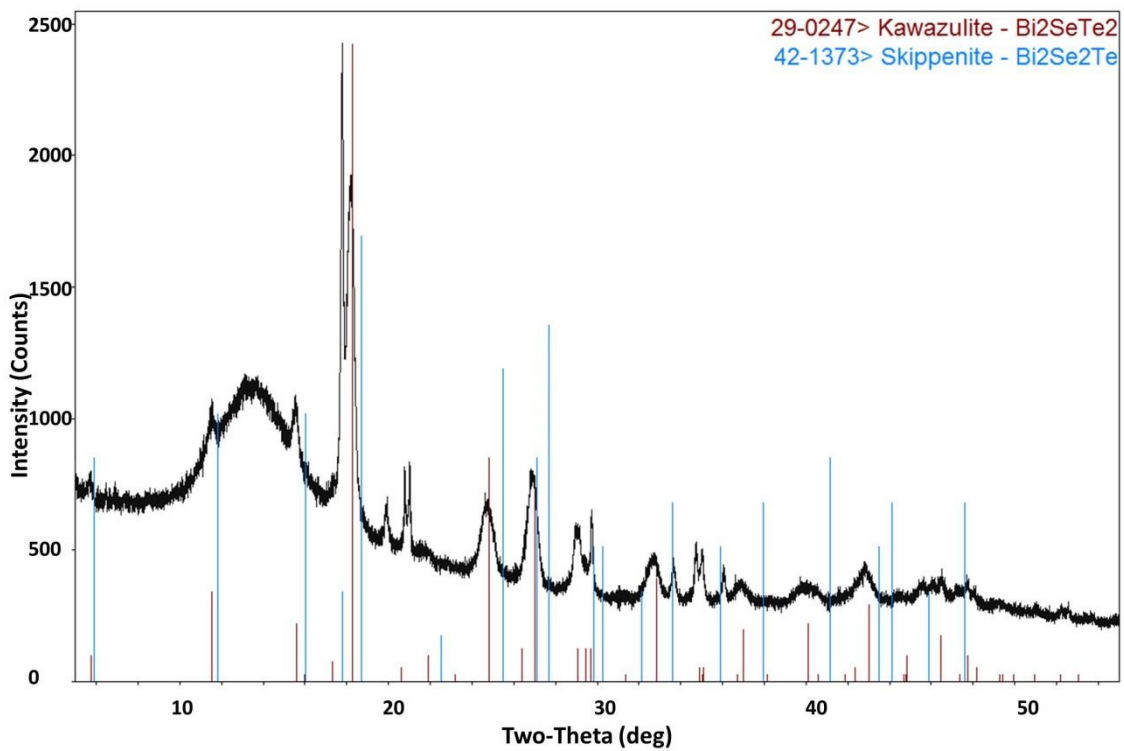


Figure S10. *In situ* PXRD pattern after 15 min in the synthesis of ternary compound using a 5 wt% precursor solution with Se:Te=1:2 at 220 °C.

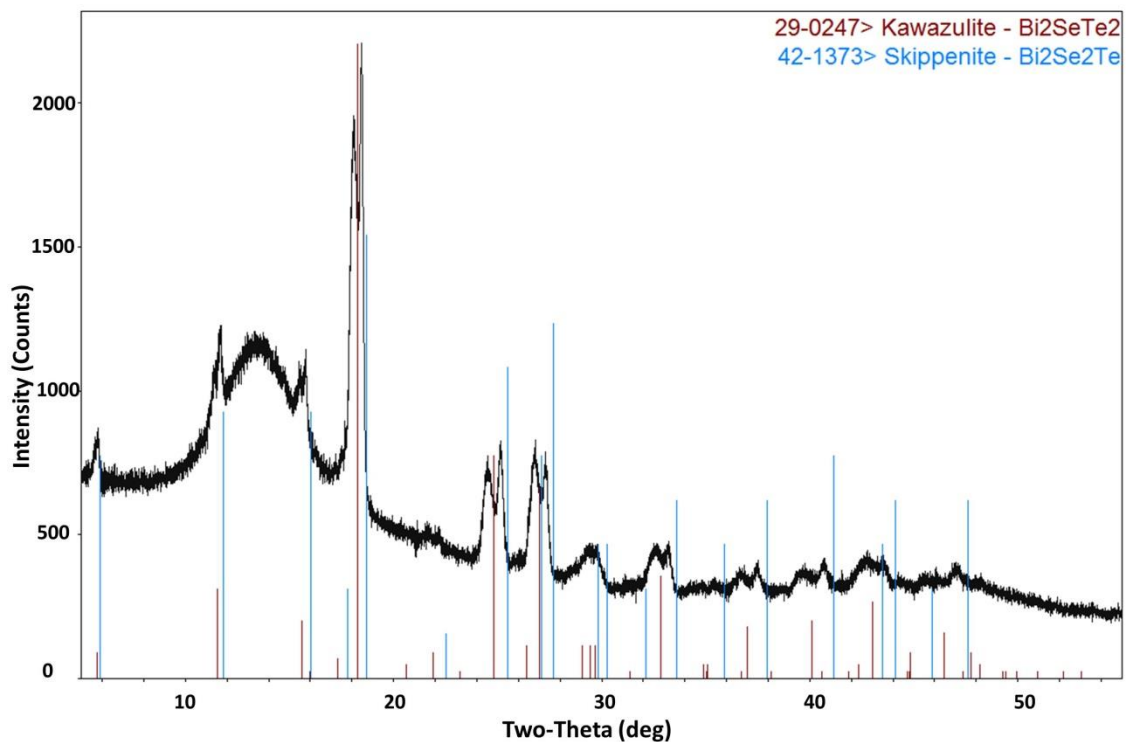


Figure S11. Final *in situ* PXRD pattern in the synthesis using a 5 wt% precursor solution with Se:Te=1:1 at 220 °C .

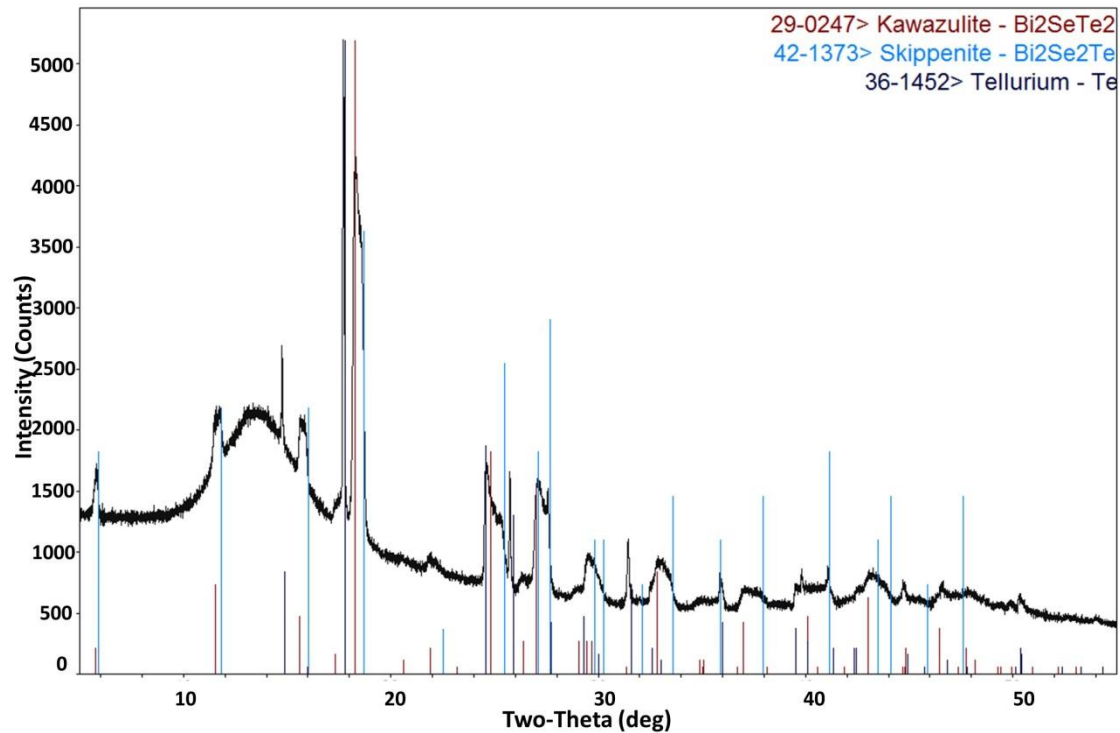


Figure S12. Final *in situ* PXRD pattern in the synthesis of ternary compound using a 5 wt% precursor solution with Se:Te=1:1 at 205 °C.

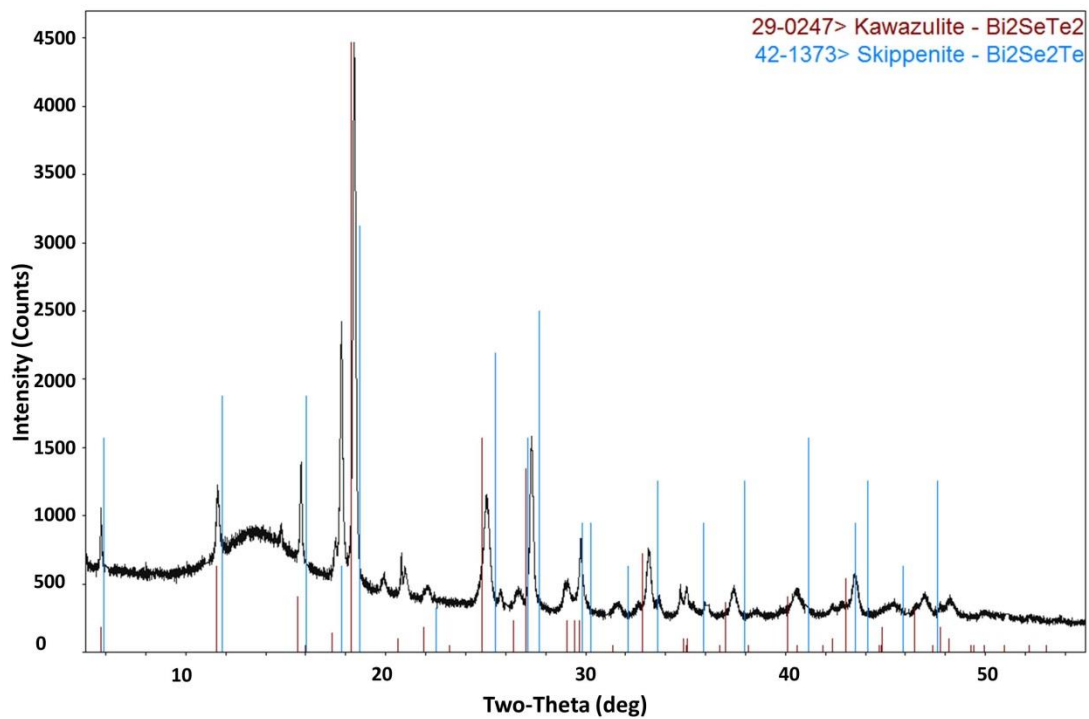


Figure S13. Final *in situ* PXRD pattern in the synthesis using a 10 wt% precursor solution with Se:Te=1:1 at 220 °C.

Reference:

(1) Cook, N. J.; Ciobanu, C. L.; Wagner, T.; Stanley, C. J. *The Canadian Mineralogist* **2007**, *45*, 665.

**Chapter 4: Large –Scale Production of Bismuth
Chalcogenide and Graphene heterostructure and Its
Application for Flexible Broadband Photodetector**

Monash University

Declaration for Thesis Chapter 4

Declaration by candidate

In the case of Chapter 4, the nature and extent of my contribution to the work was the following:

Nature of contribution	Extent of Contribution (%)
Key ideas, experimental works, analysis of results, writing up	60

The following co-authors contributed to the work. If co-authors are students at Monash University, the extent of their contribution in percentage terms must be stated:

Name	Nature of contribution	Extent of contribution (%) for student co-authors only
Jian Yuan	Experimental works	
Fang Xia	Experimental works	
Jingying Liu	Experimental works	
Yupeng Zhang	Experimental works	
Yu Lin Zhong	Experimental works	
Jialu Zheng	Experimental works	
Yan Liu	Experimental works	
Shaojuan Li	Experimental works	
Meng Zhao	Experimental works	
Zhiming Tian	Experimental works	
Rachel A. Caruso	Analysis of results	
Kian Ping Loh	Analysis of results	
Qiaoliang Bao*	Key ideas, analysis of results, writing up	Supervisor

The undersigned hereby certify that the above declaration correctly reflects the nature and extent of the candidate's and co-authors' contributions to this work*.

Candidate's Signature		Date: 16/09/2016
Main Supervisor's Signature		Date: 16/09/2016

Large-Scale Production of Bismuth Chalcogenide and Graphene Heterostructure and Its Application for Flexible Broadband Photodetector

Jingchao Song, Jian Yuan, Fang Xia, Jingying Liu, Yupeng Zhang, Yu Lin Zhong, Jialu Zheng, Yan Liu, Shaojuan Li, Meng Zhao, Zhiming Tian, Rachel A. Caruso, Kian Ping Loh, and Qiaoliang Bao*

Large-scale production of 2D van der Waals heterostructures with precisely controlled chemical composition is the major challenge hindering their practical electric and optoelectronic applications. In this work, a solvothermal method is demonstrated to produce van der Waals heterostructures consisting of metal chalcogenides and graphene in a large scale. In situ powder X-ray diffraction reveals that graphene plays an important role as atomic template to grow bismuth chalcogenide nanoplatelets with preferential stoichiometry of $\text{Bi}_2\text{Se}_{1.5}\text{Te}_{1.5}$, which is naturally unstable. It is found that $\text{Bi}_2\text{Se}_{1.5}\text{Te}_{1.5}$ has the minimum lattice mismatch with graphene (<0.1%). The release of lattice mismatch strain between $\text{Bi}_2\text{Se}_{1.5}\text{Te}_{1.5}$ and graphene sheet is evidenced by a new peak in the ultraviolet photoelectron spectroscopy. A macroscale free-standing heterostructured thin film with excellent mechanical flexibility is fabricated by simply filtering the large-scale solution processed heterostructure. The heterostructure film is used to fabricate a flexible photodetector, which shows a broadband photo response and excellent durability in a bending test. The heterostructure material and device demonstrated in this work may shed light to flexible optoelectronic devices and applications.

and mostly used strategy to fabricate 2D heterostructures is to stack one 2D crystal on top of another. This method leads to many artificial nanoarchitectures assembled in a designed sequence and with atomic layer precision, so-called van der Waals heterostructures. Representative heterostructure examples include graphene and boron nitride heterostructures,^[9–12] graphene and metal chalcogenides,^[13–19] metal chalcogenides,^[20–23] and black phosphorus and MoS_2 heterostructures.^[24] With proper alignment of the band structure, these heterostructures can be engineered to suit different applications in electronic^[11,14,21] and optoelectronic devices.^[9,24] Due to its intriguing electrical and optical properties, the topological insulator (TI) $\text{Bi}_2\text{Se}_x\text{Te}_{3-x}$ ($x = 0–3$) has been proposed for transparent flexible electrodes,^[25–27] plasmonics,^[28,29] spintronics,^[30,31] and optoelectronic devices,^[32] making it one of the ideal building block for constructing

new 2D heterostructures. In particular, the combination of graphene and Bi_2Te_3 to form a heterostructure not only affords enhanced optical response for broadband photodetection,^[32] but also provides a new approach to produce tunable saturable absorbers for pulsed lasers.^[33]

1. Introduction

The diverse range of 2D materials opens the possibility to create new 2D heterostructures and devices, giving rise to a whole new paradigm of nanoscale engineering.^[1–8] The basic

J. Song, J. Liu, Dr. Y. Zhang, Dr. Y. L. Zhong, J. Zheng, Z. Tian
Department of Materials Science and Engineering
Monash University
Clayton, VIC 3800, Australia

J. Yuan, Y. Liu, Dr. S. Li, Prof. Q. Bao
Institute of Functional Nano and Soft Materials (FUNSOM)
Jiangsu Key Laboratory for Carbon-Based Functional
Materials and Devices
Collaborative Innovation Center of Suzhou Nano Science and Technology
Soochow University
Suzhou 215123, China
E-mail: qlbao@suda.edu.cn

Dr. F. Xia
School of Engineering and Information Technology
Murdoch University
Murdoch, WA 6150, Australia

Dr. M. Zhao, Prof. K. P. Loh
Graphene Research Centre and Department
of Chemistry
National University of Singapore
Singapore 117543, Singapore

Prof. R. A. Caruso
Manufacturing Commonwealth Scientific and Industrial
Research Organization (CSIRO)
Clayton 3168, Australia

Prof. R. A. Caruso
Particulate Fluids Processing Centre
School of Chemistry
The University of Melbourne
Melbourne, VIC 3010, Australia



DOI: 10.1002/aelm.201600077

Recently, heterostructures with higher complexity in terms of more stacking layers and richer chemical compositions have shown enhanced physical and optical properties and promised a variety of applications for these materials.^[1,7] Precise control of the chemical composition in both vertical dimension and lateral dimension is challenging and meaningful, also a key factor to be solved before large-scale production.^[34] To make full use of 2D materials' important characteristic in terms of large surface area to control the growth of new 2D materials is critically important no matter the synthesis method. The simplest approach to fabricate 2D heterostructures is to pick up one layer and put it on top of another by manual transferring, in which the atomic layer can be prepared by chemical vapor deposition (CVD) or mechanical exfoliation.^[35,36] Such an assembly method requires special equipment, high technique, and experienced operation, which normally consume lots of time and labor. Furthermore, the manual control in the previous method can hardly provide a direct way to tune the chemical composition of layered materials. In this respect, the self-assembly with precise control over chemical composition as well as crystal structure is of high demand. The solution process which may fully utilize the stoichiometric selection over chemical compositions^[37,38] is an important scalable approach to produce 2D materials and heterostructures with desired interface interaction^[39,40] as well as band gap alignment. Therefore, it is nontrivial to unravel the complexity of solution synthesis of 2D materials, in particular, the material family in the form of ternary $\text{Bi}_2\text{Se}_x\text{Te}_{3-x}$ with many different phases, which provide more lattice structure flexibility during epitaxial growth.^[41]

In this work, a solvothermal method was implemented to fine tune the stoichiometry of $\text{Bi}_2\text{Se}_x\text{Te}_{3-x}$ crystals using graphene (G) as a template, resulting in $\text{Bi}_2\text{Se}_{1.5}\text{Te}_{1.5}$ -G heterostructure with perfectly matched lattice. Synchrotron-based in situ powder X-ray diffraction (PXRD) was used to investigate the crystal growth process of the heterostructure. The high yield of the production of the 2D heterostructure affords the fabrication of free-standing heterostructure thin film using a simple filtration method. Unlike our previous work which reports on a broadband photodetector prepared using a CVD-grown Bi_2Te_3 -G-heterostructured film on silicon oxide substrate,^[32] here we demonstrate a flexible photodetector based on a macroscale free-standing $\text{Bi}_2\text{Se}_{1.5}\text{Te}_{1.5}$ -G heterostructured film with excellent mechanical flexibility. The device showed high performance in terms of large photocurrent, fast response time, and most importantly, excellent flexibility and durability under mechanical deformation, which significantly enriches the capabilities of 2D material optoelectronics.^[42-44]

2. Results and Discussion

Both graphene and $\text{Bi}_2\text{Se}_x\text{Te}_{3-x}$ share layered structure with similar rhombohedral crystal lattice and hexagonal symmetry. This makes graphene a perfect atomic template for the nucleation and growth of $\text{Bi}_2\text{Se}_x\text{Te}_{3-x}$ nanocrystals. **Figure 1** schematically illustrates the synthesis process of the $\text{Bi}_2\text{Se}_x\text{Te}_{3-x}$ -G

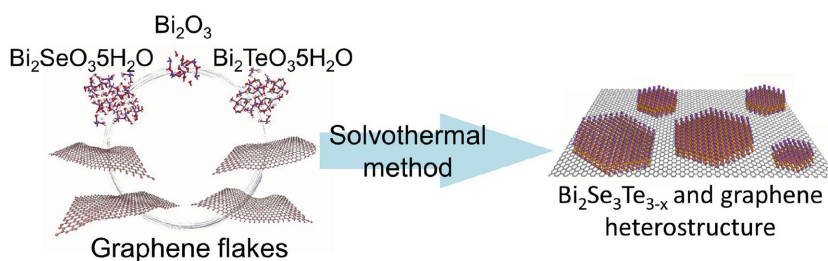


Figure 1. Schematic showing the growth of $\text{Bi}_2\text{Se}_x\text{Te}_{3-x}$ -G heterostructure in the solvothermal process.

heterostructure obtained by mixing the precursors with graphene flakes and performing the solvothermal treatment. The scanning electron microscopy (SEM) image in **Figure 2a** shows a $\text{Bi}_2\text{Se}_x\text{Te}_{3-x}$ platelet grown on a thick graphite sheet. The lateral size of the hexagonal crystal is about 500 nm. Raman spectroscopy clearly resolves characteristic peaks of a $\text{Bi}_2\text{Se}_x\text{Te}_{3-x}$ crystal (A_{1g}^1 , E_g^2 , and A_{1g}^2 vibrational modes at 68.5, 110, and 162.7 cm^{-1} , respectively^[45]) and graphitic material (D, G, and 2D peaks at 1359, 1595, and 2722 cm^{-1} , respectively), as shown in **Figure 2b**. This provides direct evidence of the coexistence of both graphene and $\text{Bi}_2\text{Se}_x\text{Te}_{3-x}$. Atomic force microscopy (AFM) was performed to reveal the topography of the heterostructure, as depicted in **Figure 2c**. The hexagonal crystal is relatively flat even though the thick graphite sheet is rough and folded. The height profile in **Figure 2d** suggests that the $\text{Bi}_2\text{Se}_x\text{Te}_{3-x}$ platelet has a thickness of $\approx 5\text{ nm}$, corresponding to about 2 unit cells along the c -direction of $\text{Bi}_2\text{Se}_x\text{Te}_{3-x}$.^[25,46]

The template-induced growth of the $\text{Bi}_2\text{Se}_x\text{Te}_{3-x}$ -G heterostructure is further characterized by electron microscopy, as shown in **Figure 3**. **Figure 3a,b** shows low-magnification SEM images of $\text{Bi}_2\text{Se}_{1.5}\text{Te}_{1.5}$ and Bi_2SeTe_2 nanoplatelets grown on larger graphene sheets, respectively. It can be seen that the

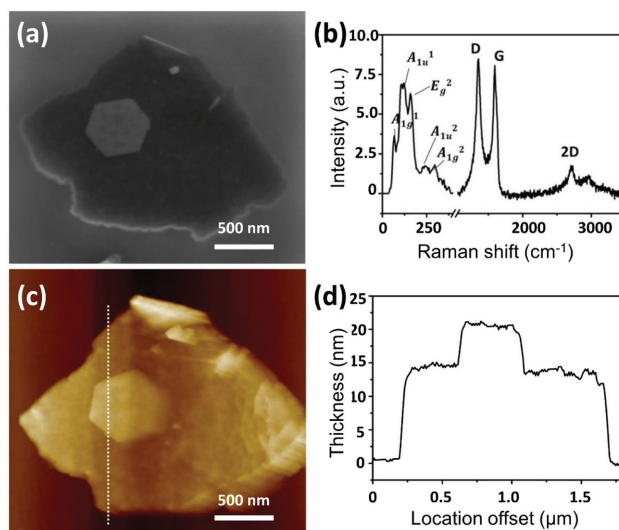


Figure 2. Material characterizations of solvothermal-processed heterostructure consisting of $\text{Bi}_2\text{Se}_{1.5}\text{Te}_{1.5}$ and thick graphite flake. a) SEM image showing single piece $\text{Bi}_2\text{Se}_{1.5}\text{Te}_{1.5}$ nanoplatelet grown on thick graphite flake. b) Raman spectrum of the heterostructure. c) AFM topography of the heterostructure. d) Height profile of the white dashed line shown in (c).

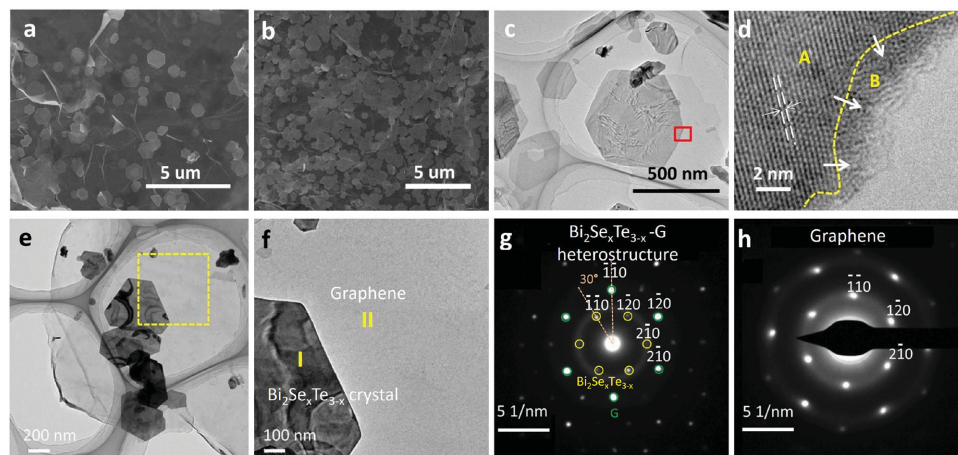


Figure 3. Electron microscopy images of $\text{Bi}_2\text{Se}_x\text{Te}_{3-x}$ -G heterostructures. a) SEM of $\text{Bi}_2\text{Se}_2\text{Te}_2$ -G heterostructure. b) SEM of $\text{Bi}_2\text{Se}_{1.5}\text{Te}_{1.5}$ -G heterostructure. c) TEM image of $\text{Bi}_2\text{Se}_{1.5}\text{Te}_{1.5}$ -G heterostructure. d) High-resolution TEM image of $\text{Bi}_2\text{Se}_x\text{Te}_{3-x}$ edge marked by the red square in (c). The yellow dashed line indicates the edge of heterostructure, and the white arrows indicate the growth direction. e, f) TEM of a few pieces of $\text{Bi}_2\text{Se}_{1.5}\text{Te}_{1.5}$ crystals grown on graphene with low (e) and high (f) magnifications. g, h) SAED patterns taken from the regions labeled as (I) and (II) in (f), respectively. The green and yellow circles in (g) indicate the diffraction patterns of $\text{Bi}_2\text{Se}_x\text{Te}_{3-x}$ and graphene, respectively. The crystallographic orientation relationship between graphene and $\text{Bi}_2\text{Se}_{1.5}\text{Te}_{1.5}$ is $\{110\}_G // \{100\}_{\text{Bi}_2\text{Se}_x\text{Te}_{3-x}}$ and $\langle 001 \rangle_G // \langle 001 \rangle_{\text{Bi}_2\text{Se}_x\text{Te}_{3-x}}$.

coverage of Bi_2SeTe_2 (Figure 3a) is lower than that of $\text{Bi}_2\text{Se}_{1.5}\text{Te}_{1.5}$ (Figure 3b) on the graphene surface, which may suggest different bonding conditions between the $\text{Bi}_2\text{Se}_x\text{Te}_{3-x}$ nanoplatelets and the graphene. Figure 3c shows a representative transmission electron microscopy (TEM) image of $\text{Bi}_2\text{Se}_{1.5}\text{Te}_{1.5}$ crystals grown on a graphene sheet. A high-resolution TEM image of the $\text{Bi}_2\text{Se}_x\text{Te}_{3-x}$ crystal edge is shown in Figure 3d, which was taken from within the region in the red square in Figure 3c. The $\text{Bi}_2\text{Se}_x\text{Te}_{3-x}$ crystal has long-range order inside the nanoplatelets (region A), whereas it is amorphous at the edge (region B). This indicates that the $\text{Bi}_2\text{Se}_x\text{Te}_{3-x}$ crystals grow epitaxially on graphene. More evidence of highly crystalline $\text{Bi}_2\text{Se}_x\text{Te}_{3-x}$ nanoplatelets grown on graphene is shown in the TEM images (Figure 3e, f). Figure 3g, h are the selected area electron diffraction (SAED) patterns of $\text{Bi}_2\text{Se}_x\text{Te}_{3-x}$ -G heterostructure and graphene taken from the regions labeled by (I) and (II) in Figure 3f, respectively. There are two sets of diffraction patterns observed in Figure 3g, which are indicated by yellow ($\text{Bi}_2\text{Se}_x\text{Te}_{3-x}$) and green (G) circles. It is found that the angle between the (110) face of $\text{Bi}_2\text{Se}_{1.5}\text{Te}_{1.5}$ crystal and the (110) face of graphene is about 30° . This suggests the crystallographic orientation relationship between graphene and $\text{Bi}_2\text{Se}_{1.5}\text{Te}_{1.5}$ is $\{110\}_G // \{100\}_{\text{Bi}_2\text{Se}_x\text{Te}_{3-x}}$ and $\langle 001 \rangle_G // \langle 001 \rangle_{\text{Bi}_2\text{Se}_x\text{Te}_{3-x}}$, indicating epitaxial growth of $\text{Bi}_2\text{Se}_x\text{Te}_{3-x}$ onto the graphene substrate due to negligible lattice mismatch between the two phases.

In order to investigate the role of lattice matching for the crystal growth, in situ PXRD technique was employed to monitor the solvothermal reaction. The synchrotron based PXRD has high angular resolution, high signal-to-noise ratio, fast data acquisition, and high wavelength electability. Thus, small lattice changes in the $\text{Bi}_2\text{Se}_x\text{Te}_{3-x}$ crystals with the addition of graphene can be identified by looking at both binary and ternary compositions' diffraction peaks. The chemical compositions of interest are Bi_2Se_3 , Bi_2Te_3 , $\text{Bi}_2\text{Se}_{1.5}\text{Te}_{1.5}$, and Bi_2SeTe_2 according to the invested chemical composition stoichiometry. Our previous in situ PXRD experiments did not show a peak shift in

the (015) peak during the synthesis of binary compositions (Bi_2Se_3 and Bi_2Te_3), while significant peak shift was observed during the synthesis of ternary composition (Bi_2SeTe_2), which is due to the competition between dissolved Se and Te species in forming crystals in the solution environment.^[41] Considering the advantage of stoichiometric flexibility in the ternary compositions, the growth of Bi_2SeTe_2 and compared the peak-shifting phenomenon without and with the addition of graphene was investigated. Figure 4a, b shows the in situ PXRD patterns taken during the growth of Bi_2SeTe_2 crystals without and with graphene templates, respectively. The major PXRD peak (015) of $\text{Bi}_2\text{Se}_x\text{Te}_{3-x}$ shifted from lower angle (18.12° in Figure 4a) to higher angle (18.20° in Figure 4b) when graphene had been added to the Bi_2SeTe_2 precursor slurry. According to the previous work,^[41] this indicates that the chemical composition of the final product changes from a Te-rich composition (i.e., Bi_2SeTe_2) to a Se-rich composition (i.e., $\text{Bi}_2\text{Se}_{1.5}\text{Te}_{1.5}$) upon the addition of graphene. The final PXRD patterns from the solvothermal experiments were quantitatively analyzed (see Experimental Section). The lattice parameter a of the $\text{Bi}_2\text{Se}_x\text{Te}_{3-x}$ crystal reduced from 4.32 to 4.29 Å after the addition of graphene (Figure 4c, d). This means a lattice shrinkage of 0.553% occurred bringing it closer to the graphene lattice in which the d -spacing of the (110) facet equals 4.26 Å. Additionally, a small amount of Te impurity formed with the addition of graphene for the ternary composition as a sharp peak appears at $2\theta = 17.72^\circ$ in the PXRD pattern (Figure 4b).

The preference for $\text{Bi}_2\text{Se}_x\text{Te}_{3-x}$ crystals to grow lattice matched structure on graphene templates was further examined by control experiments using different $\text{Bi}_2\text{Se}_x\text{Te}_{3-x}$ compositions, including perfectly matched graphene lattice (i.e., $\text{Bi}_2\text{Se}_{1.5}\text{Te}_{1.5}$) and that does not match the graphene lattice well (i.e., Bi_2Se_3 and Bi_2Te_3). Figure 4e summarizes the relationship between the Te% in the $\text{Bi}_2\text{Se}_x\text{Te}_{3-x}$ and the (015) peak position. Without graphene, the (015) peak splitting can be observed in Figure 4e. This can be understood as $\text{Bi}_2\text{Se}_{1.5}\text{Te}_{1.5}$

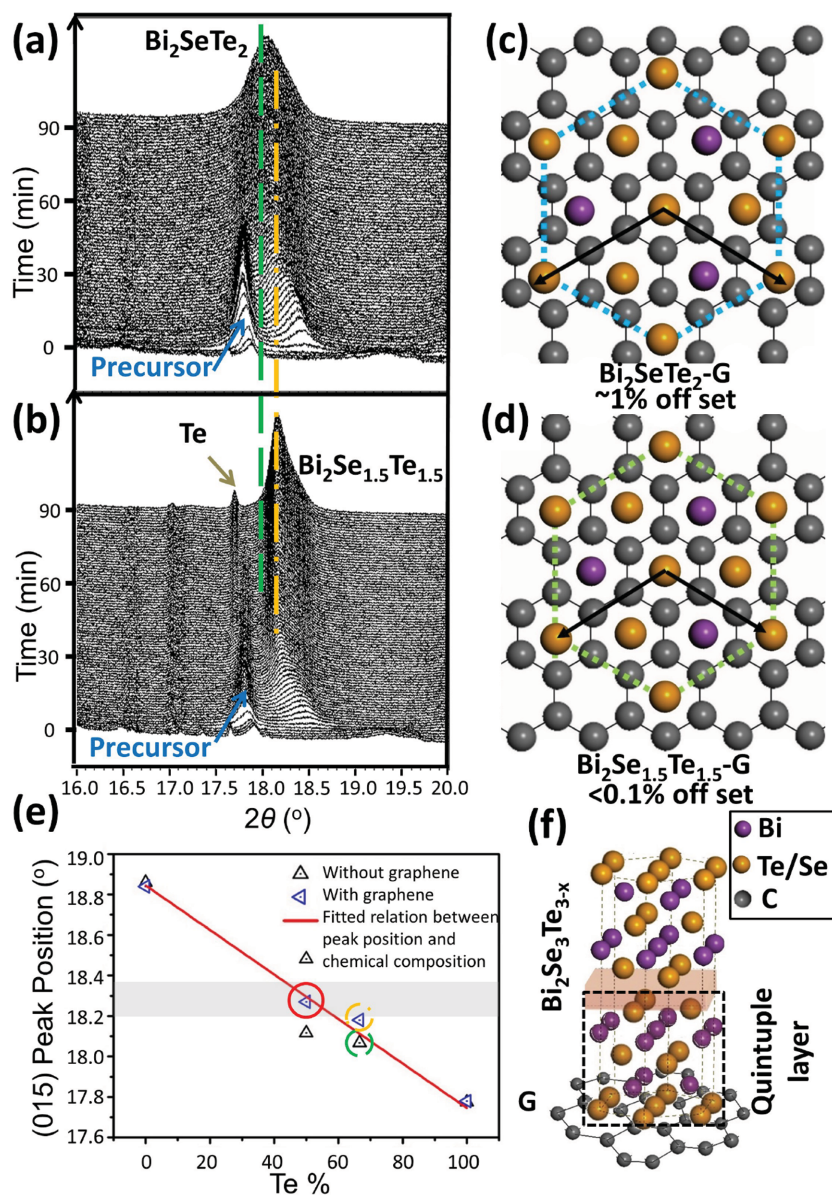


Figure 4. a,b) In situ PXRD patterns for the synthesis of Bi_2SeTe_2 nanoplatelets without (a) and with (b) addition of graphene. The green dashed line shows the final peak position of Bi_2SeTe_2 composition, and the yellow dashed line shows the peak position of $\text{Bi}_2\text{Se}_{1.5}\text{Te}_{1.5}$ composition. The eye guiding yellow and green dashed lines in (a,b) refer to (015) of $\text{Bi}_2\text{Se}_{1.5}\text{Te}_{1.5}$ and Bi_2SeTe_2 , respectively. c) Top view of $\text{Bi}_2\text{Se}_x\text{Te}_{3-x}$ -G heterostructure showing large lattice mismatch between Bi_2SeTe_2 and graphene. d) Top view of $\text{Bi}_2\text{Se}_x\text{Te}_{3-x}$ -G heterostructure schematically showing perfect lattice match between $\text{Bi}_2\text{Se}_{1.5}\text{Te}_{1.5}$ and graphene. e) The relationship between (015) peak position and different compositions, that is, Bi_2Se_3 , Bi_2Te_3 , $\text{Bi}_2\text{Se}_{1.5}\text{Te}_{1.5}$, and Bi_2SeTe_2 reaction with and without graphene. f) Side-view of two QLs of $\text{Bi}_2\text{Se}_x\text{Te}_{3-x}$ on graphene.

is a naturally unstable phase and it is difficult to form under the same experimental condition that suits the formation of other $\text{Bi}_2\text{Se}_x\text{Te}_{3-x}$ phases, such as Bi_2Se_3 , Bi_2Te_3 , and Bi_2SeTe_2 .^[41] After the addition of graphene, however, peak splitting is avoided, as shown in the red circle of Figure 4e, suggesting that a stable $\text{Bi}_2\text{Se}_{1.5}\text{Te}_{1.5}$ phase can form with the help of the templating effect of graphene. This leads to the conclusion that the more chemically versatile ternary $\text{Bi}_2\text{Se}_x\text{Te}_{3-x}$ crystals

prefer to adjust their chemical composition so that it can align its lattice to that of the graphene template. It is also noticed that at the early stage of the heterostructure growth, the $\text{Bi}_2\text{Se}_x\text{Te}_{3-x}$ crystals start in a Se-rich phase and are progressively transformed to a more Te-rich phase (Figure 4a,b). Consequently, the excess Te produces Te impurities, as seen in Figure 4b. The final (015) peak shifting phenomenon in the ternary composition is significantly different from the binary compositions in solution with graphene as well as those grown in solution without graphene.^[41] This observation confirms the hypothesis that graphene has a larger influence on lattice change in the ternary $\text{Bi}_2\text{Se}_x\text{Te}_{3-x}$ crystals rather than the binary $\text{Bi}_2\text{Se}_x\text{Te}_{3-x}$ crystals. This is mainly because the ternary composition provides much more versatility in chemical composition tuning and therefore better lattice matching options for graphene compared with the binary compositions whose lattice changes can be ignored due to the lack of lattice selectivity.

To better understand the lattice match behavior in $\text{Bi}_2\text{Se}_x\text{Te}_{3-x}$ -G heterostructure, we discussed the impact of chemical stoichiometric on $\text{Bi}_2\text{Se}_x\text{Te}_{3-x}$ crystal structure. As we known, the bismuth chalcogenide based TI family shares the rhombohedral lattice structure ($a = b \neq c$, $\alpha = \beta = 90^\circ$, and $\gamma = 120^\circ$; space group $R\bar{3}m$) which is a close analog to graphene (Figure 4f). Five atomic layers form a quintuple layer which represents the smallest repeating unit in its c -direction. It is generally believed that the minimization of lattice mismatch plays the dominant role in guiding the molecular beam epitaxial growth of topological insulators.^[26] Nevertheless, it is possible to further tune the chemical ratios in the bismuth chalcogenide family, which may result in different lattice parameters^[45] and lead to different energy band structure. $\text{Bi}_2\text{Se}_x\text{Te}_{3-x}$ crystals with different chemical compositions have different lattice mismatches with graphene. For example, the lattice parameter a of Bi_2Se_3 , Bi_2SeTe_2 , and Bi_2Te_3 are 4.143, 4.298, and 4.385 Å, respectively. Meanwhile, graphene has an a lattice parameter ≈ 2.46 Å, which gives the periodicity, 4.26 Å, along the [110] direction with which the bismuth chalcogenides are aligned. Thus, the lattice mismatch between Bi_2Se_3 , Bi_2SeTe_2 , and Bi_2Te_3 and graphene are -2.74% , 0.89% , and 2.95% , respectively. Among these compounds, the lattice of Bi_2SeTe_2 is comparable to that of graphene with less than 1% mismatch. It is noteworthy that $\text{Bi}_2\text{Se}_{1.5}\text{Te}_{1.5}$ has the smallest lattice mismatch with graphene ($<0.1\%$), attesting the experimental observation of preferable growth of $\text{Bi}_2\text{Se}_{1.5}\text{Te}_{1.5}$ on the graphene template. To further verify the template-induced

growth of $\text{Bi}_2\text{Se}_{1.5}\text{Te}_{1.5}$, a stoichiometric reaction with graphene has been carried out in the autoclaves (Figure S1, Supporting Information). The formation of the (015) diffraction peak in $\text{Bi}_2\text{Se}_{1.5}\text{Te}_{1.5}$ agrees well with that observed in the synchrotron-based in situ PXRD experiments.

The perfect lattice matched $\text{Bi}_2\text{Se}_x\text{Te}_{3-x}$ -G heterostructure contributes to an intermediate state in the valence band of the $\text{Bi}_2\text{Se}_{1.5}\text{Te}_{1.5}$ -G heterostructure by removing the in-plane strain. Ultraviolet photoelectron spectroscopy (UPS) was performed to measure the changes in the electronic states of the $\text{Bi}_2\text{Se}_x\text{Te}_{3-x}$ -G heterostructures. **Figure 5** shows the valence band spectra of graphene, $\text{Bi}_2\text{Se}_{1.5}\text{Te}_{1.5}$ -G heterostructure, Bi_2SeTe_2 -G heterostructure, and their corresponding physical mixtures. The 5 eV peak in the valence band of the $\text{Bi}_2\text{Se}_{1.5}\text{Te}_{1.5}$ -G heterostructure is obvious and nontrivial, and cannot be produced by accumulating the individual valence band spectrum of $\text{Bi}_2\text{Se}_{1.5}\text{Te}_{1.5}$ and graphene at any ratio. It is most likely a result of the addition of graphene in the growth stage as there is no such peak for those compounds without graphene. Therefore, the peak is most probably associated with the absence of lattice mismatch strain between the $\text{Bi}_2\text{Se}_{1.5}\text{Te}_{1.5}$ and the graphene sheet.^[47–50] Better alignment of the $\text{Bi}_2\text{Se}_x\text{Te}_{3-x}$ and graphene lattices would potentially initiate better coupling between

these two 2D materials and form a perfect interface for charge transfer.^[37,38,51–53]

Now we are able to imagine a scenario for the heterostructure growth. First, the Se rich ternary $\text{Bi}_2\text{Se}_x\text{Te}_{3-x}$ seeds are attached to anchoring points on the graphene surface or in tunnels between stacked multilayer graphene, which is evidenced by the peak shift at the early stage in PXRD measurements (Figure 4a,b).^[41] The anchoring points are oxygen containing groups or defects on the electrically exfoliated graphene (Figure S2, Supporting Information).^[54,55] Subsequently, $\text{Bi}_2\text{Se}_x\text{Te}_{3-x}$ nanoplatelets start to grow epitaxially (Figure 3d), during which the edges of the ternary $\text{Bi}_2\text{Se}_x\text{Te}_{3-x}$ are stoichiometrically flexible. Eventually, $\text{Bi}_2\text{Se}_x\text{Te}_{3-x}$ crystals self-optimize and grow into the most lattice matched compound on the graphene surface by taking relevant elements (Se and Te) from the precursor solution. In this step, the exfoliated graphene surface with least defects is beneficial to the epitaxial growth with minimum strain.^[56] Excess precursors will form impurities in the solution before the reaction is completed.

In order to develop flexible optoelectronic devices, free-standing $\text{Bi}_2\text{Se}_x\text{Te}_{3-x}$ thin films were fabricated by filtration of ethanol solutions containing the $\text{Bi}_2\text{Se}_{1.5}\text{Te}_{1.5}$ -G heterostructure materials with graphene weight load around 30% (Figure S3, Supporting Information). A schematic of the multilayer $\text{Bi}_2\text{Se}_x\text{Te}_{3-x}$ -G heterostructure thin film is presented in **Figure 6a**. The inset in Figure 6a illustrates the flexible device at different bending angles. As we can see from Figure 6b, the real free-standing heterostructure thin film and device can be bended easily. The layered structure of free-standing heterostructure film was confirmed by the cross-section view of SEM (Figure 6c), with an average thickness at 20–30 μm . The electrical conductivity of the free-standing heterostructure film was measured to be 0.0283 S m^{-1} with a four-probe method. The sheet resistance of the heterostructure film is $588.46 \text{ k}\Omega \square^{-1}$ on average. In comparison, the electric conductivity and sheet resistance of a bare graphene film with similar thickness are $1.81 \times 10^3 \text{ S m}^{-1}$ and $55.24 \text{ }\Omega \square^{-1}$, respectively. The effort to measure the sheet resistance of a bare $\text{Bi}_2\text{Se}_x\text{Te}_{3-x}$ thin film prepared by a similar filtration method failed to give a number as it was non-conductive and out of the measuring range ($>999 \text{ k}\Omega \square^{-1}$). Even though the conductivity of $\text{Bi}_2\text{Se}_x\text{Te}_{3-x}$ -G heterostructure film is much lower than that of pure graphene film, it is significantly higher than a pure $\text{Bi}_2\text{Se}_x\text{Te}_{3-x}$ film as stacked graphene sheets form a conductive network. The formation of a semiconductive heterostructured film may overcome the huge dark current observed in pure graphene when it is used as a photoactive channel for light detection.

Interdigital electrodes were deposited onto a free-standing heterostructure film via a shadow mask assisted e-beam evaporation to form a flexible device, as shown in Figure 6b (right bottom). Because of the good mechanical flexibility of the free-standing heterostructured film, the device can be integrated onto arbitrary soft substrates to enhance the films mechanical properties, as depicted in Figure 6b (right top). The photoresponse of the flexible device was evaluated under visible and infrared light illumination. Figure 6d reveals the photocurrent of the $\text{Bi}_2\text{Se}_{1.5}\text{Te}_{1.5}$ film and the $\text{Bi}_2\text{Se}_{1.5}\text{Te}_{1.5}$ -G heterostructural thin film as a function of source-drain bias under the illumination of 635 nm laser. Inset of Figure 6d is a zoom in

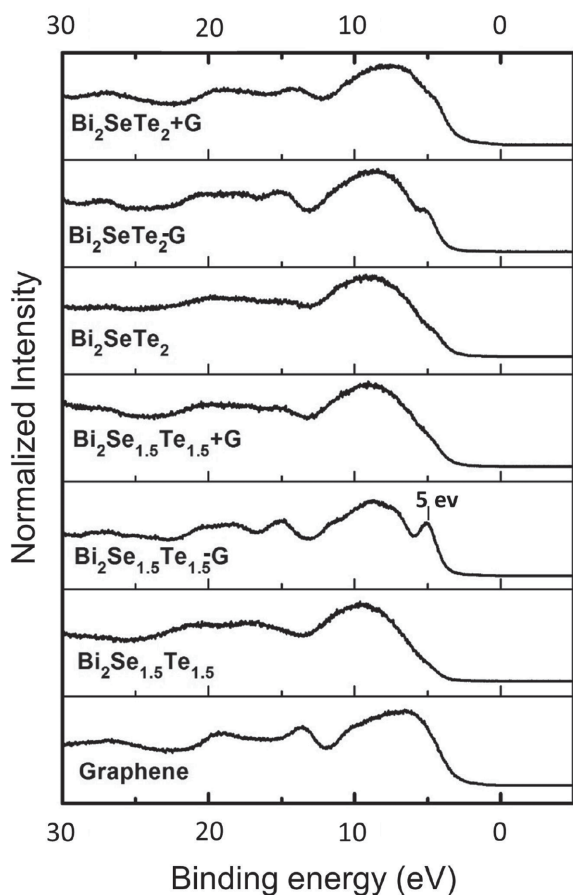


Figure 5. UPS result showing the valence band structures of different compounds. From bottom to top: graphene, $\text{Bi}_2\text{Se}_{1.5}\text{Te}_{1.5}$, $\text{Bi}_2\text{Se}_{1.5}\text{Te}_{1.5}$ -G heterostructure, $\text{Bi}_2\text{Se}_{1.5}\text{Te}_{1.5}$ and graphene mixture, Bi_2SeTe_2 -G heterostructure, Bi_2SeTe_2 and graphene mixture.

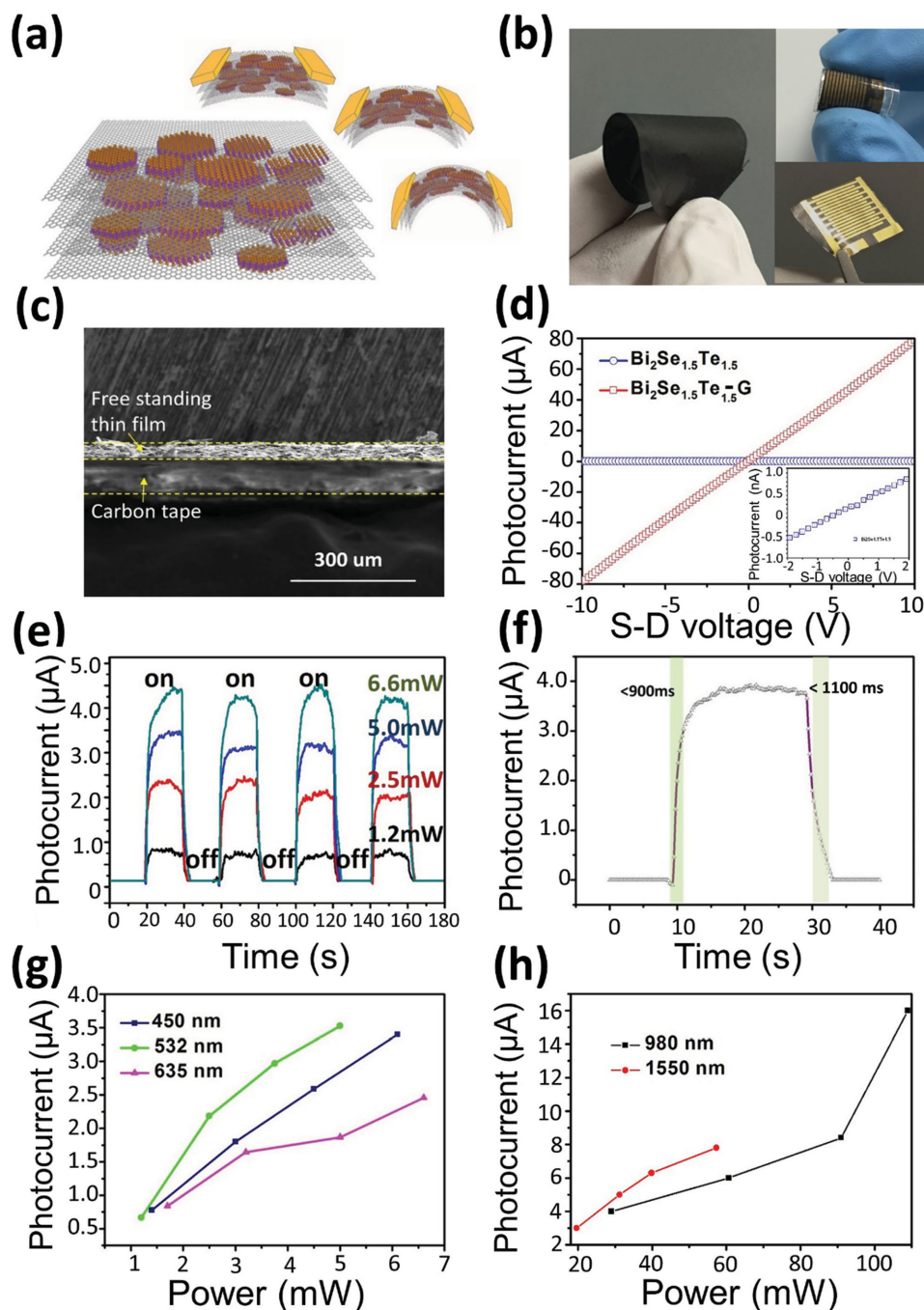


Figure 6. a) Schematic of multilayer $\text{Bi}_2\text{Se}_x\text{Te}_{3-x}\text{-G}$ heterostructures and their flexible devices (up right corner). b) Photograph of flexible free-standing thin film (left), flexible device integrated on PDMS substrate (right top), free-standing flexible device hold by a tweezer (right bottom). c) SEM image of the cross-section of the free-standing heterostructured thin film. d) Photocurrent of devices based on bare $\text{Bi}_2\text{Se}_{1.5}\text{Te}_{1.5}$ film and $\text{Bi}_2\text{Se}_{1.5}\text{Te}_{1.5}\text{-G}$ heterostructural thin film as a function of source-drain bias under illumination of 635 nm laser. Inset shows photocurrent response of $\text{Bi}_2\text{Se}_{1.5}\text{Te}_{1.5}$ -based photodetector in a smaller source-drain bias range. e) Time-dependent photocurrent under illumination of 532 nm laser with different incident powers (1.2, 2.5, 5.0, and 6.6 mW). f) Temporal photocurrent response excited at 635 nm. g) Power-dependent photocurrent at visible (450, 532, and 635 nm) wavelengths. h) Power-dependent photocurrent at infrared wavelengths (980 and 1550 nm). The photoresponse are measured at a bias of 2 V in (e), (f), (g), and (h).

photocurrent response against source-drain bias in $\text{Bi}_2\text{Se}_{1.5}\text{Te}_{1.5}$ photodetector. It is found that photocurrent of the device based on $\text{Bi}_2\text{Se}_{1.5}\text{Te}_{1.5}\text{-G}$ heterostructure film is 1000 times larger than that of a device based on a bare $\text{Bi}_2\text{Se}_{1.5}\text{Te}_{1.5}$ film. The

photoresponse of the flexible device under illumination of a 532 nm laser at different powers is investigated, as shown in Figure 6e. The photocurrent can be effectively turned on and off, and modulated by different laser powers (from 1.2 to 6.6 mW).

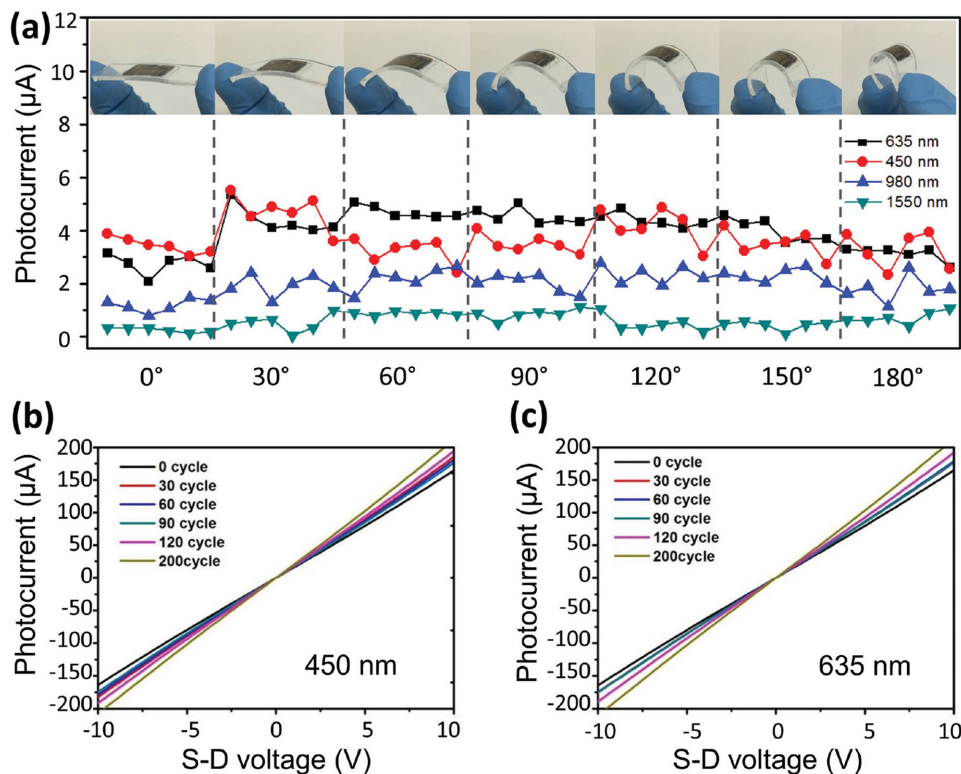


Figure 7. a) Photocurrent of the flexible photodetector at different bending angles with integral of every 30°. Illumination light: 450, 635, 980, and 1550 nm. b,c) I - V curves of the flexible photodetectors which recovered from 30, 60, 90, 120, and 200 bending cycles at 450 nm (b) and 635 nm (c) illumination, respectively. All the photocurrents measured at laser power of 10 mW.

Figure 6f shows the temporal photocurrent response excited at 635 nm. It indicates that the photocurrent has a rise time of 900 ms and fall time of 1100 ms, which is defined as the time for the photocurrent raised to and drop from 70% of the on-state current. Moreover, power-dependent photocurrent under the illumination of visible and infrared light was plotted in Figure 6g,h. Impressively, pretty high photocurrent was generated by shining 980 nm and 1550 nm light, which indicates the capability for broadband photodetection over the visible and infrared spectral range.

The flexibility and the durability of $\text{Bi}_2\text{Se}_x\text{Te}_{3-x}$ -G heterostructure based photodetector were investigated. The bending test of the photodetector device on a polydimethylsiloxane (PDMS) substrate was performed with different bending angles (Figure 7a). The photocurrent results (Figure 7a) indicate the robustness and stability of the photodetector and its response to light with broad spectral range from 450 to 1550 nm. The durability of the flexible photodetector was measured against the bending cycles. The source-drain current after different bending cycles illuminated by 450 and 635 nm lasers (Figure 7b,c) were recorded. There is no obvious current change after 120 bending cycles. It is interesting to observe slightly increase of the photocurrent after 120 bending cycles, which may attribute to the physical morphology change in the bending test. The interlayer spacing in the heterostructure become more closely repacked after 120 bending cycles, as evidenced by the thickness change shown in Figure S4 (Supporting Information). Generally, the consistency of the photocurrent after 200 bending cycles

indicates the excellent conductivity stability of the film, which may benefit from the epitaxial growth of the heterostructure material. Considering the practical application in a reasonably long period, we tested the photodetector device after storing it in ambient condition for four months and found that it still can work well (see Figure S5, Supporting Information). The high performance and excellent mechanical properties of $\text{Bi}_2\text{Se}_x\text{Te}_{3-x}$ -G heterostructure photodetector suggest the good contact between the graphene and the $\text{Bi}_2\text{Se}_x\text{Te}_{3-x}$ nanocrystal inherited from the template growth. The photocurrent generation can be explained by the exciton split at the interface of graphene and $\text{Bi}_2\text{Se}_x\text{Te}_{3-x}$.^[32] Although, the photoresponse in this work is relatively slow due to the possible Schottky-like barrier modulation at the electrode–film interface and charge carrier diffusion in the heterostructure interconnections,^[57,58] the performance of $\text{Bi}_2\text{Se}_x\text{Te}_{3-x}$ -G heterostructure photodetector could be further improved by optimizing the contact between the electrode and the heterostructure thin film.^[59]

3. Conclusions

In conclusion, a solvothermal method has been employed to produce $\text{Bi}_2\text{Se}_x\text{Te}_{3-x}$ -G van der Waals heterostructure in a large scale. The role of graphene as the template for the growth of $\text{Bi}_2\text{Se}_x\text{Te}_{3-x}$ with a particular stoichiometry preference of $\text{Bi}_2\text{Se}_{1.5}\text{Te}_{1.5}$ which is naturally unstable was revealed by a synchrotron-based PXRD technique. With enhanced interlayer

interaction in $\text{Bi}_2\text{Se}_{1.5}\text{Te}_{1.5}\text{-G}$ heterostructure, as-produced free-standing heterostructure film shows improved electrical, photoelectric, and mechanical properties, making it a promising photoresponsive material for flexible photodetector. This work marries the chemical design at atomic scale with a scalable synthesis approach, and demonstrates a practical application of the heterostructure material for flexible optoelectronic devices.

4. Experimental Section

Heterostructure Material Syntheses: The reaction slurry precursors were prepared by mixing bismuth source (Bi_2O_3 , Townson & Mercer), sodium selenite (Na_2SeO_3 , 99%, BDH Chemicals Ltd.), sodium telluride (Na_2TeO_3 , 99.5%, Alfa Aesar) into solvent (ethylene glycol) (BDH Chemicals Ltd) with the addition of polyvinyl pyrrolidone (PVP) ($M_n = 40$ K, Sigma-Aldrich) as ligands. The graphene sample used in the experiments was homemade via the electrical exfoliation methods.^[56] For synchrotron in situ PXRD experiments, precursors were added with vigorous stirring. For Bi_2Se_3 precursor slurry, 0.05 g Bi_2O_3 + 0.056 g Na_2SeO_3 + 0.08 g PVP + 0.005 g G + 2 mL ethylene glycol (EG) were added; For Bi_2Te_3 precursor slurry, 0.05 g Bi_2O_3 + 0.0715 g Na_2TeO_3 + 0.08 g PVP + 0.005 g G + 2 mL EG were added; For Bi_2SeTe_2 precursor slurry, 0.05 g Bi_2O_3 + 0.0185 g Na_2SeO_3 + 0.0475 g Na_2TeO_3 + 0.08 g PVP + 0.005 g G + 2 mL EG were added; For $\text{Bi}_2\text{Se}_{1.5}\text{Te}_{1.5}$ precursor slurry, 0.05 g Bi_2O_3 + 0.028 g Na_2SeO_3 + 0.0355 g Na_2TeO_3 + 0.08 g PVP + 0.005 g G + 2 mL EG were added. In the control experiments without graphene, the chemical ratio remains the same. All the mixed slurries were stirred vigorously to reach homogenous slurry before the experiment were carried out. For large-scale solvothermal synthesis, the same recipe was used as above while the input amount has been increased. The resulting product paste was washed using ethanol with a centrifuge at the rate of 4000 rpm for several times. The material was further dried in an oven at 70 °C overnight before it was used for further electrical characterizations and device fabrications.

Material Characterization: The morphology and microstructure were investigated by SEM (FEI Helios Nanolab 600) and TEM (FEI Tecnai G2 T20 TWIN, operated at 200 kV), respectively. The Raman data were collected with a WITec 300R Raman spectrometer. The AFM characterization was performed with a Bruker Dimension iCon system. All the measurements were carried out in the room temperature.

Synchrotron-Based In Situ PXRD Experiments: In situ PXRD experiments were conducted at the Australian Synchrotron powder diffraction beamline, using an X-ray wavelength of 1.0000 Å, which was calibrated by a LaB_6 standard (NIST SRM 660b). In each experiment, the precursor slurry was filled into a quartz microreactor (1 mm in outer diameter, 0.1 mm in wall thickness, and 35 mm in length), which was subsequently sealed onto a stainless steel Norby cell.^[60] To prevent boiling and oxidation of the slurry, external N_2 pressure (2.5 MPa) was applied to the sealed microreactor. The microreactor was then aligned at the center of the X-ray beam, and heated by a hot air blower. The temperature was monitored by a K-type thermocouple and was calibrated by a KNO_3 temperature standard before the experiments were carried out. The slurry was heated to 220 °C with a heating rate of 50 °C min^{-1} . The position-sensitive MYTHEN detector was used to collect the in situ diffraction patterns every 0.6–2.4 min over the 2θ range 1°–81°. The experiments were terminated when no noticeable changes can be observed in the diffraction pattern. The collected datasets were quantitatively analyzed by the Rietveld method with the assist of TOPAS v4.2 (Bruker-AXS).^[41]

Ultraviolet Photoelectron Spectroscopy: The valence band electronic structure of topological and graphene heterostructures was measured using UPS at Soft X-ray beamline at the Australian Synchrotron. Measurements were carried out in an ultrahigh vacuum chamber (base pressure of 1×10^{-10} Torr). The excitation energy used here was 150 eV. The sample was deposited on gold-coated substrate to compensate the charging effect.

Device Fabrication and Characterization: The thin films were prepared by simply filtration of resulting heterostructure solution using a standard millipore filtration setup with polyvinylidene fluoride membrane (0.65 μm pore size) and baked in vacuum at 50 °C for 1 h. The dried thin films were cut into 1×1 cm^2 and covered under a stainless steel shadow mask, and further deposited with 80 nm gold electrode with 8 nm chromium adhesion layer underneath. The electrical measurement was carried out using a precision source/measure unit (Agilent B2902A). For the convenience of flexible device measurement, the prepared devices were mounted on a 2 mm thick PDMS substrate to avoid the broken of fragile free-standing thin films. Specifically, the metal clamps were clipped on the device with mounted substrate to reduce the damage to the thin film. The photocurrent measurement platform (optical platform) is based on microconfocal Raman spectrometer (WITec 300R) with a 20 \times optical objective, which has the numerical aperture of 0.4. The lasers used with the measurement system have wavelength of 450, 532, 635, 980, and 1550 nm. The laser travels through an enclosure optical microscopy system and focused by the 100 \times objective. The focused laser spot size averages at 10–20 μm (measured by the optical microscope). The effective power falling onto the device is measured by the photodiode and digital handheld power energy meter console (PM100D, Thorlabs). All the electric measurements are carried out at room temperature. All the photoresponse measurements were performed under 2 V bias.

Supporting Information

Supporting Information is available from the Wiley Online Library or from the author.

Acknowledgements

J.S. and J.Y. contributed equally to this work. This research was partially undertaken on the powder diffraction beamline at Australian Synchrotron, Victoria, Australia (beam time awards AS131/PDFI/5998, AS132/PD/6494, and AS152/SXR/R9389), through the Science and Industry Endowment Fund Special Research Program-Synchrotron Science. This work was performed in part at the Melbourne Centre for Nanofabrication (MCN) in the Victorian Node of the Australian National Fabrication Facility (ANFF). Q.B. acknowledges the support of the 973 Program (Grant No. 2015CB932700), NSFC grants (Grant Nos. 51222208, 51290273, and 91433107), the Priority Academic Program Development of Jiangsu Higher Education Institutions, the ARC Future Fellowship (FT150100450), and DP (DP140101501). R.A.C. acknowledges the ARC for a Future Fellowship (FT0990583) and the CSIRO Science Leader Schemes.

Received: February 23, 2016
Published online: March 16, 2016

- [1] A. K. Geim, I. V. Grigorieva, *Nature* **2013**, 499, 419.
- [2] B. V. Lotsch, *Annu. Rev. Mater. Res.* **2015**, 45, 85.
- [3] S. Z. Butler, S. M. Hollen, L. Cao, Y. Cui, J. A. Gupta, H. R. Gutiérrez, T. F. Heinz, S. S. Hong, J. Huang, A. F. Ismach, E. Johnston-Halperin, M. Kuno, V. V. Plashnitsa, R. D. Robinson, R. S. Ruoff, S. Salahuddin, J. Shan, L. Shi, M. G. Spencer, M. Terrones, W. Windl, J. E. Goldberg, *ACS Nano* **2013**, 7, 2898.
- [4] R. F. Service, *Science* **2015**, 348, 490.
- [5] F. Xia, H. Wang, D. Xiao, M. Dubey, A. Ramasubramaniam, *Nat. Photon.* **2014**, 8, 899.
- [6] H. Wang, F. Liu, Z. Fang, W. Zhou, Z. Liu, *Nanoscale* **2014**, 6, 12250.
- [7] F. Bonaccorso, A. Lombardo, T. Hasan, Z. Sun, L. Colombo, A. C. Ferrari, *Mater. Today* **2012**, 15, 564.

- [8] Q. Bao, K. P. Loh, *ACS Nano* **2012**, *6*, 3677.
- [9] K. Zhang, F. L. Yap, K. Li, C. T. Ng, L. J. Li, K. P. Loh, *Adv. Funct. Mater.* **2014**, *24*, 731.
- [10] A. Woessner, M. B. Lundberg, Y. Gao, A. Principi, P. Alonso-González, M. Carrega, K. Watanabe, T. Taniguchi, G. Vignale, M. Polini, J. Hone, R. Hillenbrand, F. H. L. Koppens, *Nat. Mater.* **2015**, *14*, 421.
- [11] C. R. Dean, A. F. Young, I. Meric, C. Lee, L. Wang, S. Sorgenfrei, K. Watanabe, T. Taniguchi, P. Kim, K. L. Shepard, J. Hone, *Nat. Nano* **2010**, *5*, 722.
- [12] P. Gehring, B. F. Gao, M. Burghard, K. Kern, *Nano Lett.* **2012**, *12*, 5137.
- [13] L. Britnell, R. M. Ribeiro, A. Eckmann, R. Jalil, B. D. Belle, A. Mishchenko, Y.-J. Kim, R. V. Gorbachev, T. Georgiou, S. V. Morozov, A. N. Grigorenko, A. K. Geim, C. Casiraghi, A. H. C. Neto, K. S. Novoselov, *Science* **2013**, *340*, 1311.
- [14] S. Bertolazzi, D. Krasnozhan, A. Kis, *ACS Nano* **2013**, *7*, 3246.
- [15] Y. Shi, W. Zhou, A. Y. Lu, W. Fang, Y. H. Lee, A. L. Hsu, S. M. Kim, K. K. Kim, H. Y. Yang, L. J. Li, J. C. Idrobo, J. Kong, *Nano Lett.* **2012**, *12*, 2784.
- [16] W. J. Yu, Z. Li, H. Zhou, Y. Chen, Y. Wang, Y. Huang, X. Duan, *Nat. Mater.* **2013**, *12*, 246.
- [17] W. Zhang, C.-P. Chuu, J.-K. Huang, C.-H. Chen, M.-L. Tsai, Y.-H. Chang, C.-T. Liang, Y.-Z. Chen, Y.-L. Chueh, J.-H. He, M.-Y. Chou, L.-J. Li, *Sci. Rep.* **2014**, *4*, 3826.
- [18] L. Kou, B. Yan, F. Hu, S.-C. Wu, T. O. Wehling, C. Felser, C. Chen, T. Frauenheim, *Nano Lett.* **2013**, *13*, 6251.
- [19] O. Shevtsov, P. Carmier, C. Petitjean, C. Groth, D. Carpentier, X. Waintal, *Phys. Rev. X* **2012**, *2*, 031004.
- [20] Y. Gong, J. Lin, X. Wang, G. Shi, S. Lei, Z. Lin, X. Zou, G. Ye, R. Vajtai, B. I. Yakobson, H. Terrones, M. Terrones, B. K. Tay, J. Lou, S. T. Pantelides, Z. Liu, W. Zhou, P. M. Ajayan, *Nat. Mater.* **2014**, *13*, 1135.
- [21] C. Huang, S. Wu, A. M. Sanchez, J. J. P. Peters, R. Beanland, J. S. Ross, P. Rivera, W. Yao, D. H. Cobden, X. Xu, *Nat. Mater.* **2014**, *13*, 1096.
- [22] G. Hao, Y. Fan, X. Qi, Y. Liu, L. Ren, Z. Huang, X. Peng, X. Wei, J. Zhong, *Sci. Adv. Mater.* **2014**, *6*, 383.
- [23] H. Terrones, F. López-Urías, M. Terrones, *Sci. Rep.* **2013**, *3*, 1549.
- [24] Y. Deng, Z. Luo, N. J. Conrad, H. Liu, Y. Gong, S. Najmaei, P. M. Ajayan, J. Lou, X. Xu, P. D. Ye, *ACS Nano* **2014**, *8*, 8292.
- [25] W. Dang, H. Peng, H. Li, P. Wang, Z. Liu, *Nano Lett.* **2010**, *10*, 2870.
- [26] C.-L. Song, Y.-L. Wang, Y.-P. Jiang, Y. Zhang, C.-Z. Chang, L. Wang, K. He, X. Chen, J.-F. Jia, Y. Wang, Z. Fang, X. Dai, X.-C. Xie, X.-L. Qi, S.-C. Zhang, Q.-K. Xue, X. Ma, *Appl. Phys. Lett.* **2010**, *97*, 143118.
- [27] N. Kim, P. Lee, Y. Kim, J. S. Kim, Y. Kim, D. Y. Noh, S. U. Yu, J. Chung, K. S. Kim, *ACS Nano* **2014**, *8*, 1154.
- [28] H. Beidenkopf, P. Roushan, J. Seo, L. Gorman, I. Drozdov, Y. S. Hor, R. J. Cava, A. Yazdani, *Nat. Phys.* **2011**, *7*, 939.
- [29] Y. L. Chen, J. H. Chu, J. G. Analytis, Z. K. Liu, K. Igarashi, H. H. Kuo, X. L. Qi, S. K. Mo, R. G. Moore, D. H. Lu, M. Hashimoto, T. Sasagawa, S. C. Zhang, I. R. Fisher, Z. Hussain, Z. X. Shen, *Science* **2010**, *329*, 659.
- [30] D. Pesin, A. H. MacDonald, *Nat. Mater.* **2012**, *11*, 409.
- [31] T. Yokoyama, S. Murakami, *Phys. E* **2014**, *55*, 1.
- [32] H. Qiao, J. Yuan, Z. Xu, C. Chen, S. Lin, Y. Wang, J. Song, Y. Liu, Q. Khan, H. Y. Hoh, C.-X. Pan, S. Li, Q. Bao, *ACS Nano* **2015**, *9*, 1886.
- [33] H. Mu, Z. Wang, J. Yuan, S. Xiao, C. Chen, Y. Chen, Y. Chen, J. Song, Y. Wang, Y. Xue, H. Zhang, Q. Bao, *ACS Photonics* **2015**, *2*, 832.
- [34] C. Tan, H. Zhang, *J. Am. Chem. Soc.* **2015**, *137*, 12162.
- [35] X.-Q. Zhang, C.-H. Lin, Y.-W. Tseng, K.-H. Huang, Y.-H. Lee, *Nano Lett.* **2015**, *15*, 410.
- [36] X. Duan, C. Wang, J. C. Shaw, R. Cheng, Y. Chen, H. Li, X. Wu, Y. Tang, Q. Zhang, A. Pan, J. Jiang, R. Yu, Y. Huang, X. Duan, *Nat. Nano* **2014**, *9*, 1024.
- [37] L. Kou, T. Frauenheim, C. Chen, *J. Phys. Chem. Lett.* **2013**, *4*, 1730.
- [38] Y. Zhang, K. He, C.-Z. Chang, C.-L. Song, L.-L. Wang, X. Chen, J.-F. Jia, Z. Fang, X. Dai, W.-Y. Shan, S.-Q. Shen, Q. Niu, X.-L. Qi, S.-C. Zhang, X.-C. Ma, Q.-K. Xue, *Nat. Phys.* **2010**, *6*, 584.
- [39] N. Lu, H. Guo, L. Wang, X. Wu, X. C. Zeng, *Nanoscale* **2014**, *6*, 4566.
- [40] S. J. Haigh, A. Gholinia, R. Jalil, S. Romani, L. Britnell, D. C. Elias, K. S. Novoselov, L. A. Ponomarenko, A. K. Geim, R. Gorbachev, *Nat. Mater.* **2012**, *11*, 764.
- [41] J. Song, F. Xia, M. Zhao, Y. L. Zhong, W. Li, K. P. Loh, R. A. Caruso, Q. Bao, *Chem. Mater.* **2015**, *27*, 3471.
- [42] C.-H. Liu, Y.-C. Chang, T. B. Norris, Z. Zhong, *Nat. Nano* **2014**, *9*, 273.
- [43] F. H. L. Koppens, T. Mueller, P. Avouris, A. C. Ferrari, M. S. Vitiello, M. Polini, *Nat. Nano* **2014**, *9*, 780.
- [44] Z. Sun, H. Chang, *ACS Nano* **2014**, *8*, 4133.
- [45] J. Yuan, M. Zhao, W. Yu, Y. Lu, C. Chen, M. Xu, S. Li, K.-P. Loh, Q. Bao, *Materials* **2015**, *8*, 5007.
- [46] D. Kong, Y. Cui, *Nat. Chem.* **2011**, *3*, 845.
- [47] A. Koma, *Thin Solid Films* **1992**, *216*, 72.
- [48] A. Koma, *J. Cryst. Growth* **1999**, *201*, 236.
- [49] B. A. Parkinson, F. A. Ohuchi, K. Ueno, A. Koma, *Appl. Phys. Lett.* **1991**, *58*, 472.
- [50] K. Ichimura, K. Imaeda, C. Jin, H. Inokuchi, *Physica B: Condens. Matter* **2002**, *323*, 137.
- [51] H. Fang, C. Battaglia, C. Carraro, S. Nemsak, B. Ozdol, J. S. Kang, H. A. Bechtel, S. B. Desai, F. Kronast, A. A. Unal, G. Conti, C. Conlon, G. K. Palsson, M. C. Martin, A. M. Minor, C. S. Fadley, E. Yablonovitch, R. Maboudian, A. Javey, *Proc. Natl Acad. Sci. USA* **2014**, *111*, 6198.
- [52] Y. Miyamoto, H. Zhang, T. Miyazaki, A. Rubio, *Phys. Rev. Lett.* **2015**, *114*, 116102.
- [53] H. Zhao, J. Wu, H. Zhong, Q. Guo, X. Wang, F. Xia, L. Yang, P.-H. Tan, H. Wang, *Nano Res.* **2015**, *8*, 3651.
- [54] X.-Y. Zhang, H.-P. Li, X.-L. Cui, Y. Lin, *J. Mater. Chem.* **2010**, *20*, 2801.
- [55] Z.-S. Wu, W. Ren, L. Wen, L. Gao, J. Zhao, Z. Chen, G. Zhou, F. Li, H.-M. Cheng, *ACS Nano* **2010**, *4*, 3187.
- [56] J. Wang, K. K. Manga, Q. Bao, K. P. Loh, *J. Am. Chem. Soc.* **2011**, *133*, 8888.
- [57] P. Stockes, L. Liu, J. Zou, L. Zhai, Q. Huo, S. Khondaker, *Appl. Phys. Lett.* **2009**, *94*, 042110.
- [58] S. Lu, B. Panchapakesan, *Nanotechnology* **2006**, *17*, 1843.
- [59] Y. Liu, L. Yuan, M. Yang, Y. Zheng, L. Li, L. Gao, N. Nerngchamng, C. T. Nai, C. S. S. Sangeeth, Y. P. Feng, C. A. Nijhuis, K. P. Loh, *Nat. Commun.* **2014**, *5*, 5461.
- [60] P. Norby, *J. Am. Chem. Soc.* **1997**, *119*, 5215.

ADVANCED ELECTRONIC MATERIALS

Supporting Information

for *Adv. Electron. Mater.*, DOI: 10.1002/aelm.201600077

Large-Scale Production of Bismuth Chalcogenide and Graphene Heterostructure and Its Application for Flexible Broadband Photodetector

*Jingchao Song, Jian Yuan, Fang Xia, Jingying Liu, Yupeng Zhang, Yu Lin Zhong, Jialu Zheng, Yan Liu, Shaojuan Li, Meng Zhao, Zhiming Tian, Rachel A. Caruso, Kian Ping Loh, and Qiaoliang Bao**

Supporting Information for

Title: Large-scale production of bismuth chalcogenide and graphene heterostructure and its application for flexible broadband photodetector**

*By Jingchao Song[†], Jian Yuan[†], Fang Xia, Jingying Liu, Yupeng Zhang, Yu Lin Zhong, Jialu Zheng, Yan Liu, Shaojuan Li, Meng Zhao, Zhiming Tian, Rachel A. Caruso, Kian Ping Loh and Qiaoliang Bao**

J. Song, J. Liu, Dr. Y. Zhang, Dr. Y-L Zhong, J. Zheng, Z. Tian,
Department of Materials Science and Engineering
Monash University
Clayton, VIC 3800, Australia

J. Song, Prof. R. A. Caruso
Manufacturing, The Commonwealth Scientific and Industrial Research Organization (CSIRO)
Clayton, VIC 3168, Australia

Dr. F. Xia
School of Engineering and Information Technology
Murdoch University
Murdoch, WA 6150, Australia

Dr. M. Zhao, Prof. K. P. Loh
Graphene Research Centre and Department of Chemistry
National University of Singapore
Singapore 117543, Singapore

Prof. R. A. Caruso
Particulate Fluids Processing Centre, School of Chemistry
The University of Melbourne
Melbourne, VIC 3010, Australia

[*] Y. Liu, J. Yuan, Dr. S. Li, Prof. Q. Bao
Institute of Functional Nano and Soft Materials (FUNSOM)
Jiangsu Key Laboratory for Carbon-Based Functional Materials and Devices
Collaborative Innovation Center of Suzhou Nano Science and Technology
Soochow University
Suzhou 215123, P. R. China
E-mail: qlbao@suda.edu.cn

[†] These authors contributed equally

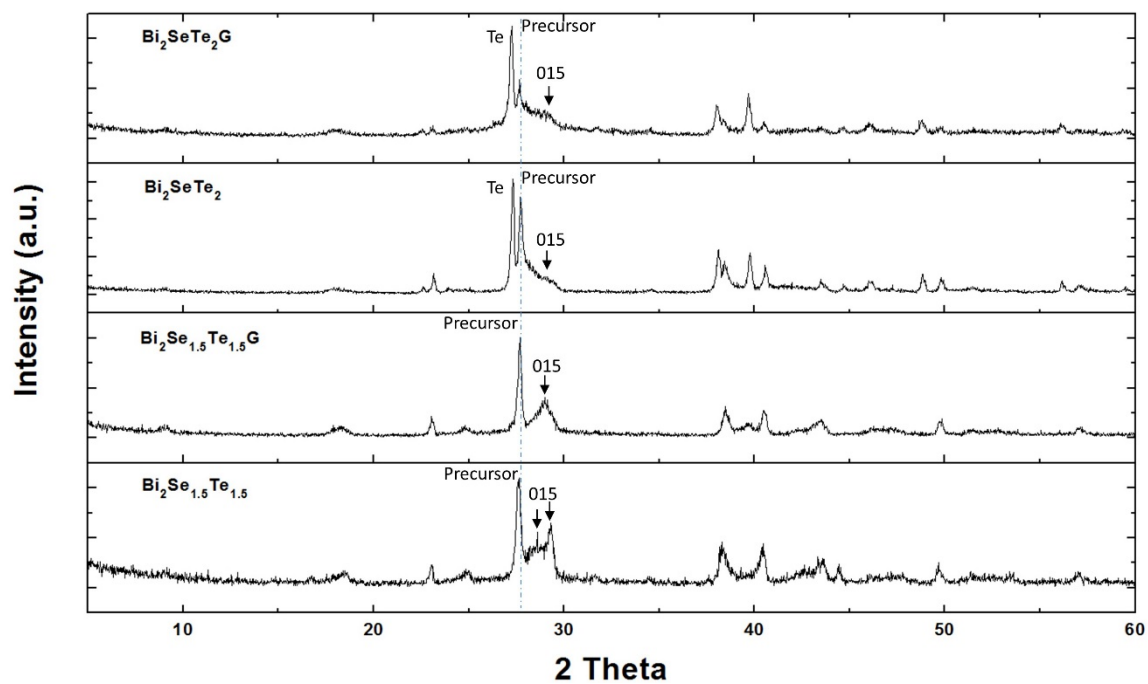


Figure S1. PXRD pattern of $\text{Bi}_2\text{Se}_{1.5}\text{Te}_{1.5}$ and Bi_2SeTe_2 crystals grown in solution, with and without graphene respectively. The (015) peak of $\text{Bi}_2\text{Se}_{1.5}\text{Te}_{1.5}$ shows greater integrity and more sharpness with the addition of graphene due to the matched lattice effect. The wavelength used in the lab X-ray source is 1.54056 \AA .

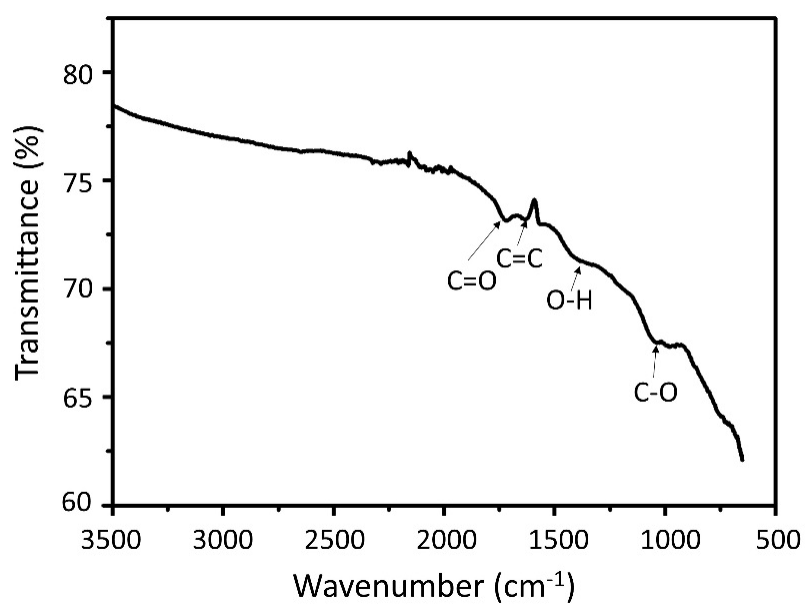


Figure S2. Fourier transform infrared spectroscopy (FTIR) spectrum of the exfoliated graphene. The FTIR measurement was carried out with a UV-Vis spectrometer.

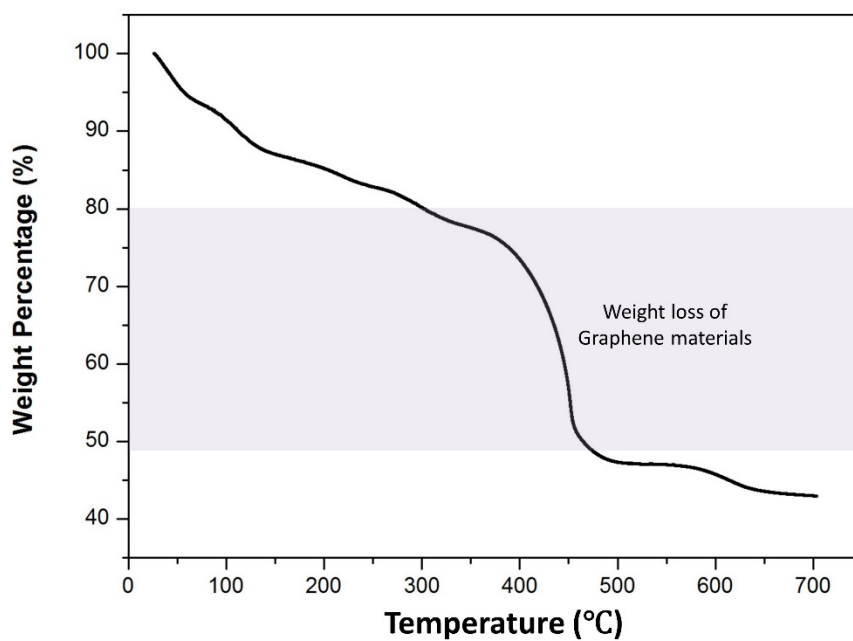


Figure S3. TGA pattern of Bi₂Se_{1.5}Te_{1.5} and graphene heterostructured thin film. The graphene weight loss according to oxidation is ~30% at about 400 °C.

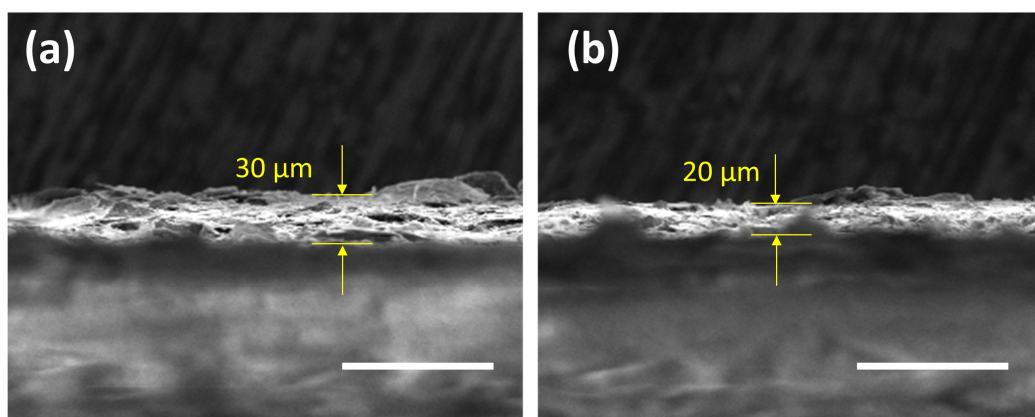


Figure S4. Cross-sectional SEM image of the $\text{Bi}_2\text{Se}_{1.5}\text{Te}_{1.5}$ and graphene heterostructural thin film before (a) and after (b) 200 bending cycles. Scale bar 100 μm.

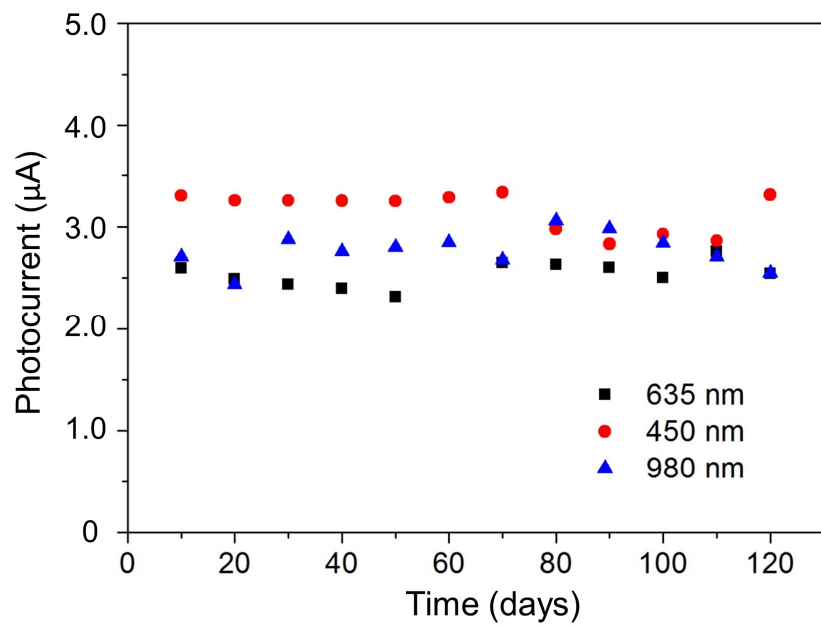


Figure S5. Photocurrent stability against time using the 450 nm, 635 nm and 980 nm lasers (power around 10 mW).

Chapter 5: Efficient and Tunable Plasmon Excitation in Graphene-Bi₂Te₃ Heterostructure

Declaration for Thesis Chapter 5

Declaration by candidate

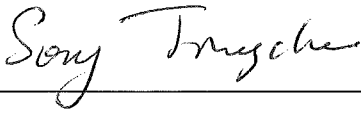
In the case of Chapter 5, the nature and extent of my contribution to the work was the following:

Nature of contribution	Extent of Contribution (%)
Key ideas, experimental works, analysis of results, writing up	50

The following co-authors contributed to the work. If co-authors are students at Monash University, the extent of their contribution in percentage terms must be stated:

Name	Nature of contribution	Extent of contribution (%) for student co-authors only
Yao Lu	Key ideas, experimental works, analysis of results, writing up	
Jiang Yuan	Experimental works, analysis of results	
Lei Zhang	Simulation works	
Steve Qing Yang Wu	Experimental works	
Wenzhi Yu	Experimental works	
Meng Zhao	Experimental works	
Jinghua Teng	Analysis of results	
Kian Ping Loh	Analysis of results	
Chao Zhang	Analysis of results	
Qiaoliang Bao*	Key ideas, analysis of results, writing up	Supervisor

The undersigned hereby certify that the above declaration correctly reflects the nature and extent of the candidate's and co-authors' contributions to this work*.

Candidate's Signature		Date: 16/09/2016
Main Supervisor's Signature		Date: 16/09/2016

Highly efficient plasmon excitation in graphene-Bi₂Te₃ heterostructure

YAO LU,^{1,†} JINGCHAO SONG,^{2,†} JIAN YUAN,^{1,†} LEI ZHANG,³ STEVE QING YANG WU,⁴ WENZHI YU,¹ MENG ZHAO,^{4,5} CHENG-WEI QIU,³ JINGHUA TENG,⁴ KIAN PING LOH,⁵ CHAO ZHANG,⁶ AND QIAOLIANG BAO^{1,2,*}

¹Institute of Functional Nano and Soft Materials (FUNSOM), Jiangsu Key Laboratory for Carbon-Based Functional Materials and Devices, and Collaborative Innovation Center of Suzhou Nano Science and Technology, Soochow University, Suzhou 215123, China

²Department of Materials Science and Engineering, Monash University, Clayton, Victoria 3800, Australia

³Department of Electrical and Computer Engineering, National University of Singapore, Singapore 117583, Singapore

⁴Institute of Materials Research and Engineering, Agency for Science, Technology and Research (A*STAR),

3 Research Link, Singapore 117602, Singapore

⁵Department of Chemistry and Graphene Research Centre, National University of Singapore, 3 Science Drive 3, Singapore 117543, Singapore

⁶School of Engineering Physics, University of Wollongong, Wollongong, New South Wales 2552, Australia

*Corresponding author: qiaoliang.bao@monash.edu

Received 18 May 2016; revised 7 July 2016; accepted 7 July 2016; posted 25 July 2016 (Doc. ID 265378); published 9 August 2016

Graphene plasmons have attracted a lot of attention due to large confinement and small mode volume. However, the graphene-based plasmonic devices are still limited in the practical applications due to relatively small light absorption of graphene and limited light–matter coupling efficiency in general excitation strategy. Here, this work reported a strong plasmonic coupling effect observed in a novel graphene-Bi₂Te₃ heterostructure on the top of silicon gratings. It is interesting to find that the extinction spectra of the graphene-Bi₂Te₃ heterostructure has shown three times greater magnitude than that of graphene. This observation is mainly attributed to two factors: first, the coupling efficiency between the graphene and Bi₂Te₃; second, the higher light absorption in the graphene-Bi₂Te₃ heterostructure. Moreover, the plasmonic resonance peak of the graphene-Bi₂Te₃ heterostructure can be easily tuned by changing the grating period just like what happens in the graphene film. In all, this work utilizes the simple silicon grating to couple the light into the graphene-Bi₂Te₃ heterostructure, and further explores the hybridized Dirac plasmons in the graphene-Bi₂Te₃ heterostructure. We believe it will stimulate the interest to study the variant plasmonic heterostructure and trigger new terahertz device applications. © 2016 Optical Society of America

OCIS codes: (250.5403) Plasmonics; (050.2770) Gratings; (160.4236) Nanomaterials.

<http://dx.doi.org/10.1364/JOSAB.33.001842>

1. INTRODUCTION

Surface plasmons (SPs), which are collective oscillations of electrons localized at the conductor/dielectric interface, have been discovered in atomically thin layered materials such as graphene [1]. Due to a number of favorable properties, such as ultrahigh confinement and electrical/chemical tunability, graphene plasmonic structures are widely studied. More importantly, the lifetime of SP modes in graphene can reach hundreds of optical cycles, which potentially circumvents one of the major bottlenecks faced by noble-metal plasmonics [2,3]. The graphene surface plasmon polariton has been verified by both infrared transmission spectroscopy and scanning near-field optical microscopy in real-space [4,5]. In order to achieve efficient light–plasmon coupling, Ju *et al.* explored plasmon excitations by engineering graphene film into microribbon arrays, and found that graphene plasmon resonance peak can be tuned over

a broad terahertz frequency range by changing microribbon width and *in situ* electrostatic doping [6]. However, it is noteworthy that the single-layer graphene supports relatively low resonance frequency/magnitude dependence on carrier concentration. Thus, Yan *et al.* fabricated graphene/insulator multi-layer stacks to effectively enhance the plasmonic magnitude, which is based on the Dirac fermions' carrier density scaling law [7]. Similarly, Zhang *et al.* used atomically thin hexagonal boron nitride films as spacers to enable strong plasmon coupling between adjacent graphene layers in the vertical dimension, which produces two times upshift of plasmonic resonance frequency and three times enhancement of its magnitude [8].

The surfaces of topological insulators (TIs) and graphene share similar low-energy electronic structures in which the conduction and valence bands touch at Dirac points. Dirac fermions also occur in the two-dimensional (2D) electron gas that

forms at the surface of TIs as a result of the strong spin-orbit interaction existing in the insulating bulk phase [9]. The spin-plasmons, collective modes originated from the transverse spin fluctuations caused by density fluctuations, have been theoretically predicted in TIs [10]. Pietro *et al.* reported the first experimental evidence of Dirac plasmon excitations in a TI (Bi_2Se_3 thin microribbon arrays) [11]. The plasmonic resonance in the TI is attributed to the bounded oscillation of Dirac quasiparticles of the conducting 2D edge state. According to theoretical studies [12], the plasmon in graphene will interact and hybridize strongly with itself by inserting a thin dielectric spacer between two layers of graphene to form a “metal-dielectric-metal” sandwich structure. Though the graphene and TI plasmons are considered to have the same origin [13], the experimental observation of hybridization between graphene plasmon and other Dirac plasmons has not been reported.

In this work, we fabricated a new graphene- Bi_2Te_3 heterostructure by growing Bi_2Te_3 on the graphene template. With the help of silicon gratings underneath the heterostructure, the normal incident light can successfully excite the plasmon resonance in the graphene- Bi_2Te_3 heterostructure [Fig. 1(a)]. It is interesting to find that the extinction spectra of the graphene- Bi_2Te_3 heterostructure has shown $3 \times$ greater magnitude of that of the graphene, which is attributed the plasmon coupling between the plasmon at the graphene surface and the top surface of the Bi_2Te_3 thin film. Moreover, the extinction peak of the plasmonic resonance of the graphene- Bi_2Te_3 heterostructure can be easily tuned in a broad terahertz (THz) frequency range by varying grating periods just like what happens in the graphene film. Since plasmon in graphene and plasmon in Bi_2Te_3 share a similar origin, the study of the hybridization between them will stimulate the interest to study variant plasmonic heterostructures and trigger new terahertz device applications.

2. RESULTS AND DISCUSSION

Bi_2Te_3 is a small bandgap (~ 0.145 eV) material with rhombohedral crystal structure, in which a sequence of Te-Bi-Te-Bi-Te along the *c*-axis is followed. Each of the smallest vertically repeated units forms one quintuple layer (QL). It is covalently bonded within the QLs, while attached together via van der Waals force between the QLs. In the *x*-*y* plane, Bi_2Te_3 shares a similar hexagonal lattice with graphene. The periodicity of Bi_2Te_3 along graphene carbon atoms is 4.38 Å, and the length of graphene C-C bond is 1.42 Å. Thus, the lattice mismatch between Bi_2Te_3 and graphene is 2.7% (0.12 Å), which is ideal for van der Waals epitaxial growth [Fig. 1(b)] [14–17]. This work utilizes the chemical vapor deposition (CVD) method to fabricate the graphene- Bi_2Te_3 plasmonic heterostructure. First, monolayer graphene film was grown on copper substrates. Then, the Bi_2Te_3 nanocrystals were deposited on the graphene film. Subsequently, they were transferred onto silicon grating substrates with the help of a thin poly-(methyl methacrylate) (PMMA) layer. Finally, the PMMA layer was removed via thermal annealing in the vacuum.

The scanning electron microscopy (SEM) images of graphene- Bi_2Te_3 heterostructure films with different thicknesses are shown in Figs. 2(a) and 2(b). The reaction times for

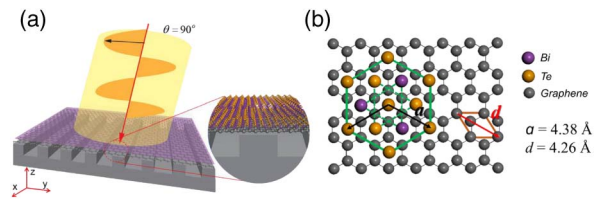


Fig. 1. Schemes showing (a) the graphene- Bi_2Te_3 heterostructure on the silicon diffraction grating and (b) lattice mismatch between graphene and Bi_2Te_3 .

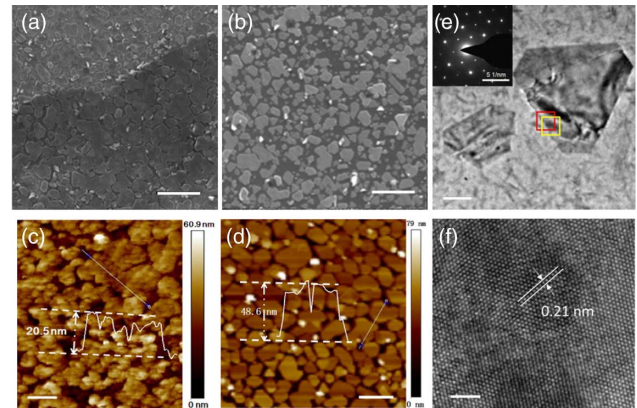


Fig. 2. Characterizations of the graphene- Bi_2Te_3 heterostructure. (a),(b) SEM images and (c),(d) AFM images of graphene- Bi_2Te_3 heterostructures with different Bi_2Te_3 thicknesses. The Bi_2Te_3 thicknesses in (a) and (c) are around 20 nm; in (b) and (d) are around 50 nm. Scale bars in (a) and (b) are 2 μm . Scale bars in (c) and (d) are 1 μm . (e) TEM image of the graphene- Bi_2Te_3 heterostructure. The inset of SAED pattern was taken at the red square area in the TEM image. Scale bar is 1 μm . (f) HRTEM images taken at the yellow square area in TEM image [Fig. 2(e)]. Scale bar is 2 nm.

growing Bi_2Te_3 samples shown in Figs. 2(a) and 2(b) are about 30 min and 60 min, respectively. The direct consequence of the deposition times is the variation in the Bi_2Te_3 thickness. As revealed in the atomic force microscopy (AFM) image [Figs. 2(c) and 2(d)], the thicknesses of Bi_2Te_3 in the heterostructure shown in Figs. 2(a) and 2(b) are 20 and 50 nm, respectively. The microstructure of the graphene- Bi_2Te_3 heterostructure film was further characterized by transmission electron microscopy (TEM) [Fig. 2(e)]. Both graphene and Bi_2Te_3 nanocrystals are revealed, in which the latter shows a quasihexagonal shape. The regular shape and sharp edges indicate an excellent crystallinity of Bi_2Te_3 [18]. The selected area electron diffraction (SAED) pattern [inset of Fig. 2(e)] exhibits a clear hexagonal symmetry, which can be indexed to along $[001]$ zone axis of graphene- Bi_2Te_3 . This further confirms the single crystalline nature of Bi_2Te_3 . The atomic structure of Bi_2Te_3 was characterized using high-resolution transmission electron microscopy (HRTEM) at 200 keV. Figure 2(f) clearly resolves the hexagonal lattice fringes. In particular, the lattice fringes are structurally uniform with a spacing of 0.21 nm. It is in good agreement with that of the $(11\bar{2}0)$ planes of the rhombohedral phase of Bi_2Te_3 [19].

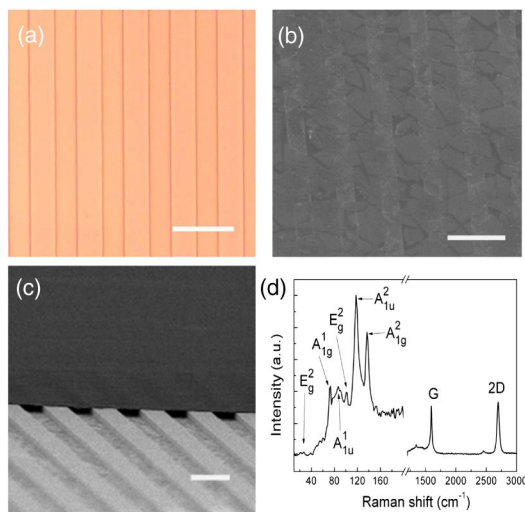


Fig. 3. Fabrication of graphene-Bi₂Te₃ plasmonic devices. (a) Optical microscope image of the silicon grating. Scale bar is 10 μm. (b) SEM image showing the graphene-Bi₂Te₃ heterostructure on the Si grating. Scale bar is 10 μm. (c) Tilted SEM image showing the graphene-Bi₂Te₃ heterostructure on a 2 μm deep silicon grating. Scale bar is 5 μm. (d) Raman spectrum of the graphene-Bi₂Te₃ heterostructure measured at 633 nm excitation.

One-dimensional gratings with the different periods (i.e., 4, 8, 12, and 16 μm) were fabricated with intrinsic silicon. Figure 3(a) shows an optical microscope image of a silicon grating with a period of 8 μm. After the wet transfer, PMMA-supported graphene and graphene-Bi₂Te₃ films are very well suspended on silicon gratings. The frames of the gratings have been revealed in the SEM image in Fig. 3(b). A clear SEM snapshot was taken from a tilted angle in Fig. 3(c). In order to avoid the mechanical damage made to graphene from solvents, high temperature annealing rather than acetone rinsing was used to remove the PMMA layer. In this way, silicon grating supported graphene and graphene-Bi₂Te₃ films are ready for spectroscopy measurements. Raman spectra were measured at room temperature with the excitation of a 633 nm laser. Sample damage is avoided by controlling the power below 0.5 mW. Figure 3(d) shows a typical Raman spectrum from 20 to 3000 cm⁻¹, which covers the interested spectrum ranges of both the TI and graphene. In the low-frequency range, the Raman spectrum exhibits five characteristic of Bi₂Te₃ crystal at 39, 69, 92, 101, 117, and 137 cm⁻¹, which correspond to the E_g^1 , A_{1g}^1 , A_{1u}^1 , E_g^2 , A_{1u}^2 , and A_{1g}^2 vibrational modes of single-crystalline Bi₂Te₃, respectively. At the same time, two characteristic peaks of graphene are observed at 1598 cm⁻¹ (G band) and 2698 cm⁻¹ (2D band). Compared with the Raman spectrum of monolayer graphene, it is interesting to observe the blueshift of the G band and significant intensity reduction of the 2D band in the graphene-Bi₂Te₃ heterostructure. This is also an indication of the doping effect on the graphene film [20].

The plasmon resonance in the graphene-Bi₂Te₃ heterostructure was studied using Fourier transform infrared (FTIR) spectroscopy. The extinction spectra of graphene and graphene-Bi₂Te₃ on various periods were shown as solid lines in Figs. 4(a) and 4(b). It is found that the plasmon resonance

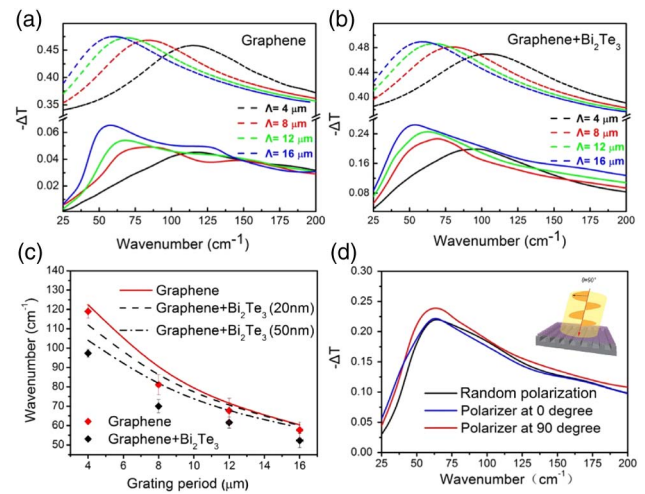


Fig. 4. Experimental and simulated spectra of the graphene and graphene-Bi₂Te₃ heterostructures. The experimental extinction spectra of (a) graphene film and (b) graphene-Bi₂Te₃ on silicon gratings with different periods, where incident light is vertically polarized to the grating axis. (c) Simulated frequency shift of graphene film (red line) and graphene-Bi₂Te₃ heterostructure (black dashed line) with various Si grating periods. (d) The extinction spectra of graphene-Bi₂Te₃ on the Si grating with polarized incident infrared light. Polarizer at 90 deg refers to the polarization perpendicular to the grating (red trace) and polarizer at 0 deg refers to the polarization parallel to the grating (blue).

peaks for both graphene and graphene-Bi₂Te₃ heterostructures shift to lower wavenumbers when the grating periodicity is reduced. In particular, the resonance peak shifts from 57.7 to 118.9 cm⁻¹ when the grating period changes from 16 to 4 μm for graphene [Fig. 4(a)]. In the graphene-Bi₂Te₃ case, the resonance peak shifts from 52.3 to 97.4 cm⁻¹ when the grating period changes from 16 to 4 μm [Fig. 4(b)]. In comparison, the fundamental mode plasmon resonance peak of the graphene-Bi₂Te₃ heterostructure blueshifts by 21.5 cm⁻¹ than that of graphene (on a 4 μm grating). It has also been noticed that the resonance tuning range of the graphene-Bi₂Te₃ is smaller than that of the graphene alone. This is caused by the addition of the more dielectric Bi₂Te₃ layer on the top of graphene. Moreover, the resonance of graphene-Bi₂Te₃ under similar incident conditions is enhanced by more than three times. This significant change can be concluded by several reasons: first, the additional Bi₂Te₃ layer enhances the light absorption in the heterostructure; second, the addition of the Bi₂Te₃ layer also introduces the plasmon coupling in graphene and Bi₂Te₃ layered structures. These characteristics attest to the strong plasmonic hybridizing effect between graphene and Bi₂Te₃.

To better understand the plasmonic resonance in graphene-Bi₂Te₃ heterostructures, numerical simulation is performed. In the simulation, the dynamic conductivity of the graphene-Bi₂Te₃ film follows the Drude mode, like graphene [2]. Only the intraband contributions of the spin-plane wave vector for the graphene-Bi₂Te₃ heterostructure have been considered. The simulated extinction spectra of the graphene and graphene-Bi₂Te₃ heterostructures are shown as dashed lines in

Figs. 4(a) and 4(b). It is found that the resonance peak position of the graphene and graphene-Bi₂Te₃ heterostructures matches well with those in the experiment results. The resonant frequency in both the graphene and graphene-Bi₂Te₃ heterostructures increases as the period of the silicon grating decreases, which is consistent with the experimental results. Comparing Fig. 4(a) with Fig. 4(b), it is also noticed that the tuning range of the graphene-Bi₂Te₃ heterostructure has been decreased from 61.2 cm⁻¹ (graphene) to 45.1 cm⁻¹ (graphene-Bi₂Te₃ heterostructure). This is attributed to the increase of dielectric constants in the graphene-Bi₂Te₃ heterostructure. It is also noticed that magnitude of the experimental graphene extinction spectra is much weaker than that of the simulated graphene extinction spectra, which could be explained by the possible defects in the real samples. However, the intensity weakening in the graphene-Bi₂Te₃ heterostructure is less obvious than that in graphene, which indicates the robustness of the graphene-Bi₂Te₃ heterostructure.

In order to have a complete picture about grating-coupled plasmon resonance in the graphene-Bi₂Te₃ heterostructure, we plotted the plasmon resonance of different materials as a function of grating period in Fig. 4(c). The experimental data points were obtained by fitting the experimental spectra in Figs. 4(a) and 4(b) with Lorentzian function. Both simulation and experimental results confirmed that the plasmon resonance in the graphene-Bi₂Te₃ heterostructure can be effectively tuned by changing the grating period. While the period of the silicon grating is fixed, the extra Bi₂Te₃ layer on graphene will cause redshift in plasmon resonance due to the change of dielectric constant. It is interesting to see that thicker Bi₂Te₃ crystals on graphene induces further redshift of the resonance frequency.

Figure 4(d) depicts the extinction spectra ($-\Delta T$) of the graphene-Bi₂Te₃ heterostructure under randomly polarized and linearly polarized illuminations. Under randomly polarized illumination and 0° polarized illumination (polarization direction parallel to the gratings), both spectra (black line and blue line, respectively) have shown a broad bump with a slight peak at 63 cm⁻¹ (~1.89 THz). While, under 90° polarized illumination (polarization direction perpendicular to the gratings), the peak at 63 cm⁻¹ is much stronger than that under 0° polarized illumination. This is because the light perpendicular to the grating axis ($\theta = 90^\circ$) can excite bounded electron oscillation [11].

3. EXPERIMENTAL RESULTS

A. Material Synthesis

Graphene films were grown on 25 μm thick copper foils (Alfa Aesar, item no. 13382) in a typical CVD system and transferred onto the silicon grating. The graphene film is p-doped as a mixed solution of FeCl₃ and HCl was used to etch away copper during the transferring process. In order to maintain the integrity of the graphene-Bi₂Te₃ heterostructures, Bi₂Te₃ nanoplatelets were epitaxially grown on the transferred graphene film on silicon gratings by the physical vapor deposition method in a separate tube furnace. Specifically, high purity Bi₂Te₃ powder (Alfa Aesar, purity: 99.999%) and silicon grating substrate with graphene were placed in the center facing downstream of the furnace, respectively. Then the furnace was heated up to 500°C

and maintained for 90–300 s with argon (with a gas flow rate of 100 sccm) as carrier and protective gas to transport Bi₂Te₃ vapor onto the graphene film. Then the furnace was cooled down naturally to room temperature.

B. Material Characterizations

The morphologies and microstructures of the silicon grating and graphene-Bi₂Te₃ heterostructure were investigated by SEM (FEI Quanta 200 FEG, acceleration voltage: 5–30 kV) and TEM (FEI Tecnai F30, acceleration voltage: 200 kV). Raman spectra were recorded by a micro-Raman system (Horiba JobinYvon, HR800) with an excitation wavelength of 633 nm. The laser spot of the Raman system is focused to <2 μm with ×100 object lens. A Bruker Vertex 80 V FTIR system covering the far-IR (40–700 cm⁻¹) wavelength range was used to investigate the transmission of the graphene-Bi₂Te₃ heterostructure. As for the far-IR characterizations, a liquid nitrogen cooled mercury-cadmium-telluride detector and a far-IR deuterated triglycine sulfate detector were used in conjunction with potassium bromide and polyethylene terephthalate beam splitters, respectively. The reference used in the spectroscopy measurement is the silicon grating without the graphene and TI layer.

C. Fabrication of Silicon Grating

Standard semiconductor fabrication processes were used to fabricate the grating on an intrinsic silicon wafer. UV lithography was applied to define the grating pattern following with dry etching to obtain the gratings.

D. Numerical Simulation

All the numerical simulations were carried out with Lumerical FDTD. Periodic boundary conditions were used along the x-axis and perfect matched layers were used along the z-axis. Linearly polarized light was normally incident on the structures. The refractive index of Si was set to be 3.42. The conductivity of single-layer graphene was calculated with Kubo formula [21], where the chemical potential and scattering rate were set to be 0.5 and 0.005 eV, respectively, to match the experimental results. A layer of Bi₂Te₃ covers the graphene layer with complex refractive index $n = 8.1 + 2.6i$ [22].

4. CONCLUSION

In summary, we have successfully demonstrated a new robust graphene-Bi₂Te₃ heterostructure. This graphene-Bi₂Te₃ heterostructure has shown three times greater magnitude of that of the graphene due to higher light absorption and strong graphene and Bi₂Te₃ coupling. The resonance peak of the graphene-Bi₂Te₃ heterostructure has been proved to be tunable by changing the grating periodicities, theoretically and experimentally. This work opens up new possibilities for the applications of graphene-Bi₂Te₃ heterostructures in various terahertz photonic devices.

Funding. A*STAR Pharos Programme (152 70 00014, R-263-000-B91-305); National Research Foundation (NRF-CRP15-2015-03); National Natural Science Foundation of China (NSFC) (51222208, 51290273, 91433107);

Youth 973 Program (2015CB932700); Priority Academic Program Development of Jiangsu Higher Education Institutions (PAPD); Collaborative Innovation Center of Suzhou Nano Science and Technology; Australian Research Council (ARC) (DE120101569, DP140101501, FT150100450).

Acknowledgment. This research was also partially supported by the National Research Foundation, Prime Minister's Office, Singapore under its Competitive Research Program. This work was performed in part at the Melbourne Centre for Nanofabrication (MCN) in the Victorian Node of the Australian National Fabrication Facility (ANFF).

[†]These authors contributed equally to this work.

REFERENCES

1. Q. Bao and K. P. Loh, "Graphene photonics, plasmonics, and broadband optoelectronic devices," *ACS Nano* **6**, 3677–3694 (2012).
2. W. Gao, J. Shu, C. Qiu, and Q. Xu, "Excitation of plasmonic waves in graphene by guided-mode resonances," *ACS Nano* **6**, 7806–7813 (2012).
3. A. Grigorenko, M. Polini, and K. Novoselov, "Graphene plasmonics," *Nat. Photonics* **6**, 749–758 (2012).
4. Z. Fei, A. Rodin, G. Andreev, W. Bao, A. McLeod, M. Wagner, L. Zhang, Z. Zhao, M. Thiemens, and G. Dominguez, "Gate-tuning of graphene plasmons revealed by infrared nano-imaging," *Nature* **487**, 82–85 (2012).
5. H. Yan, T. Low, W. Zhu, Y. Wu, M. Freitag, X. Li, F. Guinea, P. Avouris, and F. Xia, "Damping pathways of mid-infrared plasmons in graphene nanostructures," *Nat. Photonics* **7**, 394–399 (2013).
6. L. Ju, B. Geng, J. Horng, C. Girit, M. Martin, Z. Hao, H. A. Bechtel, X. Liang, A. Zettl, and Y. R. Shen, "Graphene plasmonics for tunable terahertz metamaterials," *Nat. Nanotechnol.* **6**, 630–634 (2011).
7. H. Yan, X. Li, B. Chandra, G. Tulevski, Y. Wu, M. Freitag, W. Zhu, P. Avouris, and F. Xia, "Tunable infrared plasmonic devices using graphene/insulator stacks," *Nat. Nanotechnol.* **7**, 330–334 (2012).
8. K. Zhang, F. L. Yap, K. Li, C. T. Ng, L. J. Li, and K. P. Loh, "Large scale graphene/hexagonal boron nitride heterostructure for tunable plasmonics," *Adv. Funct. Mater.* **24**, 731–738 (2014).
9. J. Zhang, C. Triola, and E. Rossi, "Proximity effect in graphene-topological-insulator heterostructures," *Phys. Rev. Lett.* **112**, 096802 (2014).
10. S. Raghu, S. B. Chung, X.-L. Qi, and S.-C. Zhang, "Collective modes of a helical liquid," *Phys. Rev. Lett.* **104**, 116401 (2010).
11. P. Di Pietro, M. Ortolani, O. Limaj, A. Di Gaspare, V. Giliberti, F. Giorgianni, M. Brahlek, N. Bansal, N. Koirala, and S. Oh, "Observation of Dirac plasmons in a topological insulator," *Nat. Nanotechnol.* **8**, 556–560 (2013).
12. J. Christensen, A. Manjavacas, S. Thongrattanasiri, F. H. Koppens, and F. J. García de Abajo, "Graphene plasmon waveguiding and hybridization in individual and paired nanoribbons," *ACS Nano* **6**, 431–440 (2012).
13. W. Dang, H. Peng, H. Li, P. Wang, and Z. Liu, "Epitaxial heterostructures of ultrathin topological insulator nanoplate and graphene," *Nano Lett.* **10**, 2870–2876 (2010).
14. H. Qiao, J. Yuan, Z. Xu, C. Chen, S. Lin, Y. Wang, J. Song, Y. Liu, Q. Khan, H. Y. Hoh, C.-X. Pan, S. Li, and Q. Bao, "Broadband photodetectors based on graphene-Bi₂Te₃ heterostructure," *ACS Nano* **9**, 1886–1894 (2015).
15. H. Mu, Z. Wang, J. Yuan, S. Xiao, C. Chen, Y. Chen, Y. Chen, J. Song, Y. Wang, Y. Xue, H. Zhang, and Q. Bao, "Graphene-Bi₂Te₃ heterostructure as saturable absorber for short pulse generation," *ACS Photon.* **2**, 832–841 (2015).
16. S. Chen, L. Miao, X. Chen, Y. Chen, C. Zhao, S. Datta, Y. Li, Q. Bao, H. Zhang, Y. Liu, S. Wen, and D. Fan, "Few-layer topological insulator for all-optical signal processing using the nonlinear Kerr effect," *Adv. Opt. Mater.* **3**, 1769–1778 (2015).
17. Y. L. Chen, Z. K. Liu, J. G. Analytis, J.-H. Chu, H. J. Zhang, B. H. Yan, S.-K. Mo, R. G. Moore, D. H. Lu, and I. R. Fisher, "Single Dirac cone topological surface state and unusual thermoelectric property of compounds from a new topological insulator family," *Phys. Rev. Lett.* **105**, 266401 (2010).
18. Y. Xu, Z. Ren, W. Ren, G. Cao, K. Deng, and Y. Zhong, "Raman spectroscopy of two-dimensional Bi₂Te₃Se_{3-x} platelets produced by solvothermal method," *Mater. Lett.* **62**, 4273–4276 (2008).
19. C. Wang, X. Zhu, L. Nilsson, J. Wen, G. Wang, X. Shan, Q. Zhang, S. Zhang, J. Jia, and Q. Xue, "In situ Raman spectroscopy of topological insulator Bi₂Te₃ films with varying thickness," *Nano Res.* **6**, 688–692 (2013).
20. Y. Jiang, Y. Y. Sun, M. Chen, Y. Wang, Z. Li, C. Song, K. He, L. Wang, X. Chen, Q.-K. Xue, X. Ma, and S. B. Zhang, "Fermi-level tuning of epitaxial Sb₂Te₃ thin films on graphene by regulating intrinsic defects and substrate transfer doping," *Phys. Rev. Lett.* **108**, 066809 (2013).
21. G. W. Hanson, "Dyadic green's functions and guided surface waves for a surface conductivity model of graphene," *J. Appl. Phys.* **103**, 064302 (2013).
22. A. Zimmer, N. Stein, L. Johann, S. Van Gils, H. Terryn, E. Stijns, and C. Boulanger, "Infrared and visible dielectric function of electroplated Bi_{2-x}Te_{3+x} films determined by spectroscopic ellipsometry," *J. Electrochem. Soc.* **152**, G772–G777 (2005).

**Chapter 6: Efficient Excitation of Multiple Plasmonic
Modes on Three-dimensional Graphene: An Unexplored
Dimension**

Declaration for Thesis Chapter 6

Declaration by candidate

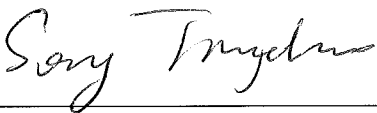
In the case of Chapter 6, the nature and extent of my contribution to the work was the following:

Nature of contribution	Extent of Contribution (%)
Key ideas, experimental works, analysis of results, writing up	50

The following co-authors contributed to the work. If co-authors are students at Monash University, the extent of their contribution in percentage terms must be stated:

Name	Nature of contribution	Extent of contribution (%) for student co-authors only
Lei Zhang	Simulation works, analysis of results, writing up	
Yunzhou Xue	Experimental works	
Steve Qing Yang Wu	Experimental works	
Fang Xia	Experimental works	
Ah Bian Chew	Experimental works	
Yu Lin Zhong	Experimental works	
Yupeng Zhang	Experimental works	
Jinghua Teng	Analysis of results	
Malin Premaratne	Analysis of results	
Cheng-Wei Qiu	Analysis of results	
Qiaoliang Bao*	Key ideas, analysis of results, writing up	Supervisor

The undersigned hereby certify that the above declaration correctly reflects the nature and extent of the candidate's and co-authors' contributions to this work*.

Candidate's Signature		Date: 16/09/2016
Main Supervisor's Signature		Date: 16/09/2016

Efficient Excitation of Multiple Plasmonic Modes on Three-Dimensional Graphene: An Unexplored Dimension

Jingchao Song,^{†,#} Lei Zhang,^{‡,#} Yunzhou Xue,^{†,‡,#} Qing Yang Steve Wu,[§] Fang Xia,^{||} Chao Zhang,[¶] Yu-Lin Zhong,[†] Yupeng Zhang,[†] Jinghua Teng,[§] Malin Premaratne,[□] Cheng-Wei Qiu,^{*,‡} and Qiaoliang Bao^{*,‡,†}

[†]Department of Materials Science and Engineering and [□]Department of Electrical and Computer Systems Engineering, Monash University, Wellington Road, Clayton, Victoria 3800, Australia

[‡]Department of Electrical and Computer Engineering, National University of Singapore, Singapore 117583, Singapore

[‡]Institute of Functional Nano and Soft Materials (FUNSOM), Jiangsu Key Laboratory for Carbon-Based Functional Materials and Devices, Collaborative Innovation Center of Suzhou Nano Science and Technology, Soochow University, Suzhou 215123, People's Republic of China

[§]Institute of Materials Research and Engineering, Agency for Science, Technology and Research (A*STAR), Singapore 138634, Singapore

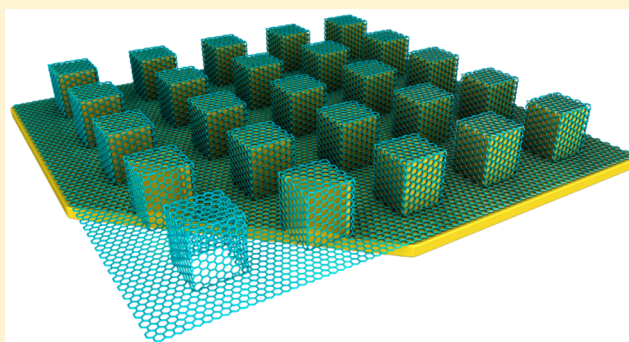
^{||}School of Engineering and Information Technology, Murdoch University, Murdoch, Western Australia 6150, Australia

[¶]School of Physics, University of Wollongong, Wollongong, New South Wales 2552, Australia

Supporting Information

ABSTRACT: Graphene is a typical two-dimensional (2D) allotrope form of carbon. Excellent optical and electric properties of graphene, such as broadband absorption and high mobility of carriers, promise prosperous applications in optic and optoelectronic devices. However, flat graphene structures (either graphene film on a structural substrate or structural graphene) hardly support efficient excitation of high-order plasmonic modes, which results in a serious deficiency in realizing efficient light–matter interaction in graphene-based devices. Here, by configuring the flat graphene into complex three-dimensional (3D) pillars, strong high-order plasmonic modes were observed and verified numerically and experimentally. It is found that, despite the influence of geometry and material parameters on resonance, the excitation efficiency of high-order modes is highly dependent on the graphene on the sidewall of pillars. Therefore, the proposed 3D graphene structures not only retain the merits of 2D materials but also introduce a new dimension to control the light–matter interaction. In addition, the fabrication technique in this work can be readily applied to other 2D materials with various geometric shapes. It is believed that the proposed 3D form of 2D materials will ignite a plethora of unprecedented designs and applications in THz communication such as THz pulse generators, modulators, detectors, and spectrometers.

KEYWORDS: graphene pillars, sidewall thickness, high-order modes, plasmon, THz



Graphene, a two-dimensional (2D) form of carbon allotrope, has shown excellent electrical and optoelectronic properties,^{1–3} which resulted in many practical applications such as optical modulators,⁴ plasmonic devices,⁵ saturable absorbers,⁶ and broadband photodetectors.^{7–9} Due to its zero-band-gap nature, graphene has obtained relatively high Dirac charge conductivity,¹⁰ large mode confinement,^{11–13} and chemical/electrical tunability.^{11,14} As a consequence, graphene is able to support highly localized plasmon resonance (LPR) modes, which makes it possible to observe stronger light–matter interactions in graphene-based structures. Specifically, graphene has boosted plasmon research in the terahertz (THz)

range^{15,16} and led to a variety of practical applications in THz pulse generators,^{17–19} modulators,^{11,20–22} photodetectors,²³ spectroscopy,²⁴ imaging,^{24,25} and telecommunications.^{26,27}

To obtain excellent optical and electrical properties based on graphene plasmonic resonances, various flat graphene structures have been proposed and studied, as shown in Figure 1a–c, such as graphene films,²⁶ graphene hole arrays,²⁸ graphene patches,²⁹ and graphene photonic crystal structures.³⁰ However, only the fundamental mode is strongly supported by the

Received: August 3, 2016

Published: September 16, 2016

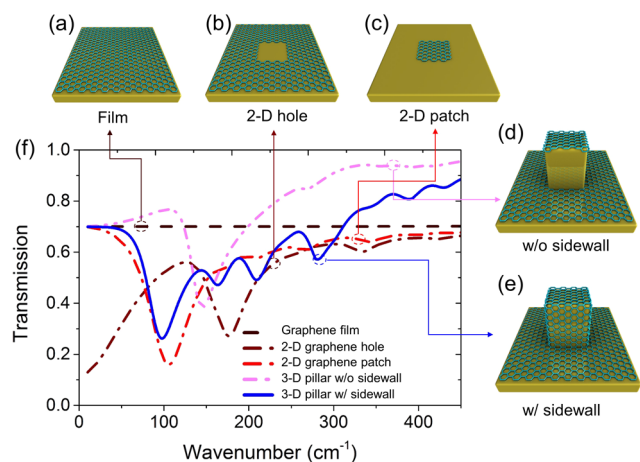


Figure 1. Comparison of transmission from a graphene film with 2D and 3D profiles: (a) graphene thin film covering a flat silicon substrate, (b) graphene thin film with square-shaped holes, (c) square graphene patches, (d) combination of graphene film with square holes and patterned graphene square patches on a silicon pillar (graphene pillar without sidewalls), (e) fully graphene-wrapped silicon pillar, (f) comparison of transmission spectra among different structures.

structural graphene, as shown in Figure 1f. In order to further enhance the light–matter interaction, multilayer stacking of graphene and an insulator has been employed.^{31,32} Nevertheless, most flat graphene structures (either graphene film on a structural substrate, structural graphene, or multilayer graphene stacking) hardly support efficient excitation of higher order plasmonic modes, which results in a limited light–matter interaction process in graphene-based devices.

In this work, a new dimension is proposed and studied based on a three-dimensional (3D) form of 2D graphene structures, which is fabricated by growing controllable graphene films on prefabricated silicon (Si) pillars. High-order plasmonic modes can thus be efficiently excited by a normally incident plane wave, which helps to surmount the obstacles occurring in flat

graphene structures. The underlying mechanism was investigated both numerically and experimentally. Significantly, it is found that the resonance features of high-order modes are highly dependent on the thickness and materials properties of graphene at the sidewall of pillars, despite the geometric dimensions. The proposed 3D graphene pillar structures not only retain the merits of 2D periodic structures^{11,33} but also introduce a new freedom (vertical sidewall of the structures^{34,35}) to control the light–matter interaction of 2D materials based devices, and the fabrication process can be readily extended to structures with various geometries based on other 2D materials. We believe that our work will definitely shine new light on the practical applications of 2D materials based optoelectronic devices.

RESULTS AND DISCUSSION

As shown in Figure 1f, the jejune response of flat graphene structures can only lead to strong excitation of the fundamental plasmonic mode. Similar mode properties also exist for a two-layer graphene structure consisting of a graphene patch and its complementary hole, as shown in Figure 1d. However, by introducing a graphene film at the sidewall of a Si pillar (Figure 1e), obvious multiple modes can be efficiently excited, which are barely achieved with other structures. Therefore, this indicates that the graphene at the sidewall plays a significant role in determining the resonance properties and provides a novel dimension to engineer light–graphene interactions.

Figure 2a shows the schematic of a 3D graphene pillar network wrapped on a Si pillar studied in this work. The graphene film was grown on Si pillar arrays predefined by photolithography, which affords a great flexibility to fabricate structures with arbitrary shapes. The thickness of the graphene layer can be well-controlled by a chemical vapor deposition (CVD) process. To confirm the graphene coverage on the real samples, scanning electron microscopy (SEM) and Raman characterizations were carried out. Figure 2b and c show the smooth silicon pillar surface before and after graphene growth,

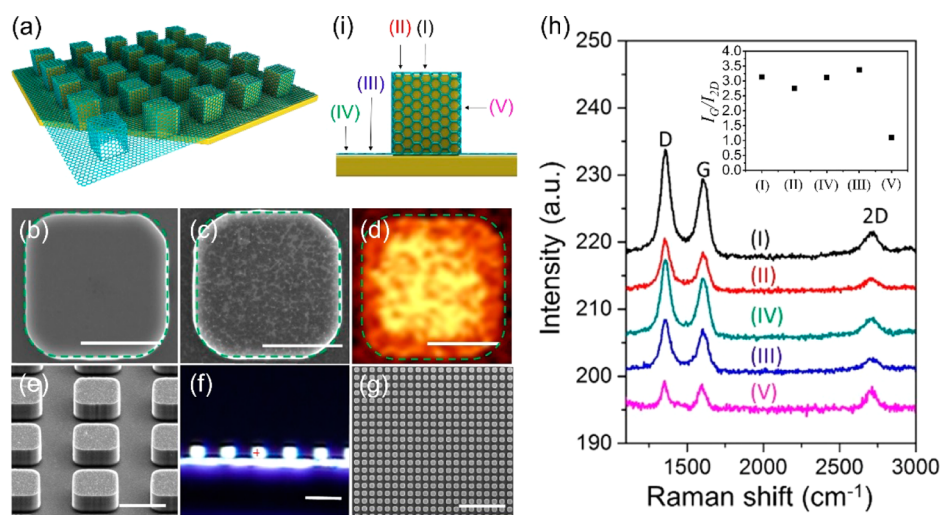


Figure 2. (a) Schematic of the 3D graphene pillar arrays. SEM images of a cubic pillar surface before (b) and after (c) graphene growth. (d) Graphene G peak Raman mapping of the graphene at the top surface of the pillar arrays. Scale bars for (b)–(d) are 5 μm . (e) SEM image of 3 \times 3 graphene pillars. Scale bar is 10 μm . (f) Cross-section optical image of the graphene pillars. Scale bar is 30 μm . (g) SEM image of a large-scale graphene pillar array. Scale bar is 200 μm . (h) Raman spectra collected from different regions of graphene pillars: top center (I), top edge (II), bottom edge (II), bottom center (IV), and sidewall (V) of the graphene pillar. Inset: Raman intensity ratio of the G mode over the 2D mode at different positions in (h). (i) Locations for measuring Raman signals.

respectively. Micrometer-sized grains of graphene crystal flakes can be clearly identified in Figure 2c, which suggest a grain-merging mechanism during the graphene growth stage. Raman mapping of the graphene G peak of the sample has confirmed that all the horizontal surfaces of the silicon pillar have been covered with graphene (Figure 2d). To examine the sidewall of the graphene pillar, an SEM image of the pillar sidewall was taken from a tilted angle (Figure 2e), and a cross-section sample was prepared by cleaving the graphene-wrapped silicon chip in dry ice (Figure 2f) for Raman characterization (Figure 2h). Furthermore, the graphene sample is continuous and uniform in a larger scale (Figure 2g). Raman spectra collected from five representative positions (top, bottom (I–IV) and sidewall (V)) are presented in Figure 2h. Three characteristic peaks of the graphene Raman spectra can be clearly identified, i.e., the D peak at 1352.2 cm^{-1} , the G peak at 1598.6 cm^{-1} , and the 2D peak at 2712 cm^{-1} . The intensity ratio between the G peak and the 2D peak from different positions suggested that the thickness of as-grown graphene is greater on the horizontal surfaces (the top surface and the bottom surface have about the same thickness), while thinner on the vertical surface (Figure 2h inset). The nonuniformity of the graphene layer is mainly caused by the nonhomogenous chemical vapor distribution, specifically the carbon source, along the substrate surface (the top and bottom surfaces are more likely to be exposed to the carbon source in comparison with the vertical surfaces).³⁶ Furthermore, by connecting the graphene at the top surface and the bottom surface of pillars with a multimeter, it is found that they are electrically shorted with each other via the graphene at the vertical sidewalls, which indicates a good conductivity and continuity of the graphene film. The mobility of thus grown graphene is measured to be $500\text{ cm}^2\text{ V}^{-1}\text{ s}^{-1}$, which agrees with the result measured in similar graphene materials.³⁷ Therefore, high-quality graphene film in a large scale is employed in our work.

To verify the abundant resonance modes on the graphene pillars, numerical transmission spectra and charge distributions are plotted in Figure 3. As shown in Figure 3a and b, multiple resonance dips can be readily observed from the transmission spectra. As the graphene layer number increases, the dips shift into the larger wavenumber region (Figure 3a). A similar trend can also be observed in the nonuniform graphene (Figure 3b), in which case a thicker graphene sidewall causes a blue-shift of the transmission dip. Furthermore, it is also noticed that the shape of the spectrum varies greatly for graphene at the sidewall with different thicknesses. For instance, for the case of 2/10 layers of the vertical/horizontal graphene, the third and the fourth resonance modes disappear into the background in comparison with the counterparts with a thicker sidewall graphene. To better identify and understand the origin of these modes, the charge distributions of the first four modes at the cross-section plane are plotted in Figure 3c–f. It is obvious that the number of charge nodes increases for higher orders. Although the charge distributions of the first and the second modes have some similarities, their dependence on the thickness of graphene differs greatly. The first and the third modes are highly dependent on the top surface of the graphene pillar, while the second mode is majorly supported by the sidewalls, and the fourth mode is supported by the complete pillar structure as a whole. Since higher order modes have more nodes on the sidewall of the graphene pillar than the lower order modes, they, especially the fourth mode, have shown distinct height-dependent resonance features in the trans-

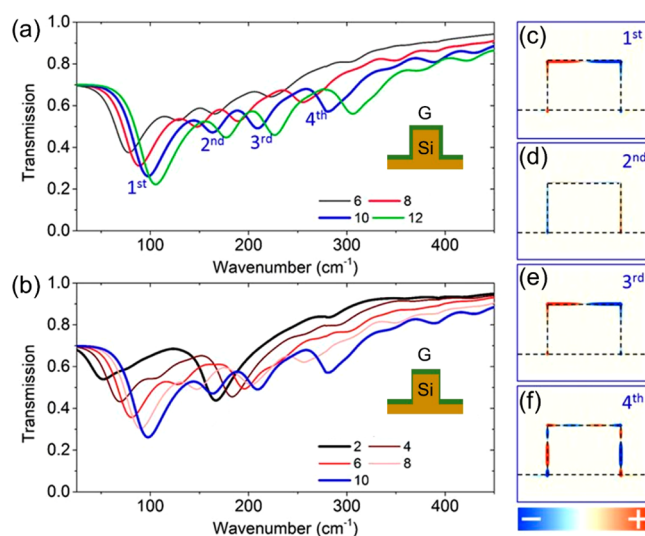


Figure 3. Dependence of plasmonic modes on the thickness of graphene at horizontal and vertical surfaces. (a) Simulated transmission of a cubic pillar array wrapped by uniform graphene at different graphene thicknesses (6, 8, 10, 12 layers). Inset: Side cross-section view of a uniform graphene pillar on a silicon substrate. (b) Simulated transmission of a cubic pillar array wrapped by nonuniform graphene, where graphene sidewall thickness is 2, 4, 6, 8, or 10 layers, while the horizontal graphene film remains 10 layers. Inset: Side cross-section view of a nonuniform graphene pillar on a silicon substrate. (c–f) Simulated charge distribution of a graphene pillar for the first four modes in the cross-section plane. The color bar is applicable to all the charge distributions. The geometry parameters are $W = 6.5\ \mu\text{m}$, $H = 4.0\ \mu\text{m}$, and $P = 10.5\ \mu\text{m}$, while the Fermi energy and scattering rate of graphene are set at 0.2 and 0.001 eV, respectively. The refractive index of Si is set at 3.42.

mission spectra shown in Figure S1. Our graphene pillar resonance model is similar to that of the hollow silver pillars in previous research,³⁸ in which a hexapolar mode on the sidewall of the silver pillar was attributed to the resonant absorption. Here, specifically, the power flow penetrates through the graphene sidewall at the position of zero net charge and then exits at the bottom, encircling the charge like a vortex. The mode energy will gradually dissipate through the graphene absorption and radiative scattering of the pillars.

However, due to the practical imperfections, resonant properties of plasmonic modes become complex in the experiment. Although the first mode is still robust (blue line in Figure 4a), the position of higher order modes deviates from the simulated result (red line calculated with a uniform graphene film in Figure 4a). In order to match the dip positions of the first mode between experiment and simulation, by retaining the horizontal surface at 10 layers while reducing the thickness of graphene at the sidewall at 4 layers, the simulated transmission (green line) tends to approach the experimental spectrum. Importantly, it is observed that some modes become invisible in the experiment. This could be attributed to the unintentional decay channels introduced during the growth process, such as point defects and residue impurity. Due to the increased decay rate, the spectrum becomes shallower and broader, which is well verified in our simulations (Figure S2). Therefore, the scattering rate has been further increased to 2 meV for better matching of the first two modes with experimental counterparts (black and blue lines in Figure 4a). These results indicate that the excitation efficiency of higher

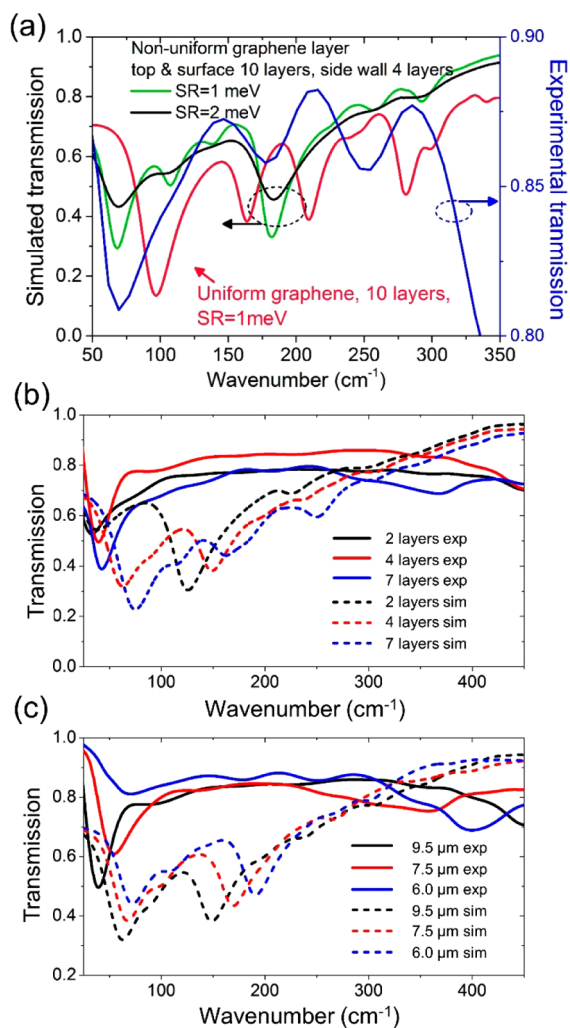


Figure 4. (a) Comparison of experimental and simulated transmission spectra (with width, spacing, and depth equal to 9.5, 4, and 4 μm , respectively, and Fermi energy $E_f = 0.2$ eV). (b) Comparison of experimental and simulation transmission spectra of graphene pillar arrays with different graphene sidewall (vertical) thicknesses (2, 4, and 7 layers) and the fixed geometry sizes and graphene thickness at horizontal surfaces (~ 10 layers). (c) Comparison of experimental and simulation transmission spectra of graphene pillar arrays with different widths (9.5, 7.5, and 6.0 μm) and fixed spacing (4 μm), depth (4 μm), and graphene thickness ($\sim 4/10$ layers at vertical/horizontal surfaces). In (b) and (c), the solid lines are experimental results and dashed lines are simulation results.

order modes is very sensitive to the thickness of graphene at the sidewall and, especially, the decay rate, which should be carefully reduced by improving the quality of the graphene samples.

To further study the spectrum dip shift caused by the graphene thickness on the sidewall, samples with the same geometry parameters and horizontal graphene thickness but with differentiated vertical graphene thickness were prepared utilizing the chemical vapor dynamics in the CVD furnace. In practice, the chemical vapor environment varies spatially. It is found that the graphene growth on the sidewalls relies more on the chemical vapor environment than the horizontal surfaces.³⁶ Therefore, a series of graphene films with the same horizontal graphene thickness but varied thickness at the sidewall were grown by manipulating the sample placement location in the

furnace (Figure S3). The pillars covered by nonuniform graphene are further discussed by comparing the measured and simulated transmission spectra. By calculating the intensity ratio of Raman peaks, the thickness of graphene at a horizontal surface is around 10 layers ($I_G/I_{2D} \approx 3.0$), while the counterpart at the vertical surface increases from 2 layers, to 4 layers, to 7 layers (close assumption made from Raman I_G/I_{2D} ratio: $I_G/I_{2D} = 1.01, 1.31, 1.60$, respectively) (Figure S4).³⁹ Accordingly, the measured transmission dip shows a prominent shift to the larger wavenumbers from 30.8 cm^{-1} to 38.5 and 43.0 cm^{-1} , respectively (Figure 4b). A similar shift trend is observed in simulations. However, the dip positions of the three different samples are at 38.4, 63.9, and 75.7 cm^{-1} , respectively. The trend of blue-shift for both experiment and simulation matches well with each other, while more flat features at larger wavenumbers in the experiment could be attributed to a larger decay rate of real graphene sample, as discussed above.

Another key factor that can cause a large shift in the spectrum dip is the lateral pillar width. In order to verify the influence of the width, we first excluded the influence from the periodicity. As the working wavelength of interest is 25–100 μm , which is much larger than the periodicity in our sample ($P = 12$ μm), no diffraction effect exists in our samples according to the diffraction equation $\sin \theta_d = \sin \theta_i + m\lambda/P$, where θ_d and θ_i are diffraction and incidence angles, respectively, and λ is the wavelength. Also there is no pronounced resonant frequency shift observed when periodicity increases from 8.0 μm to 12.0 μm , especially for the first three modes (Figure S5), where the variation in transmission magnitude could be attributed to the pillar density change. As the graphene pillar width increases from 6.0 μm to 7.5 and 9.5 μm , the transmission dip shows a significant red shift from 69.4 cm^{-1} to 53.9 and 38.5 cm^{-1} , respectively, which shows the same trend as graphene nanoribbons.^{11,20,40,41} The same shift trend is also observed in the simulation (Figure 4c). However, the dip positions of the three different samples are at 70.3, 67.38, and 60.0 cm^{-1} , respectively. The small discrepancy in dip positions may result from either nonuniformity of graphene thickness or Fermi energy, or other defects in the used samples. In the frequency range of interest, the optical conductance can be described in a Drude form. Therefore, the resonance wavenumber of the graphene surface plasmon in an isolated pillar can be estimated with the formula $1/\lambda \approx \sqrt{n\alpha_0 E_F / 2\pi c \hbar W}$, where n is the mode number, α_0 is the fine-structure constant, c is the light speed in a vacuum, and \hbar is the reduced Planck constant.⁴² The frequencies of the plasmon modes are subject to the scaling laws.^{43,44} It has also been proved that the wavenumber of the first mode matches perfectly in the theoretical linear relation with $E_f^{1/2}$ and $1/W^{-1/2}$ (Figure S6). In addition, as an excellent active material, the optical response of graphene can be well tuned by varying the Fermi energy level (Figure S7) in addition to the decay rate.

CONCLUSION

In conclusion, we have fabricated a novel graphene pillar structure with controllable geometry parameters and thickness of graphene at both horizontal surfaces and the vertical sidewall. To the best of our knowledge, this is the first time that high-order plasmonic mode excitation can be efficiently excited on the graphene network. The underlying mechanism and parameter dependence of these modes have been discussed in detail. Besides the well-known width-dependence, it is

interesting to see that the graphene thickness at the pillar sidewalls plays an important role in determining the resonance modes. As the sidewall graphene thickness increases, an obvious blue-shift in dip position has been observed. In addition, the Fermi energy, decay rate, etc., also show a strong influence on resonance modes, which provides a feasible way to achieve a dynamic device based on graphene. Our approach to access higher order resonance modes is not limited to graphene but can also be applied to other highly doped 2D materials.^{45,46} In sum, this work contributes to the designing of more sophisticated plasmonic devices and metamaterials based on 2D materials and enables new ways of controlling terahertz, far-infrared, and visible radiation.

■ EXPERIMENTAL SECTION

To fabricate the complex graphene pillar structure, a standard silicon-based fabrication process accompanied by the CVD method was employed. First, the photolithography technique was used to transfer the arrayed patterns from a photolithographic mask (Figure S8a) onto the photoresist on the substrate (Figure S8b,c). With the hard mask protected substrate (Figure S8d), the reactive ion etching process was carried out under a chilled environment ($-110\text{ }^{\circ}\text{C}$) (Figure S8e). The cryogenic etching process effectively slows the isotropic chemical etching process and finally leads to a much better controlled etching process over the Bosch process.⁴⁷ After mask removal, the intrinsic silicon substrates were cleaned by sonication with acetone and 2-propanol. Subsequently, the substrate can be placed into a high-vacuum furnace chamber for graphene seed implantation and growth (Figure S8f). The chemical environment in the furnace finally ensures full coverage of the graphene layer on the silicon pillars. Specifically, in the CVD process for direct graphene growth, oxygen was used as an aid to activate the growth substrate in a temperature-elevated atmosphere.³⁷ Thus, high-quality graphene can be grown on the nucleation spots created in the activation stage. In this way, the direct graphene growth mechanism avoids the complex graphene transfer process.

Photolithography. The fabrication of silicon pillars began with transferring the designed array patterns to the intrinsic silicon wafers with direct write photolithography techniques. The photoresist solution (AZ1512) was applied to the wafer with an optimized two-step spin-coating program (500 rpm for 20 s, 3500 rpm for 2:30 min), resulting in a $\sim 1.5\text{ }\mu\text{m}$ thick photoresist layer. The wafers were subsequently baked at $110\text{ }^{\circ}\text{C}$ for 3 min, followed by exposure using an Intelligent Micro Patterning device (IMP SF-100 XPRESS) for 2.5 s. Then the photoresist was immersed in AZ726 solution for about 50 s and rinsed with DI water for developing.

Hard Mask Deposition. After developing the photoresist, the photoresist-covered silicon wafers were deposited with 5 nm Cr and 50 nm Al with an e-beam evaporator. The reason to use a hard mask instead of the photoresist is that the AZ series photoresist can be easily cracked at low temperatures, which would cause failure in transferring the patterns to create the 3D structured silicon.

Cryogenic Etching. The cryogenic-DRIE technique was selected to manufacture these silicon pillars, as it can provide much better sidewall profiles than the standard Bosch process in the designed dimensions.⁴⁷ In the cryogenic-DRIE step, the wafers were cooled to $-110\text{ }^{\circ}\text{C}$ by liquid nitrogen to slow the chemical reaction during the etching process, thus approaching isotropic etching with a high aspect ratio and smoother

sidewalls. The DRIE system employed is an Oxford PlasmaLab 100 ICP system. The overall processing pressure was set to 10 mTorr with a SF_6 flow rate of 60 sccm and O_2 flow rate of 8 sccm. The lower bias power (13.56 MHz) and upper source power (13.56 MHz) were set to 4 and 800 W, respectively. The depth of etching was controlled by the etching time, which varied from 3 to 5 min.

Direct Graphene Growth. The graphene-wrapped surfaces were fabricated by directly growing polycrystalline graphene on the patterned 3D intrinsic silicon substrate. To directly grow graphene on the silicon wafers, the patterned intrinsic silicon chips were directly placed in a quartz tube mounted in a high-temperature furnace ($1100\text{ }^{\circ}\text{C}$). First, the cleaned silicon chip was annealed at $800\text{ }^{\circ}\text{C}$ in an atmosphere environment to activate the nucleation spots. Then, the nucleate allocated surface was exposed to the mixed reaction gas flow ($\text{CH}_4\text{:H}_2\text{:Ar} = 14\text{:}50\text{:}65$ sccm) for 3 h. The graphene nanosheets were first formed as separated islands and subsequently connected with the neighboring graphene sheets to form a large-area covered graphene surface. As the back side of the silicon chip was treated with acid, there was no graphene signal being collected.

Raman Characterization. Raman spectrum and mapping measurements were performed using a confocal microscope system (WITec, alpha 300R) with a $100\times$ objective ($\text{NA} = 0.9$) in ambient conditions. A 532 nm laser was used to illuminate the graphene samples that were placed on a piezo crystal-controlled scanning stage. The spectra were collected using 600 line/mm grating with an integration time of up to 1 min.

SEM and AFM Characterization. The morphology of the silicon pillars and the topography of the covered graphene flakes were characterized by a dual-beam FIB-SEM (FEI Helios Nanolab 600) and atomic force microscopy (Bruker, Dimension Icon SPM) in the tapping mode, respectively.

FTIR Measurements. The Fourier transform infrared (FTIR) spectroscopy measurement was carried out with a vacuum Bruker 80v FTIR instrument with a deuterated triglycine sulfate detector. The samples were mounted on the sample holder in a vacuum environment. The spectra in the range of $30\text{--}700\text{ cm}^{-1}$ and $300\text{--}7000\text{ cm}^{-1}$ were collected. All the measurements were carried out at room temperature. All the background signals resulting from intrinsic silicon were subtracted before data analysis.

Numerical Simulation. All the numerical simulations were carried out with Lumerical FDTD. Periodic boundary conditions were used along the grating direction, and perfect matched layers were used along the z -axis. Linearly polarized light was normally incident on the structures. The refractive index of Si was set to 3.42. The conductivity of single-layer graphene was calculated with the Kubo formula,⁴⁸ where the chemical potential and scattering rate were selected to match the experimental results. The number of graphene layers also varies accordingly. Detailed parameter settings are listed in the main text.

■ ASSOCIATED CONTENT

Supporting Information

The Supporting Information is available free of charge on the ACS Publications website at DOI: [10.1021/acsp Photonics.6b00566](https://doi.org/10.1021/acsp Photonics.6b00566).

Simulations results of dependence of transmission of the graphene-wrapped pillar array on the height, scattering rate, periodicity, and Fermi energy of graphene pillars;

schematic of simultaneous CVD growth of graphene pillar samples; Raman spectra for horizontal and vertical graphene films; relationship fitting between wavenumber of first mode with $E_f^{1/2}$ and $1/W^{-1/2}$; schematic of the fabrication process (PDF)

AUTHOR INFORMATION

Corresponding Authors

*E-mail (C.-W. Qiu): eleqc@nus.edu.sg.

*E-mail (Q. L. Bao): qlbao@suda.edu.cn.

Author Contributions

[#]J. Song, L. Zhang, and Y. Xue contributed equally to this work.

Notes

The authors declare no competing financial interest.

ACKNOWLEDGMENTS

The authors acknowledge support from the Youth 973 Program (2015CB932700), the National Natural Science Foundation of China (Grant Nos. 91433107, 51222208, and 51290273), ARC (DE120101569, DP140101501, and FT150100450), the Collaborative Innovation Center of Suzhou Nano Science & Technology, and the Priority Academic Program Development of Jiangsu Higher Education Institutions. Y.X. acknowledges support from China Postdoctoral Science Foundation (2014M550303). L.Z. and C.-W.Q. acknowledge the financial support from the A*STAR Pharos Programme (Grant No. 152 70 00014, with Project No. R-263-000-B91-305). C.-W.Q. acknowledges support from the National Research Foundation, Prime Minister's Office, Singapore, under its Competitive Research Programme (CRP Award No. NRF-CRP15-2015-03). J. S. acknowledges the technical support from Dr. Sasikaran Kandasamy, Dr. Ricky Tjeung, and Mr. Dan Smith. This work was performed in part at the Melbourne Centre for Nanofabrication (MCN) in the Victorian Node of the Australian National Fabrication Facility (ANFF).

REFERENCES

- (1) Bao, Q.; Loh, K. P. Graphene Photonics, Plasmonics, and Broadband Optoelectronic Devices. *ACS Nano* **2012**, *6*, 3677–3694.
- (2) Geim, A. K.; Novoselov, K. S. The rise of graphene. *Nat. Mater.* **2007**, *6*, 183–191.
- (3) Novoselov, K. S.; Falko, V. I.; Colombo, L.; Gellert, P. R.; Schwab, M. G.; Kim, K. A roadmap for graphene. *Nature* **2012**, *490*, 192–200.
- (4) Liu, M.; Yin, X.; Ulin-Avila, E.; Geng, B.; Zentgraf, T.; Ju, L.; Wang, F.; Zhang, X. A graphene-based broadband optical modulator. *Nature* **2011**, *474*, 64–67.
- (5) Grigorenko, A. N.; Polini, M.; Novoselov, K. S. Graphene plasmonics. *Nat. Photonics* **2012**, *6*, 749–758.
- (6) Bao, Q.; Zhang, H.; Wang, Y.; Ni, Z.; Yan, Y.; Shen, Z. X.; Loh, K. P.; Tang, D. Y. Atomic-Layer Graphene as a Saturable Absorber for Ultrafast Pulsed Lasers. *Adv. Funct. Mater.* **2009**, *19*, 3077–3083.
- (7) Liu, C.-H.; Chang, Y.-C.; Norris, T. B.; Zhong, Z. Graphene photodetectors with ultra-broadband and high responsivity at room temperature. *Nat. Nanotechnol.* **2014**, *9*, 273–278.
- (8) Pospischil, A.; Humer, M.; Furchi, M. M.; Bachmann, D.; Guider, R.; Fromherz, T.; Mueller, T. CMOS-compatible graphene photodetector covering all optical communication bands. *Nat. Photonics* **2013**, *7*, 892–896.
- (9) Gan, X.; Shiue, R.-J.; Gao, Y.; Meric, I.; Heinz, T. F.; Shepard, K.; Hone, J.; Assefa, S.; Englund, D. Chip-integrated ultrafast graphene photodetector with high responsivity. *Nat. Photonics* **2013**, *7*, 883–887.
- (10) Takatsuka, Y.; Takahagi, K.; Sano, E.; Ryzhii, V.; Otsuji, T. Gain enhancement in graphene terahertz amplifiers with resonant structures. *J. Appl. Phys.* **2012**, *112*, 033103.
- (11) Ju, L.; Geng, B.; Horng, J.; Girit, C.; Martin, M.; Hao, Z.; Bechtel, H. A.; Liang, X.; Zettl, A.; Shen, Y. R.; Wang, F. Graphene plasmonics for tunable terahertz metamaterials. *Nat. Nanotechnol.* **2011**, *6*, 630–634.
- (12) Chen, J.; Badioli, M.; Alonso-Gonzalez, P.; Thongrattanasiri, S.; Huth, F.; Osmond, J.; Spasenovic, M.; Centeno, A.; Pesquera, A.; Godignon, P.; Elorza, A. Z.; Camara, N.; Garcia de Abajo, F. J.; Hillenbrand, R.; Koppens, F. H. Optical nano-imaging of gate-tunable graphene plasmons. *Nature* **2012**, *487*, 77–81.
- (13) Fei, Z.; Rodin, A. S.; Andreev, G. O.; Bao, W.; McLeod, A. S.; Wagner, M.; Zhang, L. M.; Zhao, Z.; Thiemens, M.; Dominguez, G.; Fogler, M. M.; Castro Neto, A. H.; Lau, C. N.; Keilmann, F.; Basov, D. N. Gate-tuning of graphene plasmons revealed by infrared nano-imaging. *Nature* **2012**, *487*, 82–85.
- (14) Schwierz, F. Graphene transistors. *Nat. Nanotechnol.* **2010**, *5*, 487–496.
- (15) Li, Z. Q.; Henriksen, E. A.; Jiang, Z.; Hao, Z.; Martin, M. C.; Kim, P.; Stormer, H. L.; Basov, D. N. Dirac charge dynamics in graphene by infrared spectroscopy. *Nat. Phys.* **2008**, *4*, 532–535.
- (16) Peres, N. M. R.; Stauber, T.; Castro Neto, A. H. The infrared conductivity of graphene on top of silicon oxide. *Europhys. Lett.* **2008**, *84*, 38002.
- (17) Prechtel, L.; Song, L.; Schuh, D.; Ajayan, P.; Wegscheider, W.; Holleitner, A. W. Time-resolved ultrafast photocurrents and terahertz generation in freely suspended graphene. *Nat. Commun.* **2012**, *3*, 646.
- (18) Ramakrishnan, G.; Chakkittakandy, R.; Planken, P. C. M. Terahertz generation from graphite. *Opt. Express* **2009**, *17*, 16092–16099.
- (19) Schmadel, D.; Jenkins, G. S.; Drew, H. D.; Proposal for a Graphene Plasmonic THz Emitter. 2013, arXiv:1311.1605. arXiv.org preprint archive. *arXiv preprint*
- (20) Wu, Y.; La-o-vorakiat, C.; Qiu, X.; Liu, J.; Deorani, P.; Banerjee, K.; Son, J.; Chen, Y.; Chia, E. E. M.; Yang, H. Graphene terahertz modulators by ionic liquid gating. *Adv. Mater.* **2015**, *27*, 1874–1879.
- (21) Rahm, M.; Li, J.-S.; Padilla, W. THz Wave Modulators: A Brief Review on Different Modulation Techniques. *J. Infrared, Millimeter, Terahertz Waves* **2013**, *34*, 1–27.
- (22) Sensale-Rodriguez, B.; Yan, R.; Kelly, M. M.; Fang, T.; Tahy, K.; Hwang, W. S.; Jena, D.; Liu, L.; Xing, H. G. Broadband graphene terahertz modulators enabled by intraband transitions. *Nat. Commun.* **2012**, *3*, 780.
- (23) Cai, X.; Sushkov, A. B.; Jadidi, M. M.; Nyakiti, L. O.; Myers-Ward, R. L.; Gaskill, D. K.; Murphy, T. E.; Fuhrer, M. S.; Drew, H. D. Antenna Enhanced Graphene THz Emitter and Detector. *Nano Lett.* **2015**, *15*, 5295–5301.
- (24) Tomaino, J. L.; Jameson, A. D.; Kevek, J. W.; Paul, M. J.; van der Zande, A. M.; Barton, R. A.; McEuen, P. L.; Minot, E. D.; Lee, Y.-S. Terahertz imaging and spectroscopy of large-area single-layer graphene. *Opt. Express* **2011**, *19*, 141–146.
- (25) Sensale-Rodriguez, B.; Rafique, S.; Yan, R.; Zhu, M.; Protasenko, V.; Jena, D.; Liu, L.; Xing, H. G. Terahertz imaging employing graphene modulator arrays. *Opt. Express* **2013**, *21*, 2324–2330.
- (26) Vicarelli, L.; Vitiello, M. S.; Coquillat, D.; Lombardo, A.; Ferrari, A. C.; Knap, W.; Polini, M.; Pellegrini, V.; Tredicucci, A. Graphene field-effect transistors as room-temperature terahertz detectors. *Nat. Mater.* **2012**, *11*, 865.
- (27) Kleine-Ostmann, T.; Nagatsuma, T. A Review on Terahertz Communications Research. *J. Infrared, Millimeter, Terahertz Waves* **2011**, *32*, 143.
- (28) Liu, P. Q.; Valmorra, F.; Maissen, C.; Faist, J. Electrically tunable anti-dot array terahertz plasmonic crystals exhibiting multi-band resonances. *Optica* **2015**, *2*, 135.
- (29) Llatser, I.; Kermers, C.; Cabellos-Aparicio, A.; Jornet, J. M.; Alarcon, E.; Chigrin, D. N. Graphene-based Nano-patch Antenna for Terahertz Radiation. *Photo. Nano. Fundam. Appl.* **2012**, *10*, 353–358.

- (30) Yeung, K. Y. M.; Chee, J.; Yoon, H.; Song, Y.; Kong, J.; Ham, D. Far-Infrared Graphene Plasmonic Crystals for Plasmonic Band Engineering. *Nano Lett.* **2014**, *14*, 2479–2484.
- (31) Yan, H.; Li, X.; Chandra, B.; Tulevski, G.; Wu, Y.; Freitag, M.; Zhu, W.; Avouris, P.; Xia, F. Tunable infrared plasmonic devices using graphene/insulator stacks. *Nat. Nanotechnol.* **2012**, *7*, 330–334.
- (32) Zhang, K.; Yap, F. L.; Li, K.; Ng, C. T.; Li, L. J.; Loh, K. P. Large Scale Graphene/Hexagonal Boron Nitride Heterostructure for Tunable Plasmonics. *Adv. Funct. Mater.* **2014**, *24*, 731–738.
- (33) Fang, Z.; Thongrattanasiri, S.; Schlather, A.; Liu, Z.; Ma, L.; Wang, Y.; Ajayan, P. M.; Nordlander, P.; Halas, N. J.; Javier Garcia de Abajo, F. Gated Tunability and Hybridization of Localized Plasmons in Nanostructured Graphene. *ACS Nano* **2013**, *7*, 2388–2395.
- (34) Nemilentsau, A. M.; Rotkin, S. V. Vertical Single-Wall Carbon Nanotube Forests as Plasmonic Heat Pipes. *ACS Nano* **2012**, *6*, 4298–4304.
- (35) Kim, Y.; Lee, S.; Lee, K.; Shim, S.; Kim, Y. K.; Lee, H. W.; Choi, D. Self-Assembled plasmonic Nanoparticles on Vertically Aligned Carbon Nanotube Electronodes via Thermal Evaporation. *ACS Appl. Mater. Interfaces* **2014**, *6*, 20423–20429.
- (36) Li, Z.; Zhang, W.; Fan, X.; Wu, P.; Zeng, C.; Li, Z.; Zhai, X.; Yang, J.; Hou, J. Graphene Thickness Control via Gas-Phase Dynamics in Chemical Vapor Deposition. *J. Phys. Chem. C* **2012**, *116*, 10557–10562.
- (37) Chen, J.; Wen, Y.; Guo, Y.; Wu, B.; Huang, L.; Xue, Y.; Geng, D.; Wang, D.; Yu, G.; Liu, Y. Oxygen-Aided Synthesis of Polycrystalline Graphene on Silicon Dioxide Substrates. *J. Am. Chem. Soc.* **2011**, *133*, 17548–17551.
- (38) Gu, Y.; Qin, F.; Yang, J. K. W.; Yeo, S. P.; Qiu, C.-W. Direct excitation of dark plasmonic resonances under visible light at normal incidence. *Nanoscale* **2014**, *6*, 2106.
- (39) Lin, Z.; Ye, X.; Han, J.; Chen, Q.; Fan, P.; Zhang, H.; Xie, D.; Zhu, H.; Zhong, M. Precise Control of the Number of Layers of Graphene by Picosecond Laser Thinning. *Sci. Rep.* **2015**, *5*, 11662.
- (40) Gao, W.; Su, J.; Qiu, C.; Xu, Q. Excitation of Plasmonic Waves in Graphene by Guided-Mode Resonances. *ACS Nano* **2012**, *6*, 7806–7813.
- (41) Bass, M.; Franken, P.; Ward, J.; Weinreich, G. Optical Rectification. *Phys. Rev. Lett.* **1962**, *9*, 446.
- (42) Nikitin, A. Yu.; Guinea, F.; Garcia-Vidal, F. J.; Martin-Moreno, L. Surface plasmon enhanced absorption and suppressed transmission in periodic arrays of graphene ribbons. *Phys. Rev. B: Condens. Matter Mater. Phys.* **2012**, *85*, 081405.
- (43) Javier Garcia de Abajo, F. Graphene Plasmonics: Challenges and Opportunities. *ACS Photonics* **2014**, *1*, 135–152.
- (44) Javier Garcia de Abajo, F. Multiple Excitation of Confined Graphene Plasmons by Single Free Electrons. *ACS Nano* **2013**, *7*, 11409–11419.
- (45) Wang, Y.; Ou, J. Z.; Chrimes, A. F.; Carey, B. J.; Daeneke, T.; Alsaif, M. M. Y. A.; Mortazavi, M.; Zhuiykov, S.; Medhekar, N.; Bhaskaran, M.; Friend, J. R.; Strano, M. S.; Kalantar-Zadeh, K. Plasmon Resonance of Highly Doped Two-Dimensional MoS₂. *Nano Lett.* **2015**, *15*, 883–890.
- (46) Alsaif, M. M. Y. A.; Latham, K.; Field, M. R.; Yao, D. D.; Medhekar, N. V.; Beane, G. A.; Kaner, R. B.; Russo, S. P.; Ou, J. Z.; Kalantar-Zadeh, K. Tunable Plasmon Resonances in Two-Dimensional Molybdenum Oxide Nanoflakes. *Adv. Mater.* **2014**, *26*, 3931–3937.
- (47) Walker, M. J. Comparison of Bosch and cryogenic processes for patterning high-aspect-ratio features in silicon. *Proc. SPIE* **2001**, *4407*, 89–99.
- (48) Hanson, G. W. Dyadic Green's functions and guided surface waves for a surface conductivity model of graphene. *J. Appl. Phys.* **2008**, *103*, 064302.

Supporting Information for

Efficient Excitation of Multiple Plasmonic Modes on Three-dimensional Graphen : An Unexplored Dimension

Jingchao Song,^{†,#} Lei Zhang,^{‡,#} Yunzhou Xue,^{†,‡,#} Qing Yang Steve Wu,[§] Fang Xia,^{||}
Chao Zhang,[#] Yu-Lin Zhong,[†] Yupeng Zhang,[†] Jinghua Teng,[§] Malin Premaratne,[∇]
Cheng-Wei Qiu,^{‡,*} Qiaoliang Bao^{‡,†,*}

[†]Department of Materials Science and Engineering, Monash University, Wellington Road, Clayton, Victoria 3800, Australia.

[‡]Department of Electrical and Computer Engineering, National University of Singapore
Singapore
Singapore 117583, Singapore,

[‡]Institute of Functional Nano and Soft Materials (FUNSOM), Jiangsu Key Laboratory for Carbon-Based Functional Materials and Devices, Collaborative Innovation Center of Suzhou Nano Science and Technology, Soochow University, Suzhou 215123, P. R. China

[§]Institute of Materials Research and Engineering, Agency for Science, Technology and Research (A*STAR), Singapore 138634, Singapore

^{||}School of Engineering and Information Technology, Murdoch University, Perth, WA 6150, Australia

[#]School of Engineering Physics, University of Wollongong, New South Wales 2552, Australia

[∇]Department of Electrical and Computer Systems Engineering, Monash University, Melbourne 3800, Australia

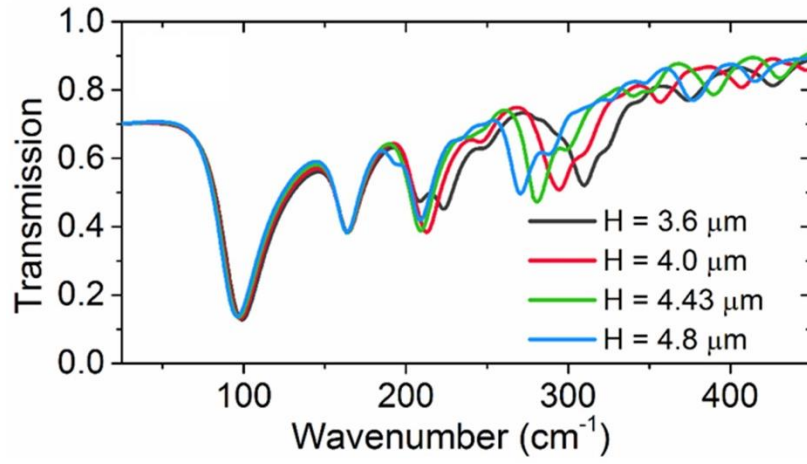


Figure S1. Dependence of transmission of the graphene wrapped pillar array on the height, where $P = 10.5 \mu\text{m}$ and $W = 6.46 \mu\text{m}$.

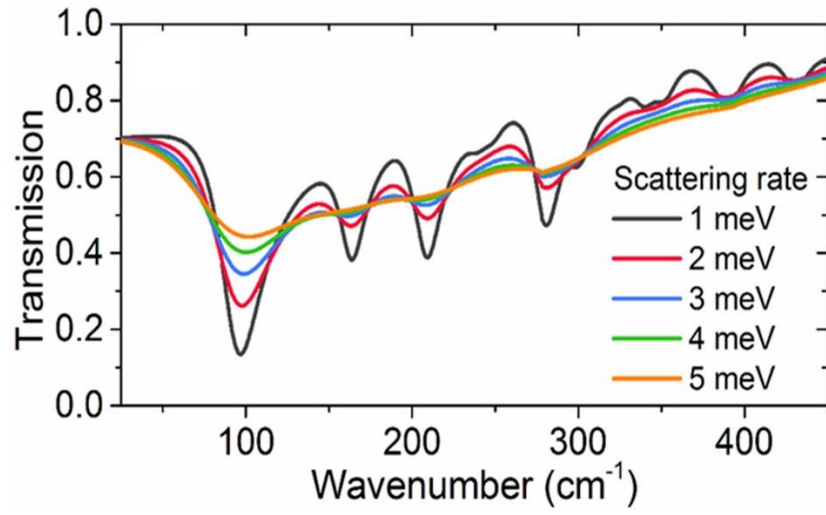


Figure S2. Dependence of transmission of the graphene wrapped pillar array on scattering rate of graphene.

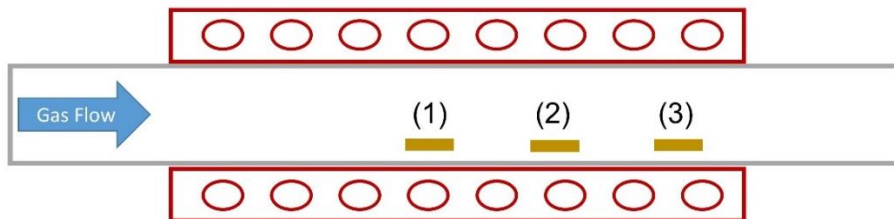


Figure S3. Schematic of the simultaneous CVD growth of graphene pillar samples. By placing the samples at different positions, (1), (2) and (3), graphene pillars with 2, 4 and 7 layers of sidewall thickness have been achieved, respectively.

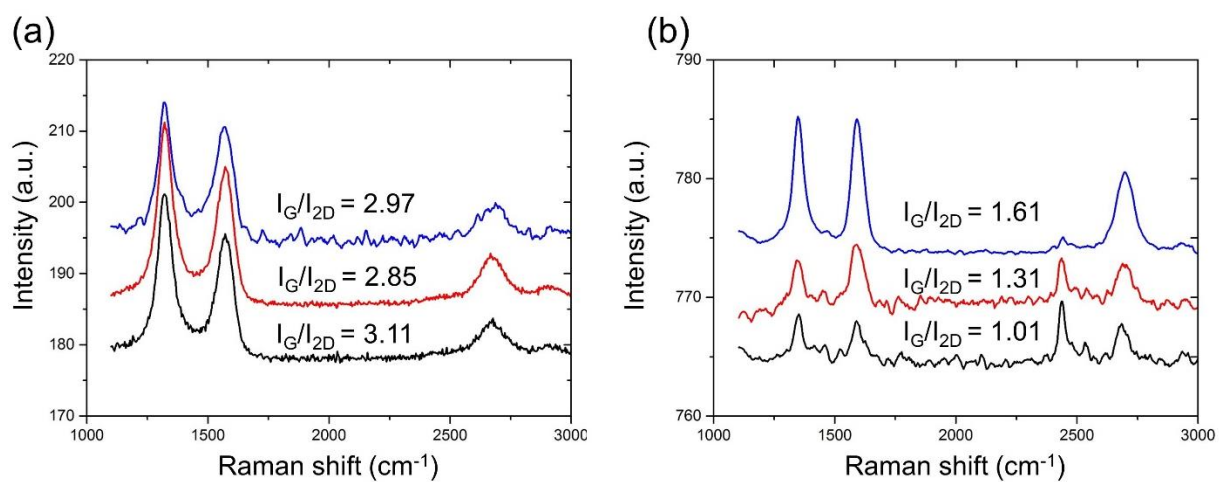


Figure S4. Raman spectrum for horizontal (a) and vertical (b) graphene film on the compared samples in Figure 5e. The black, red and blue curves represents the graphene pillar with 2, 4 and 7 layers of sidewall thickness.

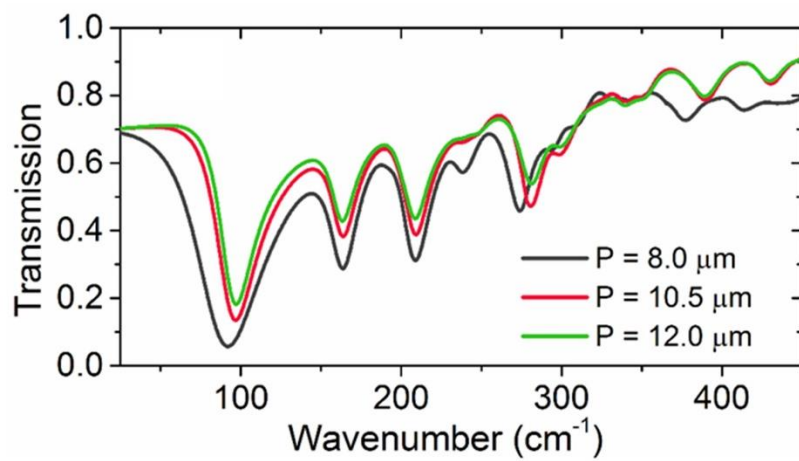


Figure S5. Dependence of transmission of the graphene wrapped pillar array on the periodicity, where $W = 6.46 \mu\text{m}$ and $H = 4.43 \mu\text{m}$.

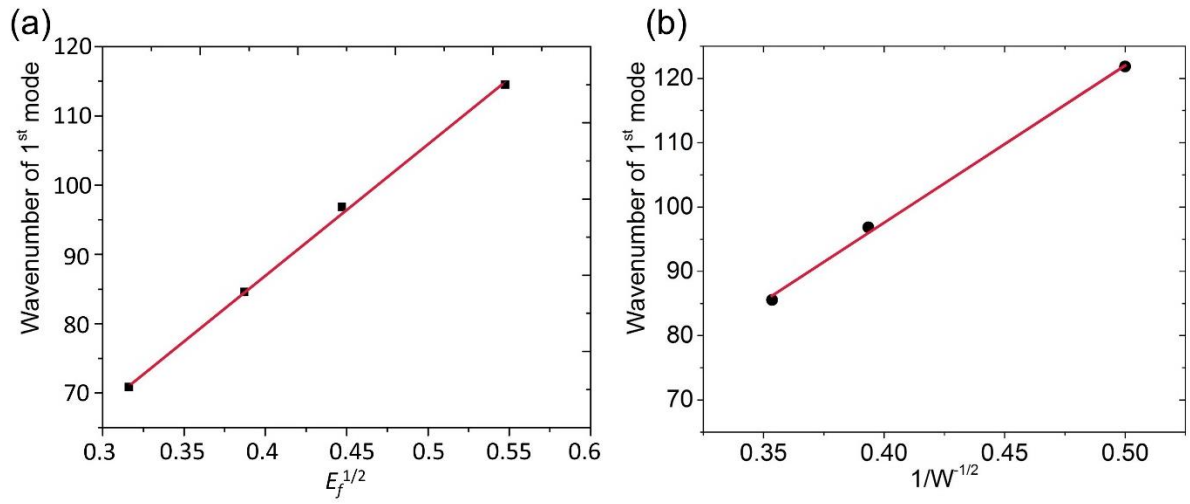


Figure S6. Relationship fitting between wavenumber of 1st mode and $E_f^{1/2}$ (a), and $1/W^{-1/2}$ (b).

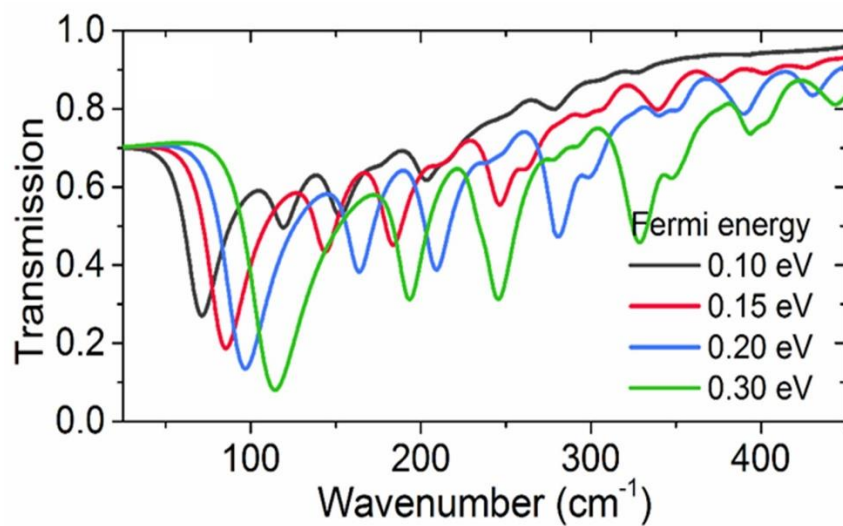


Figure S7. Dependence of transmission response of the graphene wrapped pillar array on Fermi energy of graphene.

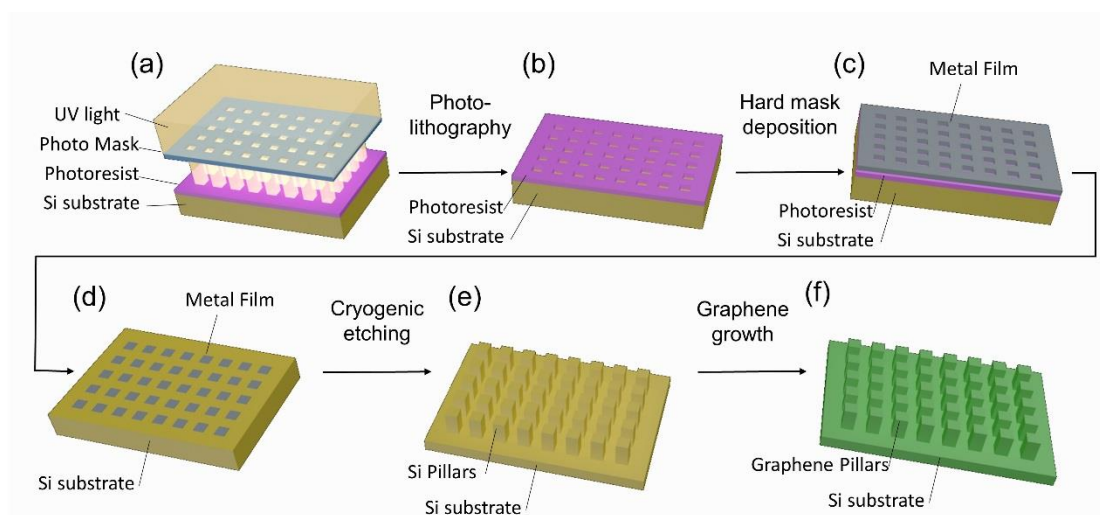


Figure S8. Schematic of the fabrication process of graphene pillars on intrinsic silicon substrate. (a) The photoresist covered substrate exposed under UV light illumination. (b) The intrinsic silicon substrate with patterned photoresist. (c) The photoresist protected silicon substrate deposited with thin metal film. (d) The silicon substrate deposited with patterned metal mask. (e) The silicon pillar arrays transferred from the hard mask protected substrate. (f) Graphene covered silicon pillar arrays.

Chapter 7 Conclusion and future work

7.1 Conclusions

This PhD dissertation focuses on the study of graphene and bismuth chalcogenides (Bi_2Se_3 , Bi_2Te_3 *et. al.*), particularly explores the large scale preparation of graphene bismuth chalcogenides and their heterostructures, and photonic and optoelectronic applications based on these materials. Utilizing the knowledge discussed in this dissertation, it is promising to improve the performance of the interested optoelectronics devices. The results demonstrated in this dissertation will enlighten future opportunities of large scale production of graphene and bismuth chalcogenides, and applications in flexible broadband optoelectronics and plasmonic devices. The major contribution of this project are outlined as below:

- Chapter 3 reveals the solvothermal growth mechanism of the bismuth chalcogenides nanoplatelets. The crystallization process of $\text{Bi}_2\text{Se}_x\text{Te}_{3-x}$ can be divided into 3 steps: (i) an introduction period for precursor dissolution and $\text{Bi}_2\text{Se}_x\text{Te}_{3-x}$ nucleation; (ii) a rapid crystal growth stage via oriented attachment of the nuclei; (iii) a slow epitaxial growth stage consuming the remaining species from the solution. It is found that the growth mechanism of binary bismuth chalcogenides nanoplatelets differs from the ternary ones. In binary bismuth chalcogenides, the nuclei share the same chemical composition and are more efficient to attach to each other and form larger crystals. However, in ternary bismuth chalcogenides, the nuclei has the different chemical composition which hindered them to grow larger and faster. Additionally, the intermediate phases (Bi_2TeO_5 , BiSeO_5 , Na_2SeO_3) are found to play a vital role in preventing the phase separation in the synthesis of ternary composition. Other parameters influences the crystal growth in the process have also been discussed in this chapter.
- Chapter 4 employs a solvothermal method to produce $\text{Bi}_2\text{Se}_x\text{Te}_{3-x}$ and graphene van der Waals heterostructures in a large scale. It is found that by using the graphene as a growth template, $\text{Bi}_2\text{Se}_x\text{Te}_{3-x}$ tend to form a particular stoichiometry of $\text{Bi}_2\text{Se}_{1.5}\text{Te}_{1.5}$ due to the minimum lattice mismatch with graphene. With enhanced interlayer interaction in $\text{Bi}_2\text{Se}_{1.5}\text{Te}_{1.5}$ and graphene heterostructure, as-produced free-standing thin film shows improved electrical, photoelectric, and mechanical properties. This chapter marries the chemical design at atomic scale with a scalable synthesis approach, and demonstrates a practical photodetector application with broad range (from visible to infrared) and flexibility.

- Chapter 5 demonstrates a new plasmonic material based on Bi₂Te₃ and graphene heterostructures. The heterostructure thin film shows strong and tunable terahertz modulation on silicon gratings with different periods. It enables about 3 times stronger plasmon coupling efficiency compared to the pure graphene thin film. The reason of the plasmon magnitude enhancement is attributed to the plasmonic hybridization effect between graphene and Bi₂Te₃. This chapter opens up new possibilities for the application of graphene- Bi₂Te₃ heterostructures in various terahertz photonic devices.
- Chapter 6 shows a novel graphene pillar structure with controllable geometry and thickness of graphene at both horizontal surfaces and vertical sidewall. Importantly, the higher order plasmonic modes can be efficiently excited on the graphene network. The underlying mechanism and parameter dependence of those modes have been discussed in details. Besides the well-known width-dependence, it is interesting to see that graphene thickness at the pillar sidewalls plays an important role in determining the resonance modes. As the side wall graphene thickness increases, obvious blue-shift in dip position has been observed. In addition, Fermi energy, decay rate, etc. also show strong influence on resonance modes, which provide feasible way to achieve a dynamic device based on graphene. The findings in chapter 6 offers a new dimension to fine tune the graphene properties in more complex 3-D structure and provide an opportunity to apply into the practical application devices, such as THz modulators and resonators. In sum, this chapter contributes to the designing of more sophisticated metamaterials based on graphene, and enables new ways of controlling terahertz and far-infrared radiation.

7.2 Future work

Our research work on the bismuth chalcogenides and graphene related 2-D materials dives into a comprehensive area, and explores a tip of the iceberg of the complex materials' synthesis and interesting properties. As the projects progressing, there are several promising aspects showing potential for further understanding and future applications. These aspects could trigger broader discussions on the material synthesis and materials optical properties, while haven't been fully explored due to the multiple reasons, such as limitation of the research equipment, finiteness of the project time line, and lack of professional support. Hence, they are proposed as future works as below:

- Firstly, our *in situ* PXRD technique has shown various advantages in observing the complex experimental processes. Regarding the complex growth process of the 2-D crystals we have demonstrated in Chapter 3 and 4 that the *in situ* PXRD technique is an important research technique to study the anisotropic growth mechanism of the crystals. Importantly, the growth mechanism have a great influence on the final morphology of the crystals, which potentially influences the final performance of the device made upon thus prepared materials. We would like to propose that the *in situ* PXRD technique could also be used in studying the solvothermal growth of other low dimensional materials, such as WS₂, MoS₂ *et. al.*. Furthermore, the same technique can be used in exploring the growth of the quasi 2-D perovskite crystal, as perovskite shows strong crystal direction dependent optoelectronic performance variations.
- Secondly, the Dirac surface of graphene and topological insulators are of great physical interests. They are promising candidate materials of the next generation on-chip photonic circuits, as these materials may enhance the heat dissipation and reduce energy consumption. To fully understand the plasmonic behaviour behind the Dirac band gap materials, more efforts should be put into the study of the Dirac surfaces on graphene and bismuth chalcogenides. For example, further study of the Dirac plasmon coupling on their metallic surfaces via both near-field and far-field methods.
- Finally, in a more forward step, we also propose the research project to navigate the surface plasmon polaritons wave in the graphene film based plasmonic circuit. Our preliminary research shows carefully designed photonic crystal with proper band gap and line defects can be created in novel EBL process. These structures are capable of trapping the near-field light in the waveguide. The light signal or the plasmonic modes in the line defect changes according to the different excitation wavelength. Therefore, we propose an active tunable photonic crystal waveguide can efficiently guide the surface plasmon on chip, which could find its promising applications in the future on-chip communication devices.

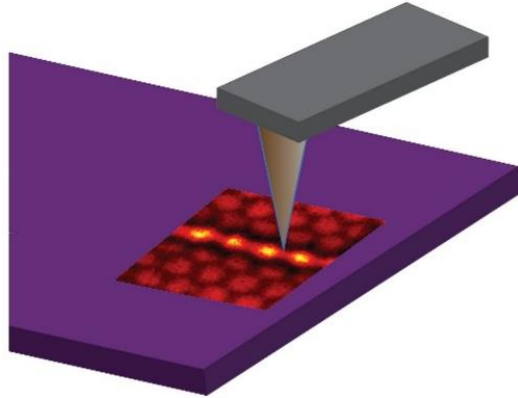


Figure 16. Schematic shows the preliminary near -field optical signal measured in a graphene based photonic crystal waveguide by the scattering NSOM.

In sum, this dissertation is the first comprehensive experimental study on bismuth chalcogenide and graphene materials regarding their synthesis, characterizations and optical applications. It ought to serve as an important source of information for future interested researches in the field of 2-D Dirac materials. Continuous research on the 2-D materials is required to generate the fundamental knowledge in this area and inspire endless creative insights on the practical applications.